Title

Nonlinear Analysis of Reinforced Concrete Panels, Slabs and Shells for Time Dependent Effects

Author

Kabir, Ahmad

Publication Date

1976-12-01

REPORT NO.
UC SESM 76-6

STRUCTURES AND MATERIALS RESEARCH
DEPARTMENT OF CIVIL ENGINEERING

NONLINEAR ANALYSIS OF REINFORCED CONCRETE PANELS, SLABS AND SHELLS FOR TIME DEPENDENT EFFECTS

BY

A. F. KABIR

Report to
National Science Foundation
NSF Grant ENG 74-02658

DECEMBER 1976

COLLEGE OF ENGINEERING
UNIVERSITY OF CALIFORNIA
BERKELEY CALIFORNIA

Structures and Materials Research
Department of Civil Engineering
Division of Structural Engineering
and
Structural Mechanics

NONLINEAR ANALYSIS OF REINFORCED CONCRETE PANELS, SLABS AND SHELLS FOR TIME DEPENDENT EFFECTS

by

Ahmad Fazlul Kabir

Faculty Investigator: A. C. Scordelis

Prepared under the Sponsorship of
National Science Foundation
Grant ENG 74-02658

College of Engineering
Office of Research Services
University of California
Berkeley, California

December 1976

NONLINEAR ANALYSIS OF REINFORCED CONCRETE PANELS, SLABS AND SHELLS FOR TIME-DEPENDENT EFFECTS

Doctor of Philosophy Ahmad Fazlul Kabir Civil Engineering

ABSTRACT

A numerical method of analysis is developed to trace the quasi-static responses of various types of reinforced concrete structures, of practical interest, under sustained load conditions. Time-dependent environmental phenomena, such as creep and shrinkage effects, are considered to obtain the evolution of the field variables of such structures in elastic and inelastic regimes. Ultimate collapses of shear panels, slabs of arbitrary geometry and free-form shell-type structures are then predicted considering local failures in steel and concrete along with the deterioration of structural stiffness due to progressive cracking.

The material behavior of concrete is characterized by a nonlinear constitutive relationship for the biaxial state of stress. This includes tensile cracking at a limiting stress level, tensile unloading after cracking and the strain-softening phenomenon beyond the maximum compressive strength. For the deformations in the concrete zones, the effects of stress history, partial creep recovery, aging and temperature variations are considered. These characterize concrete to be an aging, viscoelastic thermorheologically simple material. Creep under the biaxial state of stress is represented by the introduction of the Poisson's ratio which is observed in a uniaxial, sustained load test. The reinforcing steel, on the other hand, is represented by a bilinear, strain-hardening model exhibiting the Bauschinger effect. The unloading path due to stress reversal is also prescribed in the constitutive laws assumed for both steel and concrete.

A finite element tangent stiffness formulation, coupled with a time step integration scheme, is developed to analyze the reinforced concrete systems. Within a time step, an incremental load procedure, with an iterative approach to solve the equilibrium equations for each load increment, is adopted. The composite section of two different materials is modeled as a layer system consisting of concrete and 'equivalent smeared' steel layers. Stiffness properties of an element are then obtained by integrating the contributions from all the layers across the section.

Finally, computations for the effects of instantaneous and sustained load history are carried out for some typical examples, which include beams, panels, slabs and shells, employing membrane, plate bending, and shell elements. These numerical results demonstrate close correspondence with the available experimental data.

Signature A. C. Scordelis
Chairman of Committee

ACKNOWLEDGEMENTS

The author is deeply indebted to his thesis supervisor, Professor A. C. Scordelis, for his constant encouragement and guidance throughout all phases of this work. His friendship, sympathy and unstinted support during some difficult periods in the last five years are particularly appreciated.

Gratitude is due to Professors B. Bresler and R. DeVogelaere, members of the dissertation committee for their help and useful suggestions. Ms. L. Tsai deserves a lot of thanks for preparing the manuscript in its final form. The financial assistance provided by the National Science Foundation, under Grant No. Eng 74-02658 and the services of the Computer Centers at the University of California, Berkeley, and the Lawrence Berkeley Laboratory are acknowledged.

Finally, the author expresses his gratitude to his family and friends without whose love, affection and understanding the completion of this work would not have been possible.

TABLE OF CONTENTS

Page

ABSTRACT 1

ACKNOWLEDGEMENTS i

TABLE OF CONTENTS ii

1. INTRODUCTION 1
  1.1 General Remarks 1
  1.2 Literature Survey 3
  1.3 Objective and Scope 8

2. CONSTITUTIVE RELATIONS OF REINFORCED CONCRETE 10
  2.1 General Remarks 10
  2.2 Constitutive Relations of Concrete 10
    2.2.1 Deformation of Concrete 10
    2.2.2 Biaxial State of Stress 13
    2.2.3 Constitutive Model for Present Study 24
    2.2.4 Equivalent Uniaxial Stress-Strain Curves 27
    2.2.5 Cracking and Tension Stiffening 35
    2.2.6 Strain Softening Beyond Maximum Compressive Strength 38
    2.2.7 Stress Reversal 42
  2.3 Constitutive Relations of Steel Reinforcement 44

3. CREEP AND SHRINKAGE OF CONCRETE 47
  3.1 General Remarks 47
  3.2 Creep 47
    3.2.1 Mechanism 47
    3.2.2 Influencing Factors 48
    3.2.3 Review of Analytical Models 50
    3.2.4 Creep Under Biaxial Stress 54
    3.2.5 Creep Under High Stress Levels 58
    3.2.6 Requirements of the Creep Model 60
    3.2.7 Formulation of Analytical Model 62
    3.2.8 Determination of Creep Compliance Coefficients . . 68
    3.2.9 Comparison with Experimental Data 71
    3.2.10 Advantages of the Creep Model 74

Page

3.3 Shrinkage 78
  3.3.1 General Remarks 78
  3.3.2 Mechanism 79
  3.3.3 Influencing Factors 79
  3.3.4 Analytical Model 80

4. METHOD OF ANALYSIS 84
4.1 General Remarks 84
4.2 Finite Element Displacement Formulation 84
4.3 Sources of Nonlinearity in Reinforced Concrete Structural Response 87
4.4 Techniques for Nonlinear Analysis 88
4.5 Types of Finite Elements Used 91
  4.5.1 One-dimensional Truss Element 93
  4.5.2 Triangular Shell Element 95
  4.5.3 Triangular Membrane Element 104
  4.5.4 Triangular Plate Bending Element 104
  4.5.5 Boundary Spring Element 105
4.6 Solution Steps in the Present Method of Analysis 106
4.7 Solution Procedure for Creep and Shrinkage Effects 111
4.8 State Determination in Concrete Layers 113
4.9 Convergence Criteria 117
4.10 Computer Program 120

5. NUMERICAL EXAMPLES AND INTERPRETATION OF RESULTS 123
5.1 General Remarks 123
5.2 Example 1 - Washa-Fluck Beams C3-C6 125
5.3 Example 2 - Cervenka Wall Panel W2 139
5.4 Example 3 - McNiece Slab 152
5.5 Example 4 - Gable Hyperbolic Paraboloid Shell 167
5.6 Computer Time 203

6. CONCLUSIONS 206
6.1 Summary 206
6.2 Conclusions 208
6.3 Recommendations for Future Studies 209

Page

REFERENCES 211

APPENDIX A - Input Instructions for Computer Program NOTACS . . . .

1. INTRODUCTION

1.1 General Remarks

The usage of reinforced concrete as a building material for complex structural systems has increased tremendously over the years. Many of the structures, such as the structural units for nuclear containment systems, require sophisticated analysis and design procedures to guarantee adequate provisions for public safety. The current design methods are usually based on a linear-elastic analysis with the simplifying assumptions that the materials are uncracked, homogeneous, isotropic and linearly elastic. However, experimental and field studies of such reinforced concrete structures as shells, folded plates, etc., have indicated that many of these structures are loaded beyond the range of linear-elastic behavior. Furthermore, the behavior is influenced by long-term effects such as creep, shrinkage, temperature variation and load history. For many structures, these may prove to be more critical to the serviceability requirements than short time loading effects. Since structures are designed to serve for a period of time, it is essential that they perform satisfactorily within the design period. In order to guarantee the serviceability of any structure throughout the operating period, it may be important to perform an analysis to obtain the response history during that period incorporating inelastic and time-dependent effects. Moreover, for the correct estimation of safety against failure, an ultimate analysis becomes mandatory.

The development of an analytical model for reinforced concrete structures is complicated because of the following factors:

1. Reinforced concrete is not homogeneous, being composed of two different materials, concrete and steel. Concrete, itself, is nonhomogeneous, having aggregates and cement paste as the main components. The structural properties of concrete, such as strength and deformation, can only be determined at the macroscopic level and thus represent averaged values. The variations due to the microscopic structure are generally ignored because of the complexities involved and because satisfactory prediction of structural response can be made using properties at the macroscopic level.

2. The structural elements have a continuously changing geometry due to the progressive cracking under increasing or sustained loads and environmental changes.

3. The constitutive relationship for concrete is nonlinear and is a function of many variables. The failure criteria under multiaxial stress states are very complex and dependent on many factors.

4. Concrete deformations are dependent on the load and environmental history. Time-dependent factors such as creep, shrinkage, temperature and humidity variations are often the major contributors to the total deformations. Concrete, moreover, is an aging material and its properties change with passage of time.

5. Cracking in concrete shows randomness in the sense that although it is possible to predict the area where cracking will occur, the actual location and direction will depend on the local variations in the microstructure of concrete.

6. Effects of dowel action in the steel reinforcement, aggregate interlocking and bond-slip between the reinforcement and concrete are very difficult to model analytically.

Experiments on microconcrete models can furnish valuable insight into the behavior of prototypes but such tests are very expensive and time-consuming, particularly when time-dependent effects are to be considered. Moreover, a large number of models need to be tested to consider the possible variations of the important parameters. Therefore, it is essential to develop general methods of analysis to complement, and eventually, to replace the physical experiments. The accuracy and reliability of such methods, however, have to be confirmed by selected well-controlled experiments.

1.2 Literature Survey

The earliest published application of the finite element method to reinforced concrete structures was by Ngo and Scordelis [1.1]. Simply supported beams were studied using constant strain triangular (CST) elements for both concrete and steel. Special bond link elements were used to simulate bond between steel and concrete. Linear-elastic analyses were performed on beams with predefined crack patterns to determine principal stresses in the concrete, stresses in the steel reinforcement and bond stresses. Ngo, Scordelis and Franklin [1.2], using the same approach, studied shear in beams with diagonal tension cracks, considering the effects of stirrups, dowel shear, aggregate interlock and horizontal splitting along reinforcement near the supports.

Nilson [1.3,1.4] introduced nonlinear material and bond-slip relationships to study tensile members. Cracking was accounted for by stopping the solution, when tensile failure in any element was indicated, and redefining a new structure.

Bresler, et al. [1.6] carried out experimental and analytical studies to determine the influence of load cycling on bond between concrete and steel reinforcement. A finite element model was also developed assuming a "boundary layer" adjacent to the steel-concrete interface whose elastic constants were reduced to account for the effects of cracks and inelastic deformations.

Franklin [1.5] developed an incremental, iterative procedure to trace the response history in one continuous computer analysis. Cracking was accounted for by modifying the material properties and redistributing the unbalanced forces. Reinforced concrete frames, with or without infilled shear panels, were studied using frame-type elements, quadrilateral plane stress elements, one-dimensional truss elements, two-dimensional bond links and tie links.

Numerous investigators have studied reinforced concrete structures with plane stress elements. Most of these solutions are similar to each other and incorporate cracking and nonlinear material properties using different finite elements or different constitutive relationships and failure criteria for the concrete. Cracks are either considered to exist between the element boundaries or in the majority of the cases within an element.

Zienkiewicz, et al. [1.7] made two-dimensional stress studies which include tensile cracking and elasto-plastic behavior in compression and used an "initial stress" approach. Cervenka and Gerstle [1.8,1.9] derived a constitutive relationship for a composite concrete-steel material and studied reinforced concrete shear walls and spandrel beams under monotonically increasing or cyclic loads.

McCutcheon, Mirza, Mufti, et al. [1.10, 1.11] have studied plane stress problems incorporating automatic cracking and bond failures.

Yuzugullu and Schnobrich [1.12] analyzed shear wall frame systems with composite plane stress quadrilateral elements for walls, special flexural elements for frames and link elements to connect wall elements to frame elements. Darwin and Pecknold [1.13] proposed a solution for wall-frames which incorporated load reversals. A number of additional papers [1.14,1.15,1.16,1.17] have been published on plane stress systems, which differ slightly from those mentioned above.

Jofriet and McNiece [1.18] studied progressive cracking of reinforced concrete slabs with a semi-empirical bilinear moment-curvature relationship. Bell and Elms [1.19,1.20] used a similar approach to study slabs.

A layer-type solution, where the slab elements are assumed to be divided into layers and the layers are cracked progressively, is used by several investigators including Dotroppe, et al. [1.12]; Berg, et al. [1.22,1.23]; Backlund [1.24]; Schafer, et al. [1.25]; and Wegner, et al. [1.26]. Berg included nonlinear geometry effects in his solution.

The analysis of reinforced concrete thin shells including cracking by the finite element method is complicated by the fact that the in-plane membrane (plane stress) action and the plate bending action are coupled.

Lin [1.27,1.28] used a triangular shell element composed of a constant strain triangular (CST) membrane element and a linearly constrained curvature triangular (LCCT) plate bending element. A layered system was adopted for tracing progressive cracking. Elasto-plastic material behavior in compression and the Von Mises yield criteria were assumed.

Bell and Elms [1.29] made a shell analysis by accounting for progressive cracking in an approximate manner by using reduced flexural and membrane stiffnesses for the elements. The stiffnesses were dependent on the stress level at a particular load.

Hand, et al. [1.30] used layered shallow shell rectangular elements to analyze reinforced concrete shells.

Very little work has been done in treating reinforced concrete systems as general three-dimensional solids, because of the computational effort involved and the lack of knowledge of the concrete material behavior under three-dimensional stress states. Suidan and Schnobrich [1.31] used a 20-node three-dimensional isoparametric element for the analyses of beams. Elasto-plastic behavior of concrete and steel and the Von Mises yield criteria were assumed.

Ngo [1.32] used a network-topological approach to generate automatically crack lines in the finite elements. The elements used were a bar element, a two-dimensional isoparametric element, a bond element and a link element.

A large number of papers dealing with finite element analysis of axisymmetric solids under axisymmetric loading have been published. Rashid [1.33,1.34] and Wahl and Kasiba [1.35] made early finite element studies of prestressed concrete reactor vessels treated as axisymmetric structures. Comprehensive papers on the analysis of concrete reactor vessels have been presented by Zienkiewicz, et al. [1.36] and by Argyris, et al. [1.37].

The finite element method has also been applied to investigate the behavior of reinforced concrete structures for time-dependent effects such as creep, shrinkage, temperature changes and load history.

Bresler [1.38] described in detail the important factors that affect the long-term behavior of reinforced concrete structures. Deformation in concrete due to loading and unloading under variable environmental conditions, such as temperature and moisture changes, and variable stress history was examined. A stress-strain law, which took into account time, temperature and moisture effects, was proposed. Two methods of analysis, considering time and environment-dependent processes, were outlined for tracing the deformation and stress histories of reinforced concrete structures. The reinforced concrete composite section was modeled as a layered system, having steel and concrete layers, in order to incorporate variations of material properties across the depth of the section.

Selna [1.39,1.40] formulated a concrete constitutive model to account for creep, shrinkage and cracking. Concrete was assumed to be linear visco-elastic material. He analyzed concrete columns, beams and frames by a step-by-step integration in the temporal domain.

Aas-Jacobson [1.41] analyzed reinforced concrete frames for creep and geometric nonlinearities. An effective modulus method, rate of creep method and strain-hardening method were used to calculate creep strain. Aldstedt [1.42] analyzed plane reinforced concrete frames considering a nonlinear stress-strain relationship for concrete, geometric nonlinearity, creep and bond-slip effects.

Scanlon and Murray [1.43,1.44] extended Selna's creep model to the biaxial stress case and analyzed slabs for time-dependent effects and cracking. The concrete instantaneous stress-strain relationship was assumed to be linear elastic.

Rashid [1.45] presented analyses of two-dimensional concrete structures incorporating nonisothermal creep and reversed loadings. Sarne [1.46] analyzed three-dimensional concrete solids incorporating both nonlinear material and time-dependent effects.

A comprehensive state-of-the-art review of the finite element method for analyzing reinforced concrete structures was presented by Scordelis

[1.47]. He dealt with several types of systems such as beams, plane stress, plate bending, combined plane stress and plate bending, axisymmetric solids and general three-dimensional solids. Both short- and long-time loads were considered.

More recently, Schnobrich [1.48,1.49] and Wegner [1.50] have also surveyed the various applications of the finite element method to predict the behavior of reinforced concrete structures and the advantages and shortcomings of some of the models being used.

Since 1967 an increasing number of papers have been published on the finite element analysis of reinforced concrete. Many of these have not been mentioned here as they essentially duplicate the works mentioned above.

1.3 Objective and Scope

A numerical method of analysis is developed to trace the quasistatic responses of various types of reinforced concrete structures, for example, shear panels, beams, slabs and shells, under short-term or sustained load conditions. Time-dependent environmental phenomena, such as creep and shrinkage effects, are considered to obtain the evolution of the field variables--deflections, strains and stresses--of these structures in elastic and inelastic regimes. Ultimate collapses of these structures are then predicted considering local failures in steel and concrete along with the deterioration of structural stiffness due to progressive cracking.

A finite element tangent stiffness formulation, coupled with a time step integration scheme, is developed to analyze reinforced concrete structures. Within a time step, an incremental load procedure, with an iterative approach to solve the equilibrium equations for each load increment, is adopted to trace the nonlinear behavior of such structures.

The reinforced concrete composite section is modeled as a layered system of concrete and "equivalent smeared" steel layers. Perfect bond is assumed to exist between concrete and steel layers. Stiffness properties of an element are then obtained by integrating the contributions from all the layers across the section.

Concrete behavior under the biaxial state of stress is represented by a nonlinear constitutive relationship which incorporates tensile cracking at a limiting stress, tensile stiffening between cracks and strain-softening phenomenon beyond the maximum compressive strength. Effects of stress history, partial creep recovery, aging, temperature variations and shrinkage are included in the estimation of long-time deformations in the concrete zones. Creep under biaxial state of stress and at high stress levels is considered. The steel reinforcement is represented by a bilinear, strain-hardening model exhibiting the Bauschinger effect. The constitutive relations are based on small displacement theory. Unloading paths are prescribed in the constitutive relations for stress reversals.

Finally, several examples including beams, panels, slabs and shells, are analyzed using the present method of analysis, employing triangular membrane, plate bending and shell elements. The applicability of the method to analyze various types of reinforced concrete structures is demonstrated and the responses of these strucutres to sustained load conditions are studied. Numerical results obtained from the analyses are compared to available experimental data to check the validity of the method of analysis presented herein.

2. CONSTITUTIVE RELATIONS OF REINFORCED CONCRETE

2.1 General Remarks

Reinforced concrete is a composite material consisting of concrete and steel reinforcement. Most of the properties of steel reinforcement can be specified consistently because of the homogeneity of the material in the macroscopic sense. Concrete, on the other hand, is heterogeneous--its chief constituents being cement paste and aggregates. Concrete is unique among structural materials in that it interacts with its environment, undergoing complex physical and chemical changes with the passage of time. It is, therefore, quite a difficult task to determine accurately the changing properties of concrete with time and under changing environmental conditions.

The material properties of concrete and steel will depend on the stress or strain state of the material. It is assumed that perfect bond exists between steel and concrete, and hence, the bond-slip phenomenon will not be considered. In the case of the plate bending element and the shell element, the strain state will vary across the depth of the element causing such material states as cracking, yielding, etc., which will spread progressively through the depth. Such elements will be divided into concrete and steel layers through their depths to take into account the variation in the material properties through the depth.

2.2 Constitutive Relations of Concrete

2.2.1 Deformation of Concrete

Deformation of concrete is very important in the analysis and design of reinforced concrete structures as one of the important criteria for serviceability is based on the extent of deformation. The complexity of the factors affecting the deformation of concrete has prevented, as yet, the formulation of a general theory of deformation encompassing all experimental observations. However, the following general facts have been observed in the behavior of concrete.

Figure 2.1 shows the deformations of a concrete specimen (a cylinder or a cube) under different loading and environmental conditions to illustrate the different factors that generally influence the deformations. Figure 2.1a records the deformation of the specimen with the passage of time under no external loads. Such a deformation, which mainly occurs because of hygral inequilibrium between the specimen and environment, is defined as shrinkage.

Figure 2.1b shows the deformation history of the specimen under hygral equilibrium and a constant axial compressive load. At time t_0 when the load is applied, there is deformation which may be defined as instantaneous elastic deformation. With passage of time from t_0 to t_1, and increase in deformation is observed though there is no shrinkage deformation as hygral equilibrium is maintained between the specimen and the environment. Also, since the load is kept constant there cannot be any increment in the instantaneous deformation. The increment in deformation with time under a sustained load is defined as creep.

Creep is usually defined in the literature as that part of deformation which is in excess of nominal instantaneous elastic deformation. In reality, concrete is an aging material which means that its strength increases with the passage of time. So, the true instantaneous elastic

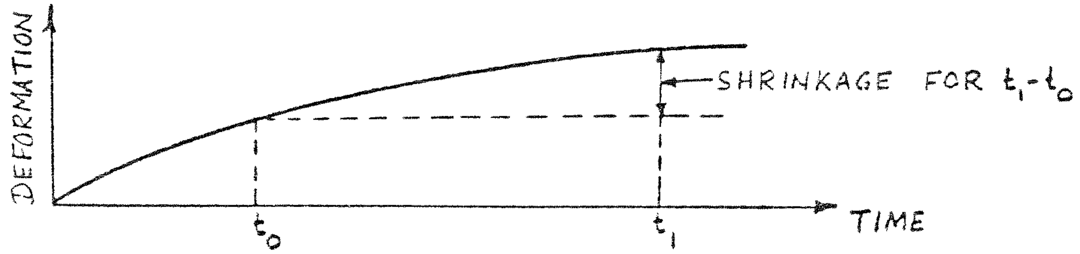

a. SHRINKAGE OF AN UNLOADED SPECIMEN

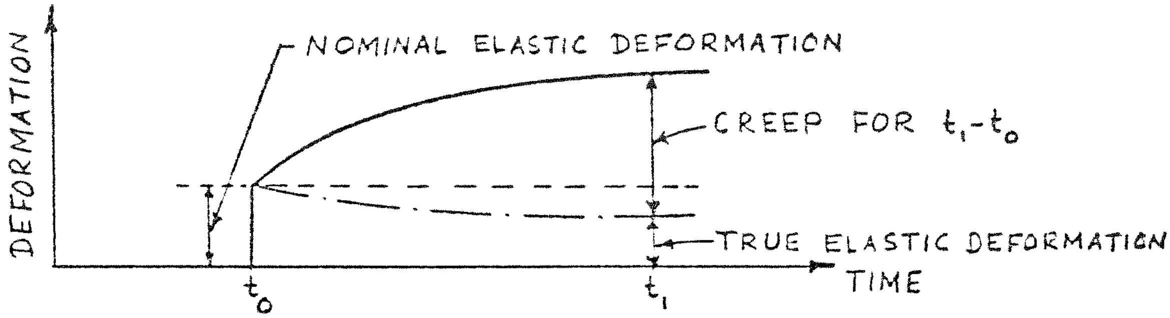

b. CREEP OF A LOADED SPECIMEN IN HYGRAL EQUILIBRIUM WITH THE AMBIENT MEDIUM

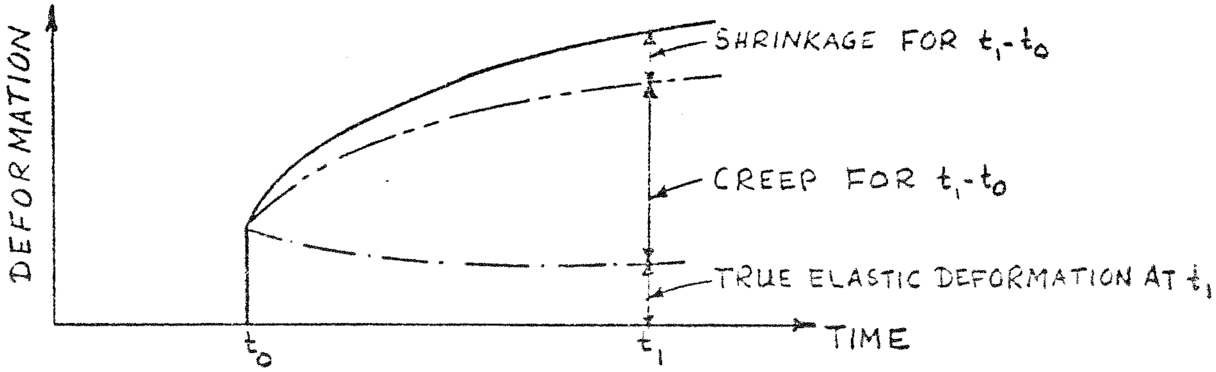

c. CHANGE OF DEFORMATION OF A LOADED AND DRYING SPECIMEN

FIG. 2.1 DEFORMATION COMPONENTS OF CONCRETE deformation at time t_1 will be less than that obtained at time t_o. The creep should, then, be defined as the deformation in excess of the true instantaneous elastic deformation.

Figure 2.1c shows the creep, shrinkage and elastic parts of the deformation of a loaded specimen. This is a simplified approach which is not fully accurate since creep and shrinkage are shown to be additive while, in reality, they are not independent phenomena. In fact, the presence of shrinkage increases creep. In the present study, the simplified approach will be adopted. In this chapter the constitutive relations of concrete for instantaneous elastic deformation will be considered while the the next chapter will deal with creep and shrinkage effects.

2.2.2 Biaxial State of Stress

Concrete under a biaxial state of stress, as assumed to occur in such structural elements as slabs, shells, folded plates, etc., shows a different behavior than that under a uniaxial state of stress. Figure 2.2 shows typical experimental stress-strain curves for concrete under biaxaial compression highlighting the differences between the uniaxial and biaxial states.

First , it is seen that the maximum compressive strength increases for the biaxial stress state. Kupfer, Hilsdorf and Rusch [2.1] obtained experimental values of biaxial compressive strengths which are as much as 27% higher than the uniaxial ones.

Second, concrete "ductility" at maximum compressive strength increases for the biaxial stress state.

Third, the stiffness of concrete in one of the principal directions increases in the presence of compressive stress in the

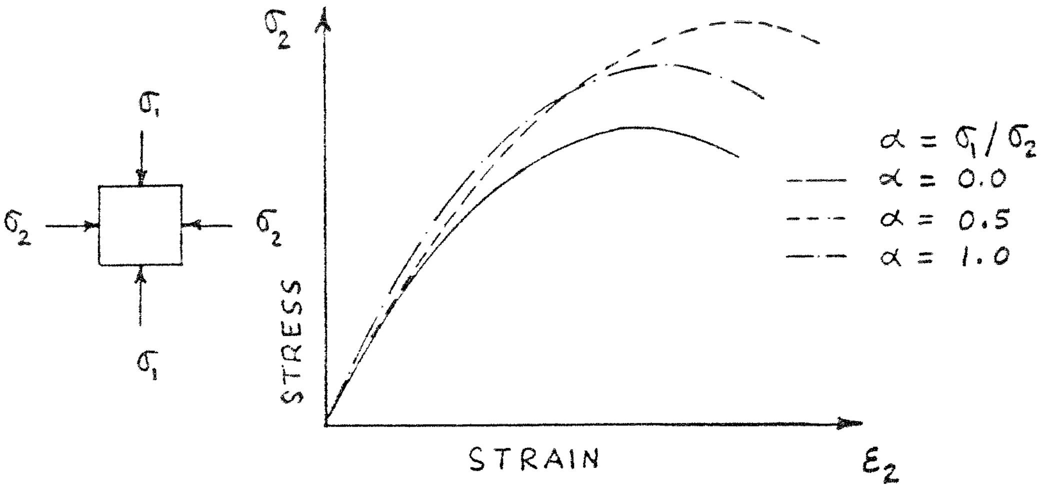

FIG. 2.2 STRESS-STRAIN RELATIONSHIPS OF CONCRETE UNDER BIAXIAL COMPRESSION

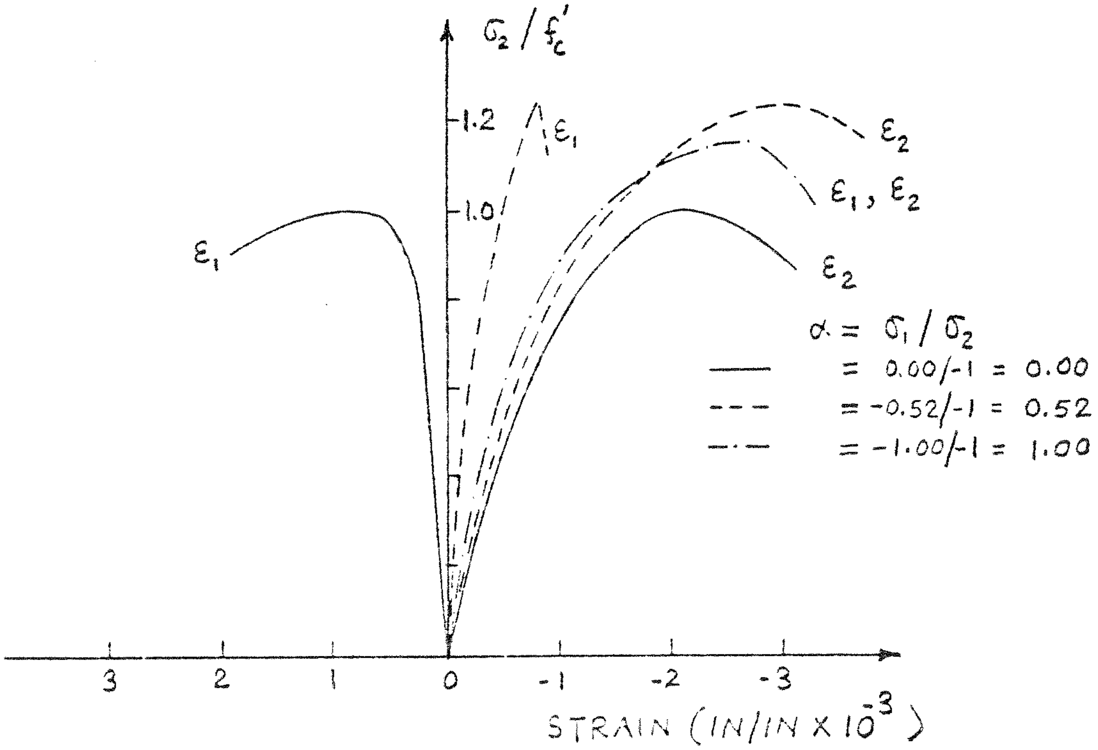

FIG. 2.3 EXPERIMENTAL STRESS-STRAIN CURVES FOR BIAXIAL COMPRESSION [2.1]

perpendicular direction. According to microcracking theory, the increase in stiffness is mainly due to the confinement of potential microcracking in the presence of biaxial stresses.

Recognizing the fact that the constitutive relationship in the biaxial state of stress will be different from that in the uniaxial case, several investigators [2.1,2.2,2.3,2.4,2.5,2.6] presented experimental data on specimens under biaxial states of stress.

Much of the early information is suspect because of the recent recognition of the technical difficulties involved in obtaining the stress state desired and measuring accurately the extremely small multiaxial strains. Kupfer, et al. [2.1], provide some of the most complete experimental information on the biaxial behavior and ultimate strength of concrete. Stress-strain curves obtained from biaxially loaded specimens tested at different ratios of principal stresses were presented (Figs. 2.3, 2.4, 2.5). The ratio of the stresses was held constant throughout loading, thus providing the proportional loading condition. Nine ratios were examined covering the entire range of compression-compression, compression-tension and tension-tension. Biaxial strength envelope (Fig. 2.6) and failure modes for various stress ratios were also presented.

Liu, et al. [2.7], modeled concrete as an orthotropic material under biaxial loading. For biaxial compression, they proposed a constitutive relationship of the form:

$$\sigma_i = \frac{\varepsilon_i E_o}{(1-\nu\alpha)\left[1 + \left(\frac{1}{1-\nu\alpha}\frac{E_o}{E_s} - 2\right)\left(\frac{\varepsilon_i}{\varepsilon_p}\right) + \left(\frac{\varepsilon_i}{\varepsilon_p}\right)^2\right]} \qquad (2.1)$$

where σ_i, ε_i = stress and strain in the principal stress direction

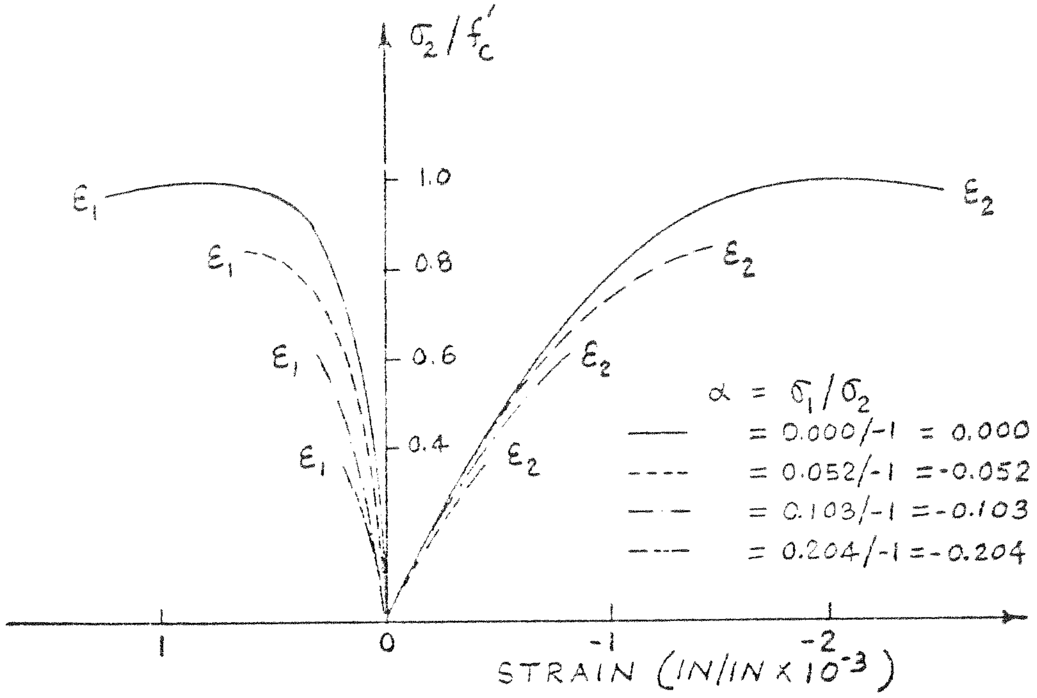

FIG. 2.4 EXPERIMENTAL STRESS-STRAIN CURVES FOR BIAXIAL TENSION-COMPRESSION [2.1]

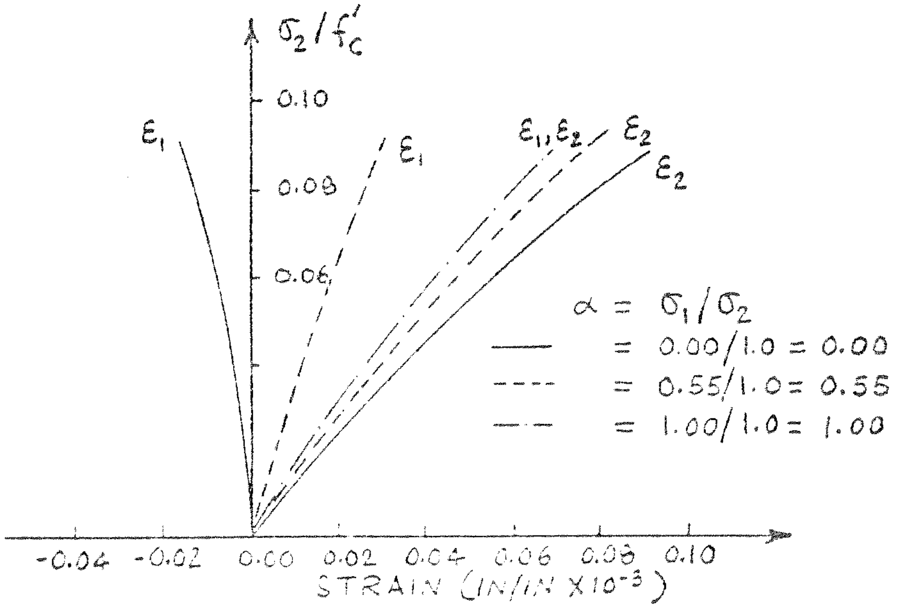

FIG. 2.5 EXPERIMENTAL STRESS-STRAIN CURVES FOR BIAXIAL TENSION [2.1]

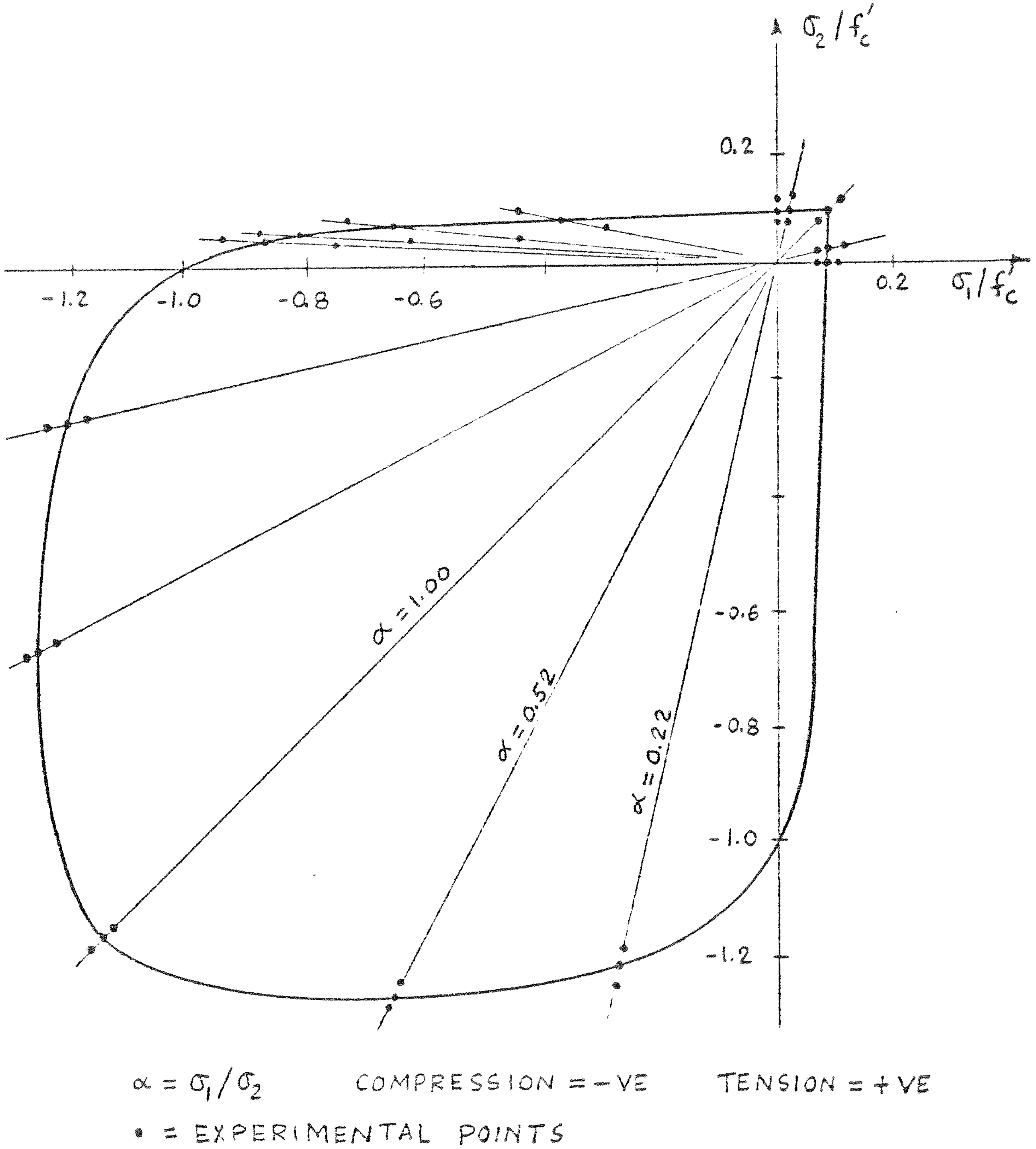

FIG. 2.6 EXPERIMENTAL BIAXIAL STRENGTH ENVELOPE [2.1]

i ; σ_p, ε_p = maximum biaxial compressive stress and corresponding strain ; ν = Poisson's ratio ; E_o = initial tangent modulus under uniaxial loadings ; E_s = secant modulus at maximum stress, σ_p/ε_p;and α = stress ratio, σ_1/σ_2, $\sigma_1 > \sigma_2$. It should be noted here that compressive stresses and strains are assumed to be negative whereas tensile stresses are assumed to be positive. This is the sign convention followed in this study unless otherwise indicated.

For a uniaxial stress state, i.e., $\alpha = 0$, Eq. (2.1) reduces to the stress-strain relationship proposed by Saenz [2.8]. Equation (2.1) is valid for biaxial compression only, and does not take into account load reversal. The value of ε_p in the major compressive direction, i.e. direction 2, is fixed at 0.0025, while ε_p in minor direction 1 varies. Maximum compressive strength, σ_p, has a constant value of 1.2 f'_c for values of α between 0.2 to 1.0. Here, f'_c refers to maximum compressive strength under uniaxial loading.

Romstad, et al.[2.9], proposed an elaborate multilinear biaxial constitutive model for concrete. In this model, the principal stress or strain space is divided into regions of equal damage, each of which possesses particular values of modulus of elasticity and Poisson's ratio.

Kupfer and Gerstle [2.10] have proposed an isotropic material model. They presented a series of expressions for the secant shear modulus and the secant bulk modulus. The expressions were derived by curve fitting the data obtained by testing three sets of concrete specimens under various combinations of monotonic biaxial stress. Octahedral shear stress is the controlling parameter of the model behavior. This model does not account for unloading and the correspondence with experimental data is not good at high stress levels. Concrete is also assumed to be isotropic in this model, whereas stress-strain curves under biaxial stresses strongly suggest stress-induced orthotropic material behavior as illustrated in Fig. 2.7.

Chen, et al. [2.11], assumed concrete to be an isotropic, homogeneous and linearly elastic, plastic, strain-hardening and fracture material. The initial discontinuous surface, loading surfaces, and failure surface of concrete are developed, and the elasto-plastic stress-strain incremental relationships of concrete are derived for plane stress case in matrix form. The loading surfaces in principal stress space and octrahedral stress space are illustrated in Figs. 2.8 and 2.9.

Darwin and Pecknold [2.12,1.13] have extended Liu's [2.7] model to incorporate cyclic loading and strain-softening in compression. This model is illustrated in Fig. 2.10. For biaxial compression, they suggested a family of curves, depending on the biaxial stress ratio, to express the constitutive relationship:

$$\sigma_i = \frac{E_o \varepsilon_{iu}}{1 + \left[\frac{E_o}{E_s} - 2\right]\left(\frac{\varepsilon_{iu}}{\varepsilon_{ic}}\right) + \left(\frac{\varepsilon_{iu}}{\varepsilon_{ic}}\right)^2} \tag{2.2}$$

where ε_{iu} = 'equivalent uniaxial strain' in the principal stress direction i ; σ_{ic}, ε_{ic} = maximum compressive stress and corresponding strain in the principal direction i to be obtained from the biaxial failure envelope of Kupfer and Gerstle [2.10] ; E_o = initial uniaxial tangent modulus;and E_s = secant modulus, $\sigma_{ic}/\varepsilon_{ic}$.

For tension,

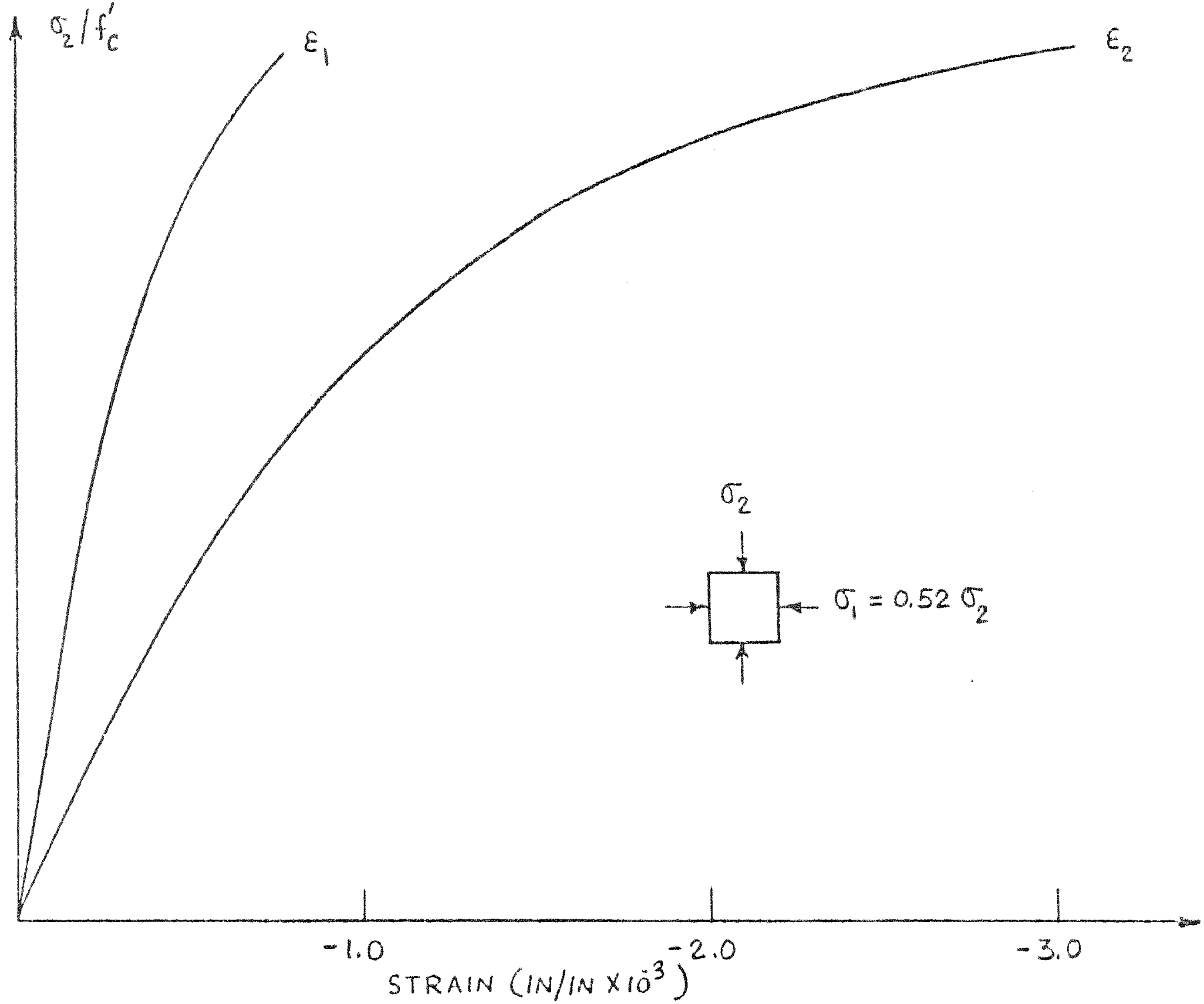

FIG. 2.7 BEHAVIOR OF PLAIN CONCRETE UNDER BIAXIAL COMPRESSION [2.1]

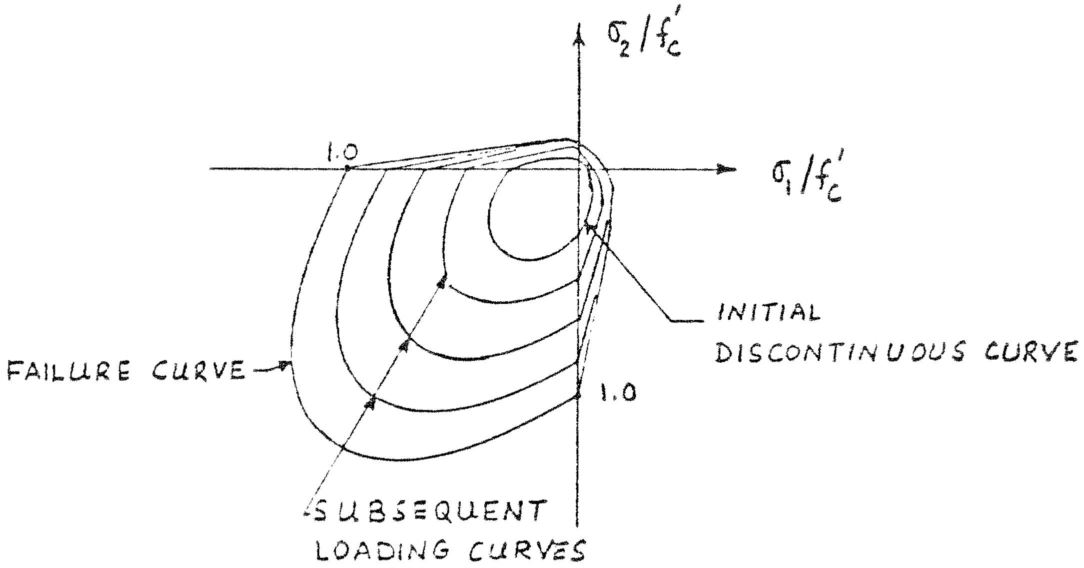

FIG. 2.8 THEORETICAL BIAXIAL LOADING CURVES IN PRINCIPAL STRESS SPACE FOR STRAIN-HARDENING CONCRETE [2.11]

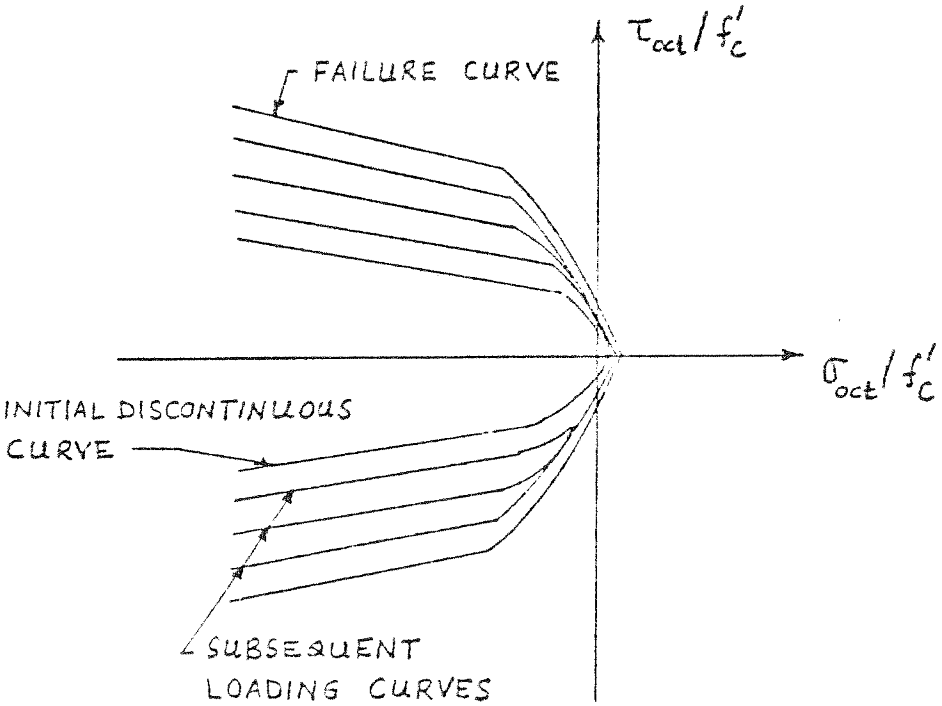

FIG. 2.9 THEORETICAL BIAXIAL LOADING CURVES IN OCTAHEDRAL STRESS SPACE FOR STRAIN-HARDENING CONCRETE [2.11]

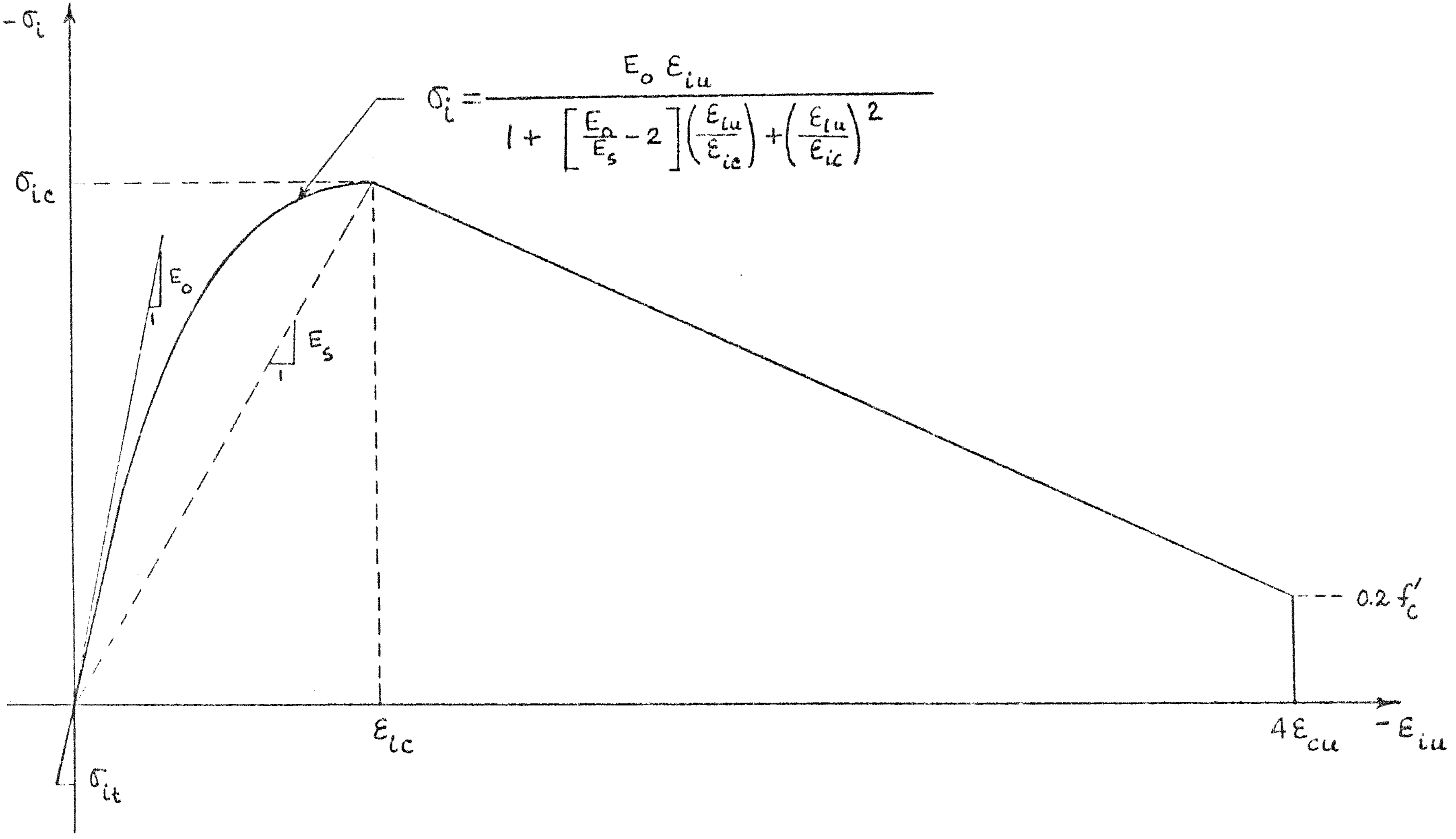

FIG. 2.10 EQUIVALENT UNIAXIAL STRESS-STRAIN MODEL FOR CONCRETE PROPOSED BY DARWIN,ET AL.[2.12]

$$\sigma_i = E_o \varepsilon_{iu} \qquad (2.3)$$

for $\sigma_i \leq \sigma_{it}$

where σ_{it} = tensile strength of concrete in principal stress direction i.

The concept of 'equivalent uniaxial strain' provides a means of separting the Poisson effect from the cumulative strain and permits a convenient representation of concrete under plane stress as an incrementally linear orthotropic material.

In the absence of any experimental data on biaxial cylic loading, Darwin, et al. adopt the envelope curve, obtained from experiments conducted by Karsan and Jirsa [2.16] on concrete specimens under uniaxial cyclic loading, as the basis for their model of the strain-softening phenomenon beyond the maximum compressive strength for biaxial cyclic loading. The strain-softening envelope is assumed to drop lienarly from maximum compressive strength, σ_{ic}, to a stress level of 0.2 f'_c at an ultimate crushing strain of 4 ε_{cu}, where f'_c and ε_{cu} are the maximum compressive strength and corresponding strain from a uniaxial load test. The stress and strain at ultimate crushing are assumed to be independent of the biaxial stress ratio. Unloading due to cyclic loading is assumed to occur with a slope equal to the initial uniaxial tangent modulus, E_o, before the maximum compressive strength, σ_{ic}, is reached. Beyond σ_{ic}, the unloading and reloading paths are modeled in a more complex fashion and will not be described here.

In the present study, the concrete material model suggested by Darwin, et al., will be adopted with some modifications. This model is easy to incorporate in an incrementally linear, orthotropic plane stress constitutive relationship as often used in the finite element analysis of structures with material nonlinearity.

2.2.3 Constitutive Model for Present Study

A displacement formulation of the finite element method is used in the present investigation for analyzing structures with material nonlinearities. To trace the nonlinear load-deformation behavior of such structures, the finite element method, which is a linear method of analysis, is used in an incremental load step solution procedure with an iterative approach at each load step. The material is assumed to be linear for each iteration. A linear solution is then obtained, the material properties are updated, and the iterative procedure is continued until the correct solution is approached within some allowable tolerances. The material matrix used for each element is to be in an incremental form to accommodate the changes after each iteration. For an isotropic material under plane stress, the incremental constitutive relationship is given as:

$$\begin{Bmatrix} d\sigma_1 \\ d\sigma_2 \\ d\tau_{12} \end{Bmatrix} = \frac{1}{1-\nu^2}\begin{bmatrix} E & \nu E & 0 \\ \nu E & E & 0 \\ 0 & 0 & (1-\nu^2)G \end{bmatrix}\begin{Bmatrix} d\varepsilon_1 \\ d\varepsilon_2 \\ d\gamma_{12} \end{Bmatrix} \tag{2.4}$$

where E = uniaxial tangent modulus , $G = E/2(1+\nu)$ = uniaxial shear modulus, ν = Poisson's ratio, and 1 and 2 are principal stress directions.

Equation (2.4) may be extended for orthotropic material as:

$$\begin{Bmatrix} d\sigma_1 \\ d\sigma_2 \\ d\tau_{12} \end{Bmatrix} = \frac{1}{1-\nu_1\nu_2}\begin{bmatrix} E_1 & \nu_2 E_2 & 0 \\ \nu_1 E_1 & E_2 & 0 \\ 0 & 0 & (1-\nu_1\nu_2)G' \end{bmatrix}\begin{Bmatrix} d\varepsilon_1 \\ d\varepsilon_2 \\ d\gamma_{12} \end{Bmatrix} \tag{2.5}$$

where 1 and 2 are the orthotropic material directions; E_1, E_2 = tangent moduli in directions 1 and 2 under uniaxial loading; ν_1, ν_2 = Poisson's ratio in directions 1 and 2; and G' = shear modulus for the orthotropic material under plane stress.

Concrete under a biaxial state of stress behaves as an orthotropic material in the two principal stress directions as illustrated by the experimental results in Fig. 2.7. In the present study, concrete is assumed to be orthotropic in the principal stress directions. Moreover, as an approximation for simplicity, it is assumed that $\nu^2 = \nu_1\nu_2$, where ν is the effective Poisson's ratio under biaxial stress; and for symmetric material behavior, $\nu_1 E_1 = \nu_2 E_2$ is assumed. No experimental data are available regarding the value of the shear modulus under the biaxial state of stress, G'. It has been demonstrated [2.12] that a value of

$$G' = \frac{1}{4(1 - \nu^2)}[E_1 + E_2 - 2\nu\sqrt{E_1E_2}\,]$$

does not show bias to any particular direction with respect to shear stiffness. The above value is also adopted in the current study. Hence:

$$\begin{Bmatrix} d\sigma_1 \\ d\sigma_2 \\ d\tau_{12} \end{Bmatrix} = \frac{1}{1 - \nu^2}\begin{bmatrix} E_1 & \nu\sqrt{E_1E_2} & 0 \\ \nu\sqrt{E_1E_2} & E_2 & 0 \\ 0 & 0 & \frac{1}{4}(E_1+E_2-2\nu\sqrt{E_1E_2}) \end{bmatrix}\begin{Bmatrix} d\varepsilon_1 \\ d\varepsilon_2 \\ d\gamma_{12} \end{Bmatrix} \qquad (2.6)$$

is the incrementally linear, orthotropic constitutive relationship adopted for concrete under a biaxial state of stress.

The above equation, Eq. (2.6), gives the constitutive relationship in the principal stress directions. If the element coordinate system x-y is such that the principal directions 1-2 make an angle, θ, with respect to x-y, then the constitutive relationship in the element coordinate system, after proper coordinate transformations, is given by:

$$\begin{Bmatrix} d\sigma_{xx} \\ d\sigma_{yy} \\ d\tau_{xy} \end{Bmatrix} = \frac{1}{1 - \nu^2} \begin{bmatrix} E_1 c^2 + E_2 s^2 & \nu\sqrt{E_1 E_2} & \frac{1}{2}(E_1 - E_2)cs \\ & E_1 s^2 + E_2 c^2 & \frac{1}{2}(E_1 - E_2)cs \\ \text{(Symm.)} & & \frac{1}{4}(E_1 + E_2 - 2\nu\sqrt{E_1 E_2} \end{bmatrix} \begin{Bmatrix} d\varepsilon_{xx} \\ d\varepsilon_{yy} \\ d\gamma_{xy} \end{Bmatrix} \tag{2.7}$$

where $c = \cos\theta$, $s = \sin\theta$, $c^2 = \cos^2\theta$, and $s^2 = \sin^2\theta$.

Thus, the concrete material properties needed at any iteration of the solution procedure are the orthotropic moduli, E_1 and E_2; and the effective Poisson's ratio, ν.

The value of Poisson's ratio is obtained from experiments. Below the elastic limit, the value of Poisson's ratio varies from 0.18 to 0.20 [2.1]. At a stress level higher than 80% of the ultimate stress, an increase in its value is observed. However, a constant value of Poisson's ratio is taken for all stress levels in the present investigation. It is felt that for the cases studied here the constant value of Poisson's ratio is a good approximation.

The terms E_1 and E_2 , as used in Eq. (2.6), are the tangent moduli from uniaxial load tests in the orthotropic directions 1 and 2. Equation (2.6) is derived on the basis that for biaxial compression, an increase in effective stiffness in either direction, in the presence of normal compression stress, is due to the Poisson effect alone. However, experimental results [2.3] indicate that a considerably greater increase in stiffness is obtained in the presence of biaxial stress than can be explained by the Poisson effect alone. The main cause of this increased stiffness seems to be the confinement of potential microcracking in the presence of biaxial compression. Therefore, the use of Eq. (2.6) is only appropriate at low stress levels when microcrack confinement is not prominent.

To account for microcracking confinement, it is obvious that values of E_1 and E_2 from uniaxial stress-strain curves cannot be used. If, on the other hand, Poisson's effect is removed from experimental biaxial stress-strain curves in compression, then a family of stress-strain curves can be constructed whose slopes would provide values for E_1 and E_2 incorporating the microcrack confinement effect and can be used in Eq. (2.6). These curves are called the 'equivalent uniaxial' stress-strain curves by Darwin, et al. [2.12]. The construction procedure for the equivalent uniaxial stress-strain curves is described in the next subsection.

2.2.4 Equivalent Uniaxial Stress-Strain Curves

A typical equivalent uniaxial stress-strain curve used in this study is shown in Fig. 2.11. The compressive loading part is described by Darwin, et al. [2.12] as:

$$\sigma_i = \frac{E_o \varepsilon_{iu}}{1 + \left[\frac{E_o}{E_s} - 2\right]\left(\frac{\varepsilon_{iu}}{\varepsilon_{ic}}\right) + \left(\frac{\varepsilon_{iu}}{\varepsilon_{ic}}\right)^2} \tag{2.8}$$

and for tension:

$$\sigma_i = E_o \varepsilon_{iu} \qquad \sigma_i \leq \sigma_{it} \tag{2.9}$$

where σ_i = stress (positive for tension, negative for compression) in the principal direction i; σ_{ic} = maximum compressive stress in the principal direction i to be obtained from the biaxial failure envelope of Kupfer and Gerstle [2.10]; ε_{ic} = equivalent uniaxial strain corresponding to peak compressive stress, σ_{ic}. It is obtained by removing the Poisson effect from experimental strain values corresponding to peak compressive stresses under biaxial stresses as observed by Kupfer, et al. [2.1]. E_o = initial uniaxial tangent modulus; E_s = secant modulus, $\sigma_{ic}/\varepsilon_{ic}$; and σ_{it} = tensile strength of concrete in principal stress direction i.

The equivalent uniaxial strain is the strain obtained by removing Poisson's effect from the biaxial strain but retaining the effects of microcrack confinement. The following illustration will indicate how this value of strain may be obtained from experimental data.

For concrete under biaxial compression, at a stress of σ_1, σ_2 where $\alpha = \sigma_1/\sigma_2$, we may write:

$$d\varepsilon_2 = \frac{d\sigma_2}{E_2} - \nu \frac{d\sigma_1}{E_1} \tag{2.10}$$

where $d\varepsilon_2$ = increment in strain in principal direction 2; $d\sigma_1$, $d\sigma_2$ = increment in stresses in principal directions 1 and 2, assuming proportional loading; E_1, E_2 = tangent moduli in directions 1 and 2, assuming the material to be piecewise linear during the increment. Equation (2.10) may be rearranged as:

$$d\sigma_2 = E_2 \frac{d\varepsilon_2}{1-\nu\alpha n}$$

$$\text{or, } d\sigma_2 = E_2 d\varepsilon_{2u} \tag{2.11}$$

where α = biaxial stress ratio, σ_1/σ_2; n = modular ratio, E_2/E_1; and

$d\varepsilon_{2u}$ = increment in equivalent uniaxial strain in direction 2, $d\varepsilon_2/(1-\nu\alpha n)$. It is obvious that the slope E_2 of the stress-strain curve represented by Eq. (2.11) does not contain the Poisson effect which is removed by the introduction of $d\varepsilon_{2u}$ and hence can be used in Eq. (2.6). However, since microcrack confinement effects influence the experimentally observed values of $d\varepsilon_2$ and hence, $d\varepsilon_{2u}$, the value of E_2 will include the microcrack confinement effect.

The total equivalent uniaxial strain is given by:

$$\varepsilon_{iu} = \sum d\varepsilon_{iu} = \sum \frac{d\varepsilon_i}{(1-\nu\alpha n)} = \sum \frac{d\sigma_i}{E_i} \tag{2.12}$$

where $\sum$ = summation for all increments.

The slope E_i of the equivalent uniaxial stress-strain curve at a point $(\sigma_i, \varepsilon_{iu})$ for loading in compression is given by differentiating Eq. (2.8):

$$E_i = \frac{\partial \sigma_i}{\partial \varepsilon_{iu}} = \frac{E_0(1-q^2)}{\left(1 + \left[\frac{E_0}{E_s} - 2\right] q + q^2\right)^2} \tag{2.13}$$

where $q = (\varepsilon_{iu}/\varepsilon_{ic})$. For tension, the slope may be obtained by differentiating Eq. (2.9):

$$E_i = \frac{\partial \sigma_i}{\partial \varepsilon_{iu}} = E_0 \tag{2.14}$$

The equivalent uniaxial stress-strain curve, obtained from biaxial loading and illustrated in Fig. 2.11, has an initial slope E_0, and passes through the point of maximum stress under biaxial loading and corresponding equivalent uniaxial strain--$(\sigma_{ic}, \varepsilon_{ic})$ in case of compression and $(\sigma_{it}, \varepsilon_{it})$ in case of tension. The point of maximum

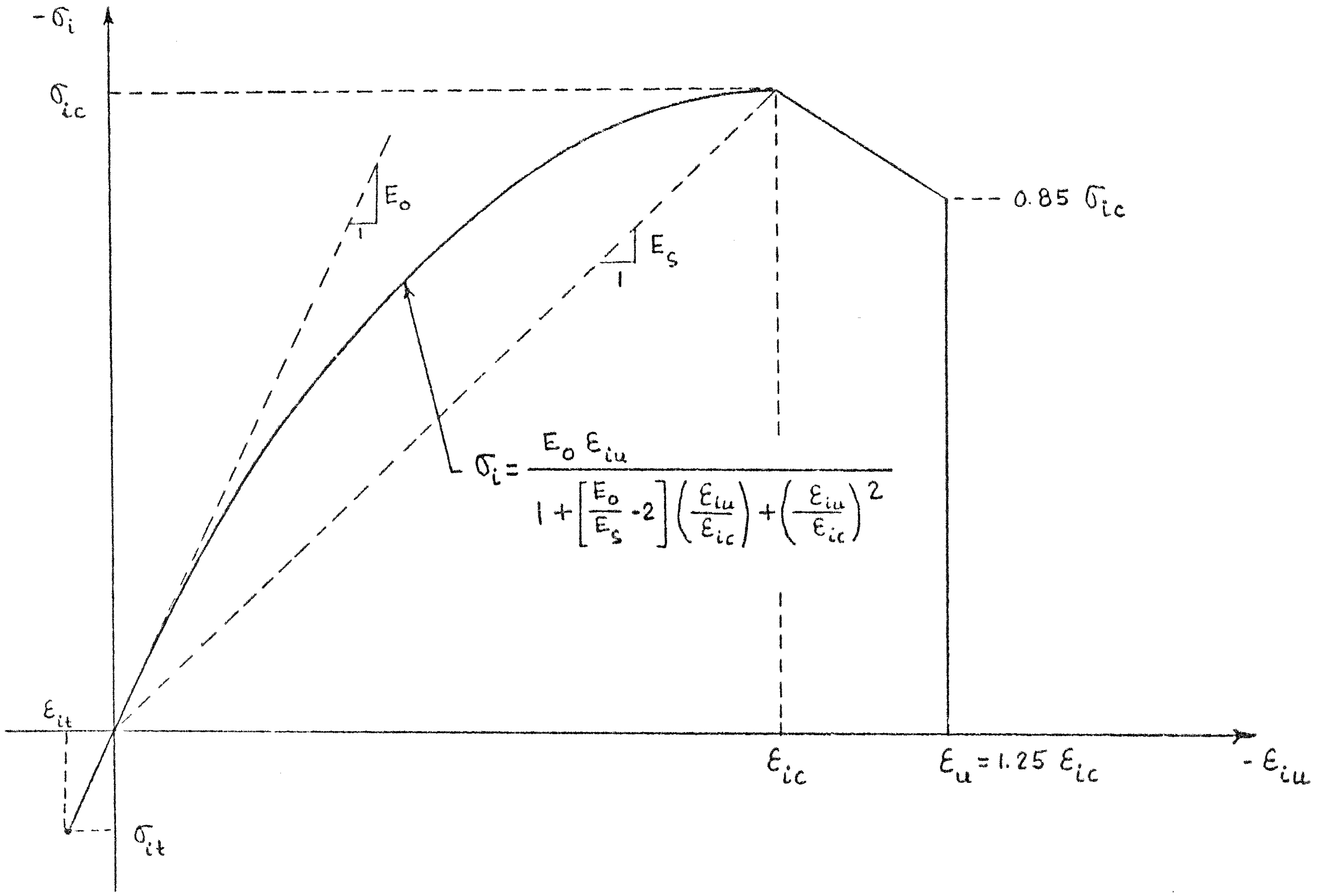

FIG. 2.11 EQUIVALENT UNIAXIAL STRESS-STRAIN CURVE USED IN THE PRESENT STUDY

stress under biaxial loading is a function of the principal stress ratio, α; the uniaxial compressive and tensile strengths, f'_c and f'_t; and strain at peak uniaxial stress, ε_{cu}. The values of the maximum stresses, σ_{1c} and σ_{2c}, in the two principal directions are obtained from the modified biaxial strength envelope of Kupfer and Gerstle [2.10] which is illustrated in Fig. 2.12. The biaxial strength envelope can be divided into several regions depending on the stress ratio and stress state. Compressive stresses are assumed to be negative while tensile stresses are taken to be positive. The principal stress directions 1 and 2 are so chosen that, algebraically, $\sigma_1 \geq \sigma_2$. The different regions and the maximum biaxial stresses, σ_{1c} and σ_{2c}; and corresponding equivalent uniaxial strain, ε_{1c} and ε_{2c}, in these regions are summarized below.

1. For σ_1 = compression, σ_2 = compression. $0 \leq \alpha \leq 1$

$$\sigma_{2c} = \frac{1 + 3.65\alpha}{(1 + \alpha)^2} f'_c \tag{2.15a}$$

$$\sigma_{1c} = \alpha\, \sigma_{2c} \tag{2.15b}$$

$$\varepsilon_{2c} = \varepsilon_{cu}[3p_2 - 2] \tag{2.16a}$$

$$\varepsilon_{1c} = \varepsilon_{cu}[-1.6p_1^3 + 2.25p_1^2 + 0.35p_1] \tag{2.16b}$$

where $p_1 = \sigma_{1c}/f'_c$ and $p_2 = \sigma_{2c}/f'_c$.

Equation (2.15) is based on the Kupfer and Gerstle [2.10] biaxial strength envelope while Darwin, et al. [2.12] proposed Eq. (2.16) based on experimental observations of strains corresponding to peak stresses under biaxial compression. Concrete is assumed to yield beyond the maximum compressive stress when a further increase in strain causes a decrease in stress and failure due to crushing occurs at a specified

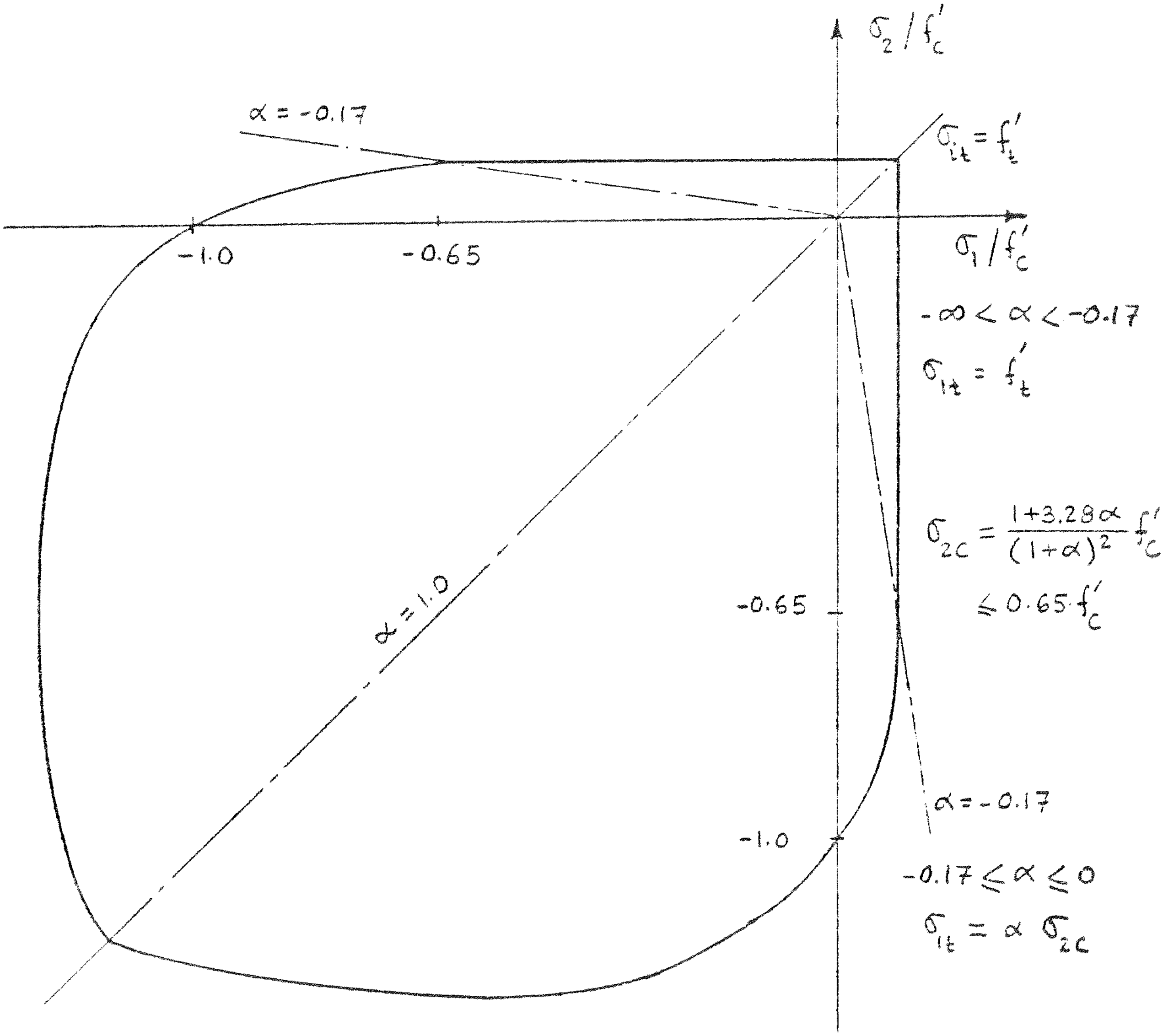

$$\sigma_{2c} = \frac{1+3.65\,\alpha}{(1+\alpha)^2}\, f_c$$

$$\sigma_{1c} = \alpha\, \sigma_{2c}$$

$$\alpha = \sigma_1/\sigma_2$$

COMPRESSION = -VE
TENSION = +VE

FIG. 2.12 BIAXIAL STRENGTH ENVELOPE USED IN THE PRESENT STUDY ultimate strain. Concrete behavior beyond yielding will be discussed in more detail in subsection 2.2.6.

2. For σ_1 = tension, σ_2 = compression. $-0.17 \leq \alpha \leq 0$

$$\sigma_{2c} = \frac{1 + 3.28\alpha}{(1 + \alpha)^2} f'_c \tag{2.17a}$$

$$\sigma_{1t} = \alpha \sigma_{2c} \tag{2.17b}$$

$$\varepsilon_{2c} = \varepsilon_{cu}[4.42-8.38p_2+7.54p_2^2-2.58p_2^3] \tag{2.18a}$$

where $p_2 = \sigma_{2c}/f'_c$

$$\varepsilon_{1t} = \sigma_{1t}/E_o \tag{2.18b}$$

Darwin, et al. [2.12] suggested Eq. (2.17) while Eq. (2.18) is given by Rajagopal [2.14]. Failure in this zone is assumed to occur due to the yielding and crushing of concrete in the compression direction.

3. For σ_1 = tension, σ_2 = compression. $-\infty < \alpha < -0.17$

$$\sigma_{2c} = 0.65 f'_c \tag{2.19a}$$

$$\sigma_{1t} = f'_t \tag{2.19b}$$

$$\varepsilon_{2c} = \varepsilon_{cu}[4.42-8.38p_2+7.54p_2^2-2.58p_2^3] \tag{2.20a}$$

where $p_2 = \sigma_{2c}/f'_c = 0.65$

$$\varepsilon_{1t} = \sigma_{1t}/E_o \tag{2.20b}$$

Failure in this zone is assumed to occur due to cracking in the tension direction.

4. For σ_1 = tension, σ_2 = tension. $1 < \alpha < \infty$

$$\sigma_{1t} = \sigma_{2t} = f'_t \tag{2.21}$$

$$\varepsilon_{1t} = \varepsilon_{2t} = f'_t/E_o \tag{2.22}$$

For biaxial tension, the uniaxial tensile strength, f'_t, is chosen as the tension cut-off point beyond which cracking is assumed to occur.

Five material properties of concrete are needed for the construction of the equivalent uniaxial stress-strain curves. These are (1) uniaxial initial tangent modulus, E_o; (2) uniaxial compressive strength, f'_c; (3) strain corresponding to uniaxial compressive strength, ε_{cu}; (4) uniaxial tensile strength, f'_t; and (5) Poisson's ratio, ν.

All five parameters may be obtained from uniaxial load tests on concrete and used. Another option, based on recommendations by different ACI committees, is also used in the present study in cases where experimental data are not available.

ACI Committee 209 [3.5] suggests that:

$$E_o(t) = 33.0\ w^{1.5} \sqrt{f'_c(t)} \tag{2.23}$$

where t = time in days after casting, $E_o(t)$ = initial uniaxial tangent modulus in psi at time t, w = unit weight of concrete in pcf and $f'_c(t)$ = uniaxial compressive strength in psi at time t.

ACI Committee 209 [3.5] also recommends that:

$$f'_c(t) = \frac{t}{4.0 + 0.85t}\, f'_c(28) \tag{2.24}$$

where $f'_c(28)$ = uniaxial compressive strength in psi, 28 days after casting.

ACI Committee 209 [3.5] also suggests that:

$$f'_t(t) = \frac{1}{3}\sqrt{w\ f'_c(t)} \tag{2.25}$$

where $f'_t(t)$ = tensile strength in psi, t days after casting.

Hognestad [2.15] suggested the following relationship for the strain corresponding to peak uniaxial compressive stress:

$$\varepsilon_{cu}(t) = 2\ f'_c(t)/E_o(t) \tag{2.26}$$

where $\varepsilon_{cu}(t)$ = strain corresponding to peak stress $f'_c(t)$ at t days after casting.

The value of Poisson's ratio is assumed to be independent of age and stress level in the present study although at a stress level higher than 0.8 f'_c, significant increase in this value has been observed [2.1]. Generally, Poisson's ratio for concrete is taken to be 0.15 in this study.

2.2.5 Cracking and Tension Stiffening

One of the most significant properties of concrete is its low tensile strength which results in tensile cracking at very low stress compared to compressive stresses. The tensile cracking reduces the stiffness of the concrete and is a major contributor to the nonlinear behavior of reinforced concrete structures.

For the proposed model, a maximum stress criterion is used to determine concrete failure in tension. Whenever one of the principal stresses exceeds the uniaxial tensile strength of concrete, a crack is assumed to form perpendicular to the direction of that stress. The constitutive relationship for concrete after a crack is formed, say in direction 1, is given by assuming tangent modulus E_1 to be equal to zero in Eq. (2.6); thus:

$$\begin{Bmatrix} d\sigma_1 \\ d\sigma_2 \\ d\tau_{12} \end{Bmatrix} = \begin{bmatrix} 0 & 0 & 0 \\ 0 & E_2 & 0 \\ 0 & 0 & \beta G \end{bmatrix} \begin{Bmatrix} d\varepsilon_1 \\ d\varepsilon_2 \\ d\gamma_{12} \end{Bmatrix} \tag{2.27}$$

where β = cracked shear constant.

The cracked shear constant is introduced to estimate the effective shear modulus along the tensile cracks due to the effect of dowel action and aggregate interlock. Lin [1.27] found that the solution was insensitive to the numerical value of the constant β where a range of 0.0 to 1.0 was used. However, numerical instability may arise if a value of 0.0 is used.

Once the concrete is cracked in one direction, the formation of a new tensile crack is restricted to a direction orthogonal to the first crack. The constitutive relationship, in case cracks in both principal directions occur, is given by:

$$\begin{Bmatrix} d\sigma_1 \\ d\sigma_2 \\ d\tau_{12} \end{Bmatrix} = \begin{bmatrix} 0 & 0 & 0 \\ 0 & 0 & 0 \\ 0 & 0 & \beta G \end{bmatrix} \begin{Bmatrix} d\varepsilon_1 \\ d\varepsilon_2 \\ d\gamma_{12} \end{Bmatrix} \tag{2.28}$$

When the concrete reaches the ultimate tensile strength, cracks are formed at finite intervals as shown in Fig. 2.13 for a reinforced concrete element under uniaxial stress. The total load is carried across the cracks by the reinforcement, but the concrete between the cracks carry stresses because of bond between the reinforcement and concrete. The concrete stress is zero at the cracks but it is not if

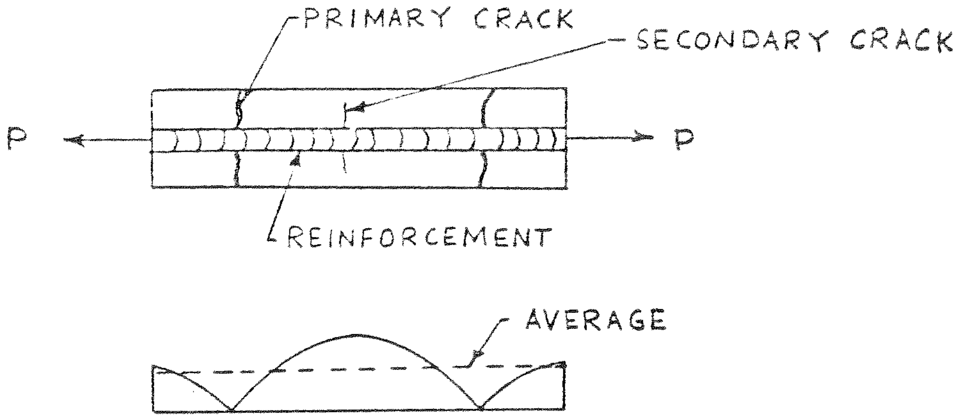

STRESS IN CONCRETE

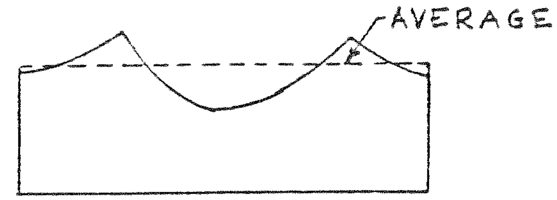

STRESS IN REINFORCEMENT

FIG. 2.13 STRESS DISTRIBUTION IN A CRACKED REINFORCED CONCRETE ELEMENT

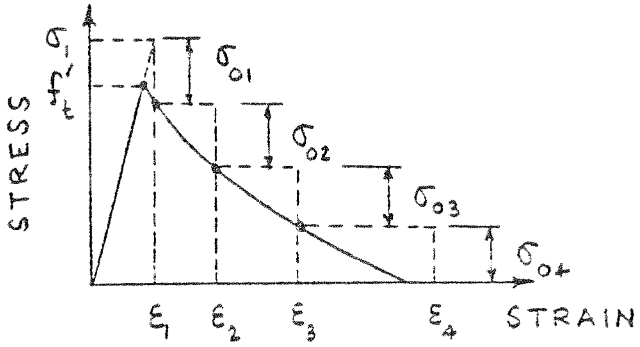

FIG. 2.14 GRADUAL UNLOADING FOR CRACKED CONCRETE ELEMENT

averaged over the length. This is known as the tension stiffening effect. With increasing load, the number of cracks over the finite length increases and the average stress taken by concrete decreases. This has been represented as an unloading curve by Lin [1.27]. The tensile modulus of the concrete is assumed to be zero once the tensile crack forms, but the unbalanced stresses are released in a step-wise fashion depending on the strain level as shown in Fig. 2.14. The same model will be adopted for the present investigation.

2.2.6 Strain-Softening Beyond Maximum Compressive Strength

Experimental results [2.1] indicate that concrete is a strain-softening material under a biaxial stress state. This implies that concrete deteriorates under further loading beyond the maximum compressive stress level. The deterioration of concrete causes unloading and further increase in strain will result in a decrease in stresses. This will cause instability and the stress-strain curve will slope downwards.

Experimental results [2.1] indicate that the ultimate strain is generally 1.2 to 1.3 times the strain corresponding to peak compressive strength in the major compression direction. The stress corresponding to ultimate strain varies between 0.8 to 0.9 times the peak compressive strength. In the present study, unless specified otherwise, the ultimate strain in compression is taken as 1.25 ε_{ic} and the corresponding stress as 0.85 σ_{ic}. The strain-softening curve is assumed linear between the peak compressive stress and the stress corresponding to the ultimate strain (Fig. 2.15).

The strain-softening model adopted here is different from

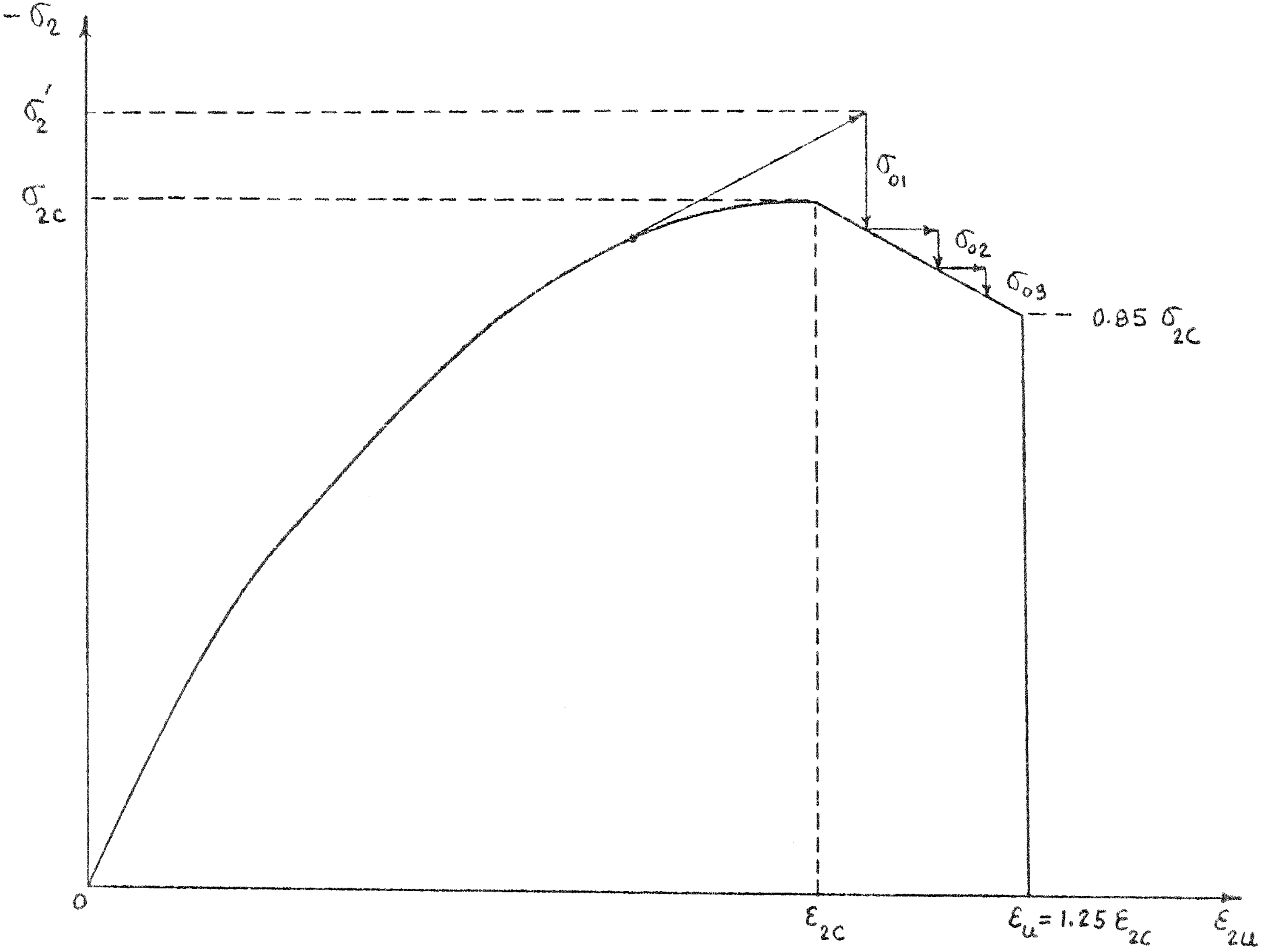

FIG. 2.15 UNBALANCED STRESSES DUE TO STRAIN SOFTENING

Darwin's [2.12] model. Darwin's strain-softening curve is based on the envelope curves (Fig. 2.16) obtained from uniaxial cyclic load tests of Karsan and Jirsa [2.16]. In the present study, stress reversals occur mainly due to unloading in the concrete fibers due to creep effects. A model based on numerous cycles of loadings and unloadings is thus not chosen to reflect these stress reversals. The strain-softening values observed in biaxial monotonic tests performed by Kupfer, et al. [2.1] are therefore chosen for the strain-softening model as a first approximation.

The tangent modulus of the unloading part is negative, which may cause computational problems if used in the constitutive equation, Eq. (2.6). To circumvent this, the following technique is adopted. When the major compressive principal stress, σ_2' in Fig. 2.15, has reached a value such that $|\sigma_2'| > |\sigma_{2c}|$, 'yielding' is assumed to have occurred. Moduli are assumed to be zero for the next load iteration. At the stress level σ_2', an unloading of σ_{01} occurs, which is the unbalanced stress. The unbalanced stress is redistributed in the next load iteration. The term σ_{02} becomes the new unbalanced stress and so on until crushing occurs at ε_u.

The reason for using a zero modulus instead of a negative one is mainly to facilitate the numerical solution of the finite element equilibrium equations. The constitutive relationship for the finite element formulation, after yielding has taken place, is:

$$d\underset{\wedge}{\sigma} = \underline{0}\; d\underset{\wedge}{\varepsilon} \tag{2.29}$$

It should be noted here than an 'unconstrained flow rule' is assumed for the unloading part once yielding has started. This implies

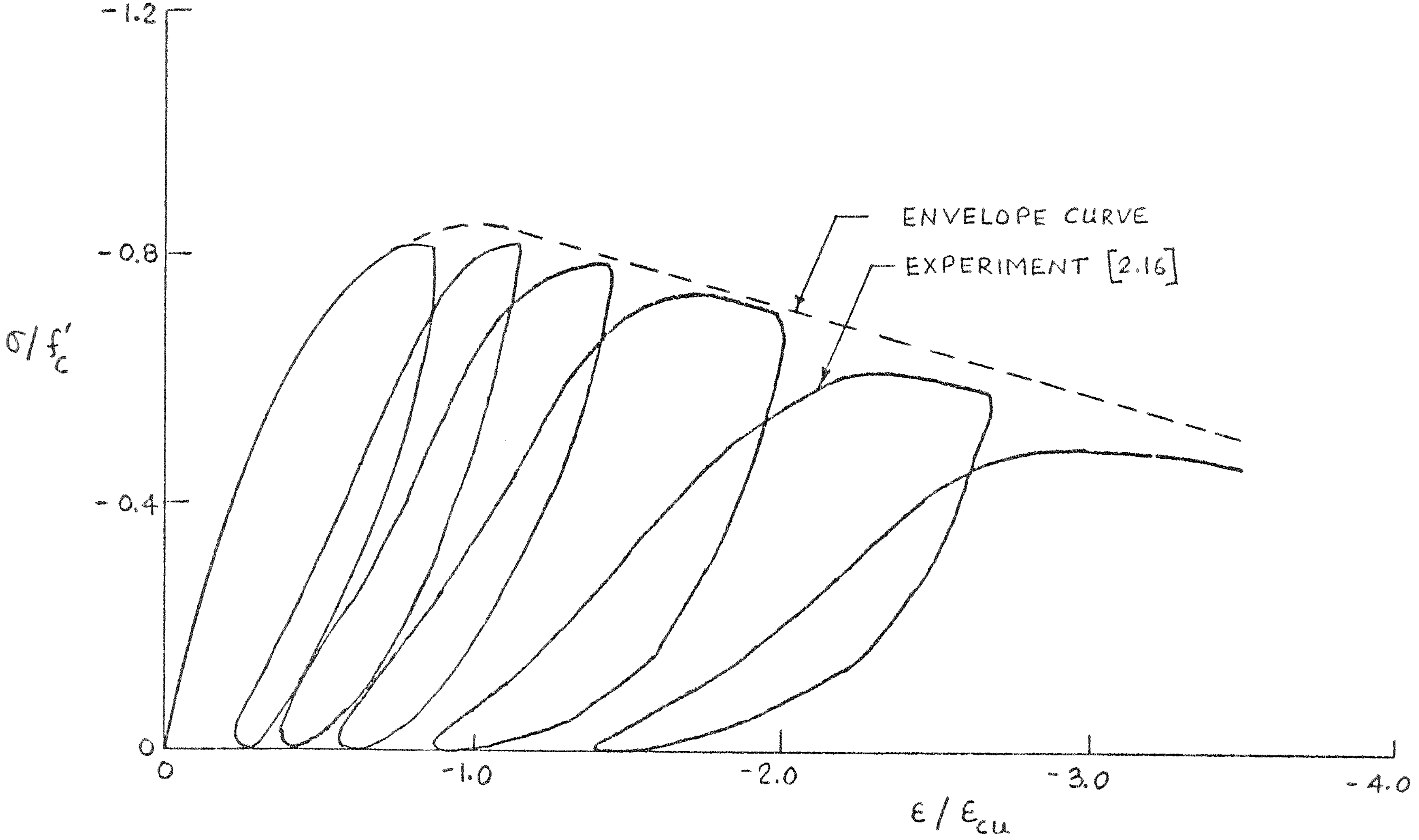

FIG. 2.16 BEHAVIOR OF CONCRETE UNDER UNIAXIAL CYCLIC LOAD [2.16]

that after the first yielding, subsequent unloading will take place along the path determined by the current unloaded stresses corresponding to the current total strains. Lin [1.27] used both the unconstrained flow rule and the normality flow rule with a Von Mises yield criterion. He found little difference in the behavior of reinforced concrete slabs and shells due to the type of flow rule used. In view of the little difference observed and the fact that the unconstrained flow rule is much simpler to formulate, this approach will be used in the present investigation.

2.2.7 Stress Reversal

A stress reversal option is incorporated in the equivalent uniaxial constitutive model to account for any unloading that may occur due to creep and shrinkage effects and applied load history. The unloading and reloading model chosen for this study is illustrated in Fig. 2.17. This simple model is adopted as a first approximation to avoid additional computational efforts and also due to the lack of available experimental data on concrete subjected to biaxial stress reversal.

In the equivalent uniaxial stress-strain curve, Fig. 2.17, there are four distinct zones--(1) AB - compressive loading up to yield, (2) BCD - compressive unloading after yield, (3) AF - tensile loading up to the initiation of cracking, and (4) FG - tensile unloading after initial cracking.

Tensile loading at A will occur along AF with a slope of E_0. Any unloading before F is reached takes place along FA. Tensile unloading beyond F will follow FG and tensile stress reduces to zero at and

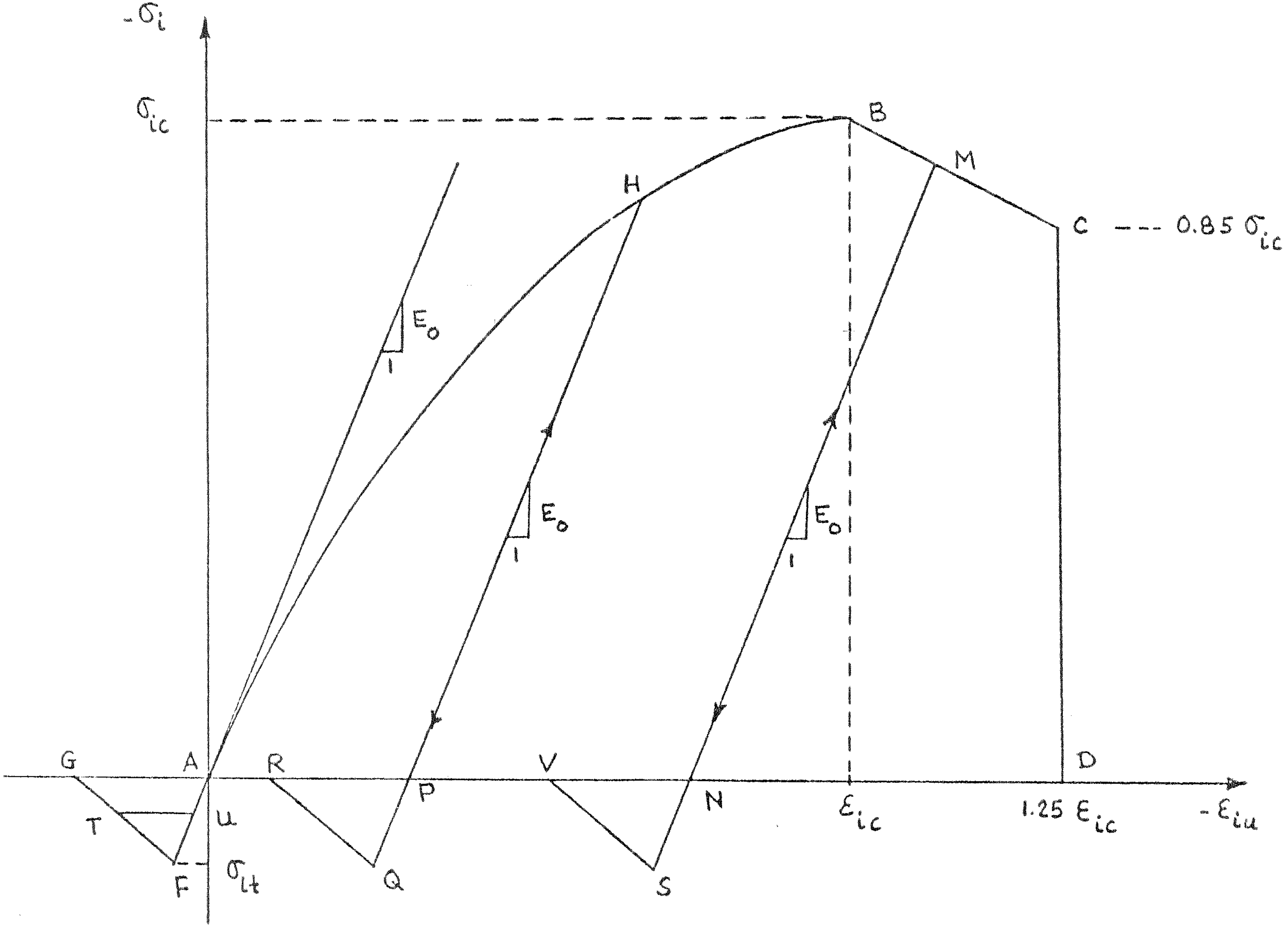

FIG. 2.17 LOAD REVERSAL MODEL FOR CONCRETE

beyond G. Concrete at this point is assumed to be in a completely cracked state. Any reloading toward the compression side will follow GA and will produce no compressive stress until point A is reached, i.e., the crack is assumed to be closed. Further compressive loading will take place along the RH line.

At a point T between F and G, unloading may occur in two directions. Further increase in tensile strain will cause unloading along TG. Reduction of tensile strain at T will cause movement along line TU until the tensile crack is closed. Further reduction in tensile strain will result in unloading along UA.

Any unloading in zone AB is assumed to have a slope of initial tangent modulus, E_o. This means that unloading from H will occur along HP. Further unloading from P occurs along PQR, which is similar to tensile loading and unloading path AFG. Any reloading in the compressive direction from R will result in no compressive stress until P is reached. Further compression will result in reloading along PH. Beyond H, the loading occurs along HB.

Once yield point B is passed, unloading can occur in two directions. For example, at M, unloading may follow either MC or MN. The strain state, in this case, will determine wheterh MC or MN will be followed. If compressive strain increases from that at M, then compressive unloading will occur along MC until crushing occurs at C. Otherwise, MN which has the same slope as E_o will be followed. Further unloading from N will occur along NSV which is similar to PQR.

2.3 Constitutive Relations of Steel Reinforcement

A simple bilinear constitutive model is used for steel reinforcement in this study. The model may either be elasto-perfectly plastic, or strain-hardening with a Bauschinger-type effect as illustrated in Fig. 2.18.

Three parameters are needed to determine the stress-strain curve--the initial modulus, E_s; the strain-hardening modulus, E_{sh}; and the yield stress, f_y. The portion AB (Fig. 2.18) of the stress-strain curve has a slope of E_s. At B, steel stress reached the yield stress value of f_y and initial yielding occurs. Beyond B, loading takes place with decreased slope E_{sh}.

Stress reversal along AB has the same slope E_s and continues to D such that:

$$\sigma_D = \sigma_B - 2 f_y \tag{2.29}$$

after which loading continues with reduced slope E_{sh}. Stress reversal at P, beyond initial yield point B, occurs with the initial slope E_s. This continues up to Q such that:

$$\sigma_Q = \sigma_P - 2 f_y \tag{2.30}$$

after which loading continues with reduced slope E_{sh}.

If 1 and 2 are the two axes parallel and orthogonal to the steel longitudinal axis, then the incremental stress-strain relationship is given by:

$$\left\{ \begin{matrix} d\sigma_1 \\ d\sigma_2 \\ d\tau_{12} \end{matrix} \right\} = \begin{bmatrix} E_s & 0 & 0 \\ 0 & 0 & 0 \\ 0 & 0 & 0 \end{bmatrix} \left\{ \begin{matrix} d\varepsilon_1 \\ d\varepsilon_2 \\ d\gamma_{12} \end{matrix} \right\} \tag{2.31}$$

In the strain-hardening range, E_s in Eq. (2.31) is replaced by E_{sh}. For elasto-perfectly plastic steel, E_{sh} is assumed to be zero.

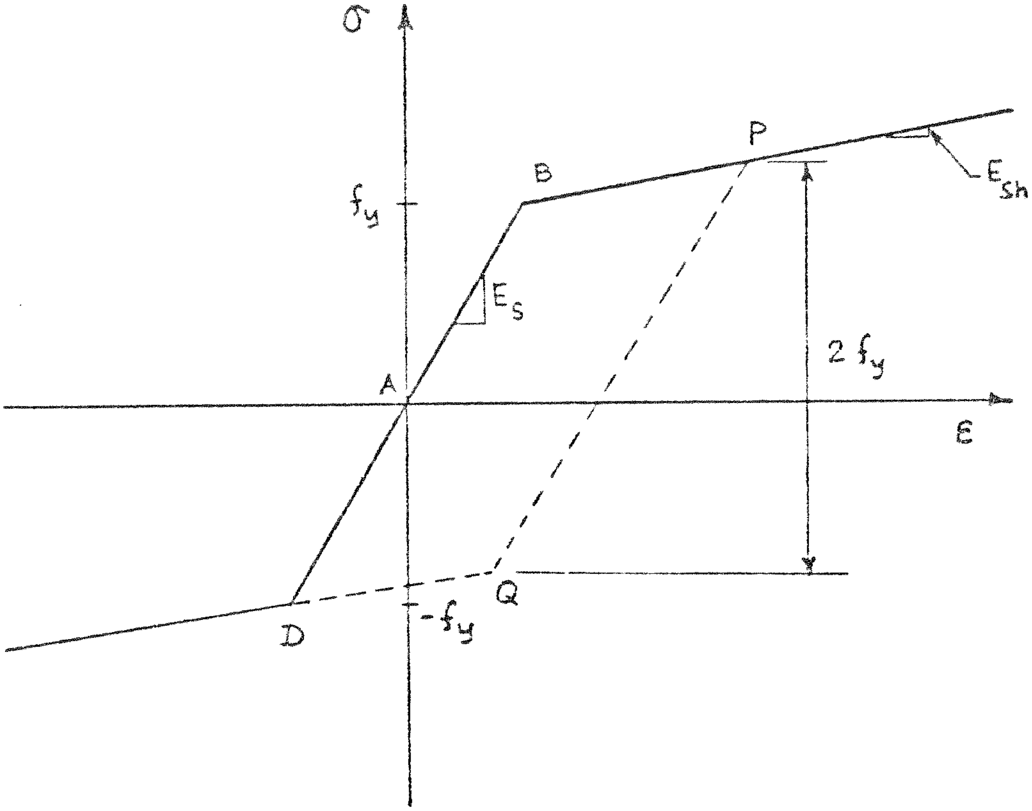

FIG.2.18 CONSTITUTIVE MODEL FOR STEEL

3. CREEP AND SHRINKAGE OF CONCRETE

3.1 General Remarks

Concrete is unique among structural materials in that it interacts with its environment, undergoing complex physical and chemical changes with the passage of time. The time-dependent changes in the concrete behavior may significantly affect the serviceability of some concrete structures. This is especially true of those structures subjected to a wide range of variations in humidity, temperature and loading conditions. For such structures, it is essential to investigate the long term deformation behavior in order to achieve adequate serviceability criteria during the design life of the structure.

Two of the most important phenomena, observed in the time-dependent deformation of concrete structures, are creep and shrinkage. These were defined in the previous chapter. It has also been assumed there that the three components of deformation--instantaneous elastic, creep and shrinkage--are independent of each other and hence additive. In this chapter, creep and shrinkage phenomena will be examined in greater detail.

3.2 Creep

3.2.1 Mechanism

The mechanism of creep is of utmost importance in arriving at an understanding of the creep phenomena. Several theories have been proposed over the years to explain the creep mechanism, but none of the theories has adequately explained all the observed information regarding creep of concrete. Several broad mechanisms of creep may, however, be distinguished. These are mechanical deformation theory, viscous flow, plastic flow, seepage of gel water, etc.

Mechanical deformation theory [3.1] attributes the behavior of concrete under load to internal stresses set up as a result of the change in the form of the capillary structure of the cement paste due to the application of load. The re-establishing of vapor pressure equilibrium between the cement paste and ambient medium results in creep.

Plastic theories [3.2] suggest that the creep of concrete may be in the nature of crystalline flow, i.e., a result of slippage along planes within the crystal lattice.

Viscous flow theories [3.3] postulate that creep is due to the hydrated cement paste which is highly viscous in nature. Under sustained load, the cement paste undergoes viscous flow causing creep.

Seepage of gel water theory [3.4] posulates that hydrated cement paste is a rigid gel. In such gels, application of load causes expulsion of the viscous components from the voids in the elastic skeleton. Thus, creep occurs due to seepage of gel water under pressure.

3.2.2 Influencing Factors

Creep in concrete is influenced by a large number of factors. The quantitative determination of these factors is a statistical problem as the experimental results are inherently random variables with coefficient of variation on the order of 15 to 20 percent at best [3.5]. However, up until now, the solutions found in the creep literature are all deterministic in nature. Moreover, they only try to establish correlations between the analytical models and laboratory specimens. The correspondence between laboratory and field conditions are not yet well established. These would put limitations on the accuracy of the quantitative measures of the factors affecting creep of concrete; and this should be kept in mind whenever some values are given to creep coefficients. The following remarks may be made on the main factors affecting creep:

1. Compressive strength: Creep deformation is inversely proportional to the strength of concrete [3.6], i.e., the greater the compressive strength at the time of application of the load, the less the ultimate creep deformation.

2. Age at loading: Creep deformation is inversely proportional to the age of concrete at the time of application of loading.

3. Type of aggregate: Creep deformation is inversely proportional to both the volume of aggregate in a given concrete mix and the modulus of elasticity of the aggregates [3.7,3.8].

4. Ambient relative humidity: Creep deformation is inversely proportional to the ambient relative humidity [3.9].

5. Temperature: Creep deformation is directly proportional to the temperature for a temperature range between 0°F to 180°F [3.10,3.11].

6. Size of the specimen: Creep deformation is inversely proportional to the thickness of the specimen [3.12].

7. Stress: Creep deformation is directly proportional to the imposed stress--proportionality is generally linear for a stress level of approximately 0.4 f'_c. above which it is nonlinear (increases more) [3.13].

8. Duration of applied stress: Creep deformation is directly proportional to the duration of applied stress. Proportionality is asymptotic--deformation increases rapidly initially, but gradually

tends to an asymptotic value [3.12,3.14].

3.2.3 Review of Analytical Models

Creep deformations in concrete under a constant hygrothermal condition is assumed to be predicted with reasonable accuracy by the linear viscoelastic theory, as long as the stress/strength ratio in concrete is less than 35-45%. The two general approaches in linear viscoelasticity are: (1) integral formulation and (2) differential formulation.

1. Integral Formulation. - The integral representation of linear viscoelastic stress-strain relations was given by Volterra [3.15] using Boltzmann's superposition principle. The constitutive relationship is expressed in terms of a superposition integral. The so-called weighting or memory functions, which happen to be Kernels in the integral formulations, are the creep or relaxation functions representing the response of the material to unit step function inputs. For a uniaxial state of stress and an aging material the constitutive relationship can be written according to Volterra as:

$$\varepsilon(t) = \int_{-\infty}^{t} \overline{C}(\tau, t-\tau) \frac{\partial \sigma(\tau)}{\partial \tau}\, d\tau \qquad (3.1)$$

where $\varepsilon(t)$ = strain at time t, $\overline{C}(\tau,t-\tau)$ = specific compliance observed at time t for initial application of load at age τ.

2. Differential Formulation. - In this approach, the creep behavior is represented by rheological models composed of discrete elastic (spring) and viscous (dash-pot) elements placed together in series and parallel. For aging materials, the general form of the differential equation is [3.16]:

$$\left[\frac{d^n}{dt^n} + p_1(t)\frac{d^{n-1}}{dt^{n-1}} + \ldots + p_n(t)\right] \varepsilon = \left[q_n(t)\frac{d^n}{dt^n} + \ldots + q_n(t)\right] \sigma \qquad (3.2)$$

where $p_n(t)$, $q_n(t)$ are time variable properties of concrete.

While both the integral and differential formulations are interrelated as shown by Gross [3.17], it appears that for concrete under age and temperature effects, an integral approach is better suited for computation than the differential approach as the latter may result in integro-differential equations which are extremely complicated to solve [3.18].

The solution of the integral Eq. (3.1) depends on the form of the Kernel function $\overline{C}(\tau,t-\tau)$. The term $\overline{C}(\tau,t-\tau)$ is generally known as the specific compliance function. Several expressions are given in the literature for the specific compliance function. In the expressions for the specific compliance function, a distinction is generally made between the instantaneous compliance function and the creep compliance function. Creep compliance function is assumed to contribute to the creep response of the material. Mathematically, we may write:

$$\overline{C}(\tau,t-\tau) = \frac{1}{E(\tau)} + C(\tau,t-\tau) \qquad (3.3)$$

where $\frac{1}{E(\tau)}$ = instantaneous compliance function and $C(\tau,t-\tau)$ = creep compliance function.

This means that we may write:

$$\varepsilon^c(t) = \int_0^t C(\tau,t-\tau)\frac{\partial\sigma(\tau)}{\partial\tau}\, d\tau \qquad (3.4)$$

where $\varepsilon^c(t)$ = creep strain.

The solution of Eq. (3.4) depends on the criteria chosen to express the creep compliance function $C(\tau,t-\tau)$. The criteria generally applied in choosing the creep compliance function $C(\tau,t-\tau)$ are:

1. The function should accurately fit the experimental compliance surface, taking into account such parameters as (a) age at loading, (b) temperature variations, (c) size of members, (d) curing, (e) relative humidity, etc.

2. The undetermined coefficients of the function should be easy to evaluate from experimental data.

3. The function should be such that the numerical evaluation of Eq. (3.4) becomes straightforward and does not require an excessive amount of storage space in the computer.

McHenry [3.19] suggested a creep compliance function in the form:

$$C(\tau,t-\tau) = \alpha\left[1 - e^{-\nu(t-\tau)}\right] + \beta e^{-p\tau}\left[1 - e^{-m(t-\tau)}\right] \tag{3.5}$$

where α, β, ν, p, and m are constants to be determined from experimental data. Arutyunyan [3.20] suggested:

$$C(\tau,t-\tau) = \left(a + \frac{b}{\tau}\right) \sum_{k=0}^{m} \beta_k e^{-\nu_k(t-\tau)} \tag{3.6}$$

where a, b, ν_k and m are constants to be determined from experimental data.

Bresler and Selna [3.21] outlined some simplifications in determining the creep compliance function. Selna [1.39] proposed:

$$C(\tau,t-\tau) = \sum_{i=1}^{3} \sum_{j=1}^{4} \alpha_i a_j \, \tau^{-0.1(j-i)}\left[1 - e^{-k_i(t-\tau)}\right] \tag{3.7}$$

where α_i, a_j, and k_i are 10 constants to be determined from experiments.

Mukaddam and Bresler [3.22] proposed a creep compliance function which took into consideration both aging and temperature effects as shift functions:

$$C(\tau,t-\tau,T) = \sum_{i=1}^{m} a_i \, e^{-\lambda_i(t-\tau)\,\phi(T)\,\overline{\Phi}(\tau)} \tag{3.8}$$

where a_i, and λ_i = constants, $\phi(T)$ = temperature shift function, $\overline{\Phi}(\tau)$ = age shift function and T = temperature at loading. This creep compliance function is the most advanced as both the aging and thermal effects are considered. The application of this model to complicated structural systems is, however, restricted at present as stress histories at all previous time steps are required in creep strain increment calculations at the present time step.

Mukaddam [3.23] recently proposed a temperature-dependent creep compliance function in the form of:

$$C(t-\tau,T) = \sum_{i=1}^{m} J_i \left[1 - e^{-\lambda_i\phi(T)(t-\tau)}\right] \tag{3.9}$$

where J_i, and λ_i = constants, $\phi(T)$ = temperature shift function. By assuming that all time steps are equal, a recursive relationship for creep strain calculation is established. This requires the stress history for a previous single time step for the creep strain calculation at the current time step. The resultant reduction, in both computer storage and computational effort needed, makes possible the application of this model to the solution of large structural problems. However, aging effects, important in structures under load history over a long period, are not considered. This and the requirement of equal time steps, place some restrictions on the use of this model to certain classes of problems.

Recently, Zienkiewicz and Cormeau [3.24] developed a visco-plastic model of material behavior to investigate a wide range of materially nonlinear problems, including, at one extreme, plasticity solutions under stationary conditions and at the other extreme, standard creep phenomena. Conceptually, their method is consistent with the principles of thermodynamics as it takes plasticity and viscoelasticity as limiting cases of a general formulation and not as separate phenomena as has been generally assumed in numerical formulations. However, not much data has been provided and its application to reinforced concrete is still to be done.

3.2.4 Creep under Biaxial Stress

It has been observed experimentally [3.25] that under uniaxial stress state, creep strains occur not only in the direction of the applied stress, but also normal to it. The normal creep strains that are induced are called lateral creep strains. The ratio of the lateral creep strain to the creep strain along the direction of the applied stress is called creep Poisson's ratio following the concept used in the case of elastic strains.

Earlier experimental studies on creep Poisson's ratio [3.25,3.26, 3.27,3.28] show a range of values from 0.05 to 0.4. Many of the discrepancies between these results were due to the methods used to measure the lateral strains. Later experimental studies [3.29,3.30] show the creep Poisson's ratio to be very close to the elastic Poisson's ratio having a range of values between 0.16 to 0.25.

In the case of biaxial stress, creep strain in any direction would consist of creep strain in that direction due to the stress in that direction plus the lateral creep strains due to the creep strains occurring in the normal direction.

The primary question that may be posed is whether the creep strain in one direction, occurring due to the corresponding stress only, is independent of the stress in the normal direction. If it is, then the principle of superposition will hold and the net creep in any direction may be calculated as an algebraic sum of the creep strain occurring in that direction and the lateral creep strains induced by the stress in the normal direction. This may be expressed as:

$$\begin{aligned} \Delta\varepsilon_x^c(t) &= \left[\Delta\sigma_x(t) - \nu_c\Delta\sigma_y(t)\right] C(\tau,t-\tau,T) \\ \Delta\varepsilon_y^c(t) &= \left[\Delta\sigma_y(t) - \nu_c\Delta\sigma_x(t)\right] C(\tau,t-\tau,T) \end{aligned} \tag{3.10}$$

where $\Delta\varepsilon_x^c(t)$ and $\Delta\varepsilon_y^c(t)$ = increment in creep strain in x, y directions at time t, $\Delta\sigma_x(t)$ and $\Delta\sigma_y(t)$ = increment in stress at time t, ν_c = creep Poisson's ratio under uniaxial stress state and $C(\tau,t-\tau,T)$ = specific creep compliance from uniaxial stress state at time t, for age at loading τ and temperature T.

Gopalakrishnan, et al. [3.29], however, found that the creep Poisson's ratio under a multiaxial stress state is a function of the relative magnitude of the principal stresses. It is also less than the uniaxial creep Poisson's ratio as shown in Fig. 3.1.

Neville [3.31] used the following relationship for creep under biaxial stress state:

$$\begin{aligned} \Delta\varepsilon_1^c &= \left[\Delta\sigma_1 - \nu_{c1}\Delta\sigma_2\right] C(\tau,t-\tau,T) \\ \Delta\varepsilon_2^c &= \left[\Delta\sigma_2 - \nu_{c2}\Delta\sigma_1\right] C(\tau,t-\tau,T) \end{aligned} \tag{3.11}$$

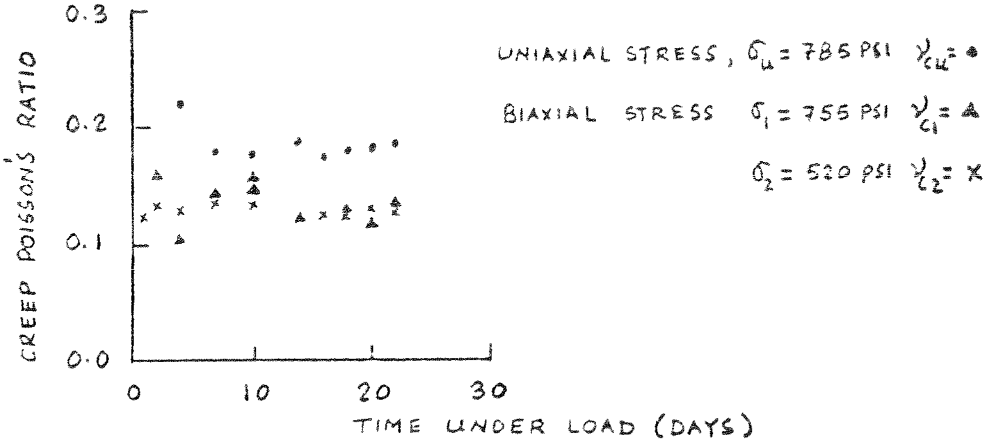

FIG. 3.1 CREEP POISSON'S RATIO FOR UNIAXIAL AND BIAXIAL STATES OF STRESS

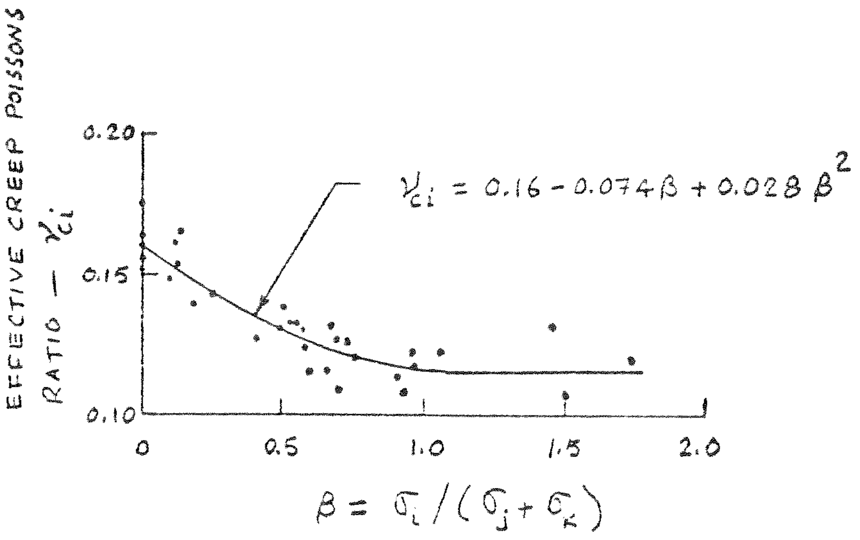

FIG.3.2 RELATION BETWEEN EFFECTIVE CREEP POISSON'S RATIO AND MAGNITUDE OF PRINCIPAL STRESSES

where ν_{ci} = effective creep Poisson's ratio

$$= A + B\left(\frac{\sigma_i}{\sigma_j+\sigma_k}\right) + C\left(\frac{\sigma_i}{\sigma_j+\sigma_k}\right)^2 \qquad (3.12)$$

where σ_i, σ_j, and σ_k are the principal stresses, and A, B, C = constants to be determined from experiments.

In Eq. (3.11), the effect of the stress state on the creep strains is being incorporated by the empirical relationship for the effective creep Poisson's ratio. The term σ_i is dependent on the stress state and hence by proper evaluation of A, B and C, the experimental behavior may be modeled analytically. This is shown in Fig. 3.2.

In the present study, however, for simplicity and considering the uncertainties involved, it is assumed that the creep Poisson's ratio in the biaxial stress state does not change, but remains the same as the elastic Poisson's ratio. We may rewrite Eq. (3.10) as:

$$\begin{Bmatrix} \Delta\varepsilon_x^c(t) \\ \Delta\varepsilon_y^c(t) \end{Bmatrix} = C(\tau,t-\tau,T)\begin{bmatrix} 1 & -\nu_c \\ -\nu_c & 1 \end{bmatrix}\begin{Bmatrix} \Delta\sigma_x(t) \\ \Delta\sigma_y(t) \end{Bmatrix} \qquad (3.13)$$

Nothing conclusive is available about creep compliance in shear. However, following Arutyunyan [3.20], it is assumed here that creep compliance in shear is equal to $2(1 + \nu_c)\ C(\tau,t-\tau,T)$. Equation (3.13) may now be extended as:

$$\begin{Bmatrix} \Delta\varepsilon_x^c(t) \\ \Delta\varepsilon_y^c(t) \\ \Delta\gamma_{xy}^c(t) \end{Bmatrix} = \begin{bmatrix} 1 & -\nu_c & 0 \\ -\nu_c & 1 & 0 \\ 0 & 0 & 2(1+\nu_c) \end{bmatrix} C(\tau,t-\tau,T)\begin{Bmatrix} \Delta\ \sigma_x(t) \\ \Delta\ \sigma_y(t) \\ \Delta\ \tau_{xy}(t) \end{Bmatrix}$$

(3.14)

The total creep strain vector, from initial age at loading t_1 to final observation time t_n, will be given by:

$$\begin{Bmatrix} \varepsilon_x^c(t_n) \\ \varepsilon_y^c(t_n) \\ \gamma_{xy}^c(t_n) \end{Bmatrix} = \underline{D}_o^{-1} \sum_{i=1}^{n} C(t_i, t_n - t_i, T_i) \begin{Bmatrix} \Delta\, \sigma_x(t_i) \\ \Delta\, \sigma_y(t_i) \\ \Delta\, \tau_{xy}(t_i) \end{Bmatrix} \tag{3.15}$$

where $\underline{D}_o^{-1} = \begin{bmatrix} 1 & -\nu_c & 0 \\ -\nu_c & 1 & 0 \\ 0 & 0 & 2(1+\nu_c) \end{bmatrix}$

3.2.5 Creep under High Stress Levels

It has been shown by several investigators [3.7,3.13,3.32] that creep of concrete is linearly proportional to stress only up to a stress level of 0.35 f_c'. Beyond this stress level, nonlinearity of creep is observed as shown in Fig. 3.3. To take into account this nonlinear effect, Becker and Bresler [3.33] suggested an 'effective stress' concept. The stress used in calculating creep is multiplied by a scale factor to account for the nonlinearity of creep strains at high stress levels. The expressions for effective stress are given by:

$$\begin{aligned} \sigma_{eff} &= \sigma \qquad \text{for } \frac{\sigma}{f_c'} \le 0.35 \\ &= 2.33\sigma - 0.465\, f_c' \qquad \text{for } \quad 1 \ge \frac{\sigma}{f_c'} > 0.35 \end{aligned} \tag{3.16}$$

Equation (3.16) implies that creep strain and stress are linearly related up to a stress level of 0.35 f_c'. After that, creep increases more rapidly than stress increment, reaching a multiplication factor of 1.865 at a stress level of f_c'. This equation is a purely empirical

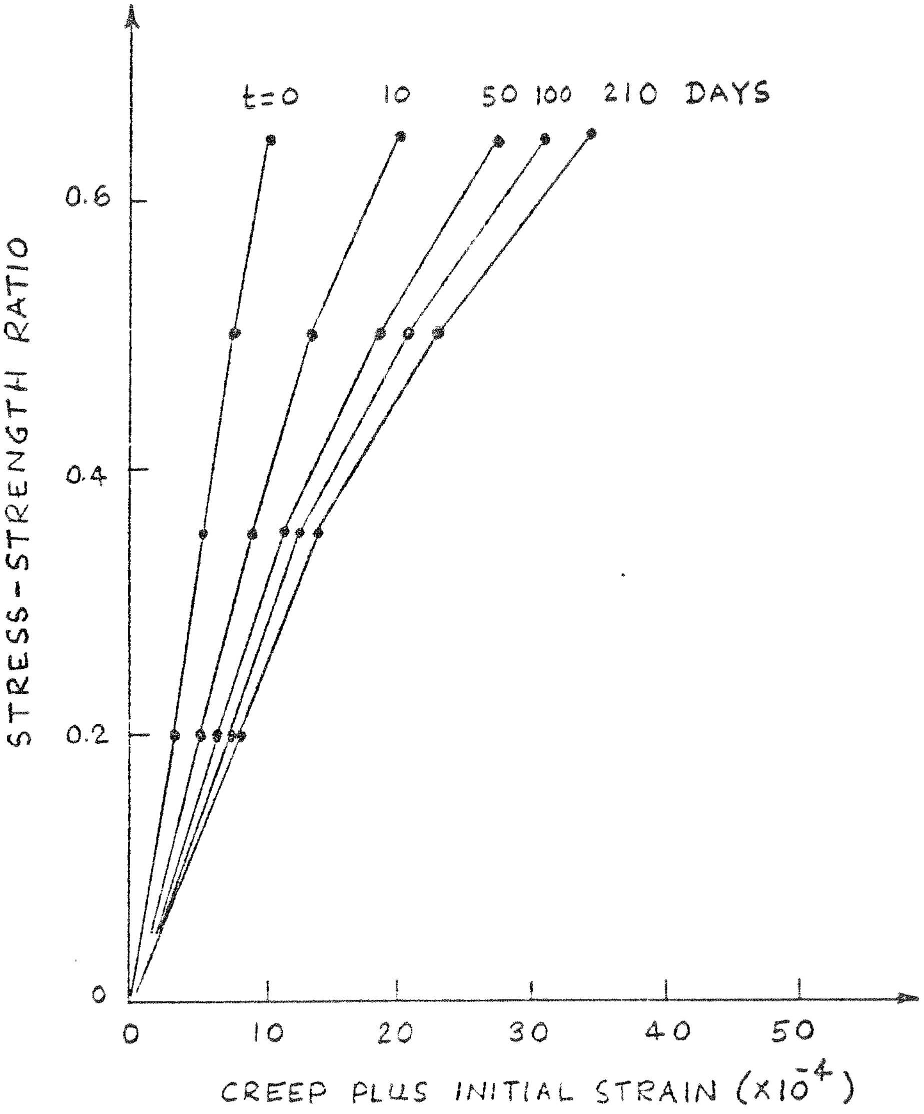

FIG. 3.3 EFFECT OF STRESS-STRENGTH RATIO ON CREEP AT HIGH STRESSES

one, based on experimental data, particularly those of Roll [3.32].

It has also been found out experimentally [3.32] that the total time-dependent creep recovery after removal of loading is linearly proportional to the stress level as shown in Fig. 3.4. This means that while calculating creep recovery, actual stresses, rather than effective stresses, need be considered.

3.2.6 Requirements of the Creep Model

The finite element analysis for reinforced concrete structures such as box girder bridges, shell roofs, flat slabs, etc., taking into account tensile cracking of concrete, yielding of reinforcing steel, etc., and incorporating time-dependent effects such as creep, is always constrained by the storage capacity of the computer and the cost of solution. Thus, in this study the search has been to formulate an efficient algorithm, while retaining the most significant physical effects.

The physical effects significant in creep studies of reinforced concrete structures such as box girder bridges, folded plate and shell roofs, etc., are the effects of aging, temperature variation, field conditions such as slump, relative humidity, size of members, etc., on creep. Since cracking, yielding, etc., are to be considered, the solution procedure must be an incremental, step-by-step approach. For this reason, the creep algorithm should be such that only a few stress histories and not the whole stress history need be stored as the storage for all the stress histories would surely tax the capacities of the presently available computers and the computational costs for realistic structures would become prohibitive.

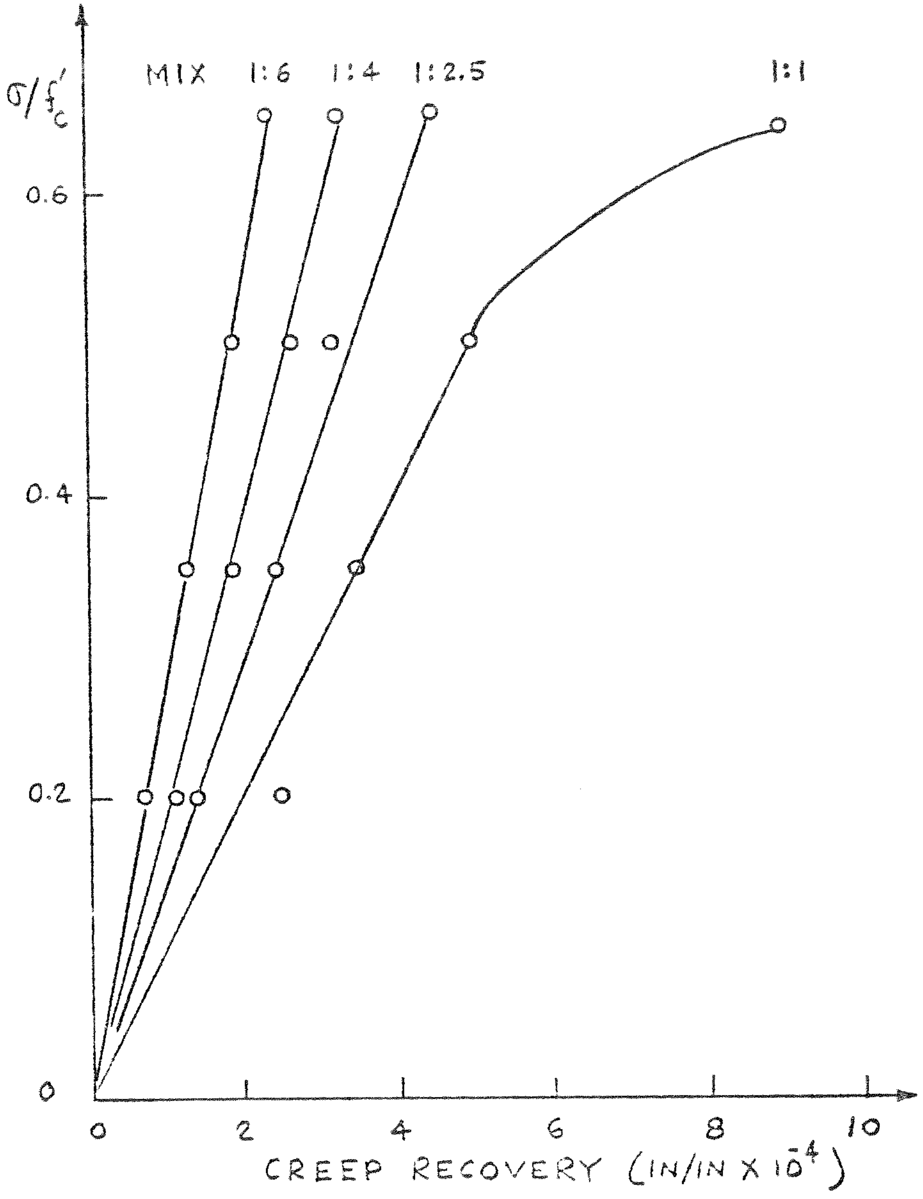

FIG. 3.4 STRESS-LEVEL VS. TOTAL TIME-DEPENDENT RECOVERY WITH MIX AS A PARAMETER

3.2.7 Formulation of Analytical Model

An incremental method is chosen for the creep strain calculation which will facilitate a step-by-step solution in the time domain. A number of assumptions have to be made in order to develop the creep model. These assumptions are:

1. Each component of strain is composed of strains produced by different effects. These effects are broadly classified into two groups--stress originated and nonstress originated. The stress originated strain is known as compliance; instantaneous and creep strains are examples of compliance. Thermal and shrinkage strains are examples of nonstress originated strains. The consequence of this assumption is that the different strain components can be calculated separately and added together. This makes the whole computational process easier.

2. The principle of superposition is assumed to be valid for creep strains. This principle asserts that the strain at a given time is the sum of the strains caused by the loads applied immediately for their respective durations of time. The assumption implicit in this principle is that there is no coupling between the single response behavior from individual load input.

3. The time-dependent response is the same in tension as in compression for uncracked concrete.

The above assumptions are implicit in Eq. (3.15) which may now be rewritten as:

$$\underline{D}_o \varepsilon_n^c = \Delta\underset{\wedge}{\sigma}_1 \; C(t_1, t_n - t_1, T_1) + \Delta\underset{\wedge}{\sigma}_2 \; C(t_2, t_n - t_2, T_2) + \ldots + \ldots$$

$$+ \Delta\underset{\wedge}{\sigma}_{n-1} \; C(t_{n-1}, t_n - t_{n-1}, T_{n-1}) \qquad (3.17)$$

where $\underset{\sim}{\varepsilon}_n^c = \left\langle \varepsilon_x^c(t_n) \quad \varepsilon_y^c(t_n) \quad \gamma_{xy}^c(t_n) \right\rangle^T$

$$\Delta\underset{\sim}{\sigma}_i = \left\langle \Delta\sigma_x(t_i) \quad \Delta\sigma_y(t_i) \quad \Delta\tau_{xy}(t_i) \right\rangle^T$$

and

t_1 = age at initial loading

t_n = final observation time

T_i = temperature at age t_i

Similarly for time t_{n+1}, we may write:

$$\underset{\sim}{D}_o \underset{\sim}{\varepsilon}_{n+1}^c = \Delta\underset{\sim}{\sigma}_1 \; C(t_1, t_{n+1}-t_1, T_1) + \Delta\underset{\sim}{\sigma}_2(t_2, t_{n+1}-t_2, T_2) + \ldots$$
$$+ \Delta\underset{\sim}{\sigma}_n \; C(t_n, t_{n+1}-t_n, T_n) \tag{3.18}$$

So, the increment in the creep strain for the time interval $\Delta t_n = t_{n+1}-t_n$ can be expressed as

$$\Delta\underset{\sim}{\varepsilon}_n^c = \underset{\sim}{\varepsilon}_{n+1}^c - \underset{\sim}{\varepsilon}_n^c \tag{3.19}$$

Equation (3.19) is graphically represented in Fig. 3.5. It is clear from Fig. 3.5 that one assumption inherent in the summation expression is that stress changes occur in steps and no stress change occurs during a time interval, say from t_1 to $t_2 = \Delta t_i$. This is obviously not true, but in most cases of load, if the time step sizes are chosen properly, the constant-step stresses will represent the load history quite accurately.

It is also evident from Eqs. (3.17) and (3.18) that the calculation of creep increment during time step n in going from t_n to t_{n+1} necessitates knowledge of all previous stress increments $\Delta\underset{\sim}{\sigma}_1$, $\Delta\underset{\sim}{\sigma}_2$, $\Delta\underset{\sim}{\sigma}_3 \ldots \Delta\underset{\sim}{\sigma}_{n-1}$ as well as the most current stress increment, $\Delta\underset{\sim}{\sigma}_n$. This

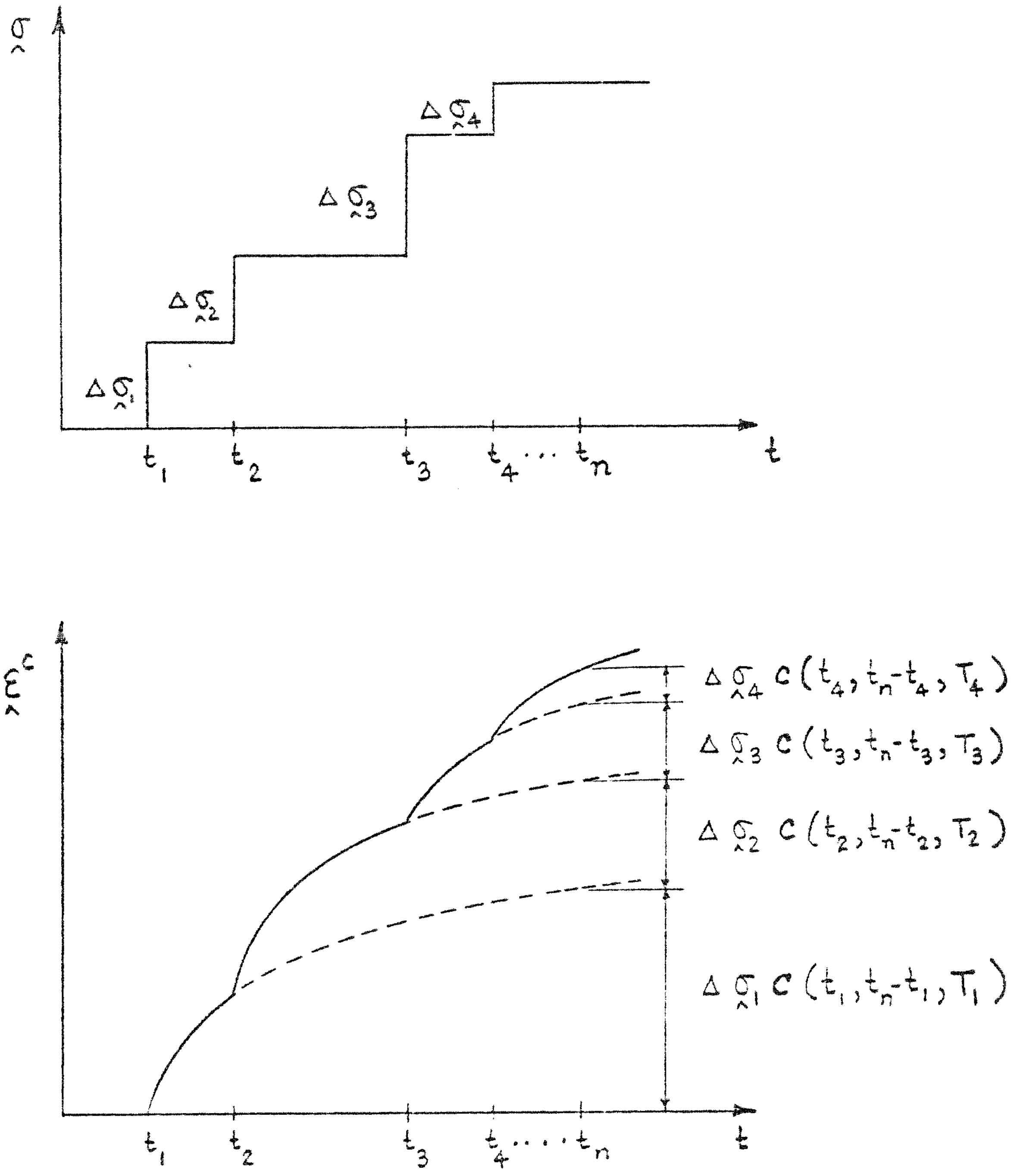

FIG. 3.5 GRAPHICAL REPRESENTATION OF CREEP STRAIN INCREMENT EVALUATION

requires a large storage capacity for even a moderately complex structural system and in fact the storage requirement, apart from being extremely large, may also become very unwieldy.

It has been found [3.33,3.34,3.35] that certain types of mathematical approximations for the creep compliance function, $C(\tau,t-\tau,T)$, while representing the experimental data accurately, overcome the necessity of storing all the stress increments of the previous time steps. A similar function is proposed in the present study for the creep compliance function:

$$C(\tau,t-\tau,T) = \sum_{i=1}^{m} a_i(\tau)\left[1 - e^{-\lambda_i \phi(T)(t-\tau)}\right] \tag{3.20}$$

where $a_i(\tau)$ = scale factor dependent on age at loading τ, λ_i = exponential constants determining the shape of the logarithmically decaying creep curve and $\phi(T)$ = shift function dependent on temperature T.

Substituting the value of C( ) from Eq. (3.20) into Eq. (3.17), we may write:

$$\begin{aligned} \underline{D}_o \underset{\wedge}{\varepsilon}_n^c = {} & \Delta\underset{\wedge}{\sigma}_1 \sum_{i=1}^{m} a_i(t_1)\left[1 - e^{-\lambda_i \phi(T_1)(t_n-t_1)}\right] \\ & + \Delta\underset{\wedge}{\sigma}_2 \sum_{i=1}^{m} a_i(t_2)\left[1 - e^{-\lambda_i \phi(T_2)(t_n-t_2)}\right] \\ & + \;.\;.\;.\;.\;.\;. \\ & + \Delta\underset{\wedge}{\sigma}_{n-1} \sum_{i=1}^{m} a_i(t_{n-1})\left[1 - e^{-\lambda_i \phi(T_{n-1})(t_n-t_{n-1})}\right] \end{aligned} \tag{3.21}$$

Equation (3.21) may be rearranged as:

$$\begin{aligned}
\underline{D}_{o}\underset{\wedge}{\varepsilon}^{c}_{n} &= \Delta\underset{\wedge}{\sigma}_{1} \sum_{i=1}^{m} a_{i_1} \left[1 - e^{-\lambda_i\phi_1\Delta t_1 - \lambda_i\phi_2\Delta t_2 \cdots\cdot -\lambda_i\phi_{n-1}\Delta t_{n-1}}\right] \\
&+ \Delta\underset{\wedge}{\sigma}_{2} \sum_{i=1}^{m} a_{i_2} \left[1 - e^{-\lambda_i\phi_2\Delta t_2 \cdots\cdots\cdots\cdots -\lambda_i\phi_{n-1}\Delta t_{n-1}}\right] \\
&+ \cdots\cdots \\
&+ \Delta\underset{\wedge}{\sigma}_{n-1} \sum_{i=1}^{m} a_{i_{n-1}} \left[1 - e^{-\lambda_i\phi_{n-1}\Delta t_{n-1}}\right] \qquad (3.22)
\end{aligned}$$

where $a_{i_j} = a_i(t_j)$

$\phi_j = \phi(T_j)$

$\Delta t_j = t_{j+1} - t_j$

Similarly, Eq. (3.18) may be written as:

$$\begin{aligned}
\underline{D}_{o}\varepsilon^{c}_{n+1} &= \Delta\underset{\wedge}{\sigma}_{1} \sum_{i=1}^{m} a_{i_1} \left[1 - e^{-\lambda_i\phi_1\Delta t_1 - \lambda_i\phi_2\Delta t_2 \cdots\cdots -\lambda_i\phi_n\Delta t_n}\right] \\
&+ \Delta\underset{\wedge}{\sigma}_{2} \sum_{i=1}^{m} a_{i_2} \left[1 - e^{-\lambda_i\phi_2\Delta t_2 - \lambda_i\phi_3\Delta t_3 \cdots\cdots -\lambda_i\phi_n\Delta t_n}\right] \\
&+ \cdots\cdots \\
&+ \Delta\underset{\wedge}{\sigma}_{n} \sum_{i=1}^{m} a_{i_n} \left[1 - e^{-\lambda_i\phi_n\Delta t_n}\right] \qquad (3.23)
\end{aligned}$$

Substituting values from Eqs. (3.22) and (3.23) into Eq. (3.19), we have:

$$\begin{aligned}
\underline{D}_{o}\Delta\underset{\wedge}{\varepsilon}^{c}_{n} &= \underline{D}_{o}\underset{\wedge}{\varepsilon}^{c}_{n+1} - \underline{D}_{o}\underset{\wedge}{\varepsilon}^{c}_{n} \\
&= \Delta\underset{\wedge}{\sigma}_{1} \sum_{i=1}^{m} a_{i_1}\, e^{-\lambda_i\phi_1\Delta t_1 \cdots\cdot -\lambda_i\phi_{n-1}\Delta t_{n-1}} \left[1 - e^{-\lambda_i\phi_n\Delta t_n}\right] \\
&+ \Delta\underset{\wedge}{\sigma}_{2} \sum_{i=1}^{m} a_{i_2}\, e^{-\lambda_i\phi_2\Delta t_2 \cdots\cdot -\lambda_i\phi_{n-1}\Delta t_{n-1}} \left[1 - e^{-\lambda_i\phi_n\Delta t_n}\right] \\
&+ \cdots\cdots
\end{aligned}$$

$$+ \; \Delta\underset{\wedge}{\sigma}_{n-1} \sum_{i=1}^{m} a_{i_{n-1}} \; e^{-\lambda_i \phi_{n-1} \Delta t_{n-1}} \left[1 - e^{-\lambda_i \phi_n \Delta t_n}\right]$$

$$+ \; \Delta\underset{\wedge}{\sigma}_{n} \sum_{i=1}^{m} a_{i_n} \left[1 - e^{-\lambda_i \phi_n \Delta t_n}\right] \tag{3.24}$$

or,

$$\underline{D}_o \Delta\underset{\wedge}{\varepsilon}_n^c = \sum_{i=1}^{m} \underset{\wedge}{A}_{i_n} \left[1 - e^{-\lambda_i \phi_n \Delta t_n}\right] \tag{3.25}$$

where

$$\underset{\wedge}{A}_{i_n} = \underset{\wedge}{A}_{i_{n-1}} \; e^{-\lambda_i \phi_{n-1} \Delta t_{n-1}} + \Delta\underset{\wedge}{\sigma}_n a_{i_n} \tag{3.26}$$

$$\underset{\wedge}{A}_{i_1} = \Delta\underset{\wedge}{\sigma}_1 a_{i_1} \tag{3.27}$$

So the relationships necessary for calculating increment of creep strain at any time step n, in going from t_n to t_{n+1}, are:

$$\underline{D}_o \Delta\underset{\wedge}{\varepsilon}_n^c = \sum_{i=1}^{m} \underset{\wedge}{A}_{i_n} \left[1 - e^{-\lambda_i \phi_n \Delta t_n}\right] \tag{3.28a}$$

$$\underset{\wedge}{A}_{i_n} = \underset{\wedge}{A}_{i_{n-1}} \; e^{-\lambda_i \phi_{n-1} \Delta t_{n-1}} + \Delta\underset{\wedge}{\sigma}_n a_{i_n} \tag{3.28b}$$

$$\underset{\wedge}{A}_{i_1} = \Delta\underset{\wedge}{\sigma}_1 a_{i_1} \tag{3.28c}$$

The above Eq. (3.28) does not require the storage of all previous stress histories in order to calculate the creep strain increment as is necessary in the case of Eq. (3.19). Rather, the stress history is stored in the vector $\underset{\wedge}{A}_{i_n}$ which can be calculated as a progressive sum by the use of Eq. (3.28) knowing the stress change $\Delta\underset{\wedge}{\sigma}_n$ at the current time t_n. This formulation reduces the computation and storage time considerably, making time-dependent analysis of reasonably large structural problems possible.

3.2.8 Determination of Creep Compliance Coefficients

The key to the formulation of creep strain computation algorithm in the previous sub-section is the assumption of a creep compliance function by Eq. (3.20) as follows:

$$C(\tau,t-\tau,T) = \sum_{i=1}^{m} a_i(\tau)\left[1 - e^{-\lambda_i\phi(T)(t-\tau)}\right]$$

Before proceeding with the creep analysis of any particular concrete structure, four sets of quantities have to be evaluated--(1) m, (2) $a_i(\tau)$, (3) λ_i and (4) $\phi(T)$. Two methods may be followed in order to evaluate the above quantities.

1. First method - experimental creep data analysis:

In this method creep data are obtained for some particular concrete. $C(\tau,t-\tau,T)$ values are given for different τ and T for a range of $t-\tau$. Then, the following procedure is followed:

(i) m and λ_i,i=1,m are chosen on a trial basis.

(ii) A particular age τ_o and temperature T_o are chosen.

(iii) Various times t_j,j-1,2,...,n are chosen such that $t_j \geq \tau_o$.

(iv) Values of $C(\tau_o,t_j-\tau_o,T_o)$ are found at j=1,2,...,n points.

(v) Then, the simultaneous equations are set up:

$$\begin{bmatrix} 1-e^{-\lambda_1(t_1-\tau_o)} & 1-e^{-\lambda_2(t_1-\tau_o)} \ldots\ldots 1-e^{-\lambda_m(t_1-\tau_o)} \\ & \\ & \\ 1-e^{-\lambda_1(t_n-\tau_o)} & 1-e^{-\lambda_2(t_n-\tau_o)} \ldots\ldots 1-e^{-\lambda_m(t_n-\tau_o)} \end{bmatrix}_{n\mathrm{x}m} \begin{Bmatrix} a_1(\tau_o) \\ a_2(\tau_o) \\ \cdot \\ \cdot \\ \cdot \\ a_m(\tau_o) \end{Bmatrix}_{m\mathrm{x}1} = \begin{Bmatrix} C(\tau_o,t_1-\tau_o,T_o) \\ C(\tau_o,t_2-\tau_o,T_o) \\ \cdot \\ \cdot \\ \cdot \\ C(\tau_o,t_n-\tau_o,T_o) \end{Bmatrix}_{n\mathrm{x}1} \quad (3.29)$$

$$\text{or, } \underset{\sim}{A}_{n\mathrm{x}m}\ \underset{\sim}{a}_{m\mathrm{x}1} = \underset{\sim}{B}_{n\mathrm{x}1} \quad n>m \qquad (3.30)$$

The least square method is applied to solve the overdeterminate systems of Eq. (3.30) to give the values of $\underset{\wedge}{a}$:

$$\underline{A}^T_{mxn}\ \underline{A}_{nxm}\ \underset{\wedge}{a}_{mx1} = \underline{A}^T_{mxn}\ \underset{\wedge}{B}_{nx1} \tag{3.31}$$

or, $(\underline{A}^T\underline{A})_{mxm}\ \underset{\wedge}{a}_{mx1} = (\underline{A}^T\underset{\wedge}{B})_{mx1}$

$$\text{or,}\quad \underset{\wedge}{a}_{mx1} = (\underline{A}^T\underline{A})^{-1}_{mxm}\ (\underline{A}^T\underset{\wedge}{B})_{mx1} \tag{3.32}$$

(vi) Choose a different m and/or λ_i and go through steps (ii) - (v).

(vii) Optimum m's and λ's are chosen based on the following criteria:

a. least square errors are minimized.

b. $a_i(\tau)$ which is the ultimate creep strain is about 4/3 of the 1-year creep strain.

c. the contributions of all $a_i(1 - e^{-\lambda_i(t-\tau)})$ terms are nearly equal.

(viii) Now choose a different age τ_1 and go through steps (iii) - (v) to determine a new set of $a_i(\tau_1)$. This is continued to give sets of $a_i(\tau)$ for different ages. The in-between ages can be determined from linear interpolation.

(ix) The temperature shift function $\phi(T)$ may be calculated from the experimental data following the procedure outlined by Mukaddam [3.18].

2. Second method - ACI Committee 209 [3.5] Table:

ACI Committee 209 [3.5] has proposed the following expression for the prediction of creep deformation:

$$C_t = K_s K_H K_h K_\tau \frac{(t-\tau)^{0.60}}{10 + (t-\tau)^{0.60}} C_u \tag{3.33}$$

where,

C_t = creep coefficient = $\frac{\text{creep strain at any time, t}}{\text{initial instantaneous strain}}$

C_u = ultimate creep coefficient to be determined from experimental data

= $\frac{\text{creep strain at infinite time after loading}}{\text{initial strain at time of loading}}$

= 2.35 for standard conditions

K_s = slump correction factor

= $0.81 + 0.07s$

K_H = humidity correction factor

= $1.27 - 0.0067\ H$, $H \geq 40$

H = relative humidity

K_h = size correction factor

= $1.0 - 0.0167\ (sz - 6.0)$, $sz > 6.0$

= 1.0, $sz \leq 6.0$

K_τ = age at loading correction factor

= $1.25\ \tau^{-0.118}$ for moist cured concrete for 7 days

s = slump in inches

sz = minimum size of member in inches

t = observation time in days

τ = age at loading in days

Standard Conditions for Creep:

(1) slump = 2.7 inches

(2) ambient relative humidity = 40% or less

(3) minimum thickness = 6 inches or less

(4) loading age = 7 days for moist cured concrete

For the standard conditions, all the correction factors are 1.0.

Using Eq. (3.33) for standard conditions, creep data are generated for 15 loading ages--7, 10, 14, 21, 28, 40, 60, 80, 91, 100, 120, 180, 270, 365, 400 days. Using $\lambda_1 = 0.1$, $\lambda_2 = 0.01$ and $\lambda_3 = 0.001$, the coefficients a_i of the Eq. (3.20):

$$C(\tau,t-\tau) = \sum_{i=1}^{3} a_i(\tau)\left[1 - e^{-\lambda_i(t-\tau)}\right]$$

are determined by least square method as described for the previous method. These a_i's are stored as data in the computer subroutine. Values of a_i for any age at loading in between these loading ages are taken as linear interpolations.

For any other state of conditions except the standard, the a_i values are multiplied by the correction factors K_s, K_H, K_h, K_τ as the case may be to give corrected a_i values. These a_i values are then used in Eq. (3.20) to calculate creep compliance.

3.2.9 Comparison with Experimental Data

To check the validity of the creep compliance expression chosen, the theoretical curve generated by Eq. (3.20) is compared to experimental values as illustrated in Fig. 3.6. The theoretical curves, when generated with a_i values obtained by least square method as described for the first method, show almost an exact fit--the maximum discrepancy being less than 2%. The curves generated by the second method from ACI tables seem satisfactory, considering the numer of uncertain factors involved, with the range of discrepancy being 0-5%.

To check the validity of the linear interpolation of a_i values for ages which are in between the 15 standard ages at loading--7, 10, 14, 21, 28, 40, 60, 80, 91, 100, 120, 180, 270, 365 and 400 days--graphs of a_i vs. different ages at loading are plotted in Fig. 3.7. The graphs show that the variation of a_i values with age at loading is quite smooth and hence linear interpolation will not give rise to

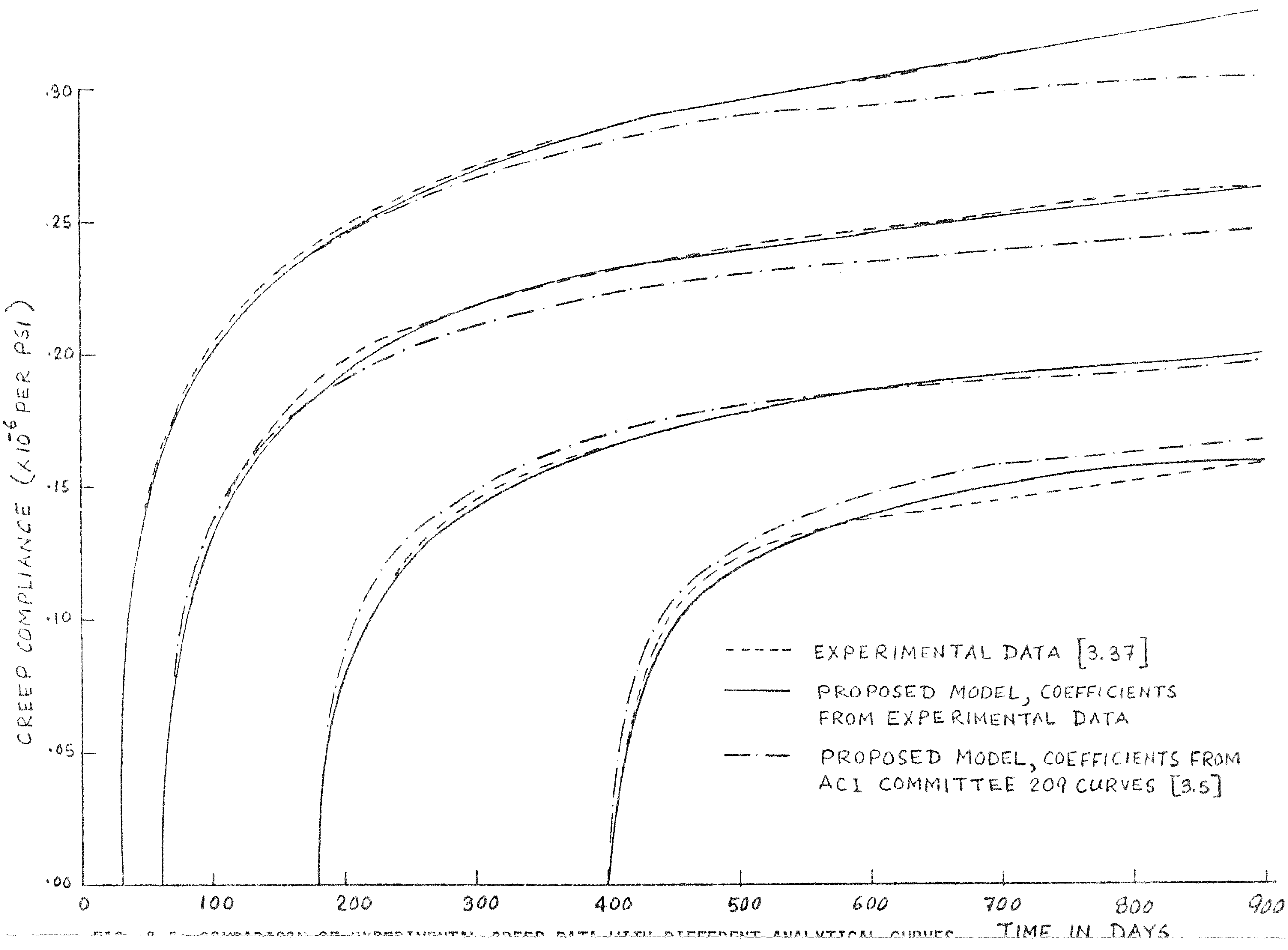

FIG. 3.5 COMPARISON OF EXPERIMENTAL CREEP DATA WITH DIFFERENT ANALYTICAL CURVES

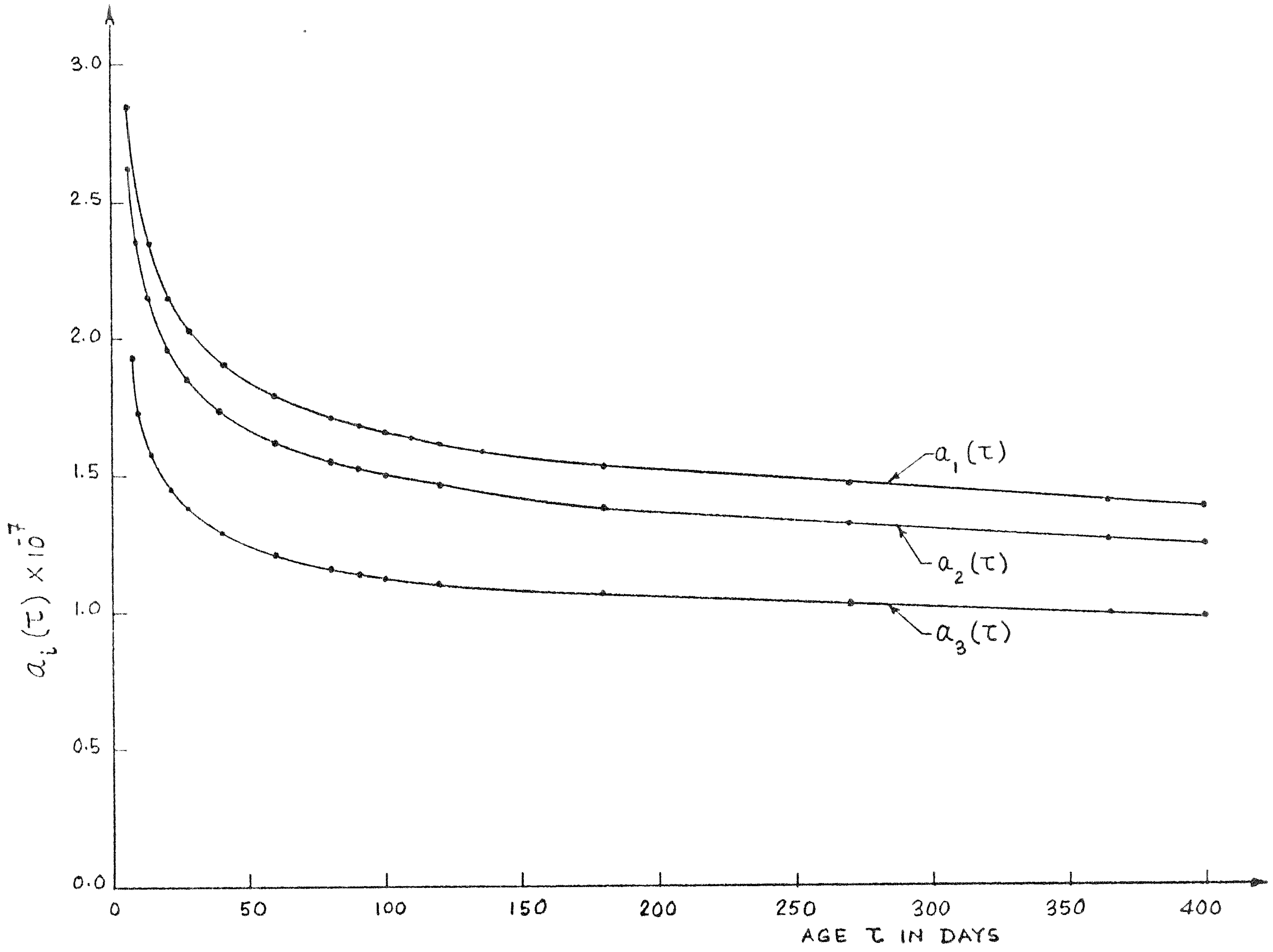

FIG. 3.7 CREEP COEFFIEICNTS VS. AGE IN DAYS

significant errors.

To check out the validity of the creep strain increment calculation procedure as outlined in subsection 3.2.7, comparisons are made with experimental and theoretical curves of Ross [3.36] and theoretical curves of Selna [1.39] for a concrete prism subjected to different stress histories. These are plotted in Figs. 3.8, 3.9, and 3.10. These show satisfactory correspondence with the experimental values. Figures 3.8 and 3.9 show that the proposed algorithm compares favorably with Selna's [1.39] method. At the same time, it requires the stress history from only a single previous time step. Selna's method requires stress histories from the previous two time steps and thus requires more computational effort.

Figure 3.10 shows the proposed algorithm and gives results which compare favorably with Ross' [3.36] method of superposition. Ross' method is very cumbersome as it requires knowledge of the stress histories at all previous time steps.

3.2.10 Advantages of the Creep Model

There are a number of advantages in adopting the proposed creep model.

First, it takes into account the three important factors which influence creep of concrete--age at application of loading, duration of loading, and temperature variations during the period under consideration.

Second, the computational procedure is very efficient as only the stress history of the last time step is needed for the calculation of the new creep strain increment. Selna's [1.39] method requires stress

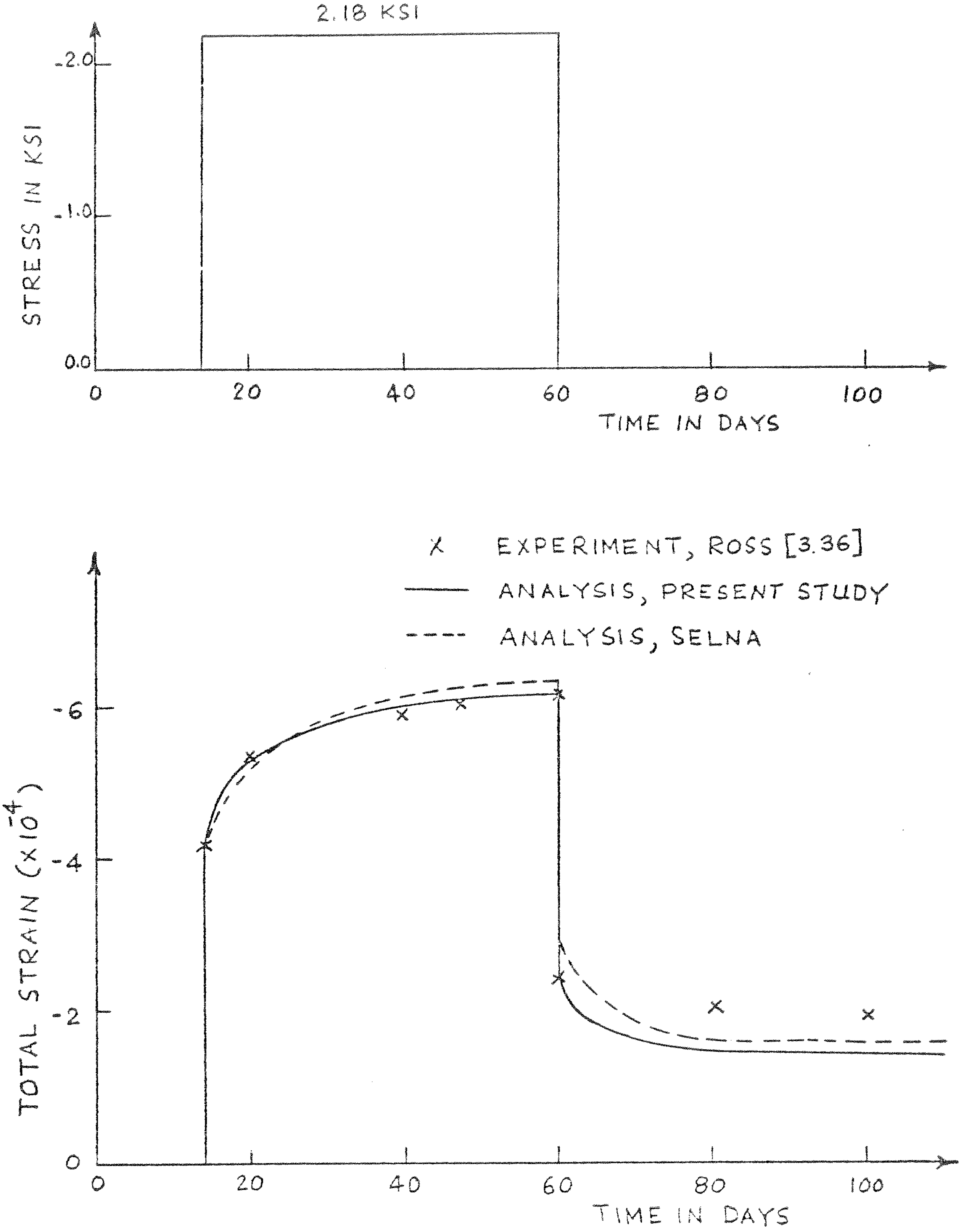

FIG. 3.8 COMPARISON OF PROPOSED ALGORITHM WITH EXPERIMENTAL VALUES FOR CONSTANT STRESS APPLICATION

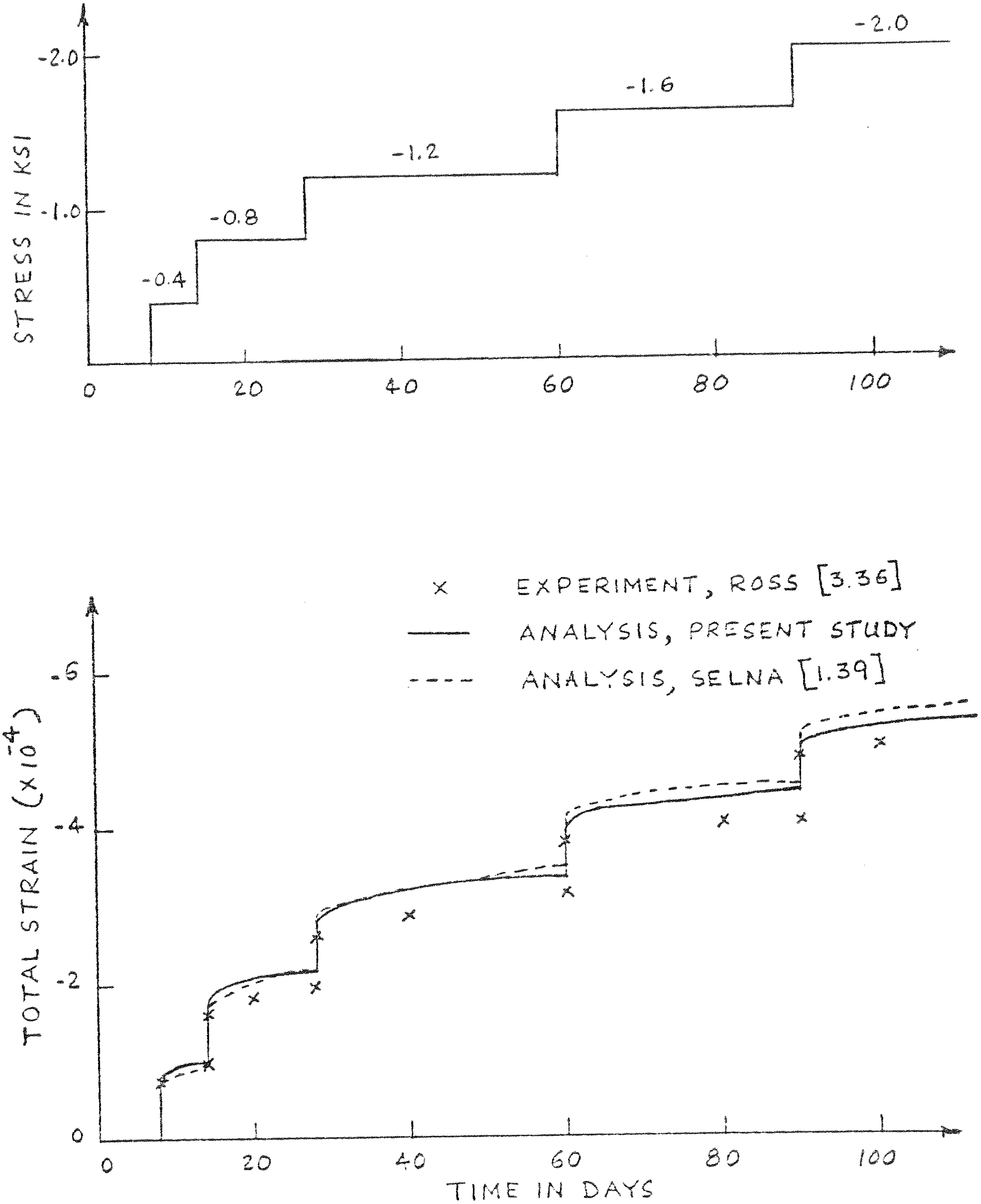

FIG. 3.9 COMPARISON OF PROPOSED ALGORITHM WITH EXPERIMENTAL VALUES FOR STEPPED-UP STRESS APPLICATION

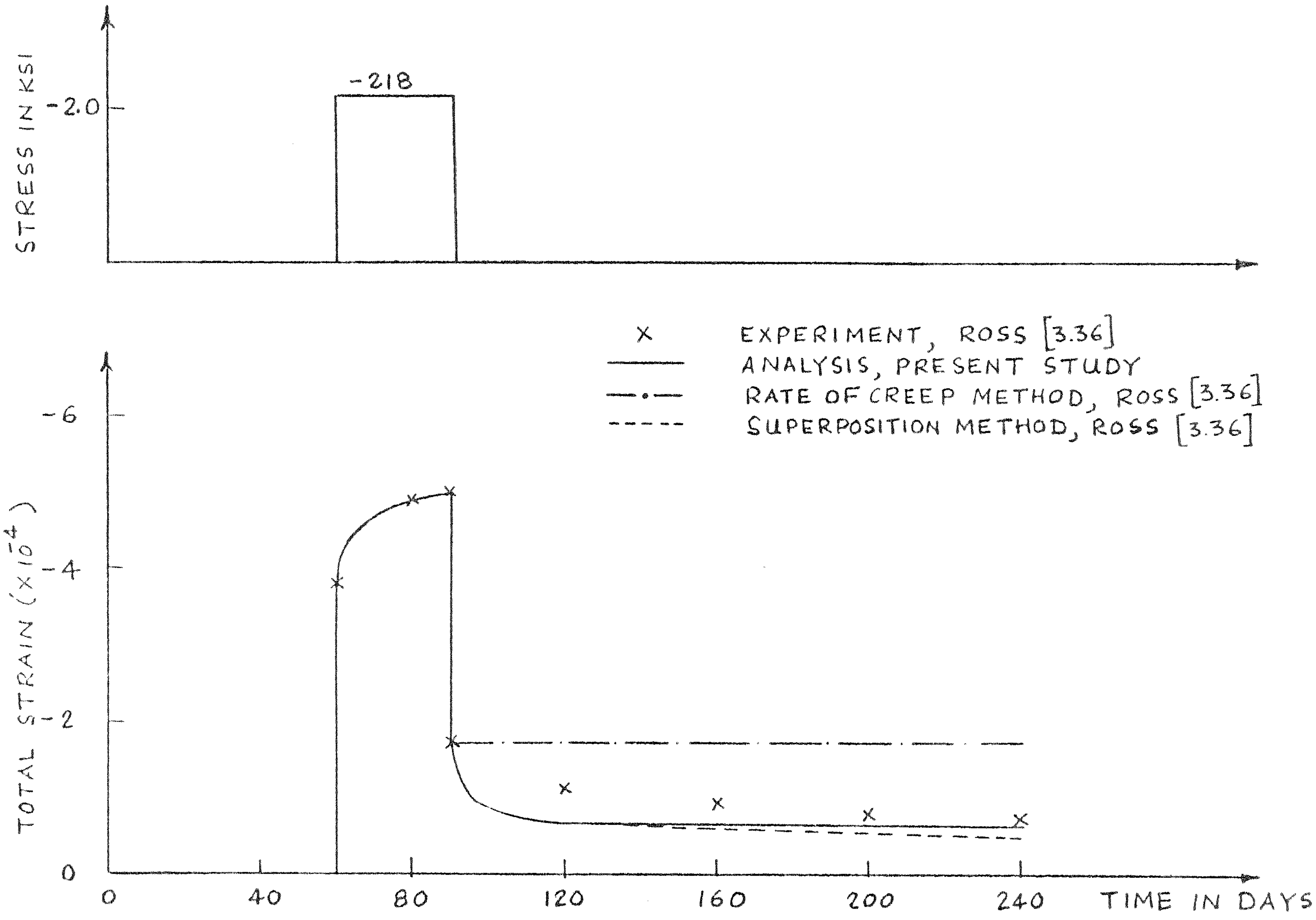

FIG. 3.10 COMPARISON PF PROPOSED ALGOTITHM WITH EXPERIMENTAL DATA

histories for the last two time steps. Mukaddam's [3.18] method requires stress histories for all the previous time steps. Āldstedt [1.42] uses a linear superposition method, where all previous instantaneous strain increments must be stored. For a realistic structural problem, the computer storage requirement would quickly become a limiting factor.

Third, the creep parameters can very easily be determined from experimental data for any concrete if available. Little effort is required in preparing input data for this method.

Fourth, the second option of using ACI tables to generate creep curves makes it possible to take into account various variables like slump, relative humidity, size of members, etc. While ACI Committee 209 [3.5] method would require storage of stress histories for all previous time steps, the proposed algorithm reduces this to the storage of the last time step while retaining the advantages of the field condition variables--slump, relative humidity, and size of members. This option can be used in cases where it is not possible to get experimental creep data to generate the creep curves.

3.3 Shrinkage

3.3.1 General Remarks

Concrete is distinguished from many other structural materials by the fact that it undergoes volume changes which take place independently of externally imposed stresses and of temperature changes. These volume changes are generally defined as shrinkage of concrete.

Structural interest in shrinkage arises from the fact that it is one of the most frequent causes of cracking of concrete and is also one of the most difficult ones to prevent. It is difficult to predict whether or not cracking will occur due to shrinkage and what are the best methods of preventing the formation of wide cracks. It is thus very important to understand the mechanism of shrinkage, the factors influencing shrinkage and how best to model it.

3.3.2 Mechanism

Shrinkage occurs primarily from two causes--loss of water on drying and volume changes on carbonation.

When curing is stopped and concrete starts drying, loss of water from the concrete to the ambient medium--in this case unsaturated air--takes place. The water, lost first, is the free water held in the capillaries; this causes practically no shrinkage. As drying continues, absored water is removed and the shrinkage starts. The process of moisture diffusion from the interior of the concrete toward the surface is exceedingly slow and complex. The surface dries more rapidly than the interior and therefore there is a nonuniform distribution of shrinkage known as differential shrinkage. However, at present, uniform shrinkage is usually considered for analysis and design purposes.

Carbonation shrinkage occurs because of the chemical reaction of hydrated cement mineral, calcium hydroxide, $Ca(OH)_2$, with atmospheric carbon dioxide, CO_2, in the presence of moisture, H_2O, to produce particles of calcium carbonate, $CaCO_3$. Carbonation shrinkage is generally not separated from drying shrinkage. In fact, most of the experimental data on drying shrinkage includes carbonation shrinkage.

3.3.3 Influencing Factors

The following factors affect the shrinkage of concrete:

1. Aggregate: Shrinkage is inversely proportional to the aggregate content in a given concrete mix. The aggregate has a restraining effect on the tendency of neat cement paste toward shrinkage.

2. Water-cement ratio: Shrinkage is directly proportional to the water content of a concrete mix because increased water content causes an increase in shrinkage.

3. Size effect: Size effect is a significant factor in shrinkage as drying takes place at a faster rate nearer the surface than near the core of the member. This nonuniform drying causes differential shrinkage to take place with the inner, more moistened core acting as a restraint against shrinkage. Thus, shrinkage is inversely proportional to the size of the member.

4. Relative humidity: Shrinkage is inversely proportional to the relative humidity of the ambient medium.

3.3.4 Analytical Model

The method of analysis developed in the present study is the displacement formulation of the finite element method. An incremental load, iterative solution procedure with a step-by-step integration in the time domain is adopted. The shrinkage strains are taken as initial strains and are assumed to occur at the end of each time step. For simplicity, it is also assumed that uniform shrinkage occurs in each element. Thus, the requirement for the solution procedure pursued in this investigation is to have a model of shrinkage which enables the shrinkage strain increments to be calculated for each time step. Two options are provided for the calculation of shrinkage strain increments at each time step.

In the first option, shrinkage strain increments for each time step are read directly from the experimental curves available. In the absence of available experimental data on the particular concrete to be analyzed, the second option is used.

In the second option, ACI Committee 209 [3.5] recommended formulas are used for predicting the shrinkage increments at each time step. The ACI Committee recommends using:

$$(\varepsilon_{sh})_t = K_s K_h K_H \frac{(t-\tau_0)^e}{f + (t-\tau_0)^e} (\varepsilon_{sh})_u \tag{3.34}$$

where

$(\varepsilon_{sh})_t$ = shrinkage strain at observation time, t

$(\varepsilon_{sh})_u$ = ultimate shrinkage strain, to be determined from experiments

t = time at observation

τ_0 = age of curing

f,e = constants, to be determined from experiments

K_s = correction factor for slump of concrete mix

K_h = correction factor for size of concrete member

K_H = correction factor for relative humidity

Normal ranges of constants e,f and $(\varepsilon_{sh})_u$, using normal- or light-weight concrete for either moist curing or steam curing, are found to be as follows:

$e = 0.90$ to 1.10

$f = 20$ to 130

$(\varepsilon_{sh})_u = 415 \times 10^{-6}$ to 1070×10^{-6} in./in.

By conveniently using Eq. (3.34) for predicting shrinkage strain, standard equations can be selected [3.5] as follows:

For concrete moist cured for 7 days:

$$(\varepsilon_{sh})_t = K_s K_h K_H \frac{(t-7)}{35 + (t-7)} \times 800 \times 10^{-6} \tag{3.35}$$

For concrete steam cured for 3 days:

$$(\varepsilon_{sh})_t = K_s K_h K_H \frac{(t-3)}{55 + (t-3)} \times 730 \times 10^{-6} \tag{3.36}$$

The correction factors are provided to take into account different field conditions that may exist for different cases under consideration.

1. Slump correction factor, K_s: Slump of concrete mix is directly proportional to the water content of the mix. Hence, the less slump, the lower will be the amount of shrinkage. Figure 3.11a shows the variation of the slump correction factor with the slump.

2. Humidity correction factor, K_H: Shrinkage decreases with increases in ambient humidity. The humidity correction factor is given by:

$$\begin{aligned} K_H &= 1.40 - 0.010\,H & \quad 40 \le H \le 80 \\ &= 3.00 - 0.030\,H & \quad 80 \le H \le 100 \end{aligned} \tag{3.37}$$

where H = relative ambient humidity.

3. Size correction factor: Shrinkage decreases for increasing thickness of concrete members. Figure 3.11c shows the size correction factors.

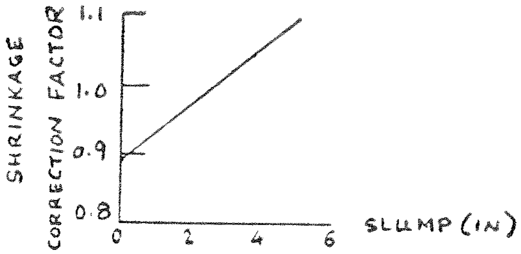

a. SLUMP CORRECTION

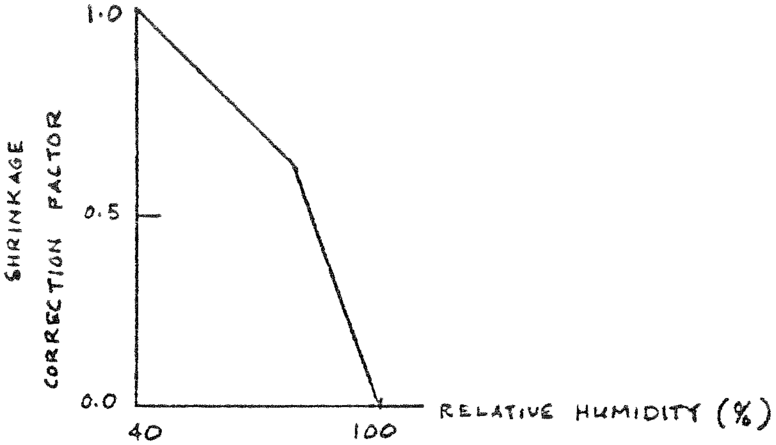

b. HUMIDITY CORRECTION

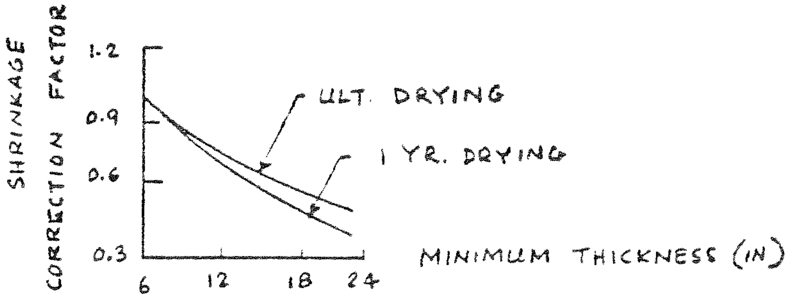

c. THICKNESS CORRECTION

FIG. 3.11 SHRINKAGE CORRECTION FACTORS

4. METHOD OF ANALYSIS

4.1 General Remarks

The method chosen for the numerical analysis of boundary value problems in this study is the well-known finite element method. It is a discretization procedure through which a continuum with an infinite number of unknowns is approximated as an assemblage of elements having a finite number of unknowns. Several texts [4.1,4.2] have been written on the finite element method. Thus, only a brief description will be given here for the finite element displacement formulation, which is the approach used in this study.

4.2 Finite Element Displacement Formulation

The following steps are taken in the displacement formulation of the finite element method:

1. The elastic continua are discretized into a number of elements.
2. The displacement vector, $\underset{\wedge}{u}$, at any point within the element, is approximated by interpolation functions, $\underline{N}$, also known as the shape functions. The interpolation functions relate $\underset{\wedge}{u}$ to the generalized coordinates, $\underset{\wedge}{r}$, which, in the displacement formulation, are the nodal displacements.

$$\underset{\wedge}{u} = \underline{N}\,\underset{\wedge}{r} \tag{4.1}$$

3. From compatibility relationships, the strain vector, $\underset{\wedge}{\varepsilon}$, at any point within the element, may be found in terms of displacement vector, $\underset{\wedge}{u}$, as:

$$\begin{aligned}\underset{\wedge}{\varepsilon} &= \underline{L}\ \underset{\wedge}{u} \\ &= \underline{L}\ \underline{N}\ \underset{\wedge}{r} \\ &= \underline{B}\ \underset{\wedge}{r}\end{aligned} \tag{4.2}$$

where $\underline{L}$ = a linear differential operator

$\underline{B} = \underline{L}\ \underline{N}$ = strain-displacement matrix

4. The constitutive relationships may be expressed as:

$$\underset{\wedge}{\sigma} = \underline{D}\ (\underset{\wedge}{\varepsilon} - \underset{\wedge}{\varepsilon}_o) + \underset{\wedge}{\sigma}_o \tag{4.3}$$

where $\underline{D}$ = elasticity matrix containing appropriate material properties

$\underset{\wedge}{\varepsilon}_o$ = initial strain vector

$\underset{\wedge}{\sigma}_o$ = initial stress vector

5. The equilibrium equation is obtained from the principle of virtual work as:

$$\delta\underset{\wedge}{r}^T\underset{\wedge}{\overline{R}} + \sum_e \int_S \delta\underset{\wedge}{u}^T\underset{\wedge}{b}dV + \sum_e \int_S \delta\underset{\wedge}{u}^T\underset{\wedge}{f}dS = \sum_e \int_V \delta\underset{\wedge}{\varepsilon}^T\underset{\wedge}{\sigma}dV \tag{4.4}$$

where $\underset{\wedge}{\overline{R}}$ = external load vector

$\underset{\wedge}{b}$ = body force vector

$\underset{\wedge}{f}$ = surface traction vector

$\sum_e$ = summation over all elements

V = volume of one element

S = surface of one element

$\delta\underset{\wedge}{r}$, $\delta\underset{\wedge}{u}$, $\delta\underset{\wedge}{\varepsilon}$ = virtual nodal displacement vector and corresponding element displacement and strain vectors.

Equation (4.4) may be rewritten, substituting values from Eqs. (4.1), (4.2) and (4.3) as follows:

$$\delta \underset{\wedge}{r}^T \underset{\wedge}{\overline{R}} + \delta \underset{\wedge}{r}^T \sum_e \int_V \underline{N}^T \underset{\wedge}{b} dV + \delta \underset{\wedge}{r}^T \sum_e \int_S \underline{N}^T \underset{\wedge}{f} dS$$

$$= \delta \underset{\wedge}{r}^T \sum_e \int_V \underline{B}^T \{ \underline{D}(\underset{\wedge}{\varepsilon} - \underset{\wedge}{\varepsilon}_o) + \underset{\wedge}{\sigma}_o \} dV \tag{4.5}$$

Since $\delta \underset{\wedge}{r}$ is arbitrary:

$$\underset{\wedge}{\overline{R}} + \sum_e \int_V \underline{N}^T \underset{\wedge}{b} dV + \sum_e \int_S \underline{N}^T \underset{\wedge}{f} dS$$

$$= \sum_e \int_V \underline{B}^T \underline{D}\underline{B} dV \underset{\wedge}{r} - \sum_e \int_V \underline{B}^T \underline{D} \underset{\wedge}{\varepsilon}_o dV + \sum_e \int_V \underline{B}^T \underset{\wedge}{\sigma}_o dV$$

or,

$$\underset{\wedge}{\overline{R}} + \underset{\wedge}{F}_b + \underset{\wedge}{F}_s + \underset{\wedge}{F}_{\varepsilon_o} + \underset{\wedge}{F}_{\sigma_o} = \underline{K} \underset{\wedge}{r} \tag{4.6}$$

where $$\underset{\wedge}{F}_b = \sum_e \int_V \underline{N}^T \underset{\wedge}{b} dV \tag{4.7a}$$

= equivalent nodal force vector due to body forces

$$\underset{\wedge}{F}_s = \sum_e \int_S \underline{N}^T \underset{\wedge}{f} dS \tag{4.7b}$$

= equivalent nodal force vector due to surface tension

$$\underset{\wedge}{F}_{\varepsilon_o} = \sum_e \int_V \underline{B}^T \underline{D} \underset{\wedge}{\varepsilon}_o dV \tag{4.7c}$$

= equivalent nodal forces due to initial strain

$$\underset{\wedge}{F}_{\sigma_o} = \sum_e \int_V \underline{B}^T \underset{\wedge}{\sigma}_o dV \tag{4.7d}$$

= equivalent nodal forces due to initial stress

$$\underline{K} = \sum_e \int_V \underline{B}^T \underline{D}\underline{B} dV \tag{4.7e}$$

= stiffness matrix

or,

$$\underset{\wedge}{R} = \underline{K} \underset{\wedge}{r} \tag{4.8}$$

where $\underset{\wedge}{R} = \underset{\wedge}{\overline{R}} + \underset{\wedge}{F}_b + \underset{\wedge}{F}_s + \underset{\wedge}{F}_{\varepsilon_0} + \underset{\wedge}{F}_{\sigma_0}$

= equivalent nodal force vector

6. Solution of Eq. (4.8) gives the unknown nodal displacement vector, $\underset{\wedge}{r}$. Strains and stresses in the elements can be obtained from Eqs. (4.2) and (4.3). This completes the solution of the structural analysis problem

4.3 Sources of Nonlinearity in Reinforced Concrete Structural Response

In the displacement formulation given in the previous section, two assumptions are made:

1. The strain-displacement relationship is linear, i.e. $\underline{B}$ is independent of $\underset{\wedge}{r}$ in Eq. (4.2).

2. The constitutive relationship is linear, i.e. $\underline{D}$ is independent of $\underset{\wedge}{\varepsilon}$ in Eq. (4.3).

The violation of the first assumption causes nonlinear behavior termed as geometric nonlinearity. Material nonlinearity occurs due to the violation of the second assumption. In this study, the first assumption is accepted to be valid. This implies the usage of the small displacement theory.

The nonlinear behavior of structures will be due to material nonlinearity. Several factors contribute toward the material nonlinearity of reinforced concrete structures. These include: (1) cracking of concrete; (2) nonlinear stress-strain relations for concrete and steel, bond and aggregate interlock; and (3) time-dependent effects such as creep, shrinkage, temperature and load history. In the present study all the above factors, except bond and aggregate interlock, will be considered.

4.4 Techniques for Nonlinear Analysis

Three basic techniques are employed for the solution of the nonlinear problems by the finite element method--(1) incremental or stepwise procedures, (2) iterative or Newton methods, and (3) step-iterative or mixed procedures.

1. Incremental Method: In this method the total load vector, $\underset{\wedge}{R}$, in Eq. (4.8) is subdivided into a number of increments.

$$\underset{\wedge}{R} = \sum_{i=1}^{m} \Delta \underset{\wedge}{R}_i \tag{4.9}$$

The load increments are applied one at a time and a fixed value of stiffness matrix, $\underline{K}$, is assumed during the application of each increment. However, $\underline{K}$ may take different values during different increments. Thus, for ith increment, Eq. (4.8) may be rewritten as:

$$\Delta \underset{\wedge}{R}_i = \underline{K}_i \, \Delta \underset{\wedge}{r}_i \tag{4.10}$$

where $\underline{K}_i = \underline{K}(\underset{\wedge}{r}_{i-1}, \underset{\wedge}{R}_{i-1})$

The total displacement vector, $\underset{\wedge}{r}$, is a summation of displacement increments $\Delta \underset{\wedge}{r}_i$ found from the solution of Eq. (4.10).

$$\underset{\wedge}{r} = \sum_{i=1}^{m} \Delta \underset{\wedge}{r}_i \tag{4.11}$$

The method is illustrated in Fig. 4.1.

2. Iterative Method: In this procedure, the structure is fully loaded and then a series of iterations is executed to obtain an approximate solution close to the correct solution. Since at each iteration a linear solution is obtained for the load vector, the equilibrium condition is not

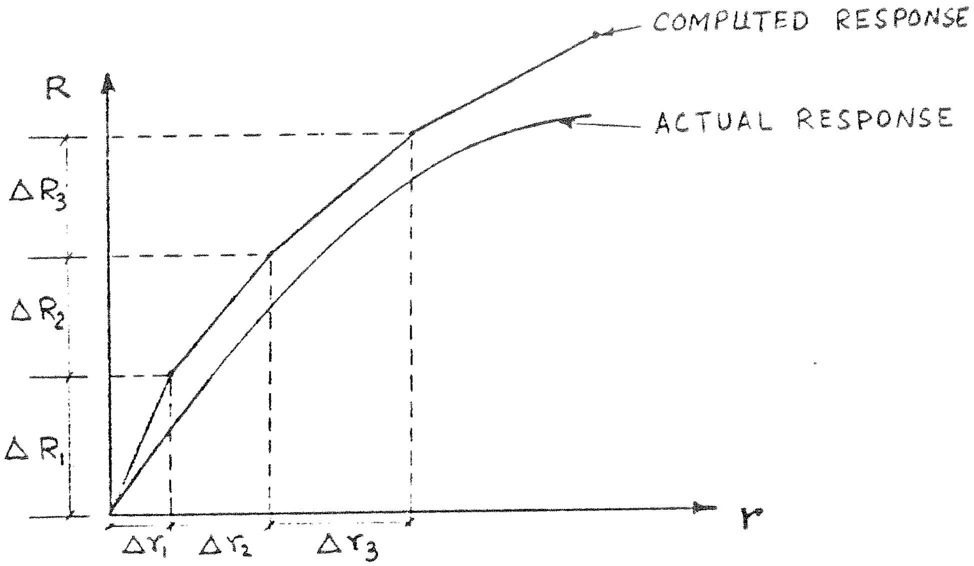

FIG. 4.1 INCREMENTAL METHOD

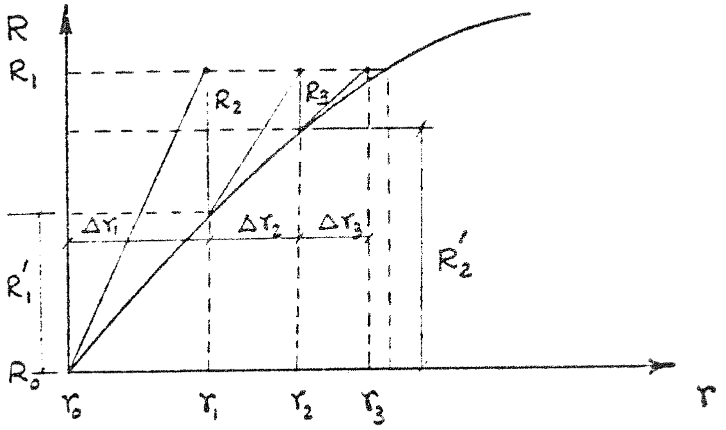

FIG. 4.2 ITERATIVE METHOD

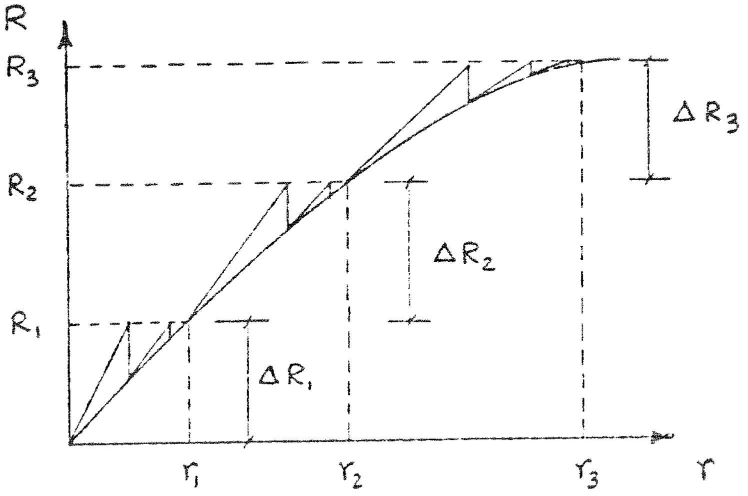

FIG. 4.3 STEP-ITERATIVE METHOD

satisfied. After each iteration, the portion of the load that is not balanced is calculated and used in the next iteration to compute additional displacement.

At the <u>ith</u> iteration:

$$\underset{\wedge}{R}_i = \underset{\wedge}{R} - \underset{\wedge}{R}'_{i-1} \tag{4.12}$$

where $\underset{\wedge}{R}_i$ = load vector to be used in the <u>ith</u> cycle

$\underset{\wedge}{R}'_{i-1}$ = equilibrium load vector at the end of (i-1)<u>th</u> cycle

Now, $$\underset{\wedge}{R}_i = \underline{K}_i \, \Delta \underset{\wedge}{r}_i \tag{4.13}$$

where $\Delta \underset{\wedge}{r}_i$ = displacement increments at <u>ith</u> iteration

$$\underline{K}_i = \underline{K}(\underset{\wedge}{r}_{i-1}, \underset{\wedge}{R}'_{i-1})$$

Now, total displacement is given by:

$$\underset{\wedge}{r}_i = \sum_i \Delta \underset{\wedge}{r}_i \tag{4.14}$$

This procedure is repeated until either $\underset{\wedge}{R}_i$ or $\Delta \underset{\wedge}{r}_i$ falls within some tolerance limit when the solution is stopped. Figure 4.2 illustrates this method.

3. Step-iterative Method: This method utilizes a combination of the above two methods. The load vector is divided into several increments and for each increment, an iterative method is followed. Figure 4.3 illustrates this method.

The above three methods have their advantages and disadvantages. Selection of any one method will depend on the type of problem to be solved, the computational effort needed for the solution and the degree of accuracy required. The third method will yield results much more accurate than those given by the first two methods, but at the cost of greater computational effort. All the methods are, obviously, a series of linear solutions attempting to approximate the nonlinear problem in a piecewise linear fashion. Ultimately, the degree of accuracy and the computational efforts required to achieve that accuracy are the two vital factors that will determine the choice of method to be used.

One of the significant steps in the iterative methods is the determination of the stiffness matrix, $\underline{K}$, which is to be used in the solution of Eq. (4.8) for each load step or each iteration as the case may be. The three commonly used methods are known as the initial stiffness method, secant stiffness method, and tangent stiffness method; these are illustrated in Fig. 4.4. The convergence is fastest with the tangent stiffness method, but at each iteration, a new stiffness matrix must be formed, requiring considerable computational effort. The initial stiffness method, on the other hand, uses the same stiffness matrix for all iterations. Thus, the triangularized stiffness matrix for the first iteration may be stored and used for solving the later iterations at a very fast rate. The convergence, however, is very slow and for highly nonlinear materials may take an excessive number of iterations. It is obvious that the choice of any one of the methods or a combination of the three will depend on the type of problem to be solved, the degree of accuracy to be achieved, and the amount of computational effort required.

4.5 Types of Finite Element Used

Five types of finite elements are used to model different

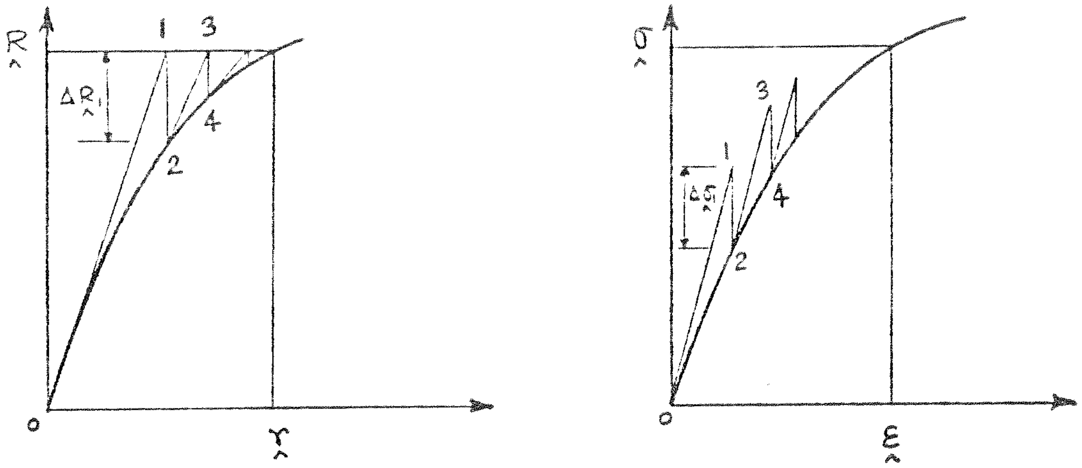

a. INITIAL STIFFNESS METHOD

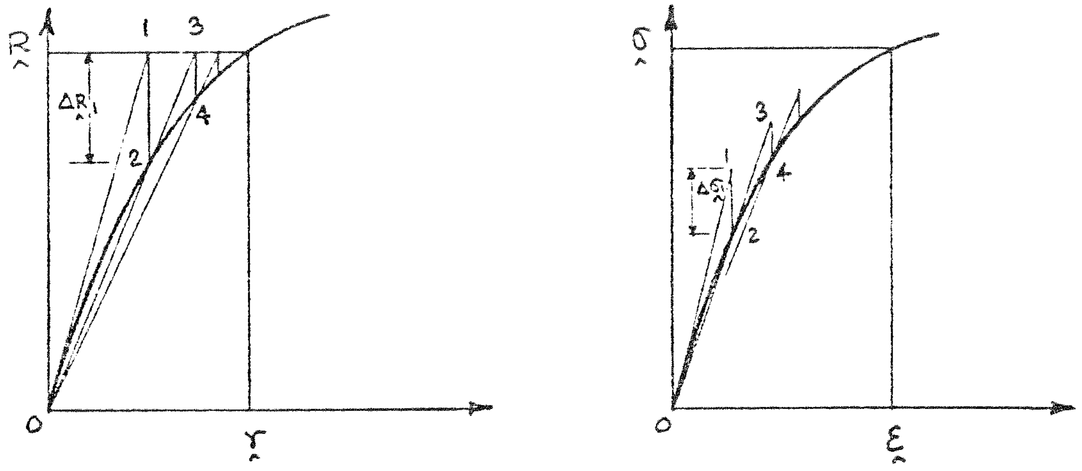

b. SECANT STIFFNESS METHOD

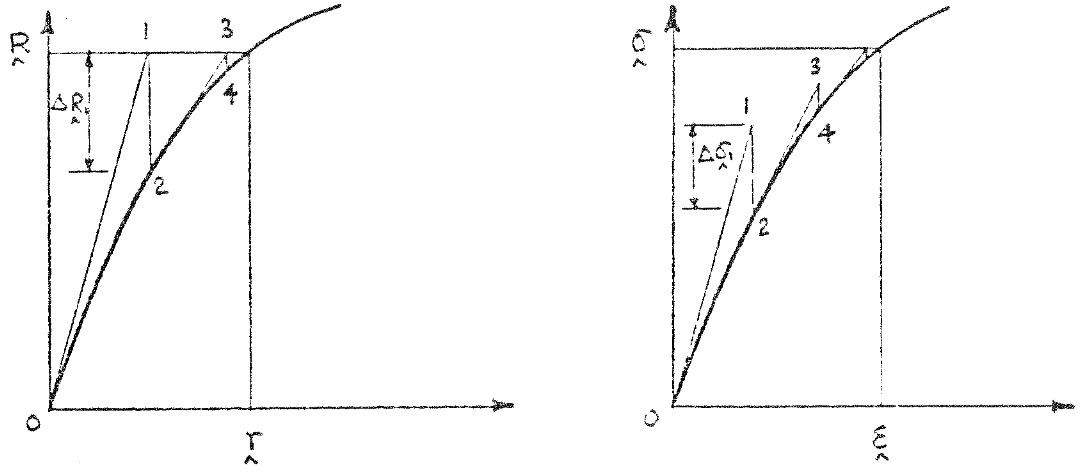

C. TANGENT STIFFNESS METHOD

FIG. 4.4 ITERATION METHODS

structural elements in the present study. The elements are chosen on the basis of efficiency with regard to the computational effort needed in forming the element stiffness matrix, the accuracy of the element displacement interpolation functions to represent the actual displacement distribution and the ability of the element geometry to represent accurately the shapes of various structures considered in the present study. Brief descriptions of the elements are presented below.

4.5.1 One-dimensional Truss Element

This element may be used to model either a steel reinforcing bar in a reinforced concrete structural component, or a concrete cylinder under concentric axial load or a reinforced concrete column under concentric axial load as shown in Fig. 4.5. In the first two cases, a truss element having the appropriate section and material properties is used. For the third case, two truss elements--having material and section properties of either steel or concrete-- are used in combination. Perfect bond is assumed to exist between both steel and concrete elements. The stiffness of the composite section is obtained by adding the stiffness contributions from each component element.

Displacement distribution is assumed to be linear along the length of the element. The axial distribution, u, at any point in the element is given by (Fig. 4.5):

$$u = \underline{N}\,\underset{\wedge}{r} \tag{4.16}$$

where $\underline{N}$ = shape functions

$= [1-s \quad s]$

$s = x/L$

$$r = \begin{Bmatrix} r_1 \\ r_2 \end{Bmatrix}$$

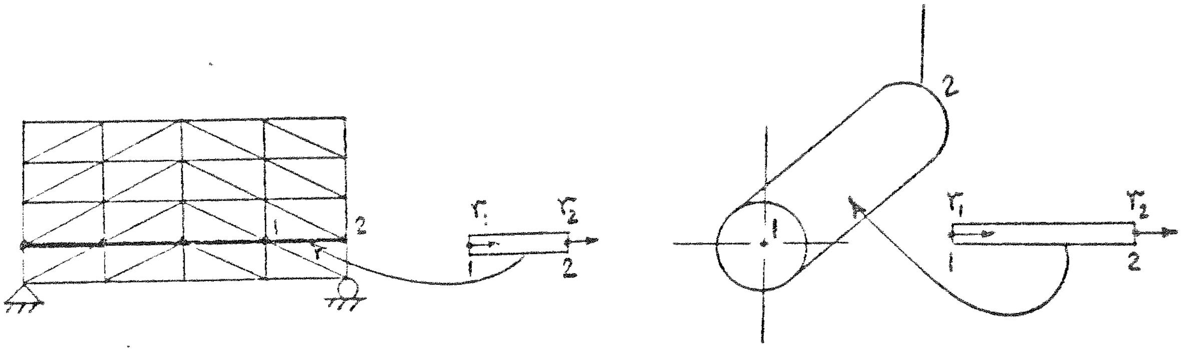

a. MODEL OF STEEL REINFORCING BAR

b. MODEL OF CONCRETE CYLINDER

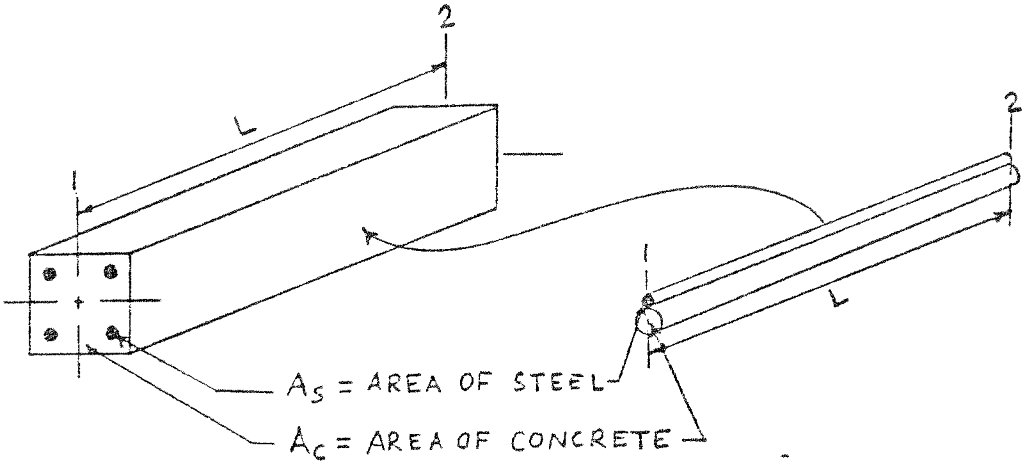

C. MODEL OF RC COLUMN

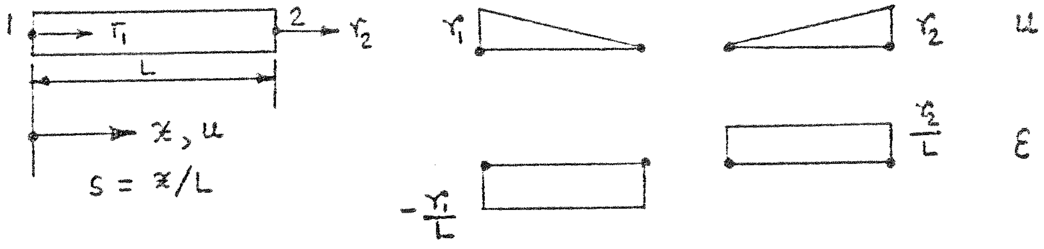

d. LINEAR SHAPE FUNCTIONS

FIG. 4.5 ONE-DIMENSIONAL TRUSS ELEMENT

The strain at any point is given by:

$$\varepsilon = \frac{du}{dx} = \underset{-}{B}\ \underset{\wedge}{r} \tag{4.16}$$

where $\underset{\sim}{B} = \frac{1}{L}[-1 \quad 1]$

The element stiffness matrix is given by:

$$\underset{-}{K} = \int_V \underset{-}{B}^T E\ \underset{-}{B}\ dV = \frac{EA}{L}\begin{bmatrix} 1 & -1 \\ -1 & 1 \end{bmatrix} \tag{4.17}$$

where E = modulus of elasticity, A = axial area of the element, and L = length of the element.

4.5.2 Triangular Shell Element

The triangular shell element, developed by Lin [1.27] for reinforced concrete shells of general form, is used to study shell-type structures in the present investigation. The usually curved shell surface is approximated as an assemblage of flat surfaces by the use of this element. The size and shape of the flat triangular elements are defined by the coordinates of the nodal points lying on the reference surface of the shell.

The shell is a three-dimensional body (Fig. 4.6) and some assumptions are needed to reduce the problem to a two-dimensional case. Kirchoff's classical hypotheses are adopted for this purpose. These hypotheses are:

1. A plane section normal to the reference surface remains plane after deformation.

2. Stresses normal to the reference surface are neglected.

Based on the above assumptions, the displacements at any point

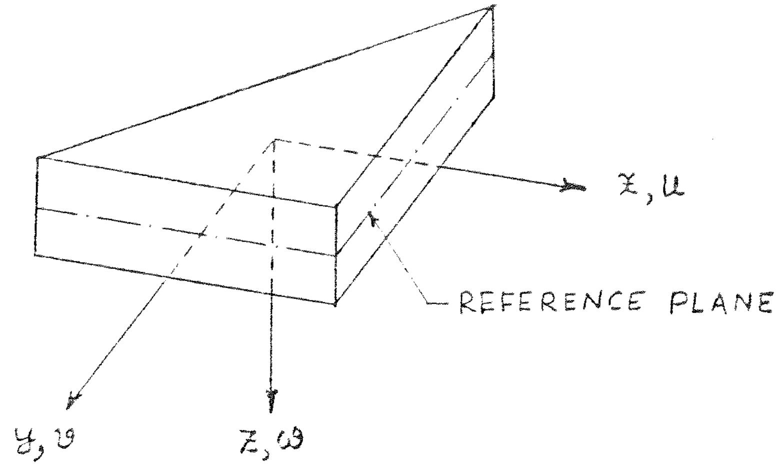

FIG. 4.6 COORDINATE SYSTEM IN A TRIANGULAR SHELL ELEMENT

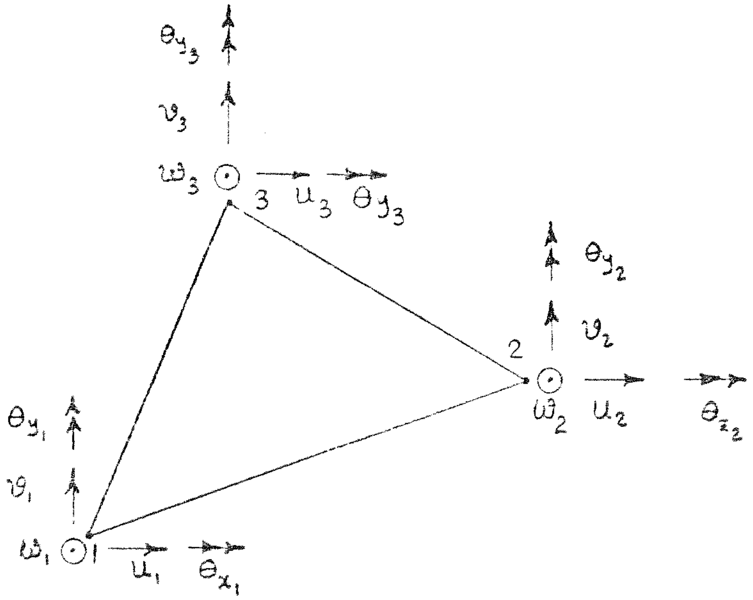

FIG. 4.7 NODAL DEGREES OF FREEDOM OF A TRIANGULAR SHELL ELEMENT

in the element may be expressed in terms of the displacements and their derivatives on the reference surface (Fig. 4.6).

$$\begin{aligned} w &= w_o(x,y) \\ u &= u_o(x,y) - z\,\frac{\partial w}{\partial x} \\ v &= v_o(x,y) - z\,\frac{\partial w}{\partial y} \end{aligned} \qquad (4.18)$$

where u,v,w are the displacements in the x,y,z directions at any point on the element, while u_o, v_o, w_o are those on the reference surface.

The reference surface displacements may be written in terms of the nodal degrees of freedom (Fig. 4.7) as:

$$\begin{aligned} w_o &= \underline{M}(x,y) \begin{Bmatrix} \underset{\wedge}{w} \\ \underset{\wedge}{\theta}_x \\ \underset{\wedge}{\theta}_y \end{Bmatrix} \\ u_o &= \underline{N}(x,y)\, \underset{\wedge}{u} \\ v_o &= \underline{N}(x,y)\, \underset{\wedge}{v} \end{aligned} \qquad (4.19)$$

where $\underline{M}(x,y)$ and $\underline{N}(x,y)$ are the shape functions,

$$\begin{aligned} \underset{\wedge}{u} &= \langle\, u_1 \quad u_2 \quad u_3 \,\rangle^T \\ \underset{\wedge}{v} &= \langle\, v_1 \quad v_2 \quad v_3 \,\rangle^T \\ \underset{\wedge}{w} &= \langle\, w_1 \quad w_2 \quad w_3 \,\rangle^T \\ \underset{\wedge}{\theta}_w &= \langle\, \theta_{x1} \quad \theta_{x2} \quad \theta_{x3} \,\rangle^T \\ \underset{\wedge}{\theta}_y &= \langle\, \theta_{y1} \quad \theta_{y2} \quad \theta_{y3} \,\rangle^T \end{aligned}$$

The strain vector at any point in the element is given by:

$$\underset{\wedge}{\varepsilon} = \begin{Bmatrix} \frac{\partial u}{\partial x} \\ \frac{\partial v}{\partial y} \\ \frac{\partial u}{\partial y} + \frac{\partial v}{\partial x} \end{Bmatrix} = \begin{Bmatrix} \frac{\partial uo}{\partial x} \\ \frac{\partial vo}{\partial y} \\ \frac{\partial uo}{\partial y} + \frac{\partial vo}{\partial x} \end{Bmatrix} -z \begin{Bmatrix} \frac{\partial^2 w}{\partial x^2} \\ \frac{\partial^2 w}{\partial y^2} \\ 2\frac{\partial^2 w}{\partial x \partial y} \end{Bmatrix} = \underset{\wedge}{\varepsilon} - z\,\underset{\wedge}{\chi} \tag{4.20}$$

Now, $\underset{\wedge}{\varepsilon}_o$ and $\underset{\wedge}{\chi}$ are the strain and curvature vectors at the reference surface and may be expressed as:

$$\underset{\wedge}{\varepsilon}_o = \begin{bmatrix} \underline{N},x & 0 \\ 0 & \underline{N},y \\ \underline{N},y & \underline{N},x \end{bmatrix} \begin{Bmatrix} \underset{\wedge}{u} \\ \underset{\wedge}{v} \end{Bmatrix} = \underline{B}_m \begin{Bmatrix} \underset{\wedge}{u} \\ \underset{\wedge}{v} \end{Bmatrix} \tag{4.21}$$

and

$$\underset{\wedge}{\chi} = \begin{bmatrix} \underline{M},xx \\ \underline{M},yy \\ \underline{M},xy \end{bmatrix} \begin{Bmatrix} \underset{\wedge}{w} \\ \underset{\wedge}{\theta}_x \\ \underset{\sim}{\theta}_y \end{Bmatrix} = \underline{B}_b \begin{Bmatrix} \underset{\wedge}{w} \\ \underset{\wedge}{\theta}_x \\ \underset{\sim}{\theta}_y \end{Bmatrix} \tag{4.22}$$

Equation (4.20) may be rewritten as:

$$\underset{\wedge}{\varepsilon} = [\underline{B}_m \quad -z\ \underline{B}_b]\ \underset{\wedge}{r} = \underline{B}\ \underset{\wedge}{r} \tag{4.23}$$

where $\underset{\wedge}{r} = \langle \underset{\wedge}{u} \quad \underset{\wedge}{v} \quad \underset{\wedge}{w} \quad \underset{\wedge}{\theta}_x \quad \underset{\sim}{\theta}_y \rangle^T$

The element stiffness is given by:

$$\underline{K} = \int_V \underline{B}^T \underline{D}\,\underline{B}\ dV = \begin{bmatrix} \underline{K}_{mm} & \underline{K}_{mb} \\ \underline{K}_{bm} & \underline{K}_{bb} \end{bmatrix} \tag{4.24}$$

where $\underset{\sim}{K}_{mm}$ = membrane stiffness matrix

$$= \int_V \underset{\sim}{B}_m^T \, \underset{\sim}{D} \, \underset{\sim}{B}_m \, dV$$

$$= \int\int \underset{\sim}{B}_m^T \, [\int \underset{\sim}{D} \, dz] \, \underset{\sim}{B}_m \, dxdy$$

$$= \int\int \underset{\sim}{B}_m^T \, \underset{\sim}{D}_{mm} \, \underset{\sim}{B}_m \, dxdy \qquad (4.25)$$

$\underset{\sim}{K}_{bb}$ = bending stiffness matrix

$$= \int_V \underset{\sim}{B}_b^T \, \underset{\sim}{D} \, \underset{\sim}{B}_b \, dV$$

$$= \int\int \underset{\sim}{B}_b^T \, [\int z^2 \, \underset{\sim}{D} \, dz] \, \underset{\sim}{B}_b \, dxdy$$

$$= \int\int \underset{\sim}{B}_b^T \, \underset{\sim}{D}_{bb} \, \underset{\sim}{B}_b \, dxdy \qquad (4.26)$$

$\underset{\sim}{K}_{bm}$ = coupling stiffness matrix

$$= \int_V \underset{\sim}{B}_b^T \, \underset{\sim}{D} \, \underset{\sim}{B}_m \, dV$$

$$= \int\int \underset{\sim}{B}_b^T \, [\int -z \, \underset{\sim}{D} \, dz] \, \underset{\sim}{B}_m \, dxdy$$

$$= \int\int \underset{\sim}{B}_b^T \, \underset{\sim}{D}_{bm} \, \underset{\sim}{B}_m \, dxdy \qquad (4.27)$$

$\underset{\sim}{D}$ = material matrix

It is to be noted here that $\underset{\sim}{B}_m$ and $\underset{\sim}{B}_b$ are functions of x and y only, and their values depend on the type of shape functions chosen to describe the displacement distribution in the elements. Thus, computations for element stiffness matrix hinge primarily on the evaluation of the material matrices $\underset{\sim}{D}_{mm}$, $\underset{\sim}{D}_{bb}$, and $\underset{\sim}{D}_{bm}$. To evaluate these material matrices, the reinforced concrete composite section is assumed to be a layered system consisting of concrete and 'equivalent smeared' steel layers as shown in Fig. 4.8. The steel reinforcement is converted into uniform layers with equivalent thicknesses given by:

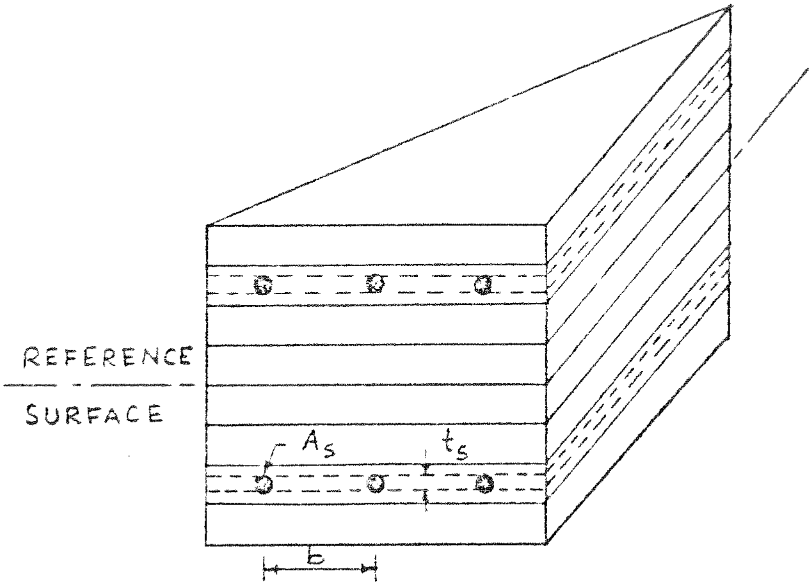

a. CONCRETE AND 'EQUIVALENT SMEARED' STEEL LAYERS

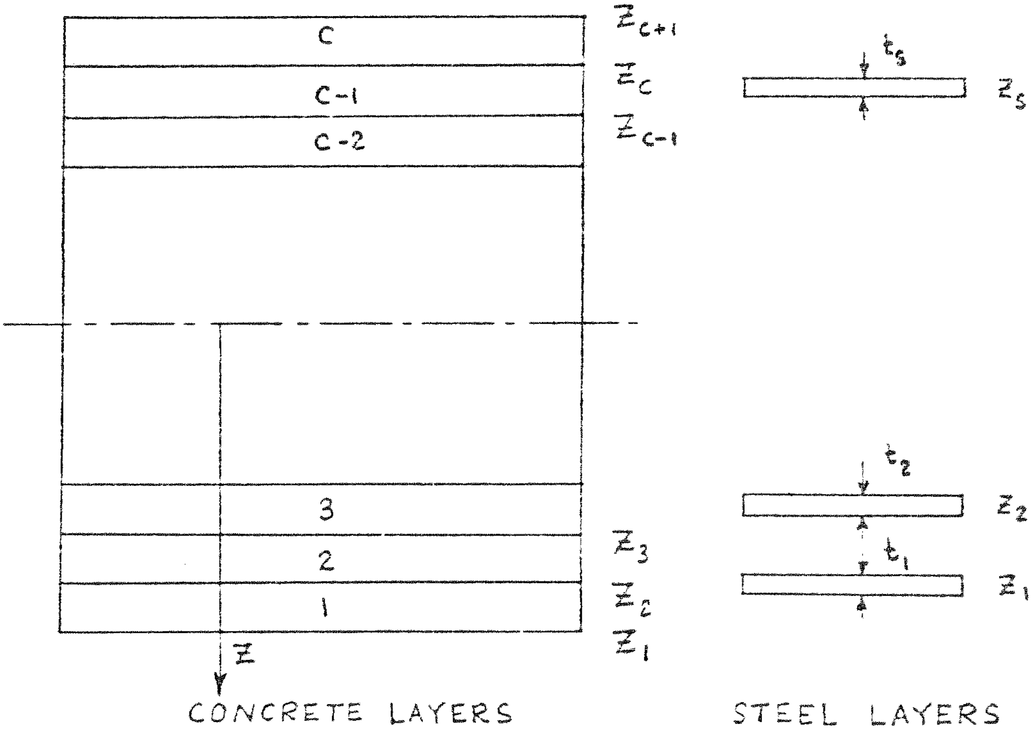

b. LAYER SYSTEM OF A TRIANGULAR ELEMENT

FIG. 4.8 LAYER SYSTEM OF A TRIANGULAR ELEMENT

$$t_s = \frac{A_s}{b} \tag{4.28}$$

where A_s = area of one reinforcing bar, and b = spacing of reinforcing bar.

Compatibility between the different steel and concrete layers is maintained by the Kirchhoff assumption of plane section normal to the reference surface remaining plane. The consequence of this assumption is that no bond slip occurs between steel and concrete layers and every layer is in a state of plane stress. The material matrix for each layer will be dependent on the deformation state of that layer. The material matrices, $\underset{\sim}{D}_{mm}$, $\underset{\sim}{D}_{bb}$ and $\underset{\sim}{D}_{bm}$, for the whole element may be obtained by adding up the contributions from each layer. Assuming material properties to be constant for each layer, one may write (Fig. 4.8):

$$\underset{\sim}{D}_{mm} = \int \underset{\sim}{D}\, dz = \sum_{i=1}^{c} (z_{i+1} - z_i)\, \underset{\sim}{D}_{ci} + \sum_{i=1}^{s} \underset{\sim}{D}_{si}\, t_i \tag{4.29}$$

where $\underset{\sim}{D}_{ci}$ = material matrix for ith concrete layer, similar to Eq. (2.7), and $\underset{\sim}{D}_{si}$ = material matrix for ith steel layer, similar to Eq. (2.31). Similarly:

$$\underset{\sim}{D}_{bm} = -\int z\, \underset{\sim}{D}\, dz = -\sum_{i=1}^{c} \frac{1}{2} (z_{i+1}^{2} - z_i^{2})\, \underset{\sim}{D}_{ci} - \sum_{i=1}^{s} z_i\, \underset{\sim}{D}_{si}\, t_i \tag{4.30}$$

$$\underset{\sim}{D}_{bb} = \int z^2\, \underset{\sim}{D}\, dz = \sum_{i=1}^{c} \frac{1}{3} (z_{i+1}^{3} - z_i^{3})\, \underset{\sim}{D}_{ci} + \sum_{i=1}^{s} z_i^{2}\, \underset{\sim}{D}_{si}\, t_i \tag{4.31}$$

The nodal degrees of freedom (DOF) required to describe the displacement field within the triangular shell element is shown in Fig. 4.7. At each node five DOF are prescribed--two in-plane or membrane displacements u and v, and three out-of-plane or plate bending displacements w, θ_x and θ_y. A constant strain triangular (CST) membrane element is combined with a linearly constrained, curvature triangular (LCCT9) plate bending element to form the triangular shell element.

The CST element has been derived by Turner, et al. [4.3], and the derivation is available in any standard text on finite element methods [4.1]. The LCCT9 element has been formulated by Felippa [4.4] using a triangular coordinate system. Figures 4.9 and 4.10 show the nodal degrees of freedom associated with CST and LCCT9 element, respectively. Bending deformations are represented very well by the LCCT9 element. Membrane actions, on the other hand, are not modeled very accurately by the CST element. However, the above shell element is used to keep the computational effort, needed for nonlinear analyses of reinforced concrete structures of practical interest, within reasonable limits.

It should be noted that in the above formulation, the in-plane rotation, i.e. θ_z, is not considered as a degree of freedom at any node. For a number of nearly co-planar elements meeting at a node, the global stiffness in the θ_z direction will be very close to zero. This may present severe numerical difficulties in the solution of the equilibrium equations. To avoid such difficulties, a fictitious rotational stiffness, about normal to the shell surface at a node, is provided by a boundary spring element. The value of the fictitious rotational stiffness is taken to be about 10% of the bending stiffness of the shell to avoid the above numerical difficulties and also any ill-conditioning due to large off-diagonal terms in the structural stiffness matrix which may occur if a very large value is used and the rotational stiffness contributes to more than one global degree of freedom.

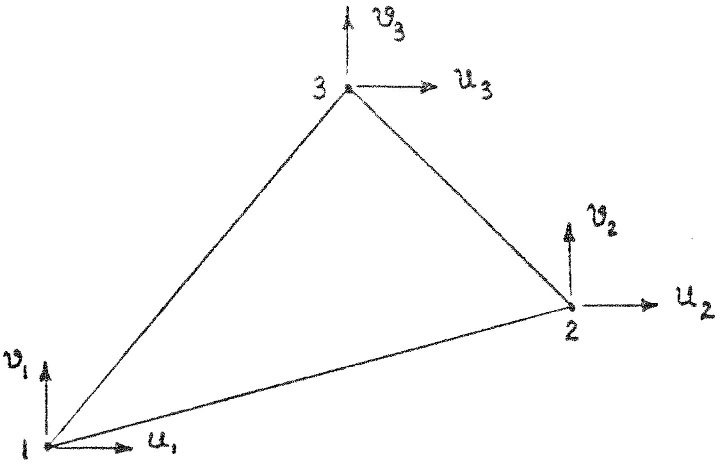

FIG. 4.9 CONSTANT STRAIN TRIANGULAR ELEMENT

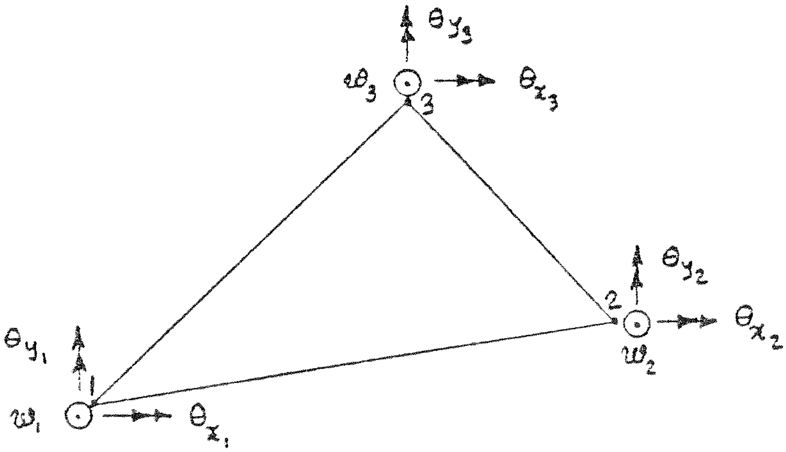

FIG. 4.10 LINEARLY CONSTRAINED CURVATURE TRIANGULAR ELEMENT

4.5.3 Triangular Membrane Element

This element is used for analyzing shear panel type structures where the load-carrying action is taken by in-plane or membrane forces. The constant strain triangular element, CST, having a total of six degrees of freedom at the three corner nodes (Fig. 4.9) is chosen for this purpose.

Detailed formulation of this element is given in several standard texts on the finite element method and will not be repeated here. The expression for the stiffness matrix of such an element is given by Eq. (4.25) and the expression for the material matrix for a composite material such as reinforced concrete is given by Eq. (4.29).

Since only in-plane forces are assumed to exist in such an element, the material properties about the reference surface must be symmetric. This is a restriction on the type of layer system that can be used for such an element. Usually, concrete properties do not vary across the thickness of any element and as such, generally one layer of concrete is used.

4.5.4 Triangular Plate Bending Element

This element may be used for the analysis of slab-type structures where transverse bending of the slabs is the predominant load-carrying mechanism and the membrane action is not significant. A linearly constrained curvature triangular element, LCCT9 (Fig. 4.10), is chosen to represent the plate bending action. This element was reformulated by Felippa [4.4] using a triangular coordinate system.

Since a plate is a three-dimensional rather than a two-dimensional body, Kirchhoff's classical hypotheses are used, as in the case of the shell element, to reduce the problem to a two-dimensional one. The expression for the stiffness matrix is given by Eq. (4.26) while the expression for the material matrix for a composite material such as reinforced concrete is given by Eq. (4.31).

The composite section is modeled as a layered system (Fig. 4.8). Kirchhoff's hypotheses reduce each layer to a state of plane stress, but each layer will be under a different state of deformation due to the plate bending action. This will result in local failures in some layers where the stress state or the strain state has violated any specified failure criteria. Thus, the layered system can trace the progressive cracking in reinforced concrete and the resulting deterioration in stiffness. The beginning of other failures and their progression is also possible. It should, however, be emphasized that for each layer the field variables considered are at the centroid of the triangular layer and thus tensile cracks or steel yielding, etc., can only be indicated over an area. This implies that only averaged values are being considered. Stress concentrations can be captured with better accuracy only if mesh sizes are made finer, thereby reducing the area of each triangular element.

4.5.5 Boundary Spring Element

This element is used for three purposes in this study--to limit nodal displacements or rotations to specified values, to compute support reactions, and to provide linear-elastic supports to nodes. This element has been developed by Wilson [4.5].

The boundary element is defined by a single directed axis through a specified nodal point, by a linear extensional stiffness along the axis or by a linear rotational stiffness about the axis. The element stiffnesses are added directly to the total structural stiffness matrix and hence have no effect on the size of the stiffness matrix.

4.6 Solution Steps in the Present Method of Analysis

A finite element tangent stiffness formulation, coupled with a step-by-step integration scheme in the time domain, is developed to analyze reinforced concrete systems. Within each time step, an incremental load procedure, with an iterative approach to the solution of the equilibrium equations for each load increment, is used.

The entire time period, for which the response history of the structure is to be traced, is divided into a number of time steps, Δt_1, Δt_2, $\Delta t_3 \ldots\ldots \Delta t_n$, as shown in Fig. 4.11. It is assumed that changes in the external nodal loads, if any, occur only at the beginning or at the end of a time step, e.g., at t_1, t_5, t_8, and so on. During a time step, the external loads are assumed to remain constant. The increment in the external nodal loads at any particular time, may be subdivided into a number of load steps to follow the nonlinear responses of the structures in more detail. For example, $R(t_1)$, the increment in the external nodal load vector at time t_1 (Fig. 4.11), is divided into three load steps, ΔR_1, ΔR_2, and ΔR_3. An iterative approach is then used to solve for each load step and the increments in the field variables--deformations, strains, and stresses--are added to the previous totals to give the current state of the structure. The basic steps of this numerical method of analysis are presented below

1. Read in the control parameters such as the number of nodal points, element types, time steps, convergence and divergence norms,

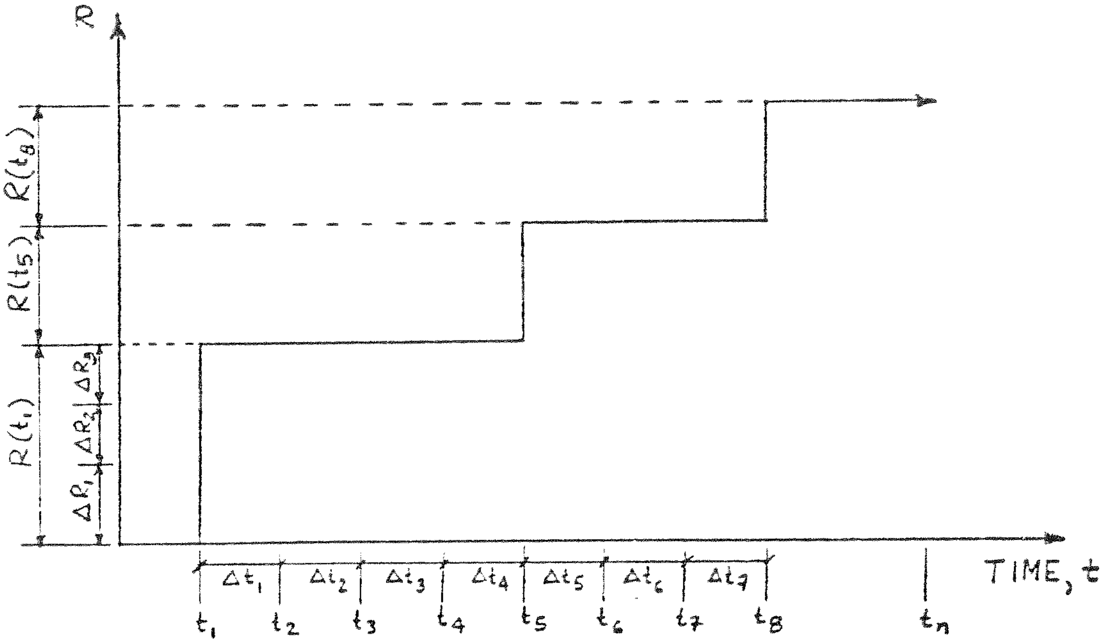

a. EXTERNAL LOAD HISTORY

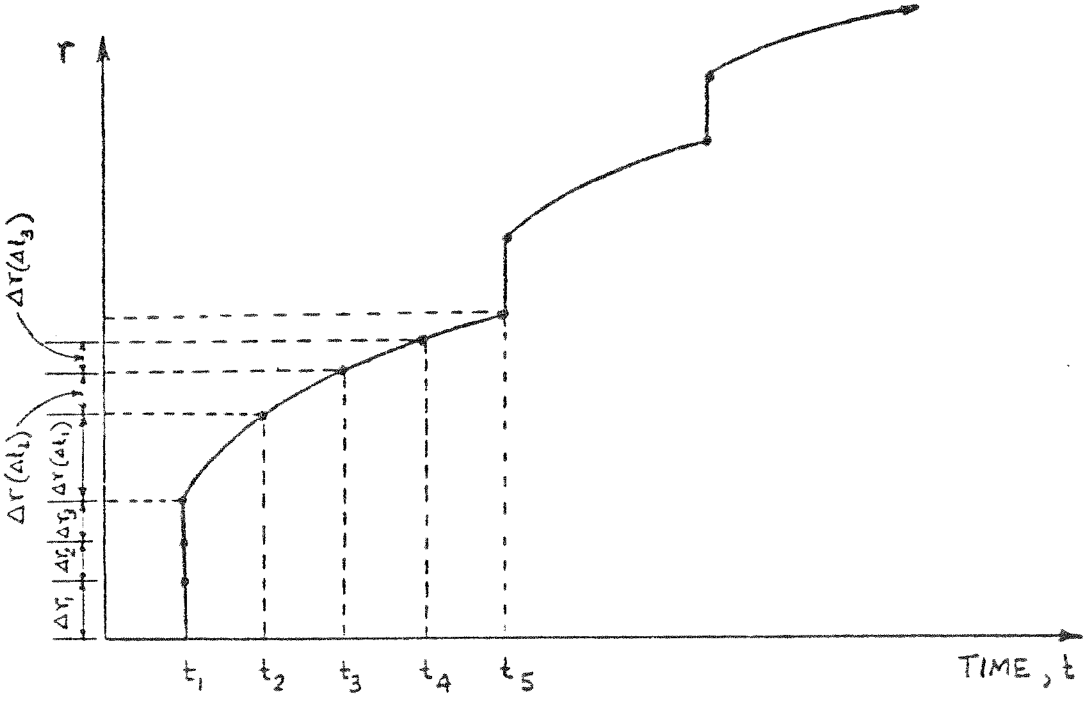

b. DISPLACEMENT HISTORY

FIG. 4.11 RESPONSE HISTORY OF A STRUCTURE DUE TO EXTERNAL LOADS, CREEP AND SHRINKAGE EFFECTS and indicators specifying type of analysis to be performed, for example, external load only, creep only, shrinkage only, or a combination thereof.

2. Read in coordinates for each node. Input data for constitutive relations and time-dependent properties of the materials, types of layer systems, and layout and properties of elements.

3. Start solution at t_1, which is the beginning of the first time step, Δt_1. Form material matrix for each concrete layer of an element, calculate the layer stiffnesses, and integrate to form element stiffness matrices. Assemble element stiffnesses into structural stiffness matrix.

4. The external nodal load increment vector, for example, $R(t_1)$ at t_1 is assembled into the structural load increment vector. If there is no external load increment, then go to step 17.

5. Start solution for the load steps. Divide the structural load increment vector to obtain the load vector for each load step of the increment.

6. Start iterative solution procedure for this load step.

7. Solve the equilibrium equations to obtain the nodal displacement increment vector. Add this to the previous total displacement vector to obtain the current total nodal displacement vector in the global coordinate system. From the second iteration onwards, check the displacement increment vector against divergence and convergence norms.

8. For each element, steps 9 through 13 are executed to obtain the current state of stress and strain.

9. Nodal displacement increment vector in global coordinate system is transformed to the element coordinate system and strain increment vector at the reference surface is calculated.

10. Strain increment vector for each layer is calculated and the total strain vector is obtained by adding the strain increment vector to the total strain vector from the previous iteration.

11. Stress increment vector for each layer is estimated by multiplying the current layer material matrix by the layer strain increment vector. The piecewise linear constitutive relationship, used in the stress computation, causes some approximations in these stress values. The total approximate stress vector is obtained by adding the approximate stress increment vector to the stress vector in the layer at the end of the previous iteration. The total approximate stress vector is transformed to obtain approximate principal stresses.

12. Equivalent uniaxial stress-stain curves are constructed assuming the layer to be under the biaxial principal stress ratio existing at the end of the previous iteration. Equivalent uniaxial strain increments are calculated from the current approximate principal stresses, the principal stresses from the previous iteration, and the tangent moduli in the principal directions at the end of the previous iteration. The equivalent uniaxial strain increments are added to the total equivalent uniaxial strains from the previous iteration to obtain current total equivalent uniaxial strains. From the equivalent uniaxial stress-strain curves, the stresses corresponding to the current total equivalent uniaxial strains are obtained. These are the actual principal stresses for this iteration. These are transformed to the element coordinate system to obtain the total stress vector.

13. Calculate the unbalanced stresses in each layer by subtracting the total stress vector of step 12 from the total approximate stress vector from step 11. Integrate the unbalanced layer stresses to obtain

the unbalanced element nodal forces. Update the element stiffness matrix incorporating the changes that occur in the layer material matrix.

14. Assemble unbalanced element nodal loads into the structural load increment vector. Check the assembled structural load increment vector against convergence and divergence norms. If divergence norms are not satisfied, stop the solution. If convergence norms are not satisfied, go to step 15. Otherwise go to step 16.

15. Assemble the new structural stiffness matrix with updated element stiffnesses. Go to step 7 for next iteration. When the maximum number of iterations is exceeded, go to step 16.

16. Go to step 6 until solution is obtained for all the load steps specified in step 5.

17. If solution cycle just completed is not for external loads, go to step 4. Otherwise go to step 18.

18. Solution is started at the time corresponding to the end of the time step. For example, in Fig. 4.11, for the first time step, Δt_1, this will be time t_2. If the number of time steps specified in step 1 is exceeded, stop the solution. If not, calculate the material properties at the current time. For each element, steps 19 through 21 are then executed.

19. Update layer material matrices with the material properties calculated in step 18.

20. Calculate creep and shrinkage strain increment vectors for each layer for the time step under consideration. The stresses in each layer are assumed constant during the time step.

21. Treating creep and shrinkage strain increments as initial

strains, equivalent nodal loads due to these initial strains may be obtained by using an expression similar to Eq. (4.7c).

22. The equivalent nodal loads for each element is assembled into the structural load increment vector. Go to step 5.

Two of the complex parts in the above solution algorithm are (1) steps 18 through 21 which deal with the solution procedure for creep and shrinkage strains and (2) steps 9 through 13 which determine the states of stress and strain in the concrete layers. These will be described in more detail in Sections 4.7 and 4.8, respectively.

4.7 Solution Procedure for Creep and Shrinkage Effects

A step-by-step integration scheme in the time domain is adopted to consider the effects of such time-dependent phenomena as creep and shrinkage strains on the behavior of reinforced concrete structures. The total time period for which a structure is under study is divided into several smaller time steps to trace the nonlinear response history of the structure over the entire period. An 'initial strain' approach, as described by Zienkiewicz[4.1], is then adopted to determine the responses of the structure due to creep and shrinkage strain increments occurring during a time step. This procedure is presented below for a time step t_2-t_1 where t_1 and t_2 are the times at the start and end of the time step (Fig. 4.11).

1. Assume all load changes to occur at the beginning of the time step t_1. By solving the equilibrium equations for these load changes, all the field variables--nodal displacement vector $\underset{\wedge}{r}$, strain $\underset{\wedge}{\varepsilon}$, and stress $\underset{\wedge}{\sigma}$--are known for all elements. A creep law and a shrinkage law (similar to those discussed in Chapter 3) are also specified.

2. Calculate the strain increments due to creep and shrinkage that occur in each concrete layer in the elapsed time period t_2-t_1 by assuming the stress state to be constant at the value calculated in step 1. Details of the computations for the creep and shrinkage strain increments are given in Chapter 3.

4. Treat creep and shrinkage strain increments as initial strains $\underset{\wedge}{\varepsilon}_o$ as introduced in Eq. (4.3) wherein:

$$\Delta\underset{\wedge}{\varepsilon}_{oi} = \Delta\underset{\wedge}{\varepsilon}_i^c + \Delta\underset{\wedge}{\varepsilon}_i^s \tag{4.32}$$

where $\Delta\underset{\wedge}{\varepsilon}_i^c$ and $\Delta\underset{\wedge}{\varepsilon}_i^s$ are creep and shrinkage strain increment vectors in layer i, and $\Delta\underset{\wedge}{\varepsilon}_{oi}$ is the initial strain increment vector similar to the initial strain vector of Eq. (4.3).

5. Calculate the equivalent nodal forces produced by the initial strain increments:

$$\Delta\underset{\wedge}{F}_{\varepsilon o} = \sum_e \sum_{i=1}^{c} \int_{V_i} \underline{B}_i^T \, \underline{D}_i \, \Delta\underset{\wedge}{\varepsilon}_{oi} \, dV_i \tag{4.33}$$

where $\Delta\underset{\wedge}{F}_{\varepsilon o}$ is the equivalent nodal load vector due to the initial strain increment, $\sum_e$ is the sum of all elements, $\sum_{i=1}^{c}$ is the sum over the concrete layers, $\underline{B}_i$ is the strain-displacement relationship for layer i, $\underline{D}_i$ is the material matrix for concrete layer i at time t_2, and V_i is the volume of layer i. Equation (4.33) is similar to Eq. (4.7c).

6. The structural stiffness matrix $\underline{K}$ is assembled at time t_2 and the equilibrium equations are solved for the equivalent nodal load vector produced by initial strain increments:

$$\Delta\underset{\wedge}{r} = \underline{K}^{-1} \, \Delta\underset{\wedge}{F}_{\varepsilon o} \tag{4.34}$$

where $\Delta \underset{\wedge}{r}$ is the nodal displacement increment vector.

7. The strain increment vector $\Delta \underset{\wedge}{\varepsilon}_i$ in any layer is obtained by:

$$\Delta \underset{\wedge}{\varepsilon}_i = \underline{B}_i \, \Delta \underset{\wedge}{r} \tag{4.35}$$

8. The stress increment vector $\Delta \underset{\wedge}{\sigma}_i$ in concrete layer i is obtained by:

$$\Delta \underset{\wedge}{\sigma}_i = \underline{D}_i (\Delta \underset{\wedge}{\varepsilon}_i - \Delta \underset{\wedge}{\varepsilon}_{io}) \tag{4.36}$$

Equation (4.36) is simlar to Eq. (4.3) where $(\Delta \underset{\wedge}{\varepsilon}_i - \Delta \underset{\wedge}{\varepsilon}_{io})$ is the increment in the elastic strain in the time period $t_2 - t_1$.

9. Increments in the field variables--displacements, strains and stresses--are added to the total values at step 1 for time t_1 to obtain the values for the current time t_2.

10. Steps 1 through 9 are repeated for the next time step.

4.8 State Determination in Concrete Layers

In the present study, the material behavior of concrete is characterized by a nonlinear constitutive relationship for the biaxial state of stress. This includes tensile cracking at a limiting stress level, tensile unloading after cracking, influence of the biaxial stress ratio, and strain-softening phenomenon beyond the maximum compressive strength. These are described in full detail in Chapter 2.

Since the finite element method is a linear solution procedure, a step-iterative method (as discussed in Section 4.4) is used to trace the nonlinear response of the structure due to material nonlinearity. The following steps are used to estimate, at a particular load level, the actual state of stress and strain in a concrete layer within specified tolerance limits.

1. For any load increment $\Delta \underset{\wedge}{R}$ (Fig. 4.12), the following iterative scheme is used to determine the stress and strain states in the concrete layers.

2. For the n<u>th</u> iteration, the equilibrium equations may be solved as:

$$\Delta \underset{\wedge}{r}^{n} = \underline{K}_{n-1}^{-1} \, \Delta \underset{\wedge}{R}^{n} \tag{4.37}$$

where for the first iteration, $n = 1$, $\underline{K}_o$ = stiffness matrix at the end of the last load increment solution, $\Delta \underset{\wedge}{R}' = \Delta \underset{\wedge}{R}$; and $\Delta \underset{\wedge}{r}'$ = nodal displacement increment vector.

3. The strain increment in a layer is given by:

$$\Delta \underset{\wedge}{\varepsilon}_{x}^{\;n} = \underline{B} \, \Delta \underset{\wedge}{r}^{n} \tag{4.38}$$

where $\underline{B}$ is the appropriate strain-displacement vector.

The current total strain vector is then obtained by:

$$\underset{\wedge}{\varepsilon}_{x}^{\;n} = \underset{\wedge}{\varepsilon}_{x}^{\;n-1} + \Delta \underset{\wedge}{\varepsilon}_{x}^{\;n} \tag{4.39}$$

4. Stress increments in the layer are obtained by:

$$\Delta \underset{\wedge}{\bar{\sigma}}_{x}^{\;n} = \underline{D}^{n-1} \, \Delta \underset{\wedge}{\varepsilon}_{x}^{\;n} \tag{4.40}$$

where $\underline{D}^{n-1}$ is the linearized, plane stress orthotropic material matrix [Eq. (2.7)], whose values are obtained at the end of the previous iteration. Since Eq. (4.40) is a linear relationship, the values of the stress increments are only approximate estimates.

The total approximate stresses in the layer are then computed as:

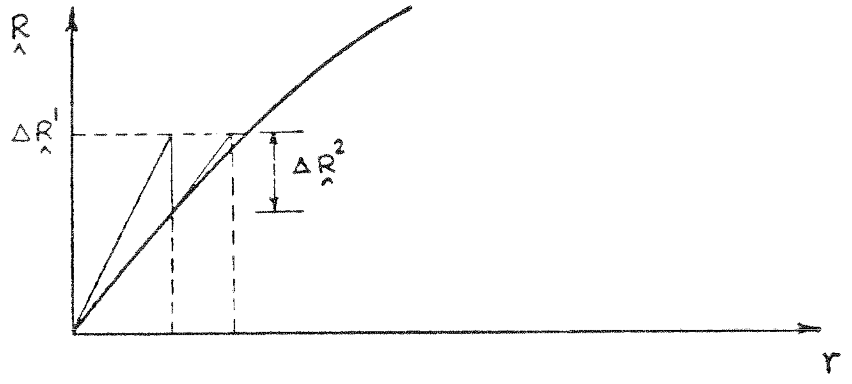

a. LOAD-DEFLECTION CURVE

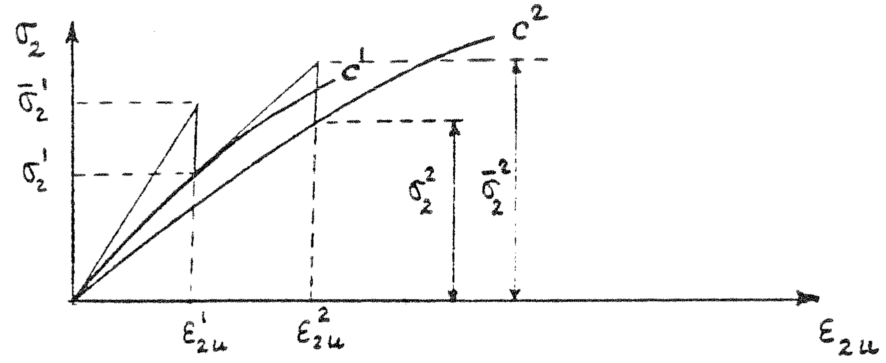

b. PRINCIPAL STRESS VS. EQUIVALENT UNIAXIAL STRAIN IN PRINCIPAL DIRECTION-2

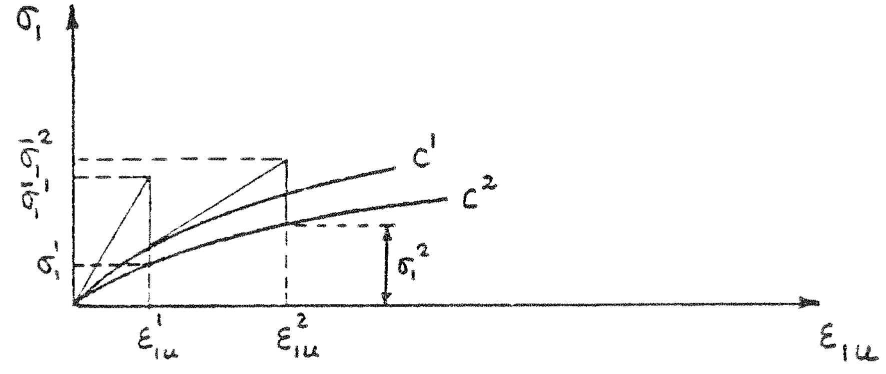

c. PRINCIPAL STRESS VS. EQUIVALENT UNIAXIAL STRAIN IN PRINCIPAL DIRECTION-1

FIG. 4.12 STEP-BY-STEP ITERATIVE FORMULATION FOR THE SOLUTION OF THE EQUILIBRIUM EQUATIONS

$$\bar{\sigma}_{\underset{\wedge}{x}}^{\,n} = \sigma_{\underset{\wedge}{x}}^{\,n-1} + \Delta\bar{\sigma}_{x}^{\,n} \tag{4.41}$$

5. The principal stresses are computed from the total approximate stress vector $\bar{\sigma}_{\underset{\wedge}{x}}^{\,n}$. These are designated $\bar{\sigma}_1^{\,n}$ and $\bar{\sigma}_2^{\,n}$ and are shown in Fig. 4.12. Because of the linearized constitutive relations of step 4, $\bar{\sigma}_1^{\,n}$ and $\bar{\sigma}_2^{\,n}$ are approximate estimates of the actual principal stresses; and 1 and 2 are approximate principal directions.

6. Calculate the increment in the equivalent uniaxial strains by [Eq. (2.12)]:

$$\begin{aligned} \Delta\varepsilon_{1u}^{n} &= (\bar{\sigma}_1^{\,n} - \sigma_1^{\,n-1})/E_1^{\,n-1} \\ \Delta\varepsilon_{2u}^{n} &= (\bar{\sigma}_2^{\,n} - \sigma_2^{\,n-1})/E_2^{\,n-1} \end{aligned} \tag{4.42}$$

where $\sigma_1^{\,n-1}$, $\sigma_2^{\,n-1}$ are the principal stresses and $E_1^{\,n-1}$, $E_2^{\,n-1}$ are the tangent moduli at the start of this iteration.

The total equivalent uniaxial strains are given by:

$$\begin{aligned} \varepsilon_{1u}^{n} &= \varepsilon_{1u}^{n-1} + \Delta\varepsilon_{1u}^{n} \\ \varepsilon_{2u}^{n} &= \varepsilon_{2u}^{n-1} + \Delta\varepsilon_{2u}^{n} \end{aligned} \tag{4.43}$$

7. Determine the biaxial stress ratio at the start of this iteration:

$$\alpha^{n-1} = \sigma_1^{\,n-1}/\,\sigma_2^{\,n-1} \tag{4.44}$$

8. From α^{n-1} and concrete properties f_c', f_t', ε_{cu} and E_o, the equivalent uniaxial curve C^n can be drawn (Subsection 2.2.4) as shown in Fig. 4.12.

9. Principal stresses σ_1^n and σ_2^n corresponding to ε_{1u}^n and ε_{2u}^n

are calculated from Eqs. (2.8) and (2.9). The material matrix $\underline{D}$ is also updated.

10. The principal stresses are transformed to the element coordinates to obtain the total stress vector $\underset{\wedge}{\sigma}_x^n$. The unbalanced stresses in the layers are now obtained by:

$$\Delta \underset{\wedge}{\sigma}_u^n = \underset{\wedge}{\sigma}_x^n - \underset{\wedge}{\sigma}_x^{n-1} \tag{4.45}$$

11. The unbalanced nodal load vector $\Delta \underset{\wedge}{R}^{n+1}$, Fig. 4.12, is now calculated by:

$$\Delta \underset{\wedge}{R}^{n+1} = \sum_e \sum_\ell \int_V \underline{B}^T \, \Delta \underset{\wedge}{\sigma}_u^n \, dV \tag{4.46}$$

where $\sum_e$ and $\sum_\ell$ are summation over elements and layers respectively and V is the volume of a layer.

12. Compare $\Delta \underset{\wedge}{R}^{n+1}$ or $\Delta \underset{\wedge}{r}^n$ against convergence and divergence criteria. If these are satisfied, then go to step 13. Stop solution if divergence criteria are violated. If convergence criteria are not satisfied, go back to step 2 for next solution.

13. End of iterations for this load increment.

4.9 Convergence Criteria

A step-iterative approach is adopted in the present numerical method to trace the nonlinear behavior with a series of piecewise linear solutions. Since considerable computational effort is needed for each iteration, convergence criteria are set to minimize the computer costs when successive iterations give solutions hardly differing from one another.

In the solution process, a large system of equilibrium equations are used to obtain nodal displacements. Two criteria can be set to study the convergence of such a system of equations in the nth iteration--(1) the extent of the violation of the equilibrium state as given by the unbalanced nodal load vector, $\Delta \underset{\wedge}{R}^{n}$, in Fig. 4.13; and (2) the accuracy of the total displacements as indicated by the nodal displacement increment vector, $\Delta \underset{\wedge}{r}^{n}$, as shown in Fig. 4.13.

In the computer program developed in this study, both options are provided. In the input data, the following requirements may be specified.

1. Control code indicating whether a displacement or force convergence criterion is to be used.

2. Control code indicating whether absolute values or percentages of already obtained solutions are to be set as convergence limits.

3. Values, either in absolute or percentile form, of the convergence tolerances are specified.

4. A maximum number of iterations is also specified to limit computational costs in case tolerance limits, which are too stringent, are set.

5. Due to deteriorating structural stiffness with high load levels, the displacements may diverge under a particular increment of load, indicating structural collapse. It is unnecessary at this stage to carry the solution process further. Values, either in absolute or percentile form, are provided to check the solution for divergence. Solution is stopped in case of divergence.

The following steps are executed if a displacement convergence criterion is used.

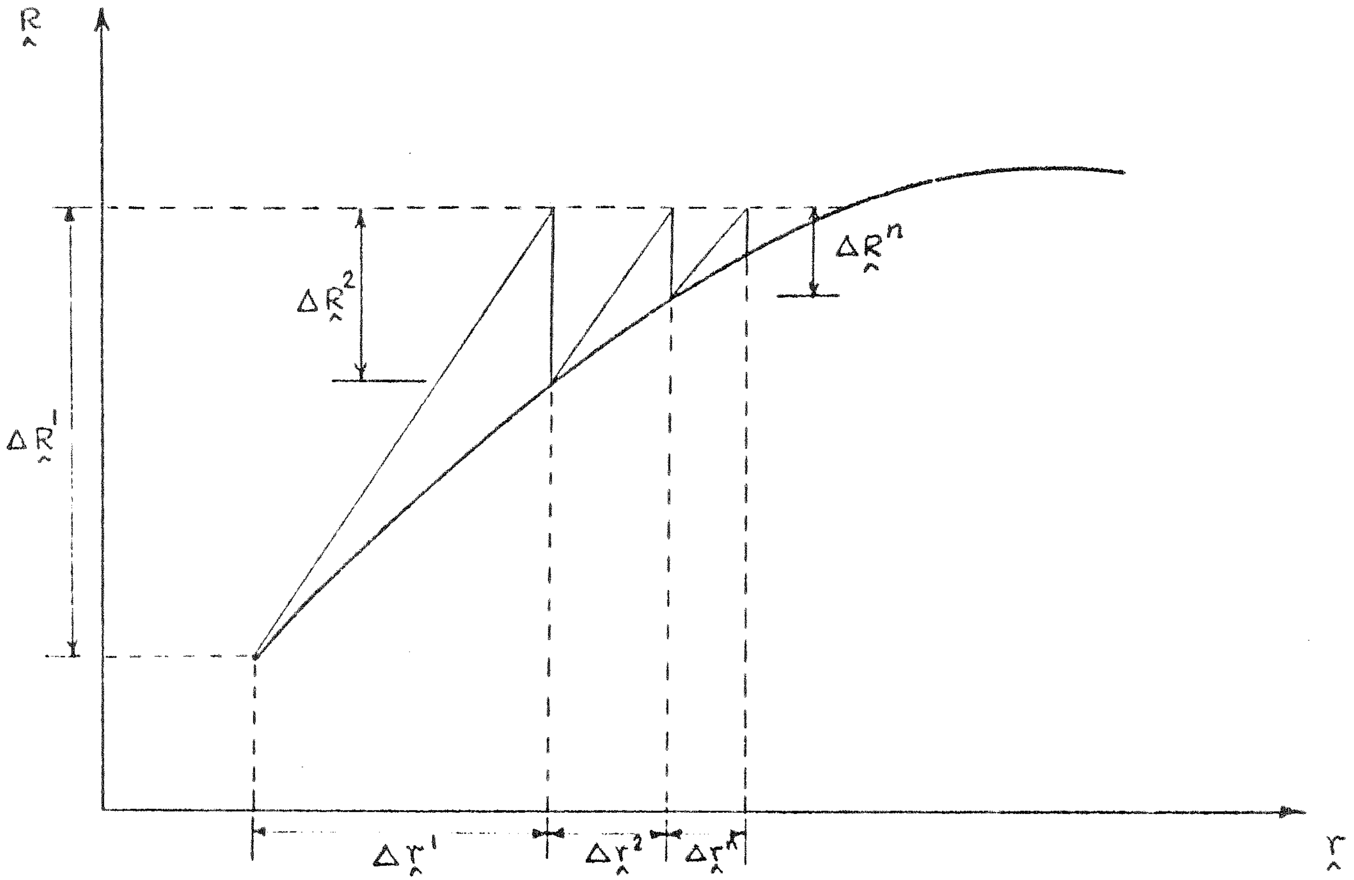

FIG. 4.13 UNBALANCED FORCES AND DISPLACEMENT INCREMENTS FOR ITERATIVE SOLUTION

The nodal displacement increment vector, $\Delta \underset{\wedge}{r}^{n}$, at the nth iteration, is checked to find the maximum absolute values in the direction of the six global degrees of freedom, u, v, w, θ_x, θ_y, and θ_z (Fig. 4.6). The components of the error vector, $\underset{\wedge}{e}^{n}$, are given by:

$$e_i^n = \max_k \left| \Delta \underset{\wedge}{r}_{ik}^{n} \right| \tag{4.47}$$

where i = 1, 6; and k = number of nodes.

If the tolerances are given in absolute terms, $\underset{\wedge}{\delta}$, then convergence at the nth iteration is assumed by:

$$\underset{\wedge}{e}^{n} \leq \underset{\wedge}{\delta} \tag{4.48}$$

If the tolerances are given in percentile terms, $\underset{\wedge}{p}$, then convergence is assured by:

$$\underset{\wedge}{e}^{n} \leq \underset{\wedge}{p}^{T} \underset{\wedge}{e}' \tag{4.49}$$

where $\underset{\wedge}{e}'$ is the maximum vector obtained by Eq. (4.47) for the displacement increment solution for the first iteration, $\Delta \underset{\wedge}{r}'$ (Fig. 4.12).

The force convergence criteria and the divergence criteria are also checked in a similar fashion.

4.10 Computer Program

A computer program NOTACS (NOnlinear Time-dependent Analysis of Concrete Structures) has been developed to analyze reinforced concrete panels, slabs and shells under short term or sustained load histories and subjected to time-dependent phenomena such as creep and shrinkage effects. The program can be used to trace the load-deformation response and crack propagation through the elastic, inelastic and ultimate ranges. Stress and strain states in concrete and steel reinforcement can also be determined for any stage of the response history.

The program is coded in FORTRAN IV language and has been tested on CDC 6400 and 7600 computers at the University of California, Berkeley. The blank common is dynamically dimensioned so that the blank common length can be either expanded or shortened to fit exactly the requirements of the problem under consideration. By this option, efficient use is made of the central memory capacity of the computer and thus cost of execution in the computer is greatly reduced. A flow chart describing the logical structure of the program is presented in Fig. 4.14. A description of the input and the output and detailed input instructions are presented in Appendix A.

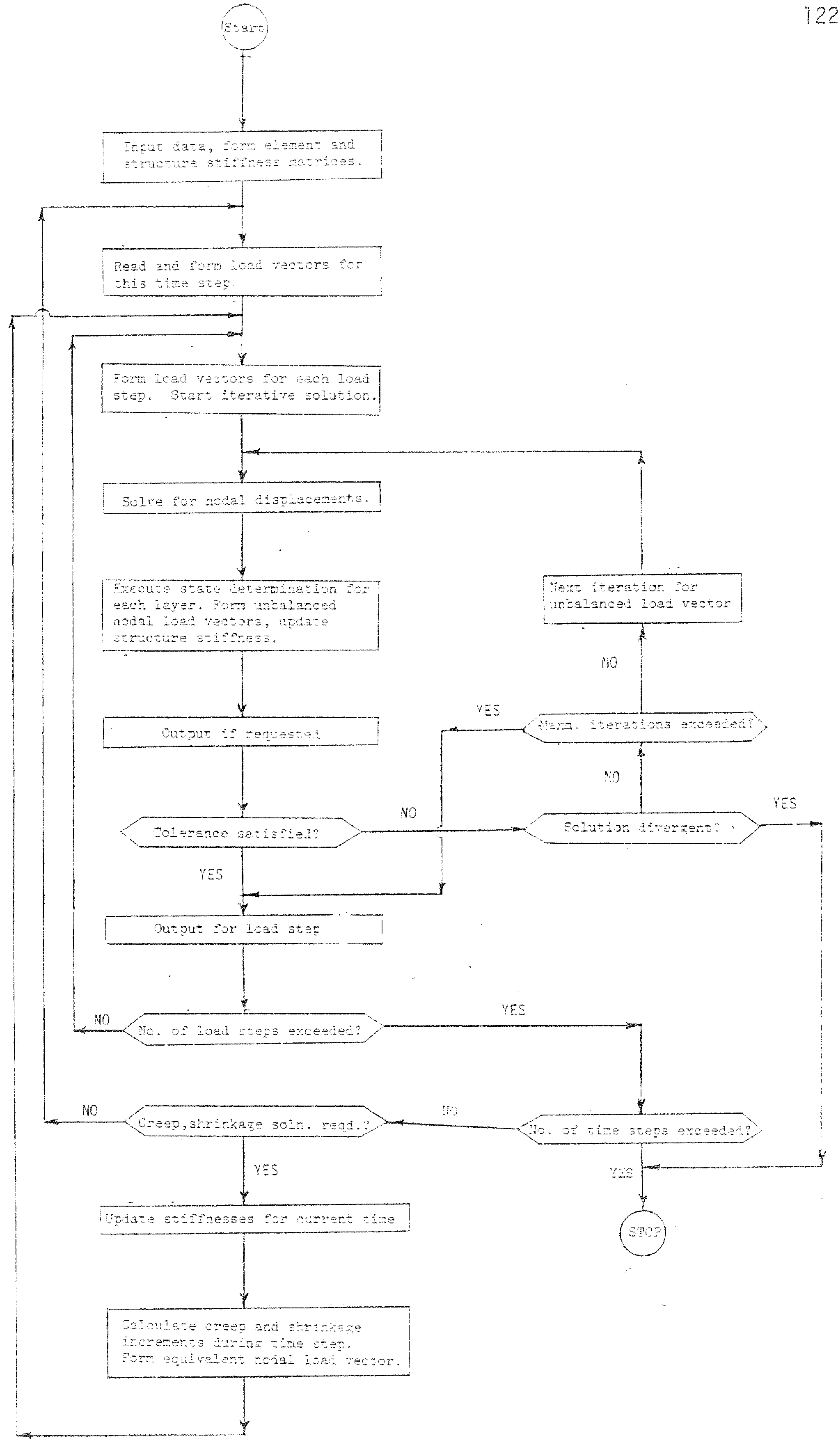

FIG. 4.14 FLOW CHART FOR NOTACS

5. NUMERICAL EXAMPLES AND INTERPRETATION OF RESULTS

5.1 General Remarks

Four numerical examples, in a sequence of increasing complexity, are chosen for study. The purpose of these numerical examples are as follows.

(1) Check the validity of the material models and the structural idealizations. The numerical results obtained from the analyses are compared with the available experimental data for this purpose.

(2) Demonstrate the applicability of the proposed models to different types of structural components and load histories.

(3) Study the influence of creep and shrinkage on the performance of various structures.

The first example is a beam tested by Washa and Fluck [5.1] under sustained uniform load. This example is chosen to check the validity of the creep model adopted in this study. Although this study is primarily concerned with panels, slabs and shells where a biaxial state of stress is generally prevalent, a beam example where the uniaxial state of stress is usually dominant is chosen due to the lack of experimental data on the response of panels, slabs and shells under time-dependent effects.

The second example is a panel tested by Cervenka [1.8] for instantaneous loading to ultimate. This specimen, in the present study, is considered both under an instantaneous and an assumed sustained high load level and shrinkage effects. The purpose of the instantaneous ultimate analysis was to check the ability of the biaxial constitutive model and the triangular membrane elements to predict correctly the experimental behavior. The time-dependent analysis under the assumed load history, for which no experimental data are available, is carried out to examine the differences, if any, in the panel behavior due to creep and shrinkage.

The third example is a rectangular square slab tested by McNiece [1.18]. This slab is analyzed for instantaneous ultimate loading and an assumed stepped-up load history including creep and shrinkage effects. The purpose of the instantaneous ultimate analysis was to check how well the plate bending triangular element and the biaxial constitutive model predict the experimental behavior. Again, the time-dependent analysis, for which no experimental data are available, was undertaken to study the differences in the slab behavior due to creep and shrinkage effects.

In the fourth example, a comprehensive study is made of the behavior of gable hyperbolic paraboloid roof shells. This study may be divided into three phases.

In the first phase, linear-elastic analyses for dead load were executed for two gable HP shells. These two shells were also analyzed by Schnobrich [5.4,5.5] for a linear-elastic material using higher order shell and beam elements. The elastic solutions from the present study are compared with Schnobrich's results to check the accuracy of the triangular shell element to model the gable HP shell. The relative significance and interaction of the shell, the crown beams and the edge beams in carrying the load are also studied and discussed.

In the second phase, one of the gable HP shells was designed for its required steel reinforcement and then loaded to ultimate incorporating nonlinear biaxial concrete behavior. The purpose of this analysis is to determine the overload capacity of such shells as well as the failure mechanism and the interaction between the different elements of the shell, namely, the crown beam, the edge beam, and the shell proper.

In the third phase, the gable shell is analyzed for creep and shrinkage effects under a sustained dead load. The stress redistributions occurring among the different structural components are examined and the stiffness degradation in the form of progressive crack patterns are traced. Finally, after carrying this sustained load for a long period of time, the gable shell is loaded to failure to see whether there are significant changes in the ultimate behavior because of the creep and shrinkage effects.

5.2 Example 1 - Washa-Fluck Beams C3-C6

A series of beams were tested by Washa and Fluck [5.1] to determine the effects of creep on their behavior. Two such beams, C3 and C6 are chosen for analysis in this study. The purpose of the analysis is to check the validity of the creep model chosen and to test its ability to reflect reality with reasonable accuracy.

Beams C3 and C6 are two geometrically identical beams having some variations in their material properties. The overall dimensions and the material properties are shown in Fig. 5.1. These beams were loaded at 14 days after casting with uniform load 82 lbs./ft. The loads were kept in place until 913 days after casting. The important experimental data obtained were the deflection history at midspan and the strain histories at tensile and compressive steel levels.

Figure 5.2 shows the finite element idealization of the beam for analysis and the material properties chosen. The layered triangular shell element has been chosen to represent the beam behavior which may be taken to be the same as one-way slabs. Since transverse shear deformations are neglected in the basic kinematic assumptions, each

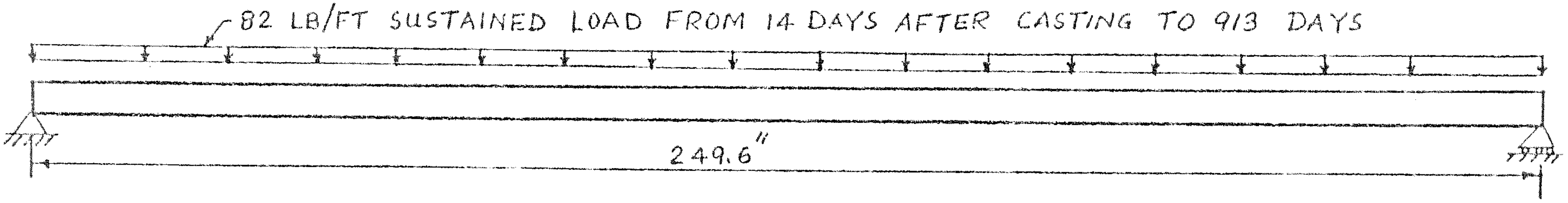

a. ELEVATION

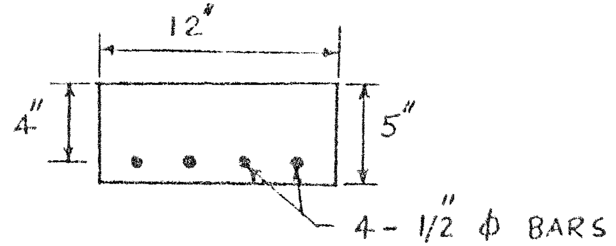

b. CROSS-SECTION

MATERIAL PROPERTIES :

1. CONCRETE :

		C3	C6	
f'_c	= AT 14 DAYS :	2720	3160	PSI
	= AT 28 DAYS :	3000	3580	PSI
	= AT 913 DAYS :	3190	3580	PSI
E_c	= AT 14 DAYS :	2.61×10^6	2.74×10^6	PSI
	= AT 28 DAYS :	3.00×10^6	2.89×10^6	PSI
	= AT 913 DAYS :	3.41×10^6	3.34×10^6	PSI

2. STEEL :

f_Y = 51000 PSI

f_u = 79500 PSI

ε_u = 0,195 IN/IN

FIG. 5.1 EXAMPLE 1 - DIMENSIONS AND MATERIAL PROPERTIES OF WASHA-FLUCK BEAMS C3 AND C6 [5.1]

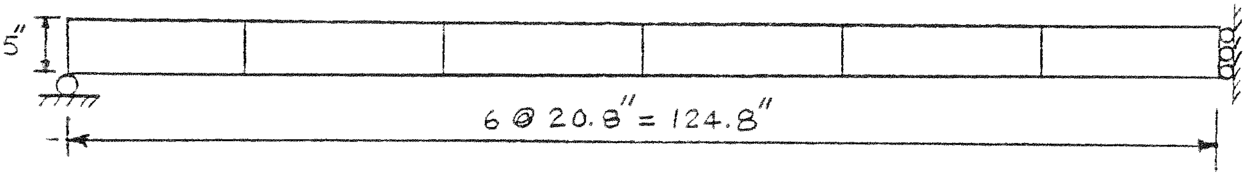

a. ELEVATION OF HALF OF THE SYMMETRIC BEAM

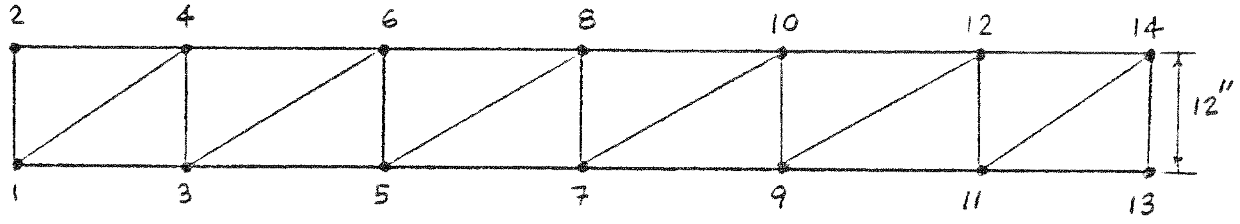

b. PLAN OF HALF OF THE SYMMETRIC BEAM WITH NODES

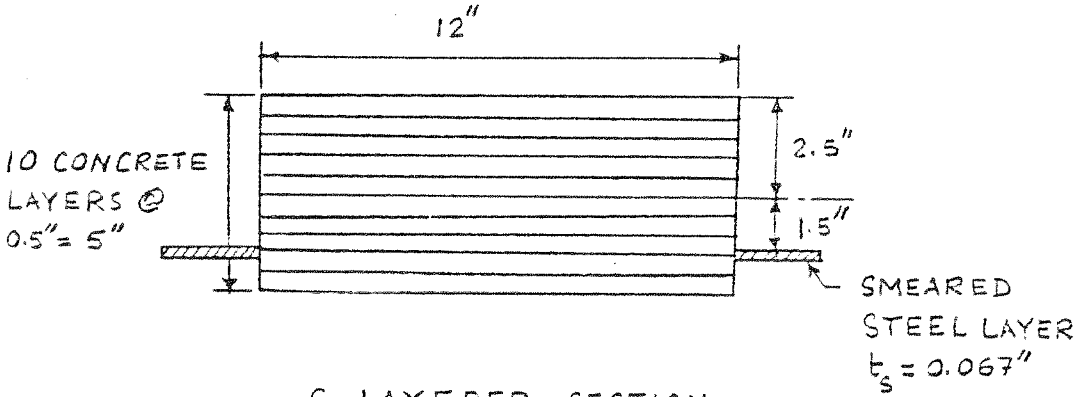

C. LAYERED SECTION

MATERIAL PROPERTIES :

1. CONCRETE : $f_c' =$ 2940 PSI 14 DAYS
3290 " 28 "
3385 " 913 "

$E_c =$ 2.675×10^6 " 14 "
2.945×10^6 " 28 "
3.375×10^6 " 913 "

$\varepsilon_{ut} =$ 0.0001 IN/IN (ASSUMED) NO TENSION STIFFENING

$\varepsilon_u =$ 0.004 IN/IN (ASSUMED)

2. STEEL : $f_y =$ 51000 PSI

$E_s =$ 29×10^6 PSI (ASSUMED)

FIG. 5.2 EXAMPLE 1 - FINITE ELEMENT IDEALIZATIONS AND AVERAGED MATERIAL PROPERTIES ASSUMED FOR THE ANALYSIS OF WASHA BEAM C3 - C6 layer is always in a state of plane stress. The diagonal tension phenomena, due to the combination of flexural and shear stresses, thus, cannot be taken into account. However, for the beams under consideration, the dominant effect is that due to flexure. The beams had very long spans and shallow depths. The shear span-to-depth ratio (M/Vd) of these beams is 15.6. Generally, flexural types of cracks and failure occur for beams with shear span-to-depth ratio of 6 to 7 or greater.

The material properties chosen are the average of the two beams C3 and C6 and are also shown in Fig. 5.2. The analysis is carried out for a total of 300 days after casting. The analysis is not carried further to minimize the computer cost and also because about 98% of the 913-day deflection has taken place by 300 days.

The load is applied at 14 days in three equal load steps. Then analyses for time-dependent effects are done with the following 28 time steps--9-2-days, 10-4-days, 1-8-days, 2-10-days, 1-20-days, 4-30-days, and 1-60-days.

The creep coefficients α_i and λ_i are chosen by least square curve fitting of the experimental creep curve. Both the experimental and the theoretically generated creep curves are shown in Fig. 5.3. Since the experimental curve is given for loading age at 14 days, the creep coefficient α_i corresponds to 14 days. To obtain the α_i corresponding to other loading ages, for example 20 days, 28 days, etc., a correction factor for age, as recommended by ACI Committee 209 [3.5] has been chosen. The age correction factor is given by the formula:

$$C.F._{age} = 1.25\ \tau^{-0.118}$$

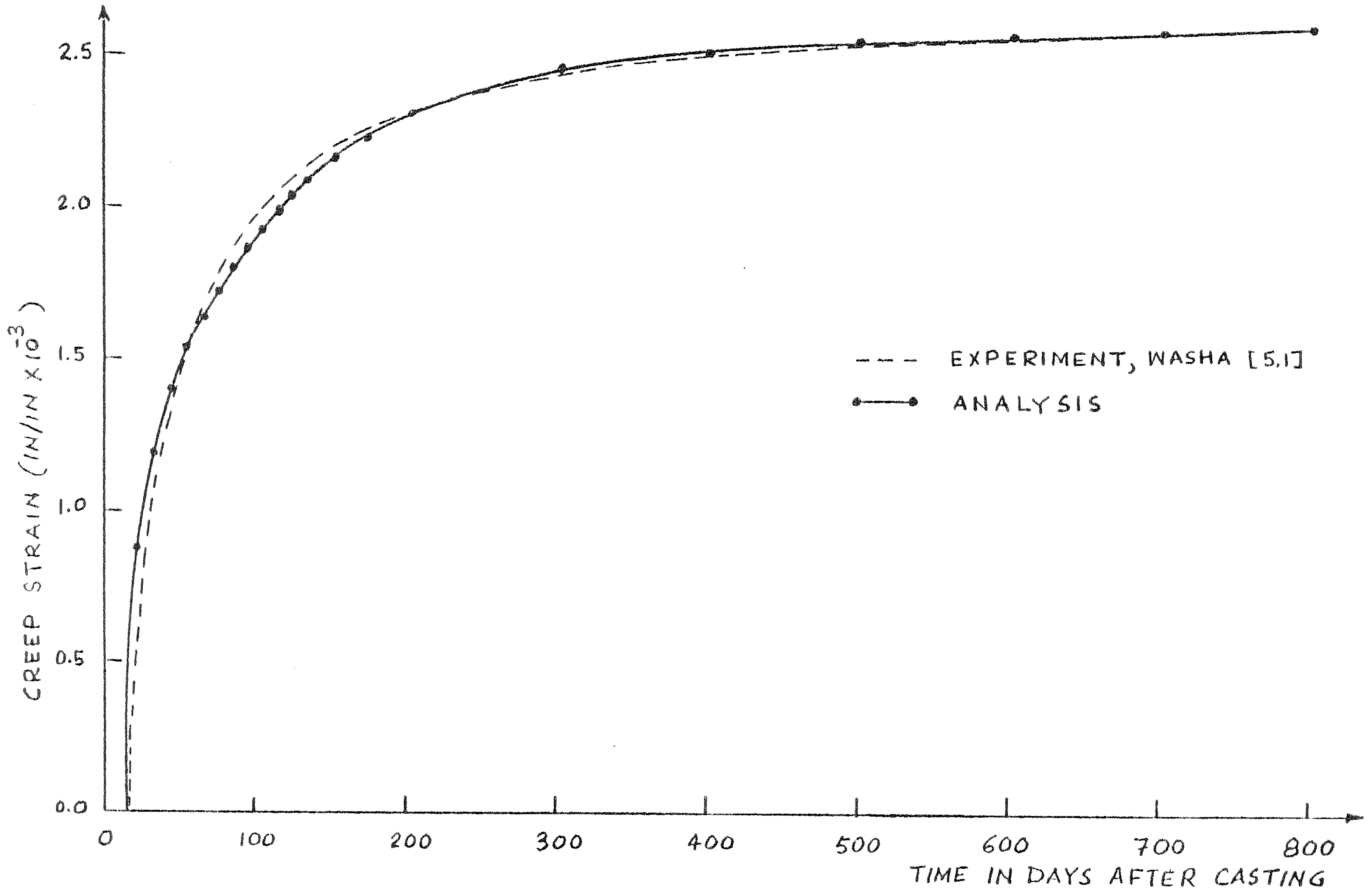

FIG. 5.3 EXAMPLE 1 - CREEP STRAIN FOR THE CONTROL CYLINDERS UNDER SUSTAINED LOAD OF 1575 PSI APPLIED 14 DAYS AFTER CASTING

where τ = age at loading.

The correction factors at 14 and 20 days are:

$$C.F._{14} = 1.25(14)^{-0.118} = 0.92$$

$$C.F._{20} = 1.25(20)^{-0.118} = 0.88$$

The α_i at 14 days must be scaled by a factor $C.F._{20}/C.F._{14} = 0.96$ to get the α_i corresponding to loading age 20 days. A similar procedure is followed to obtain the creep coefficients at other ages.

Figure 5.4 shows the deflection histories at midspan, as obtained from the experiment and the theory. The theoretically generated values compare satisfactorily with the experimental observations. The discrepancies, near the period immediately following application of load, are mainly due to the discrepancies in the curve fitting of the experimental creep curve as illustrated in Fig. 5.3.

Figure 5.5 shows the theoretical strain profiles at midspan for 0, 86, and 286 days after application of load. The experimental values at the compressive and tensile steel levels, i.e. 1 in. from the top surface and 1 in. from the bottom surface, are also plotted. The agreement between theoretical and experimental values is satisfactory. One of the factors contributing to the discrepancies between theoretical and experimental strain values in the period immediately following load application is the difference between the experimental creep curve and the theoretically generated creep curve as illustrated in Fig. 5.3. Furthermore, the experimental creep curve corresponds to an age of loading of 14 days. The ACI recommended age scaling factor has been used to determine the creep coefficients for other ages. This also contributes to the discrepancies.

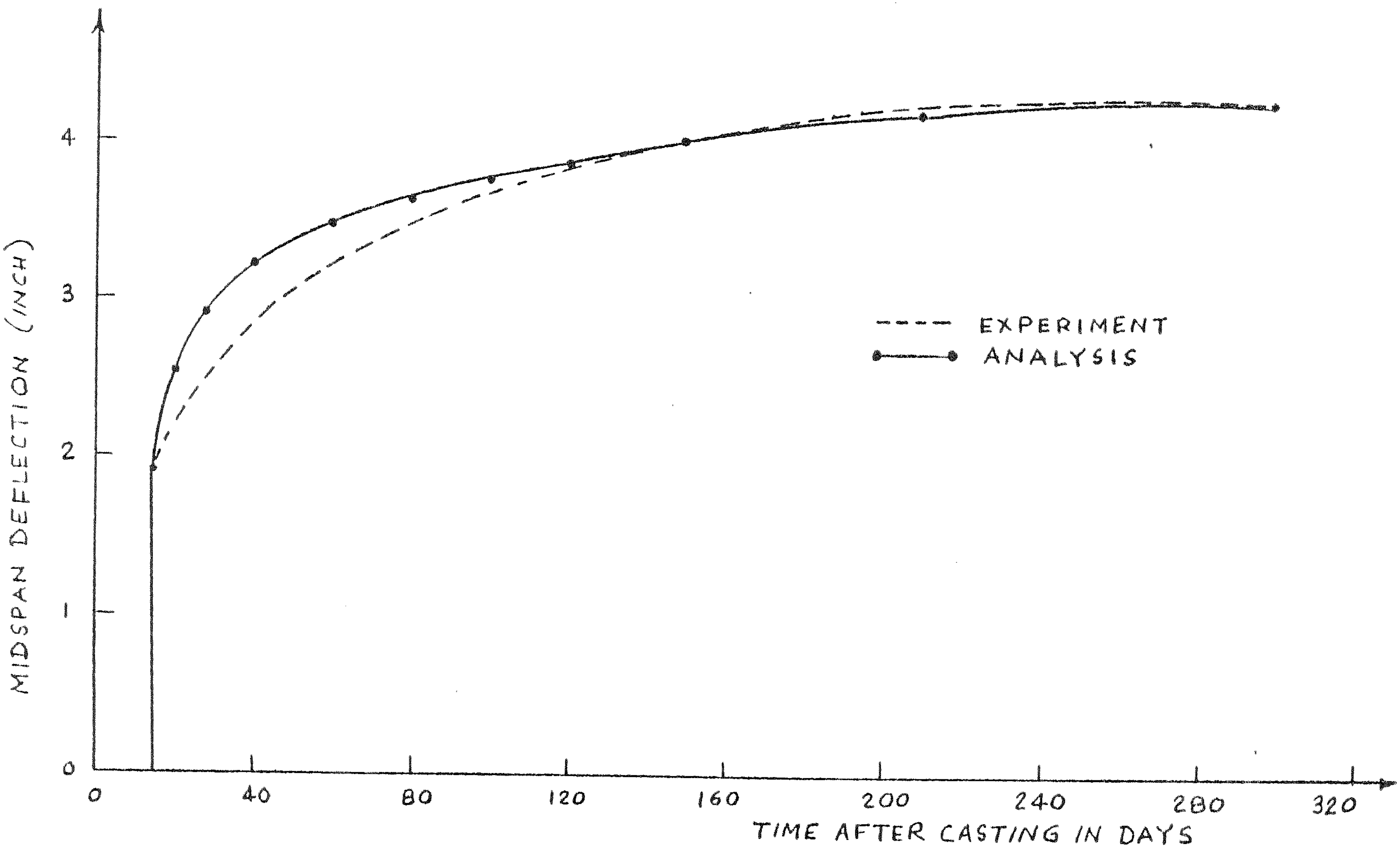

FIG. 5.4 EXAMPLE 1 - DEFLECTION HISTORY AT MIDSPAN OF THE BEAM C3 - C6

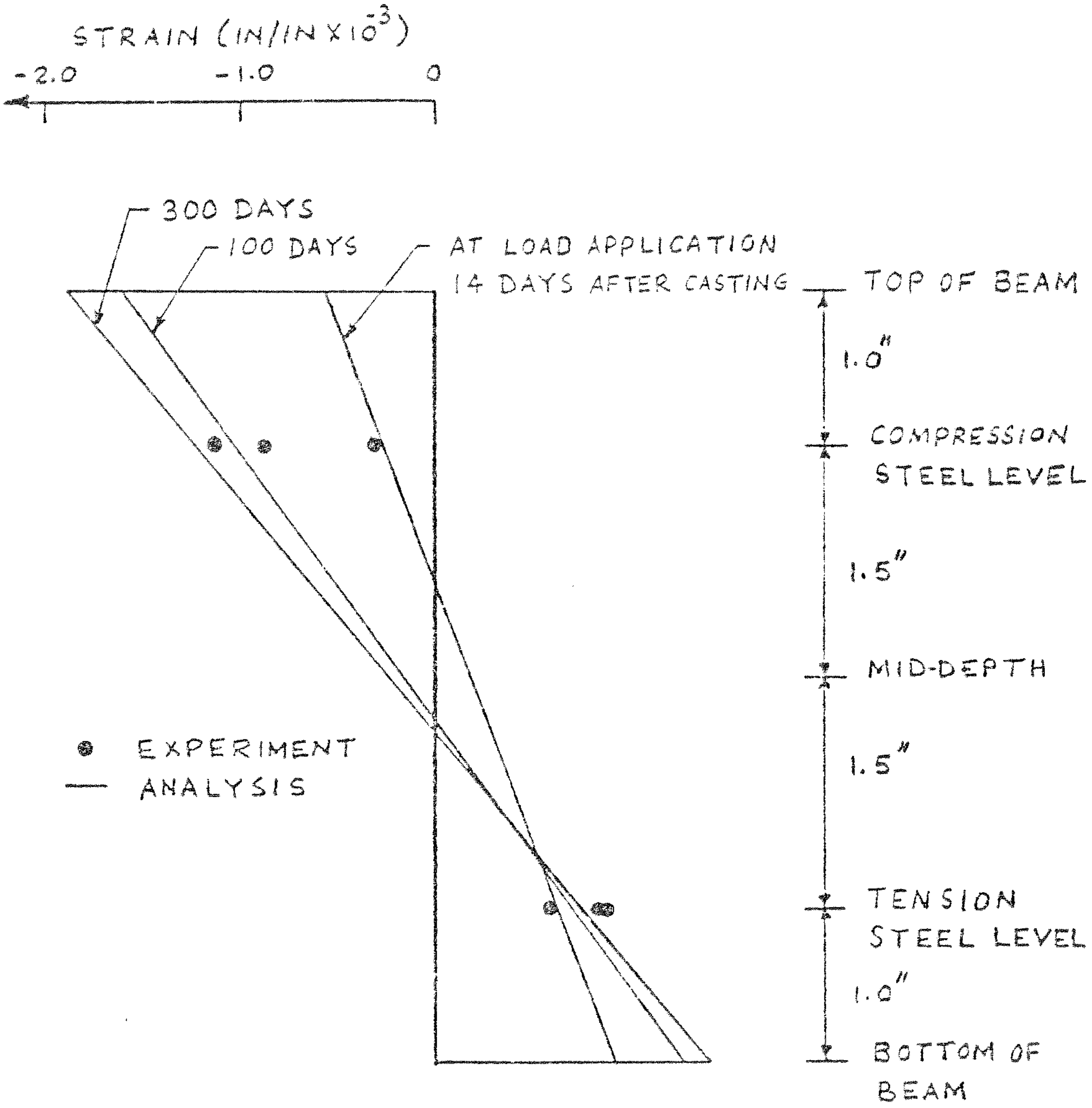

FIG. 5.5 EXAMPLE 1 - STRAIN PROFILE AT MIDSPAN OF THE BEAM C3 - C6 AT DIFFERENT TIMES AFTER CASTING

Figure 5.6 shows the concrete stress profile at midspan at different times. The redistribution of compressive stress with passage of time is significant. The compressive stresses at the top fibers relax and the incursion of the compressive zone into the cracked tensile zone of the section takes place to balance the applied constant external moment. Starting from an almost linear distribution of stresses at instantaneous loading, the redistributed stress profile becomes increasingly nonlinear. The causes of nonlinearity of stress distribution are twofold. First, in the extreme fibers the compressive stress exceeds 0.35 f'_c and thus the nonlinear effects due to high stress level is introduced. Second, in the cracked tensile zone, the nonlinear effect is inherent in the problem formulation as discussed by Sackman and Nickell [5.2]. In the cracked tensile zone, creep strains do not occur with initial loading but only after the tensile zone comes under the compression regime. This causes the stress in the cracked tensile zone to be nonlinearly dependent on the depth from the neutral axis.

Figure 5.7 shows the relaxation of compressive stress in the topmost layer at midspan due to creep effects. The stress relaxation is very rapid from 14 to 40 days and then gradually becomes asymptotic.

Figure 5.8 shows the variation in tensile stress in the steel reinforcement at midspan with time. The tensile stress increases gradually with time due to the shifting of the compressive zone towards the tensile reinforcement and the resultant decrease in the lever arm between compression and tension forces. This requires an increase in steel tensile stress to carry the moment which remains constant. The decrease in the lever arm, however, is very small, necessitating only a small increase in the tensile stress.

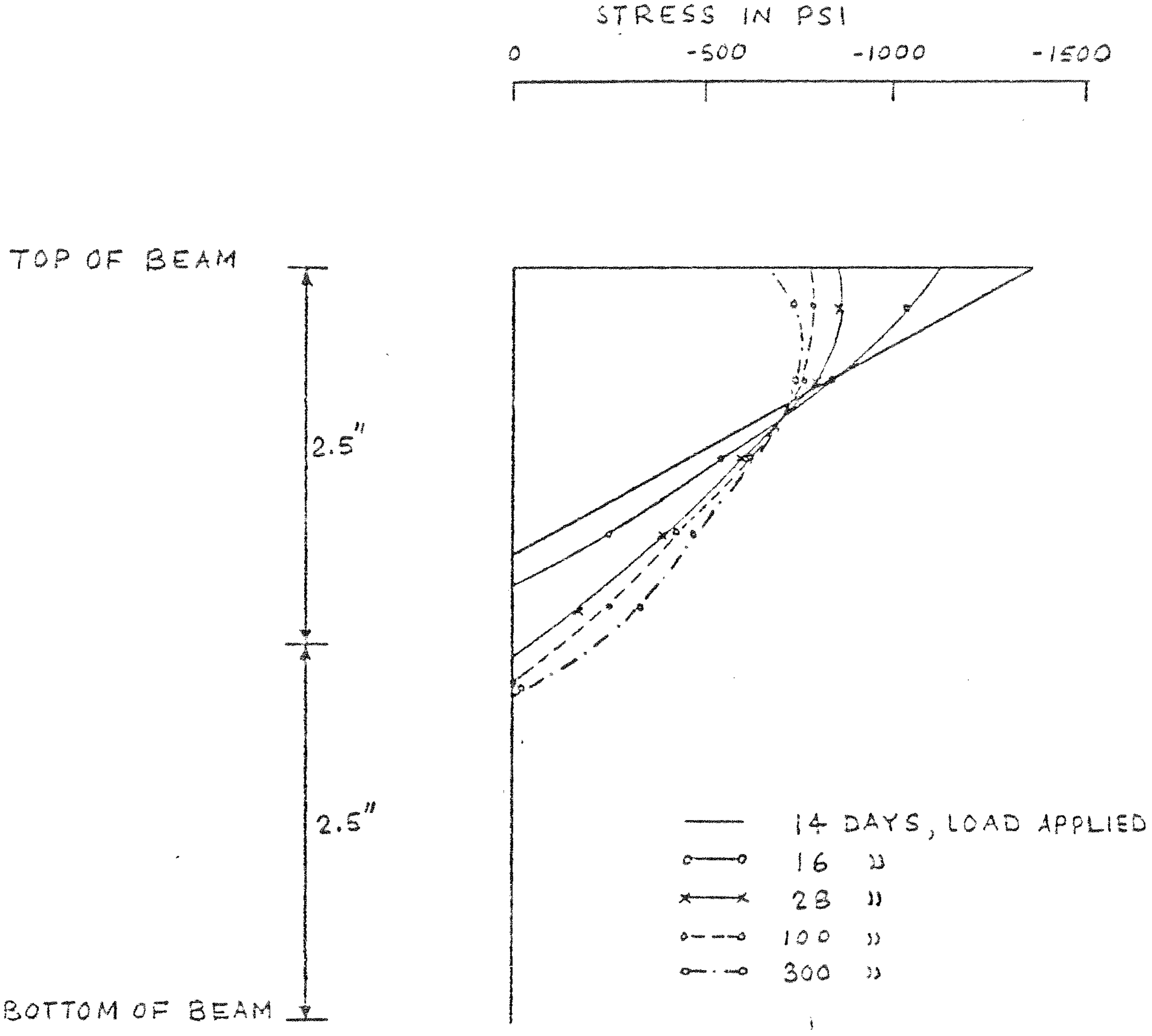

FIG. 5.6 EXAMPLE 1 - CONCRETE STRESS PROFILE AT MIDSPAN OF THE BEAM C3 - C6 AT DIFFERENT TIMES AFTER CASTING

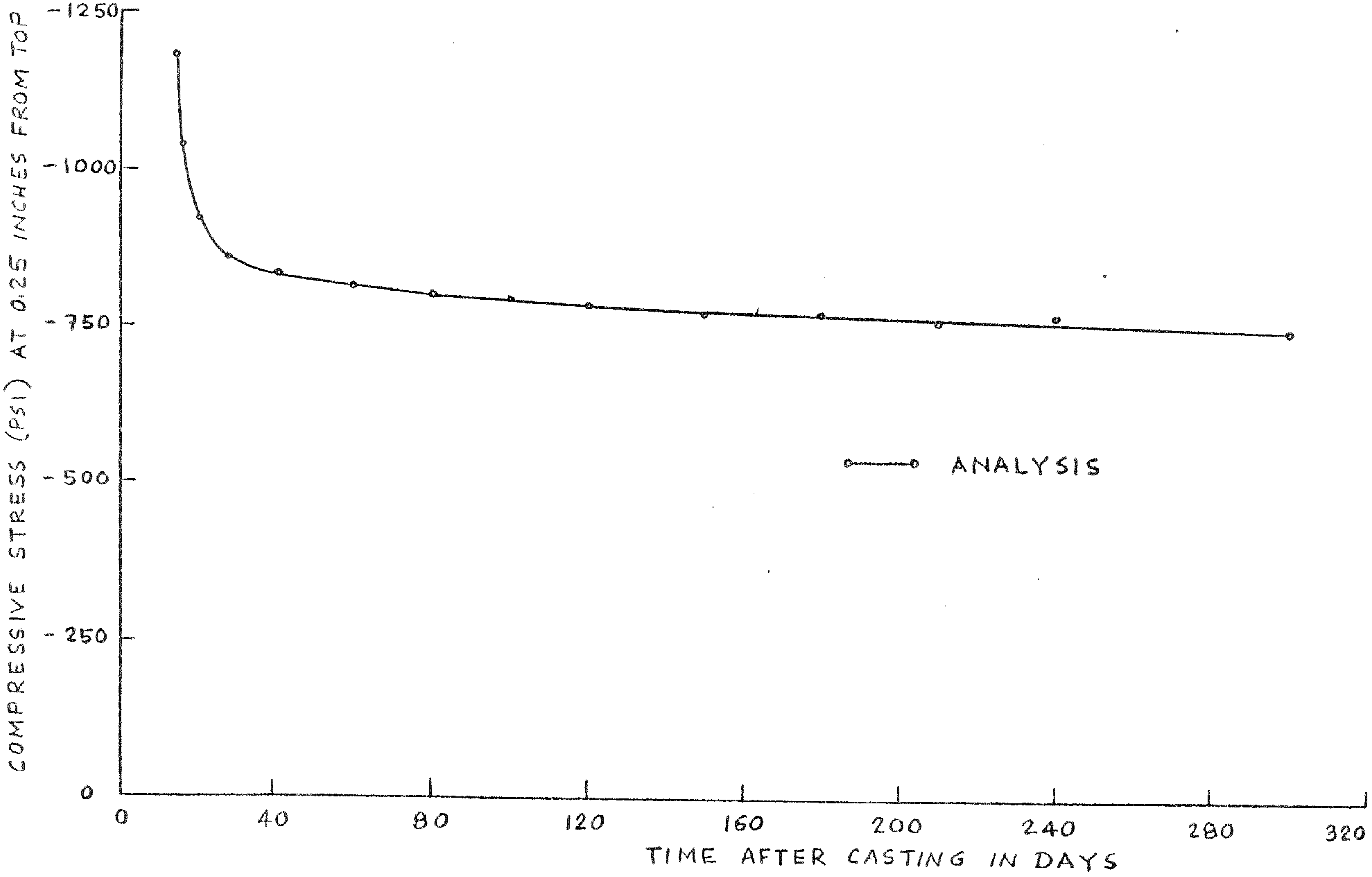

FIG. 5.7 EXAMPLE 1 - COMPRESSIVE STRESS HISTORY FOR TOPMOST CONCRETE LAYER AT MIDSPAN OF THE BEAM C3 - C6

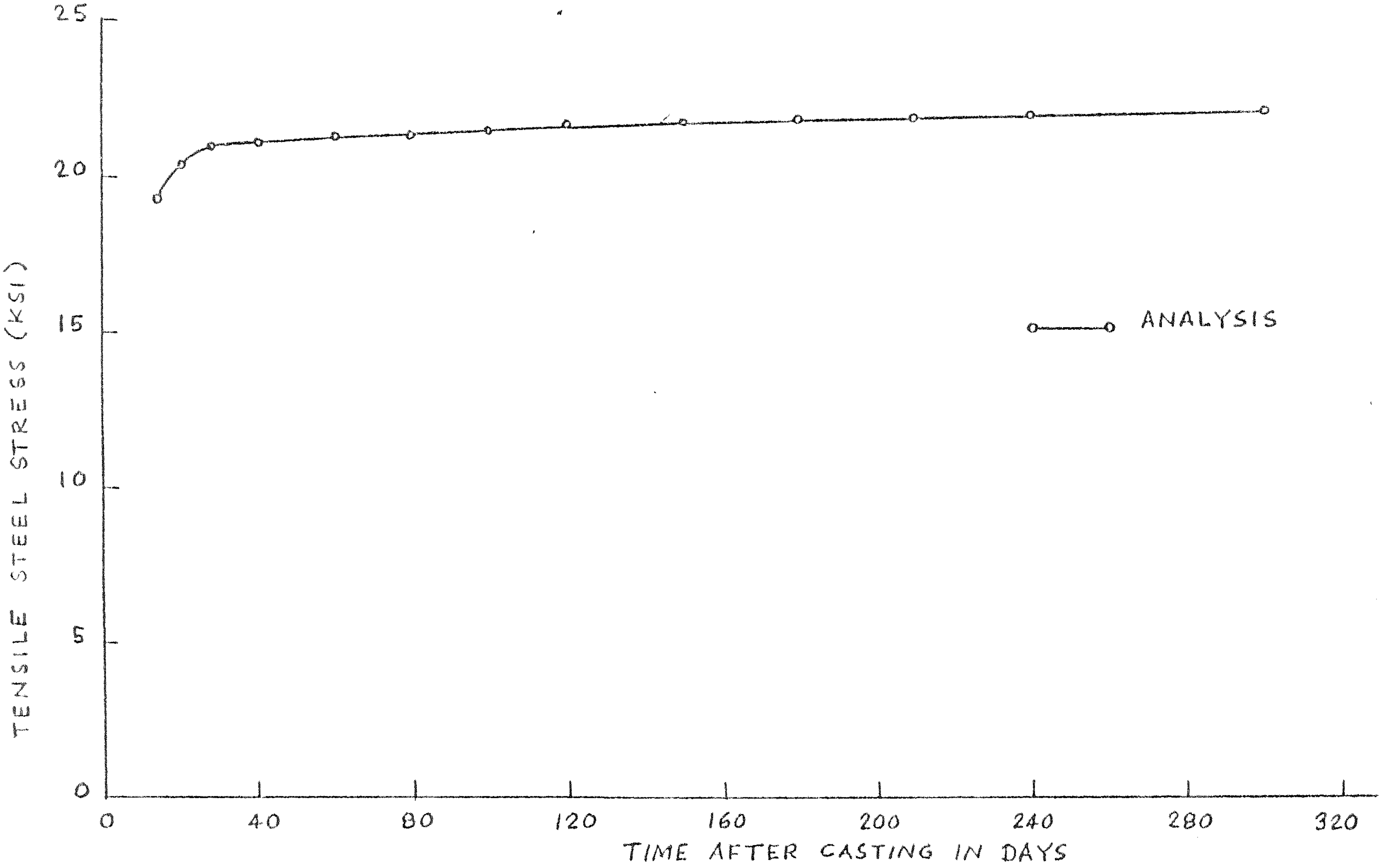

FIG. 5.8 EXAMPLE 1 - TENSILE STRESS HISTORY FOR STEEL REINFORCEMENT AT MIDSPAN OF THE BEAM C3 - C6

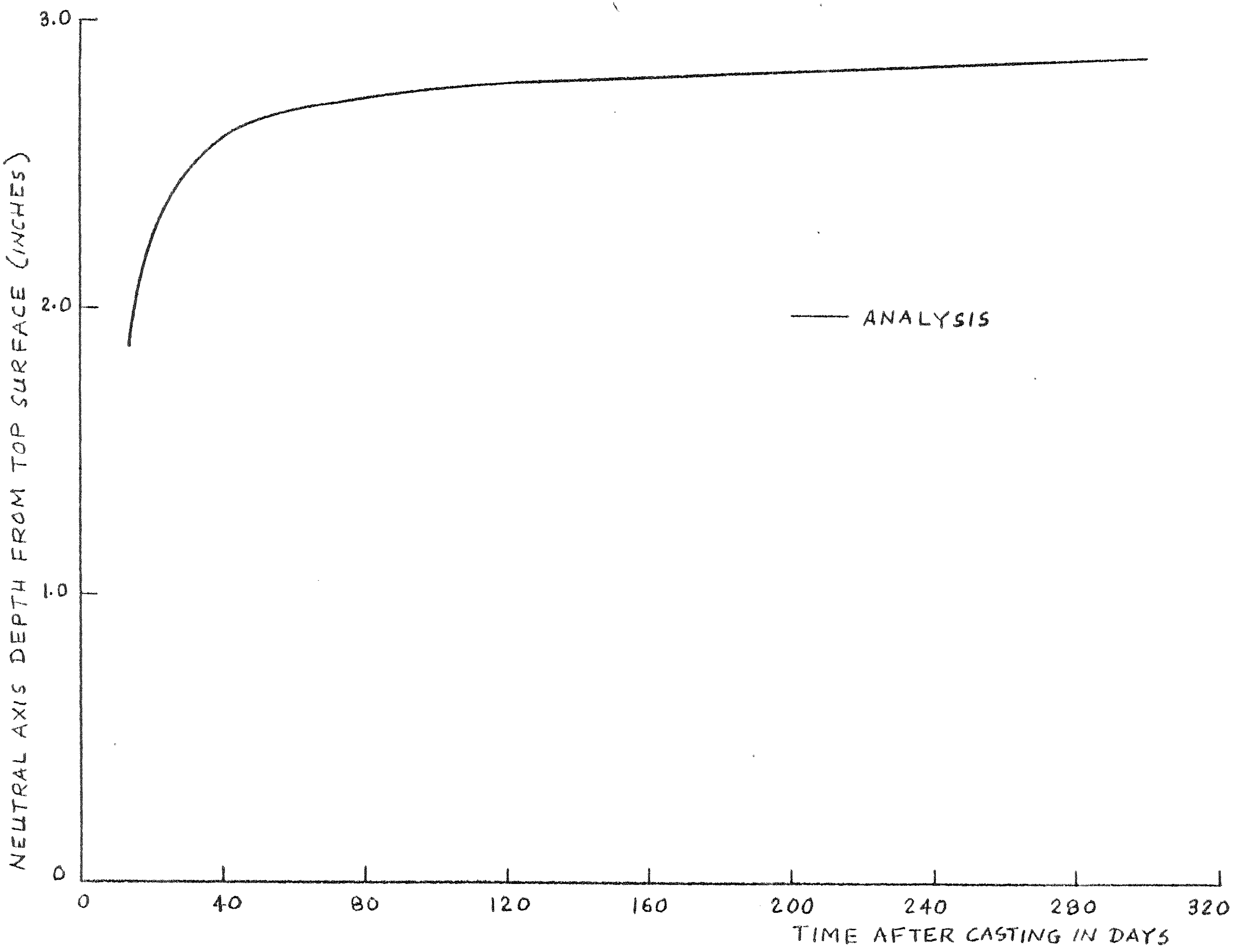

FIG. 5.9 EXAMPLE 1 - VARIATION OF NEUTRAL AXIS DEPTH AT MIDSPAN OF THE BEAM C3 - C6

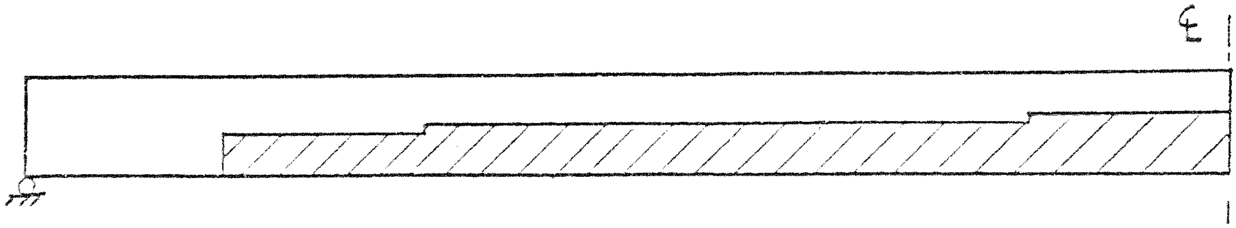

a. 14 DAYS AFTER CASTING, LOAD APPLIED

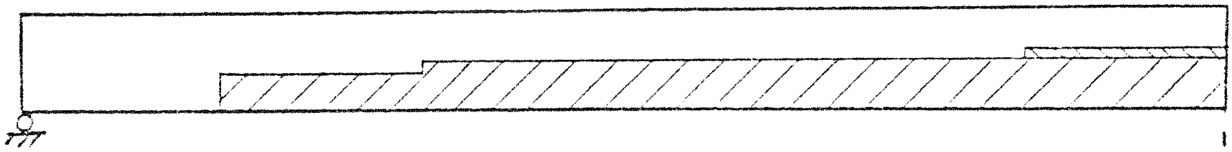

b. 20 DAYS AFTER CASTING, 6 DAYS OF SUSTAINED LOAD

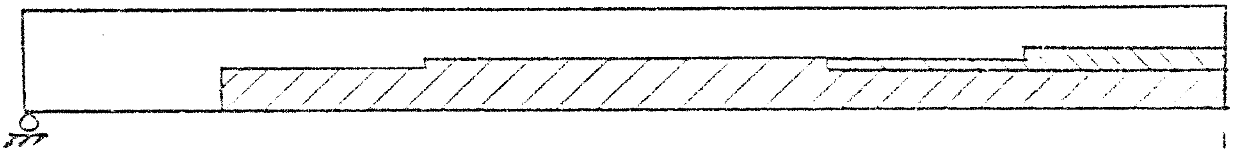

c. 120 DAYS AFTER CASTING, 106 DAYS OF SUSTAINED LOAD

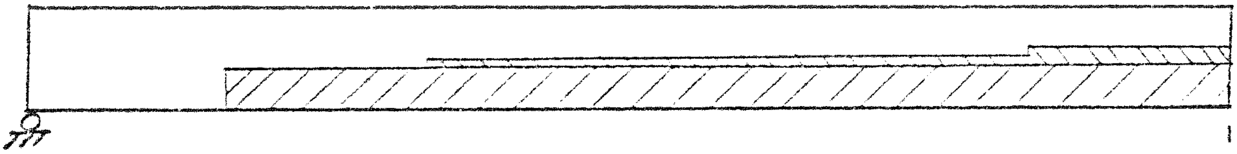

d. 300 DAYS AFTER CASTING, 284 DAYS OF SUSTAINED LOAD

▨ LAYER CRACKED   ▧ CRACK CLOSED

FIG. 5.10 EXAMPLE 1 - ANALYTICAL CRACK PATTERNS OF THE BEAM C3 - C6

A phenomenon observed in Fig. 5.5 is the increase in the depth of the neutral axis from the top surface with time. This is plotted in Fig. 5.9 which shows a rapid increase from 14 to 40 days and then the increment rate slows down. The depth of neutral axis increases to accommodate the stress redistribution which takes place due to creep of concrete.

Figure 5.10 demonstrates the crack patterns at different stages of load history. The beam is extensively cracked at the time of the application of load. With passage of time, cracks in the layers at mid-depth are closed and compressive stresses occur in those layers.

It may be said in conclusion that the creep model chosen predicted the experimental behavior very accurately. The beam specimen was under high stresses and was cracked extensively. The close correspondence of the theoretical analysis with the experimental values for this case under very severe conditions suggest that under lower levels of stresses, as would generally occur in most structures, the correspondence will be even better.

5.3 Example 2 - Cervenka Wall Panel W2

Cervenka [1.8] conducted experiments on a series of reinforced concrete wall panels to investigate their behavior in the inelastic range. Proper understanding of the behavior of reinforced concrete wall panels is extremely important in the study of multistory buildings under wind and earthquake excitations as the lateral stability of such structures are mainly provided by the shear walls. In the present study, wall panel specimen W2 of Cervenka has been analyzed under both instantaneous load and sustained load. The purpose of the study has been to compare the instantaneous response to the time-dependent response to determine whether significant changes in the structural behavior are introduced by the creep and shrinkage effects.

Figure 5.11 presents the dimensions and reinforcing scheme of specimen W2. Because of symmetry, each half of the deep beam can be considered similar to a wall panel subjected to a single transverse load.

Figure 5.12a presents the finite element discretization of one-half of the test specimen. A mesh size of 7 x 5 is used. This provides for the wall panel proper a 5 x 5 mesh with 50 plane stress CST elements. This is a rather coarse mesh compared to that used by Cervenka, a 10 x 10 mesh with 200 CST elements. The coarse mesh has been used here to keep computer costs down without sacrificing too much accuracy. The load history for the creep and shrinkage analysis is shown in Fig. 5.12b. A load of P = 20 kips is applied at 28 days after casting which is sustained for another 92 days, i.e. 120 days after casting. Analyses for creep and shrinkage are carried out at 2, 6, 12, 22, 32, 62, and 92 days after loading. After that, the specimen is loaded further to reach the ultimate load. The instantaneous analysis is done at 28 days after casting.

Figure 5.13 presents the material properties chosen for the analysis. The theoretical properties correspond very closely to the experimental values. For creep and shrinkage, the ACI Committee 209 [3.5] recommended values are adopted.

Figure 5.14 compares the theoretical load-deflection curve at point A with experimental values for instantaneous loading. Considering the coarseness of the mesh used, the correspondence of theoretical

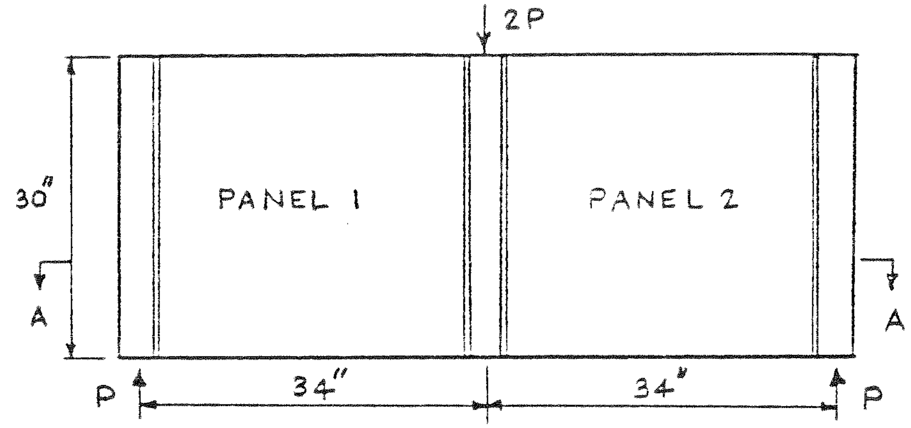

a. ELEVATION

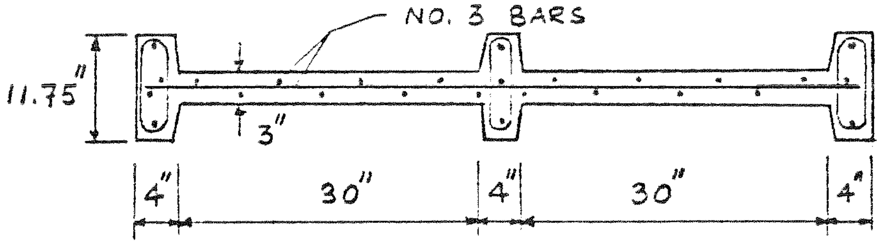

b. SECTION AA

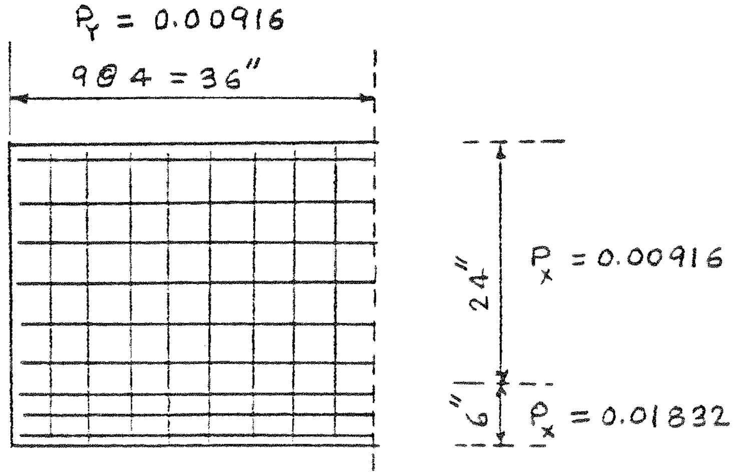

c. NO. 3 REINFORCEMENTS

FIG. 5.11 EXAMPLE 2 - DETAILS OF WALL PANEL SPECIMEN W2 [1.8]

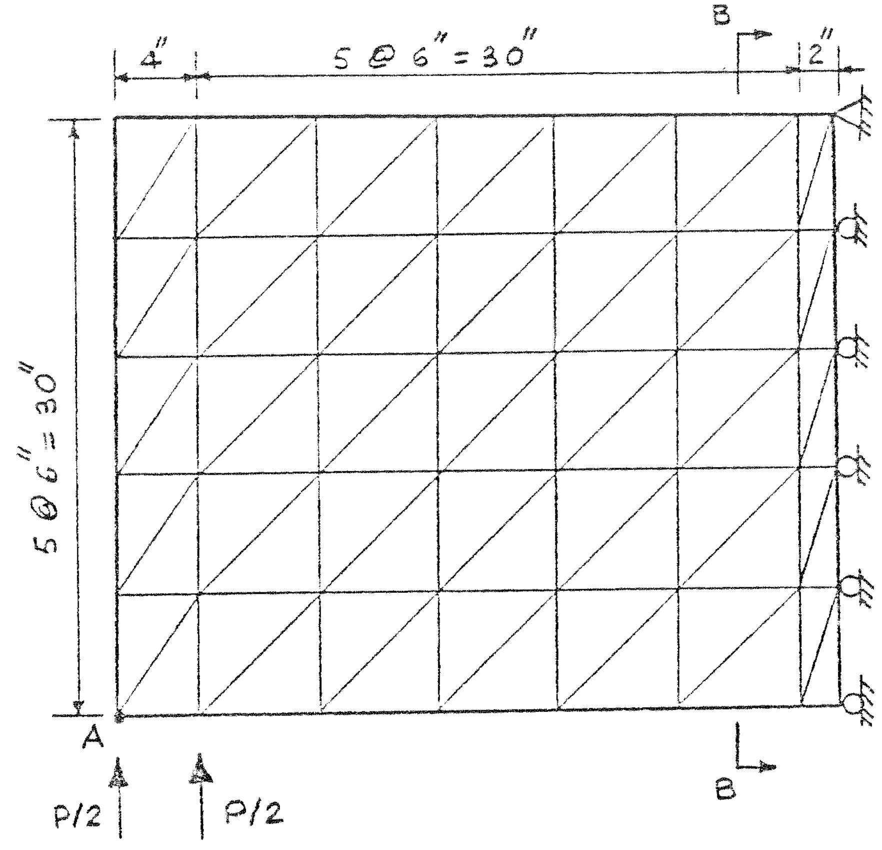

a. FINITE ELEMENT IDEALIZATION

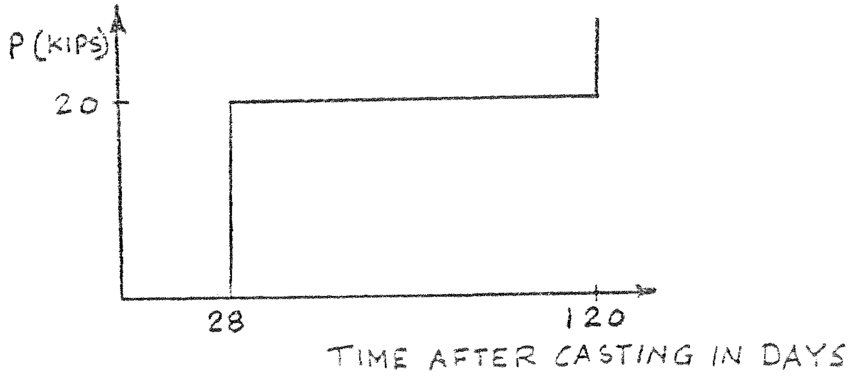

b. LOAD HISTORY FOR ANALYSIS

FIG. 5.12 EXAMPLE 2 - FINITE ELEMENT IDEALIZATIONS AND LOAD HISTORY

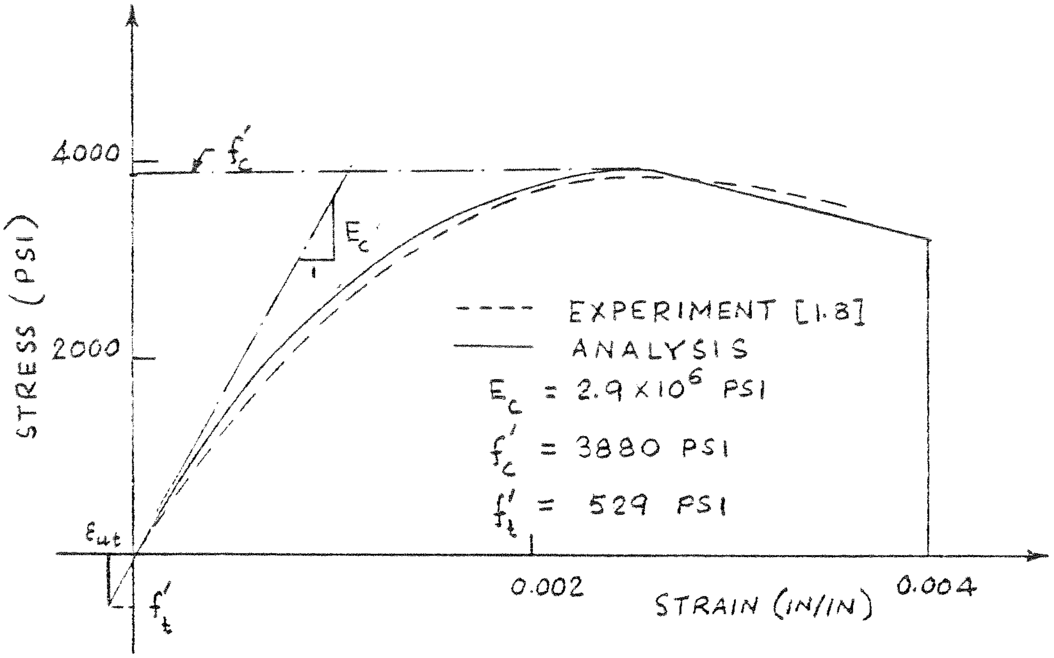

a. CONCRETE PROPERTIES FOR ANALYSIS

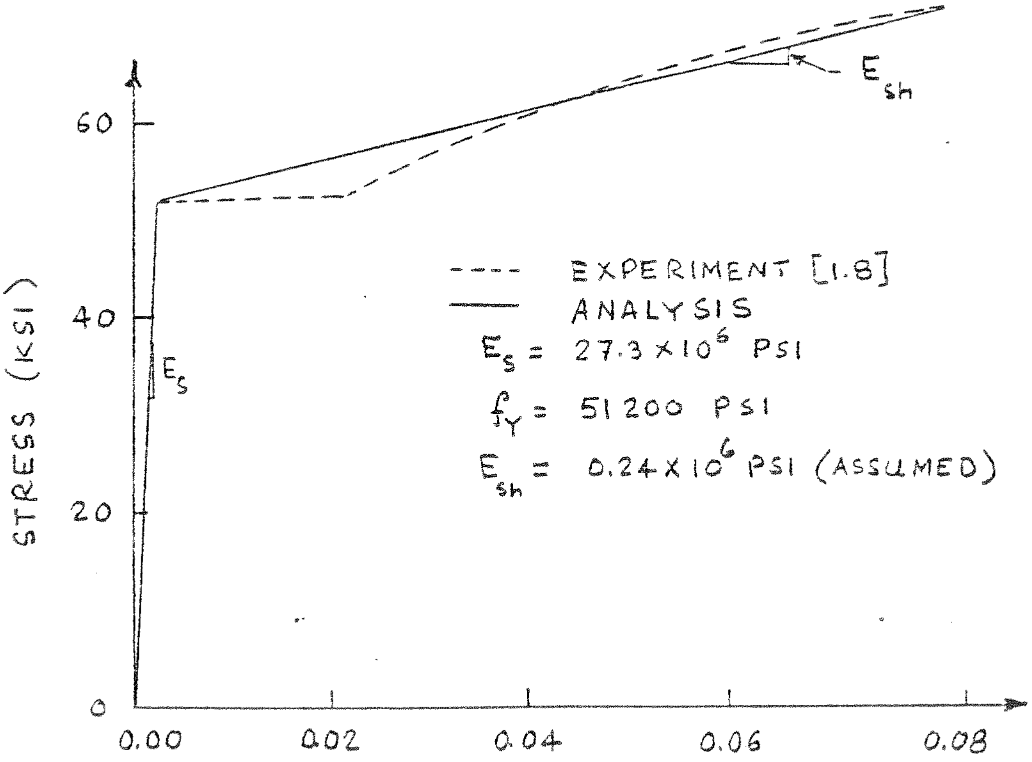

b. STEEL PROPERTIES FOR ANALYSIS

FIG. 5.13 EXAMPLE 2 - MATERIAL PROPERTIES ADOPTED FOR ANALYSIS

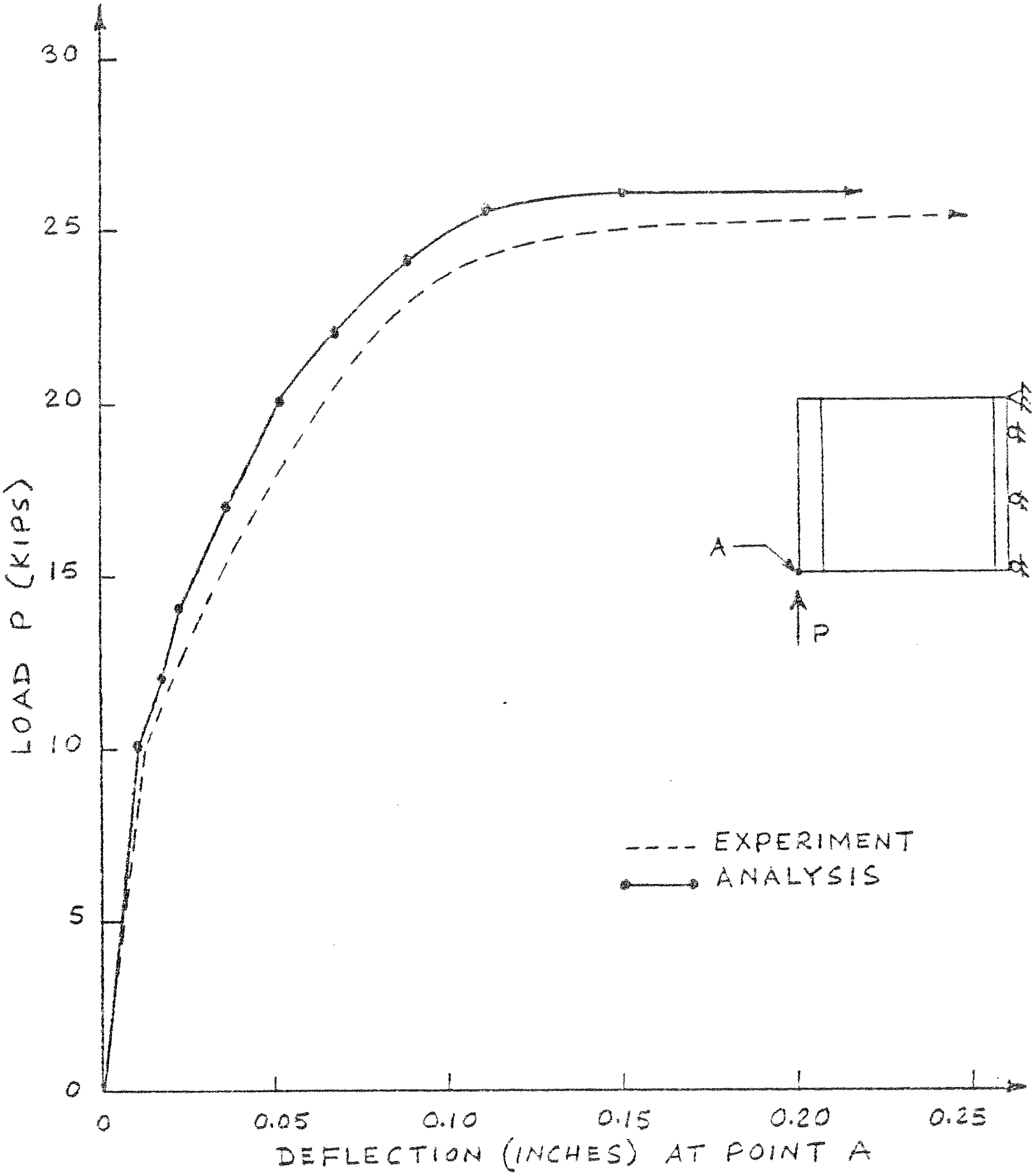

FIG. 5.14 EXAMPLE 2 - LOAD-DEFLECTION CURVE FOR POINT A UNDER INSTANTANEOUS LOAD

and experimental values are good.

Figure 5.15 illustrates the crack patterns obtained from the present analysis at load levels of 14, 24 and 25.5 kips. The cracked regions as well as the crack directions correspond very well with the experimental values. Considerable cracking occurs in the specimen at higher load levels causing nonlinearity in the load-deflection curve of Fig. 5.14. The steel reinforcement in the tensile zone yields causing the cracks to widen. The failure ultimately occurs due to the yielding and crushing of concrete in compression (designated by "YL" in Fig. 5.15).

Figure 5.16 illustrates the deflection at point A due to a sustained load of P = 20 kips applied from 28 to 120 days after casting. The deflection increases by about 50% at the end of the sustained period of 3 months.

Figure 5.17 compares the load-deflection curves for instantaneous and time-dependent loadings. It may be noted from the two load-deflection curves that the ultimate behavior is not much altered by this particular load history from the instantaneous behavior.

Figures 5.18 and 5.19 show the distribution of net compressive forces in concrete and tensile forces in steel across section BB at 0 and 92 days after load application. The concrete compressive force reduces at the outer layer and some tensile area changes to the compressive zone causing the neutral axis to shift towards the tensile steel. This is similar, qualitatively, to the behavior of the beam in Example 1. The stress redistribution, however, is not as severe. The tensile force increases in the tensile steel reinforcement, but, here again, the increase is not much. This is because the lever arm

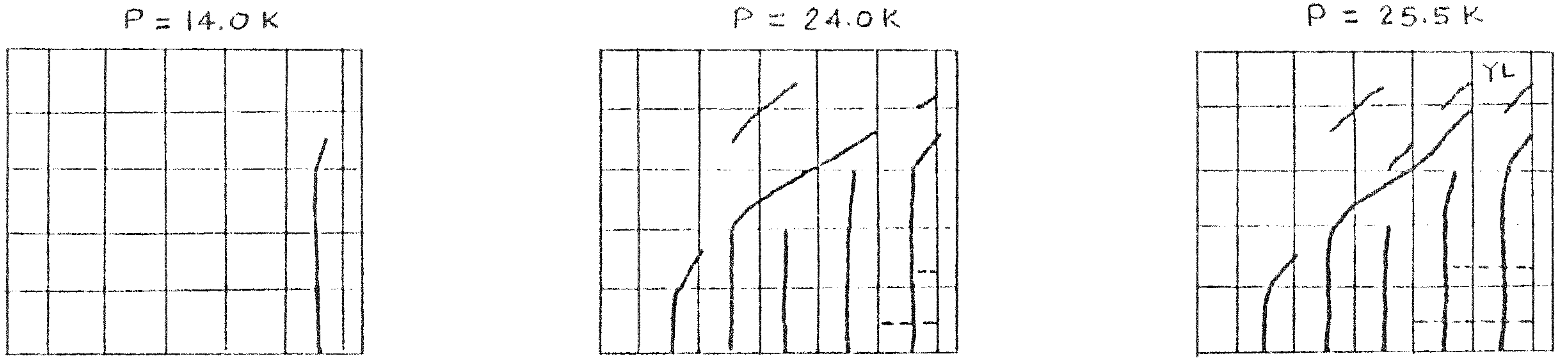

a. ANALYTICAL CRACKS

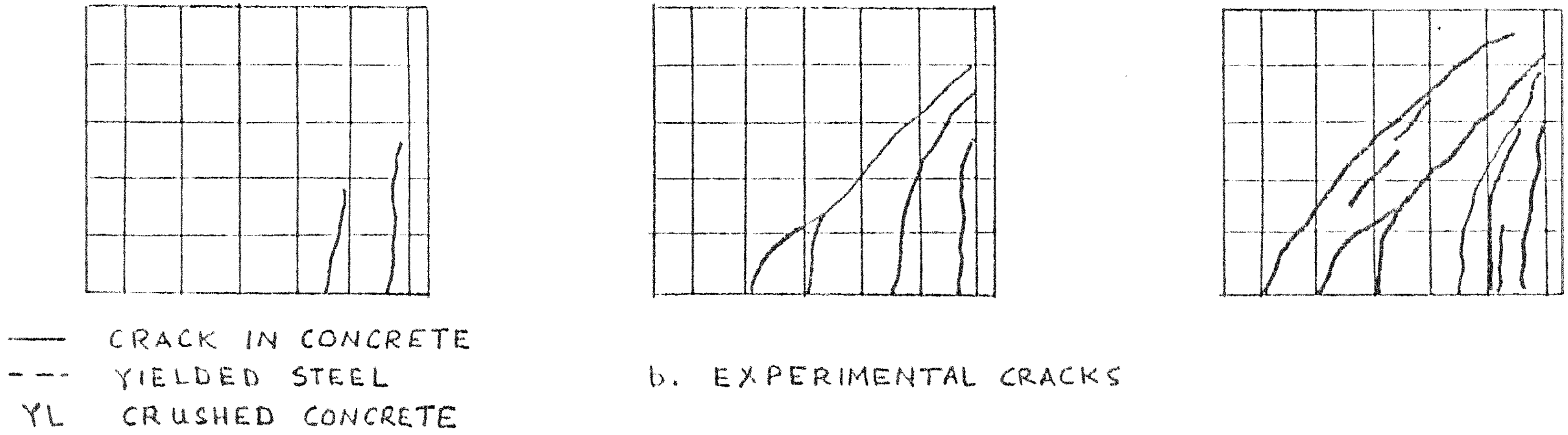

b. EXPERIMENTAL CRACKS

FIG. 5.15 EXAMPLE 2 - ANALYTICAL AND EXPERIMENTAL CRACK PATTERNS FOR INSTANTANEOUS LOAD

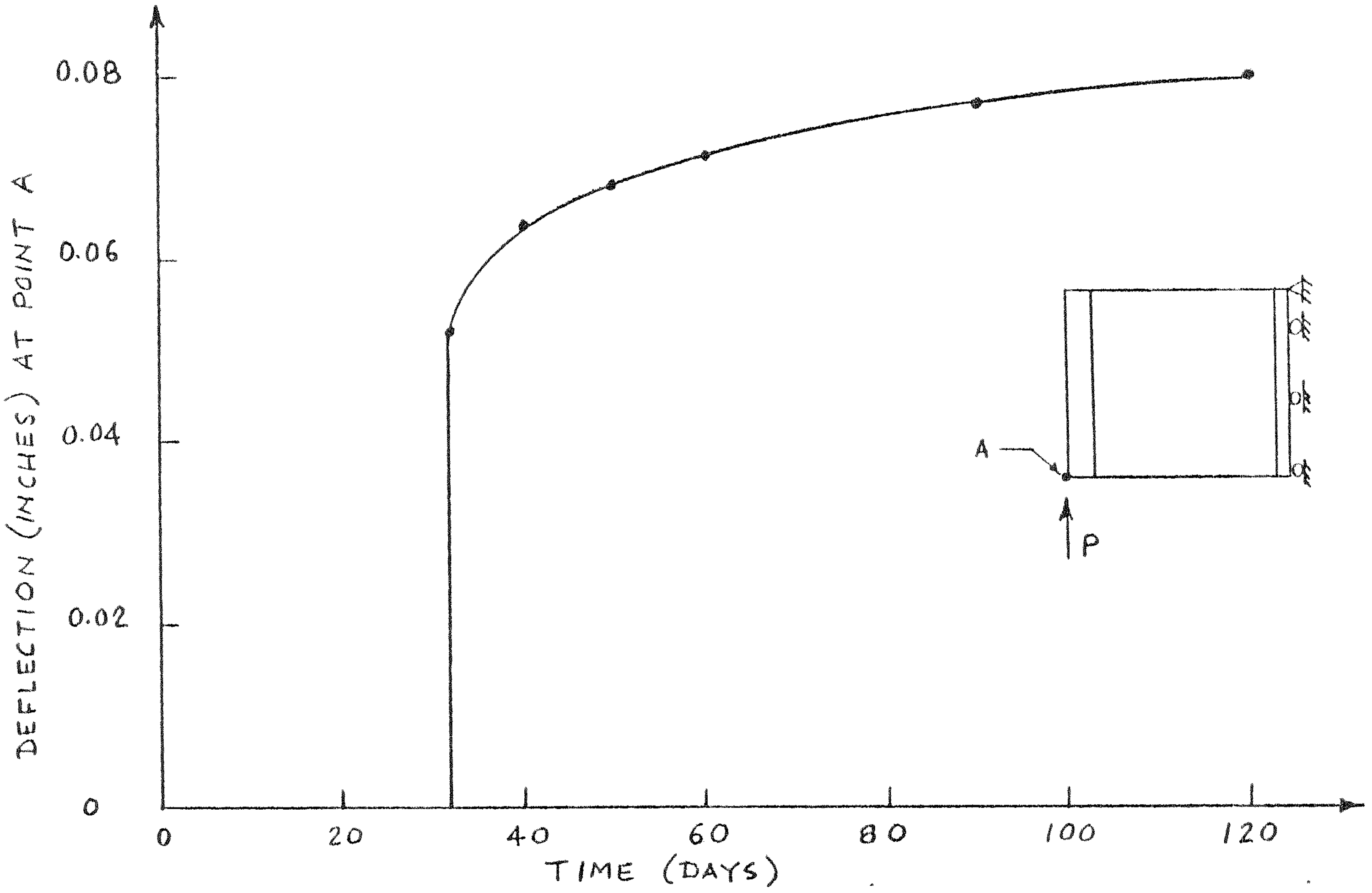

FIG. 5.16 EXAMPLE 2 - DEFLECTION HISTORY FOR POINT A UNDER A SUSTAINED LOAD OF 20 KIPS

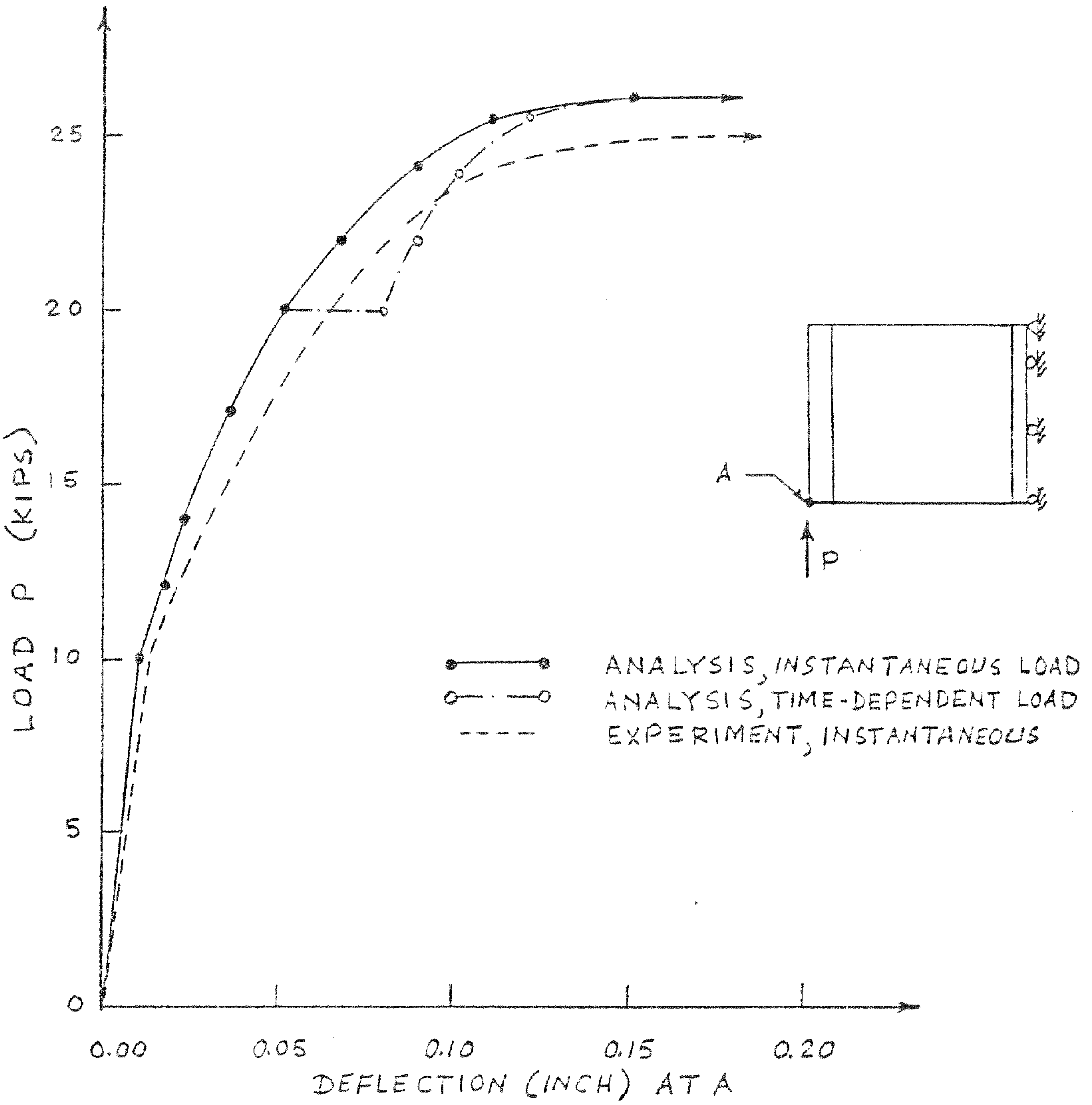

FIG. 5.17 EXAMPLE 2 - LOAD-DEFLECTION CURVES AT POINT A DUE TO DIFFERENT LOAD HISTORIES

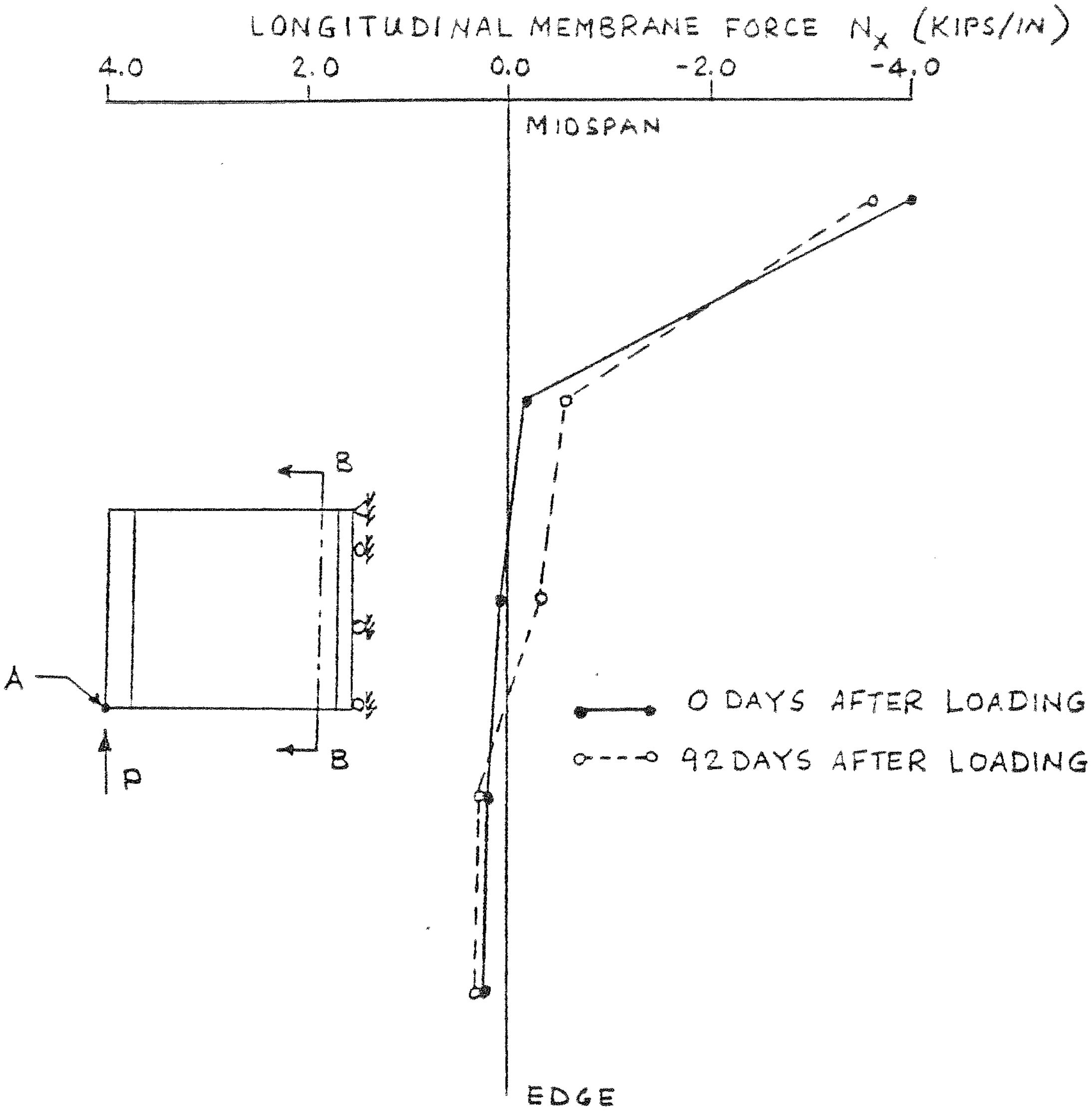

FIG. 5.18 EXAMPLE 2 - TRANSVERSE DISTRIBUTION OF LONGITUDINAL MEMBRANE FORCES IN CONCRETE AT SECTION BB

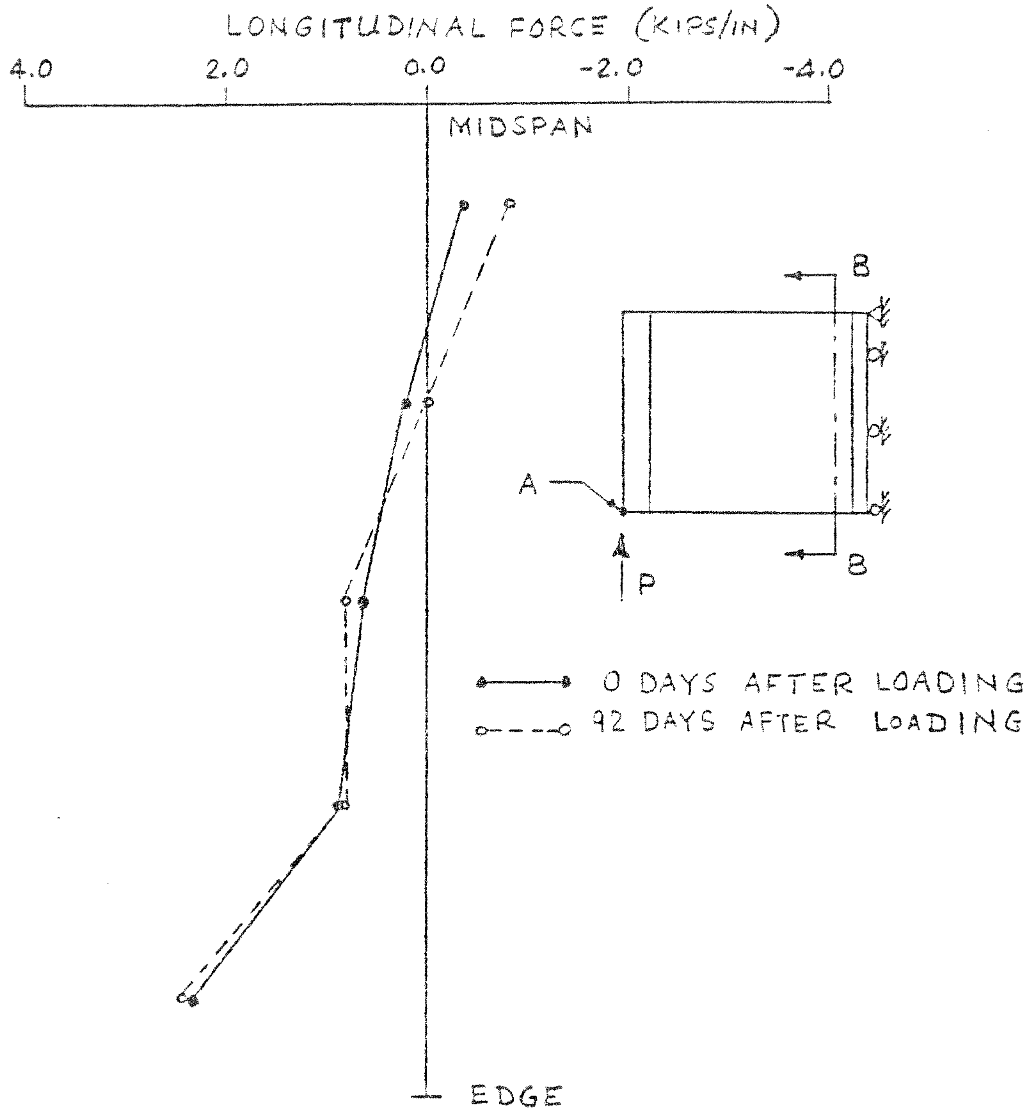

FIG. 5.19 EXAMPLE 2 - TRANSVERSE DISTRIBUTION OF LONGITUDINAL FORCES IN STEEL REINFORCEMENT AT SECTION BB

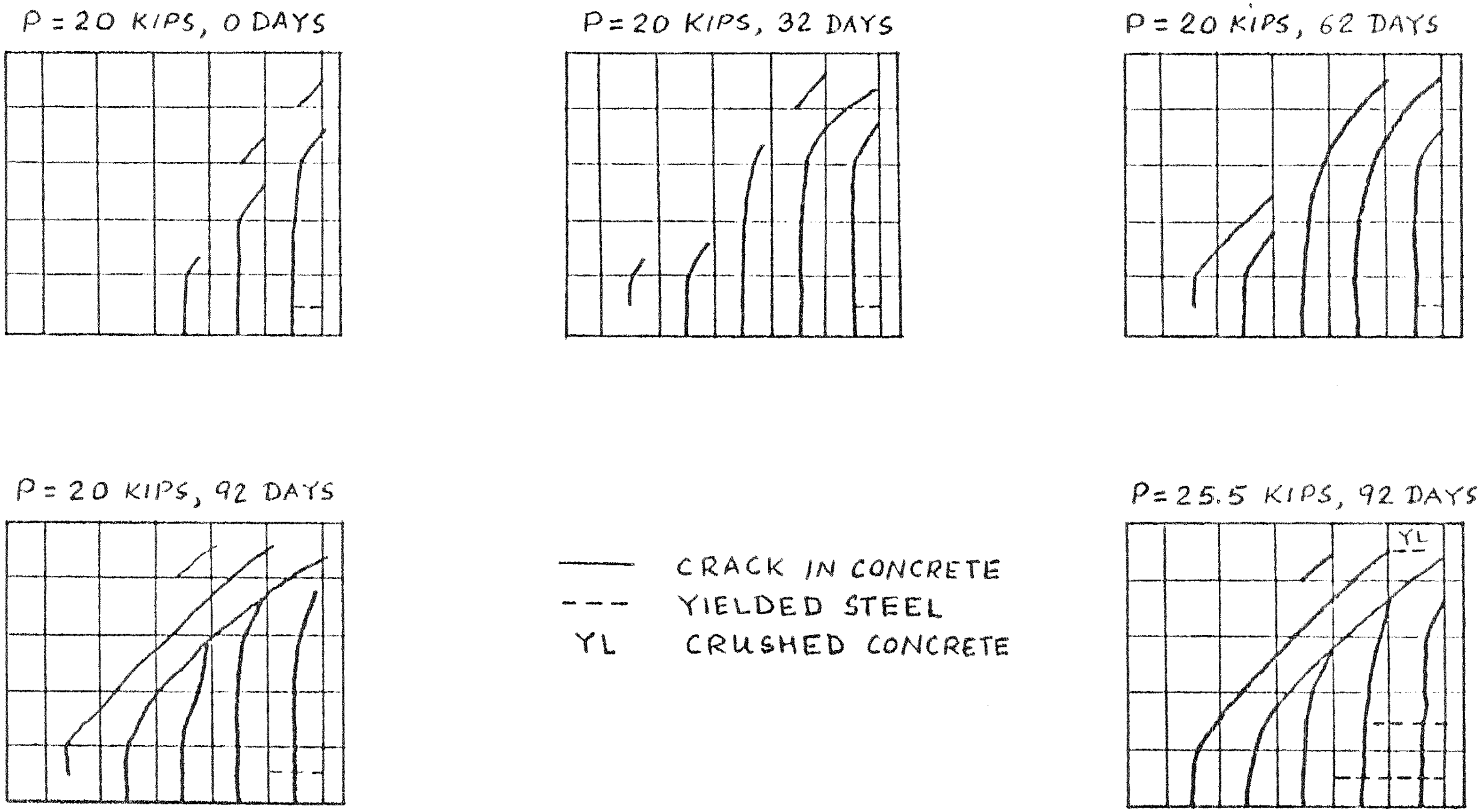

FIG. 5.20 EXAMPLE 2 - CRACK PROPAGATION WITH TIME UNDER A SUSTAINED LOAD OF 20 KIPS

between the tensile and compressive forces do not change much as observed in Example 1.

Figure 5.20 presents the crack patterns at 0, 32, 62, and 92 days after the application of load. The crack propagation is extensive. The crack pattern, after 92 days under 20 kips of load, is as severe as that under 25.5 kips of instantaneous load. Further increment of loading causes yielding of tensile and compressive reinforcement and failure occurs at P = 26.0 kips due to crushing of concrete in the compressive zone.

5.4 Example 3 - McNiece Slab

An isotropically reinforced square slab, tested by McNiece [1.18], is analyzed for both instantaneous loading and assumed load history considering creep and shrinkage effects. In the literature available to the author, no well-documented experimental data on the behavior of reinforced concrete slabs subjected to creep and shrinkage was found. Hence, the purpose of this example is to see how a slab performs under a time-dependent loading including creep and shrinkage effects and in which way this slab behavior differs from that due to instantaneous loading.

The slab is simply supported at the four corners and is subjected to a concentrated load at the center as shown in Fig. 5.21. The overall dimensions, finite element mesh system, and layer system used for analysis are also shown. Due to symmetry, only one quarter of the slab is needed for analysis.

The material properties given and those assumed for the analysis are presented in Fig. 5.22. The ACI Committee 209 [3.5] recommended

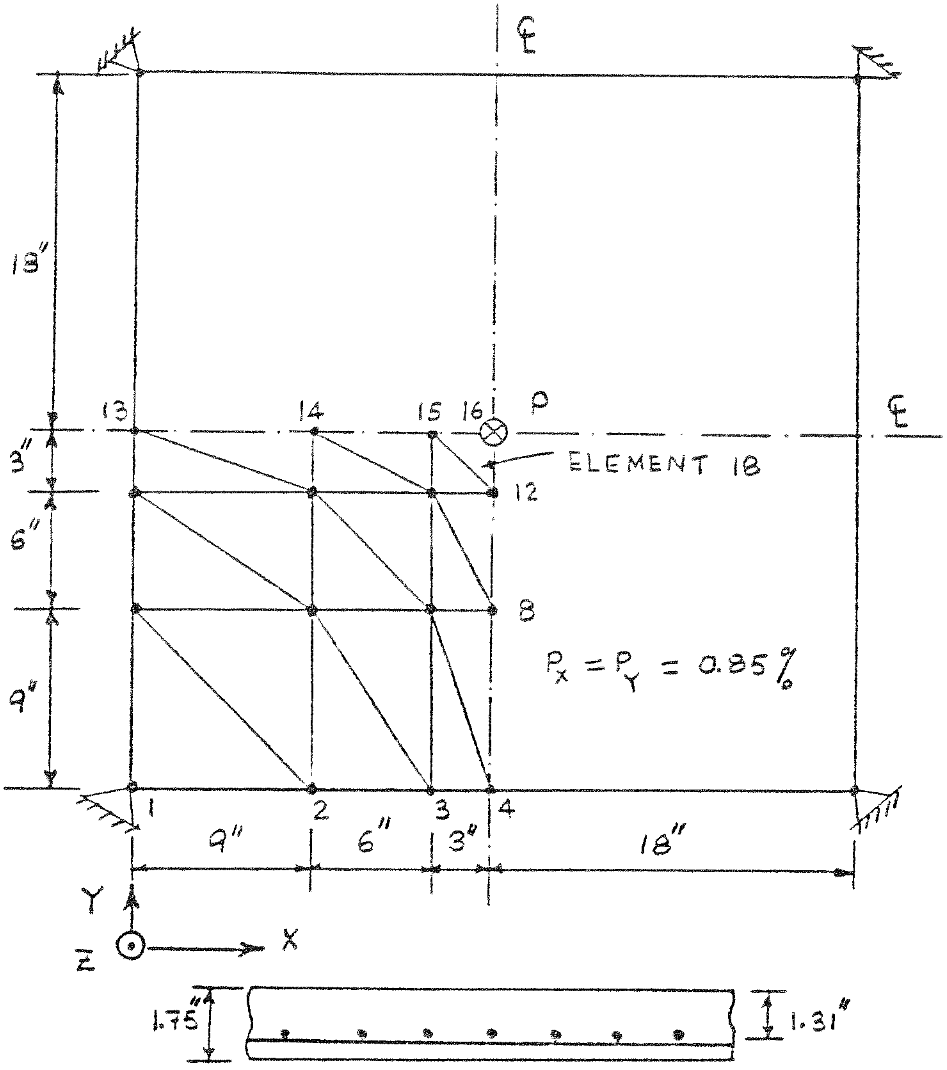

a. PLAN VIEW AND CROSS-SECTION

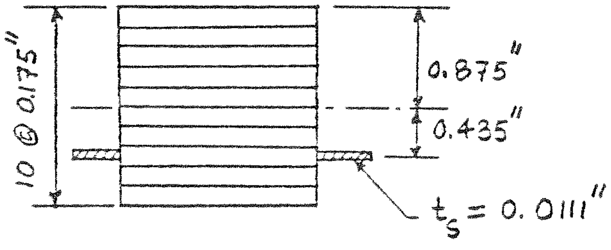

b. LAYER SYSTEM

FIG. 5.21 EXAMPLE 3 - OVERALL DIMENSIONS AND FINITE ELEMENT MESH FOR ANALYSIS OF MCNIECE SLAB [1.18]

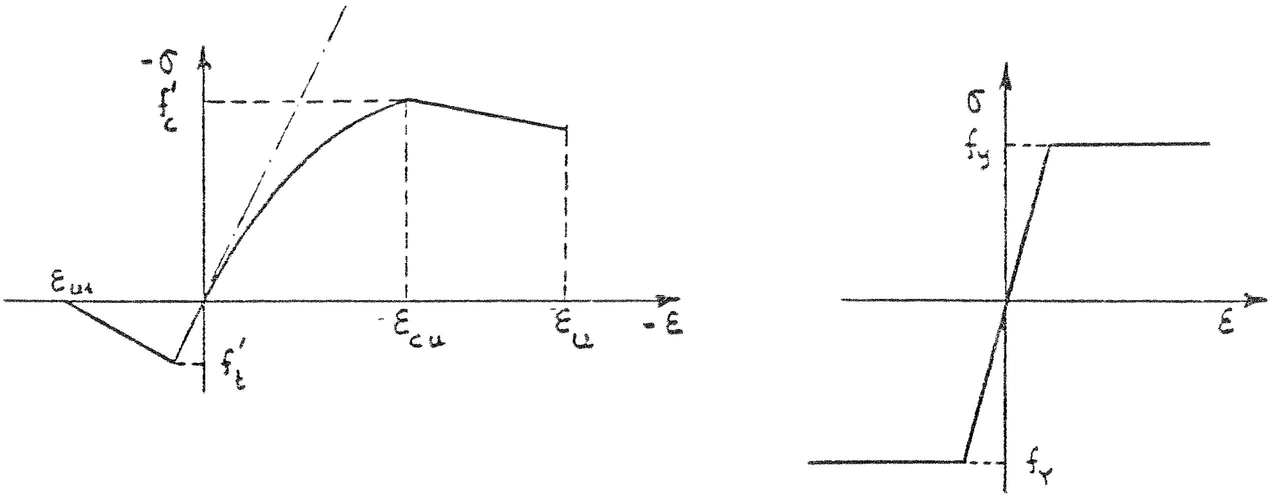

a. CONCRETE σ-ε CURVE

b. STEEL σ-ε CURVE

GIVEN:

$E_c = 4.15 \times 10^6$ PSI

$E_s = 29.0 \times 10^6$ PSI

$f'_c = 5500$ PSI

$\nu = 0.15$

ASSUMED:

$f'_t = 550$ PSI

$\varepsilon_u = 0.004$ IN/IN

$\varepsilon_{ut} = 0.000663$ IN/IN

$f_y = 60000$ PSI

$\varepsilon_{cu} = 2f'_c/E_c$

CREEP AND SHRINKAGE FROM ACI COMMITTEE CURVES

c. MATERIAL PROPERTIES GIVEN AND ASSUMED

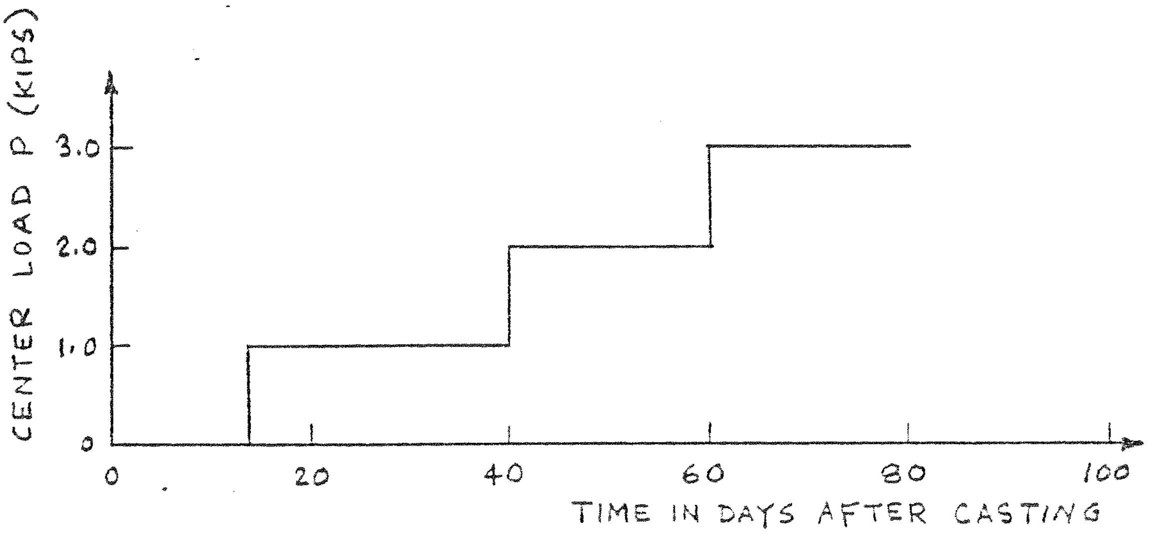

d. LOAD HISTORY FOR THE SLAB ANALYSIS

FIG. 5.22 EXAMPLE 3 - MATERIAL PROPERTIES AND LOAD HISTORY FOR ANALYSIS formulas are used to calculate the creep and shrinkage strains.

Figure 5.22d shows the load history applied to the slab. A load of 1.0 kip is applied at 14 days after casting. This is kept constant for 26 days when the load is increased to 2.0 kips. The load is sustained for 20 more days and then another 1.0 kip of load is added. The total 3.0 kip load is kept on the slab for another 20 days.

For the instantaneous load analysis, the following load steps are used: first, 1.0 kip load is applied in 1 increment; second, 1.0 kip load in 3 increments; third, 1.0 kip load in 6 increments; and fourth, 1.0 kip load in 8 increments. This scheme of load steps is followed to take into account the increasing nonlinearity of the slab behavior with higher loads.

Figure 5.23 presents the load-deflection curve at node 12 obtained from the present analysis. Also presented are the experimental load-deflection curve and the theoretical curve obtained by Lin [1.26] using a 3 x 3 mesh and similar concrete properties in tension. The concrete properties in compression, however, are different as Lin used an elasto-perfectly plastic model with no biaxial effects while in the present study, a series of parabolic curves dependent on biaxial stress ratio are used.

It is found that the deflections are underestimated at the earlier post-cracking stage but match well with the experimental curve at the later stage. Unfortunately, the experimental curve is available only up to a load of P = 3.0 kips and so the behavior near the ultimate stage cannot be compared. The difference in the initial post-cracking behavior, as examined by Lin in detail, is due mainly

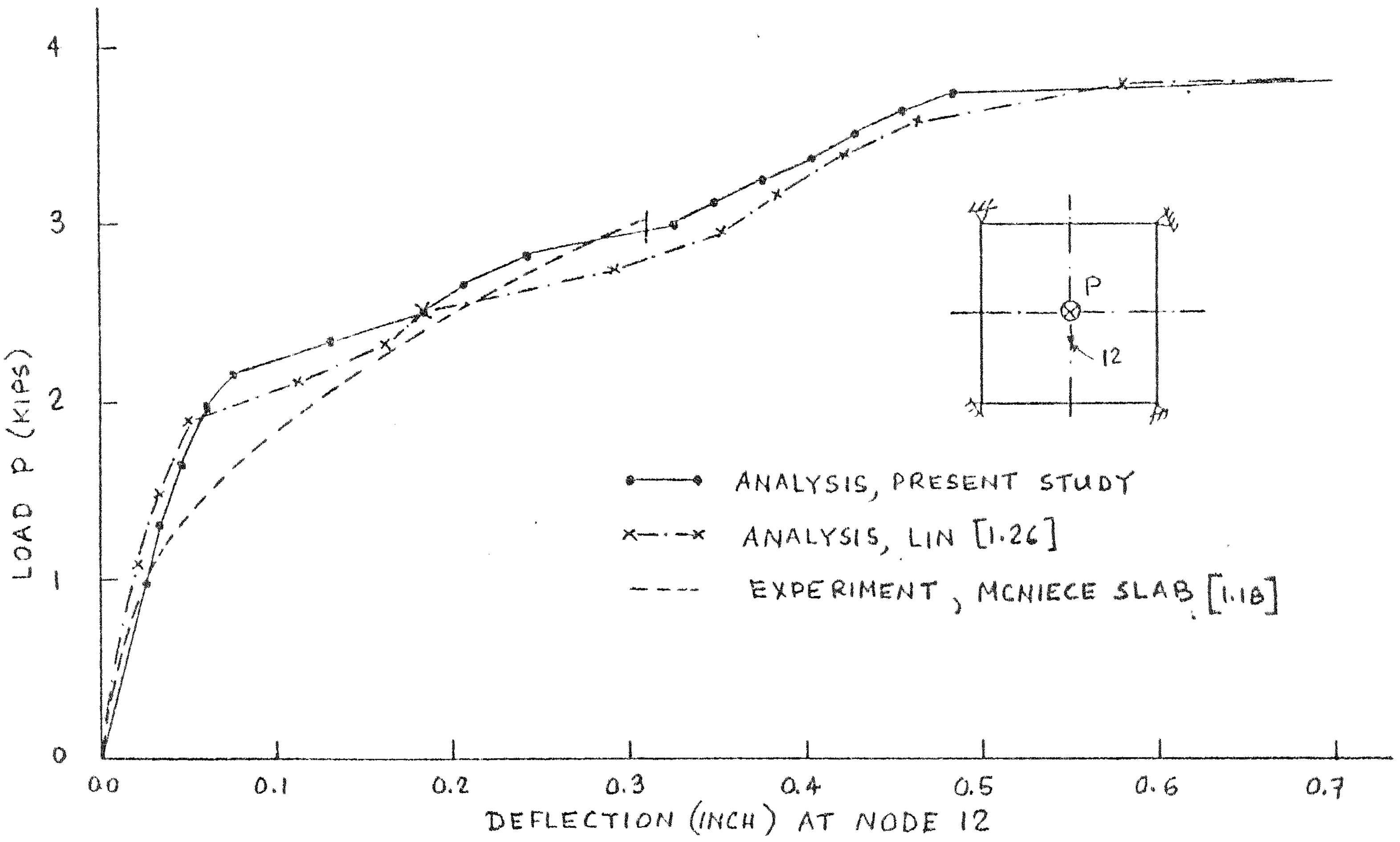

FIG. 5.23 EXAMPLE 3 - EXPERIMENTAL AND ANALYTICAL LOAD-DEFLECTION CURVES AT NODE 12 DUE TO INSTANTANEOUS LOAD NOT INCLUDING CREEP AND SHRINKAGE EFFECTS

to the magnitude of the concrete tensile strength assumed in the analysis and the tension stiffening effect. The two theoretical curves converge at the ultimate range which implies that the ultimate response is not very sensitive to the concrete model chosen in compression. This is because the slab is rather under-reinforced and the yielding of steel is responsible for the large displacements near 4.0 kips load.

Figure 5.24 shows the crack patterns in the bottom layer due to instantaneous loading. The dotted lines are the yield line patterns formed by the cracking in each element. At P = 3.875 kips, the load-deflection curve becomes almost horizontal. Extensive cracking occurs and steel yields as shown in Fig. 5.24b.

Figure 5.25 shows the deflection history at node 12 due to the assumed load history. In the 26 days following the application of 1.0 kip load at 14 days after casting, the deflection at node 12 increases by 100% due to creep and shrinkage effects. In the 20 days following the application of 2.0 kips load at 40 days after casting, the deflection increases by 64% while another 11% increment is observed at the end of 20 days following the application of 3.0 kips load. This illustrates the decreasing rate of creep and shrinkage deflections due to passage of time after loading and aging effects.

Figure 5.26 compares the instantaneous and time-dependent load-deflection curves at node 12. It is interesting to note that the stiffness of the slab deteriorates due to creep and shrinkage effects. However, the deterioration is not very significant for this particular load history.

Figure 5.27 presents the crack patterns at the bottom layer of the slab due to sustained loading. The patterns are similar to those

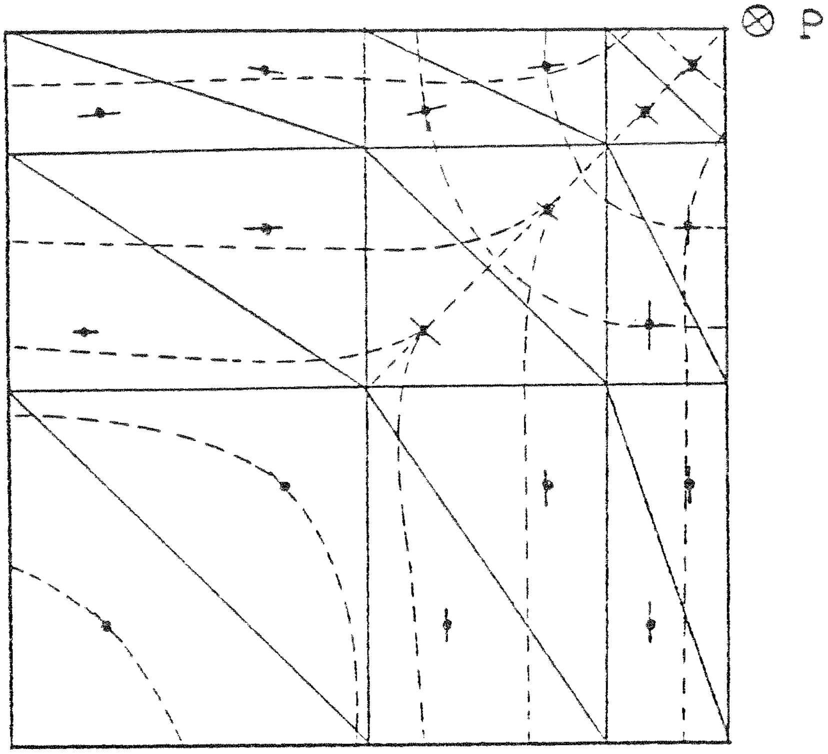

a. CRACK PATTERN, SHORT TERM LOAD P= 3.0 KIPS

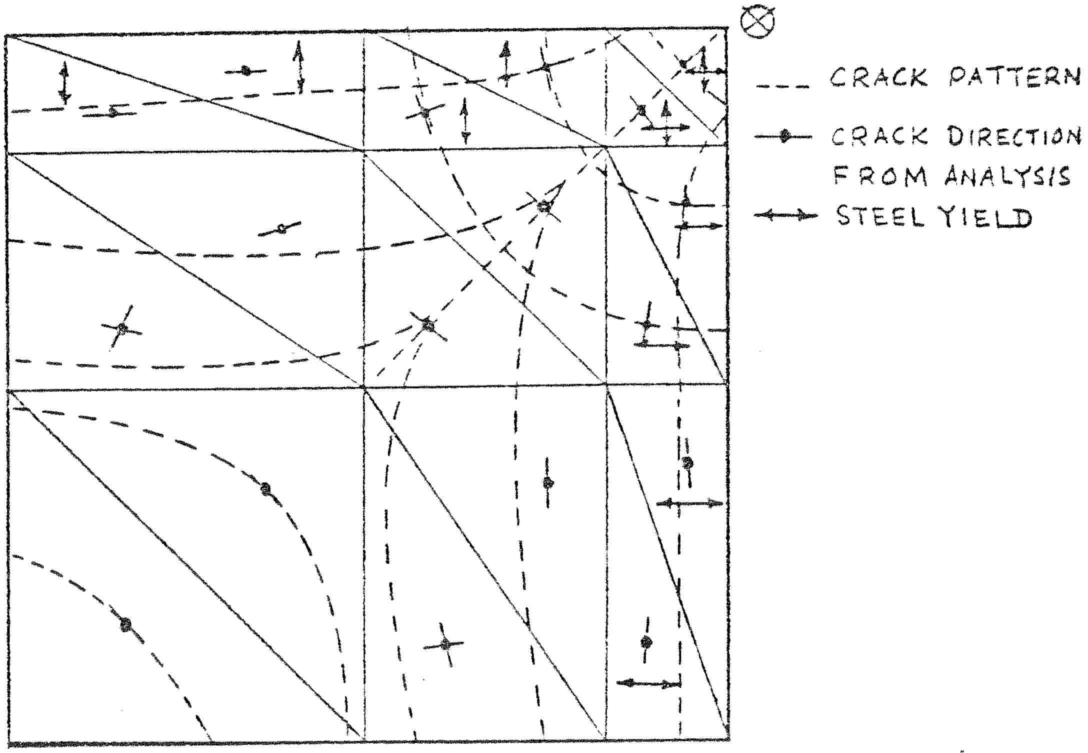

b. CRACK PATTERN, SHORT TERM LOAD P= 3.875 KIPS

FIG. 5.24 EXAMPLE 3 - CRACK PATTERNS AT THE BOTTOM LAYER DUE TO SHORT TERM LOAD

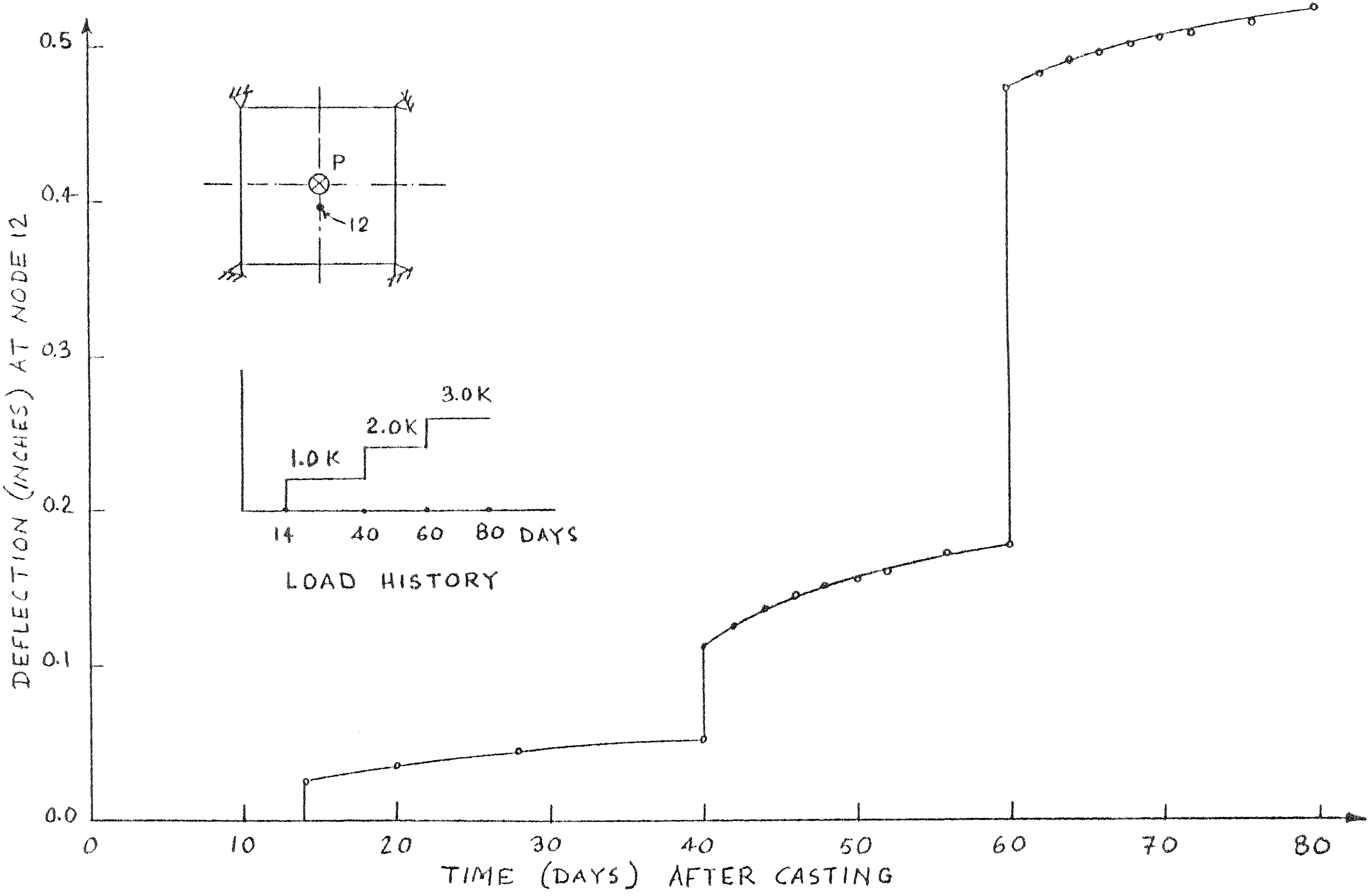

FIG. 5.25 EXAMPLE 3 - DEFLECTION HISTORY AT NODE 12 DUE TO TIME-DEPENDENT LOAD HISTORY INCLUDING CREEP AND SHRINKAGE EFFECTS

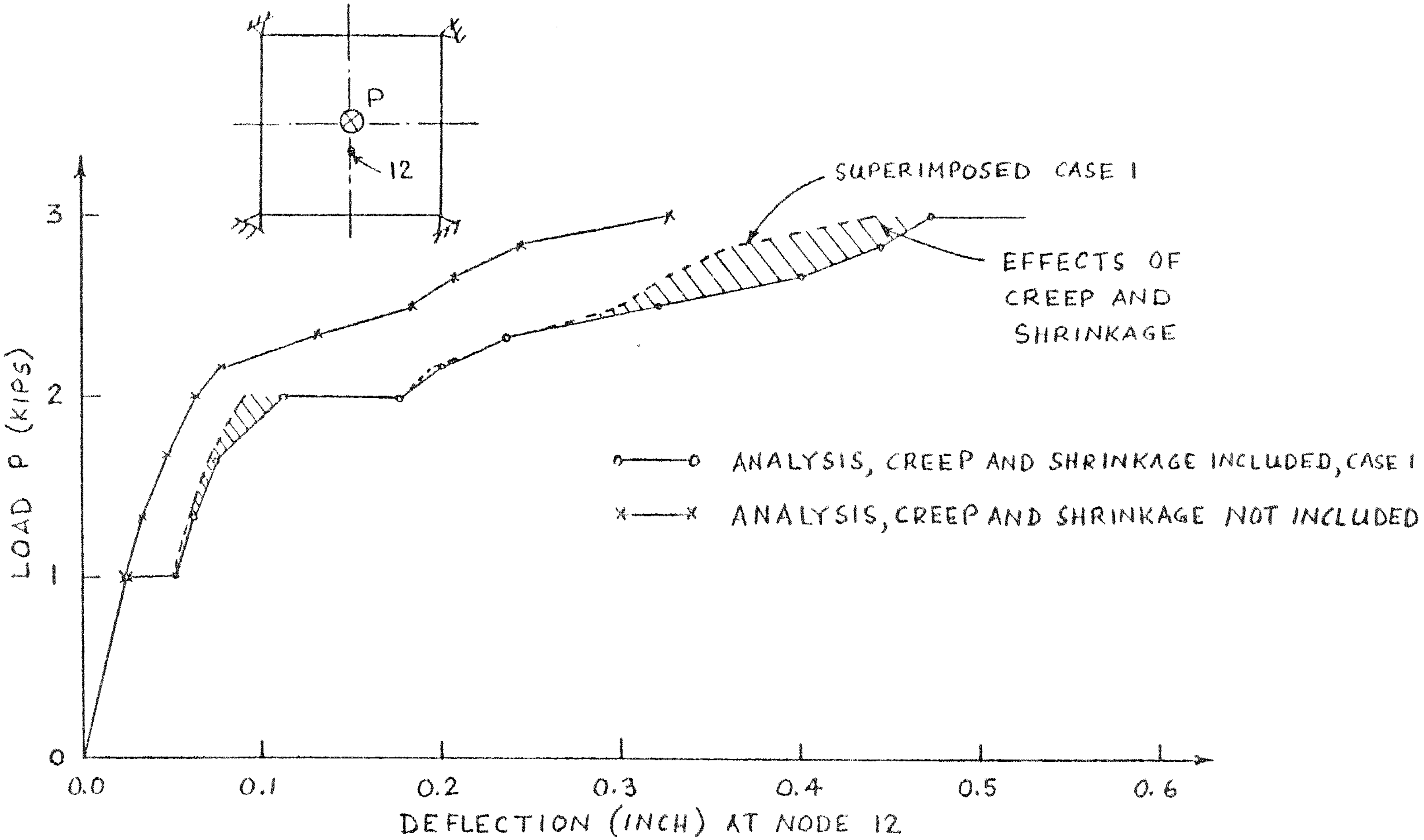

FIG. 5.26 EXAMPLE 3 - LOAD-DEFLECTION CURVES FOR SHORT TERM LOAD AND TIME-DEPENDENT

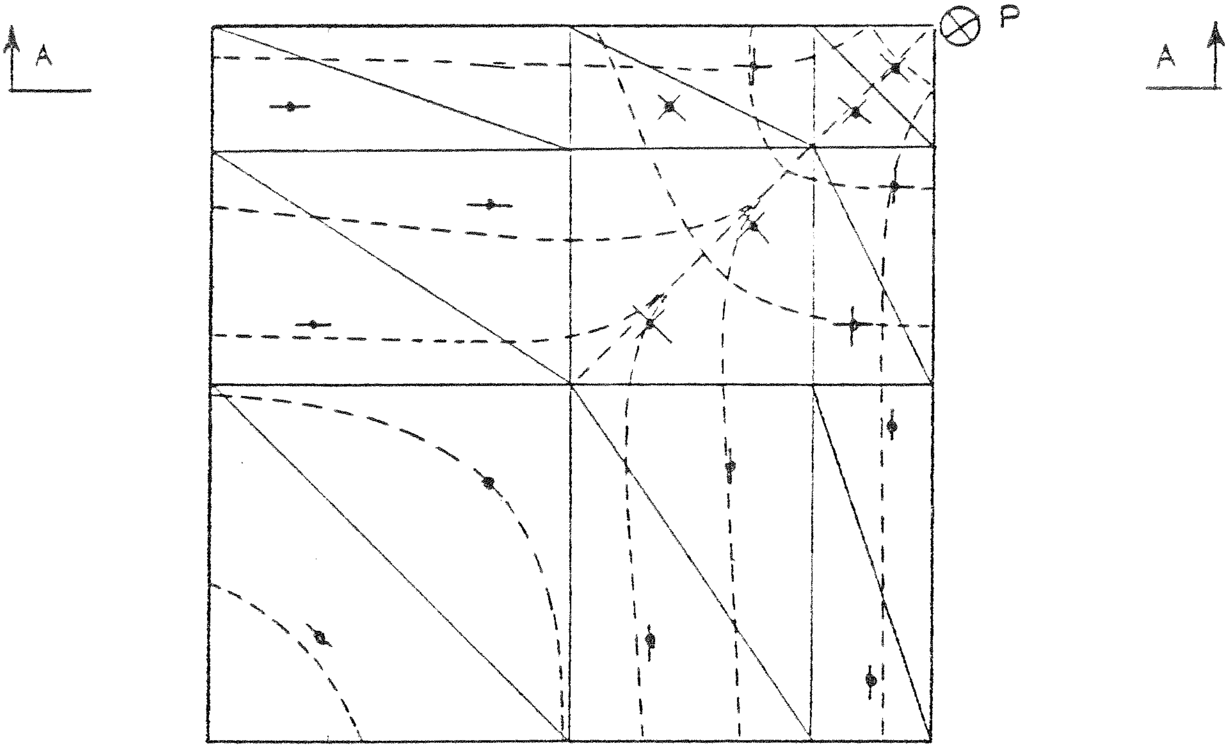

a. CRACK PATTERN AT 60 DAYS, P=3.0KIPS

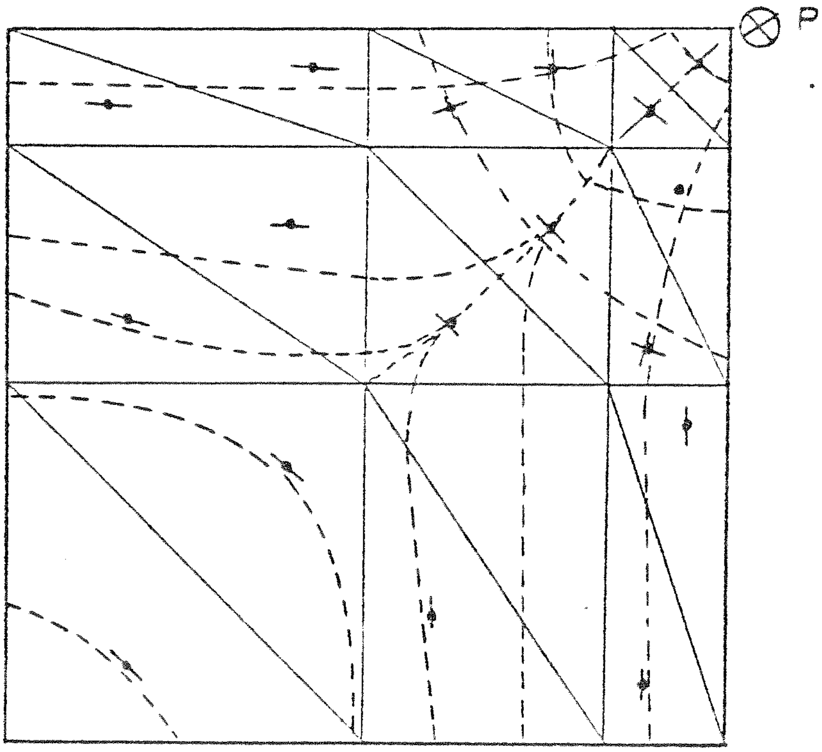

b. CRACK PATTERN AT 80 DAYS, P= 3.0 KIPS

FIG. 5.27 EXAMPLE 3 - CRACK PATTERNS OF THE BOTTOM LAYER FOR TIME-DEPENDENT LOAD HISTORY due to instantaneous loading, Fig. 5.24. Figure 5.28 shows the cracking across the depth at midspan and the cracking increases due to sustained loading as the differences between Figs. 5.28a and 5.28b and those between Figs. 5.28c and 5.28d illustrate.

Figure 5.29 presents the concrete stress profile across depth at point B of the midspan section AA at various times. Under 1.0 kip load, the stress profile is linear. When this load is sustained from 14 days to 40 days after casting, i.e. for 26 days, the only change is a shift of the stress profile to the tension side. This shift occurs mainly due to shrinkage effects which are predominant in the initial period after loading. Due to shrinkage, concrete tends to shrink and the steel reinforcement tries to prevent concrete from shrinking. This produces compressive forces in the steel and tensile forces in the concrete. The concrete stress profile, as a result, shifts to the tension side. This is more apparent from Figs. 5.30 and 5.31 which present the net compressive and tensile force distribution at midspan in the concrete and steel reinforcement, respectively. In Fig. 5.30, the net concrete forces are on the compression side under the instantaneous load of 1.0 kip. At 40 days after casting, the net concrete forces, however, have become tensile due to shrinkage effects as discussed above. The steel reinforcement forces, Fig. 5.31, on the other hand, have changed from tension to the compression side.

Creep effects begin to dominate under higher stresses. Under a load of 3.0 kips, considerable redistribution of concrete stresses take place as shown in Fig. 5.29. The concrete compressive stresses at the top layers unload and the neutral axis shifts towards the tensile steel reinforcement, bringing tension zones under compression.

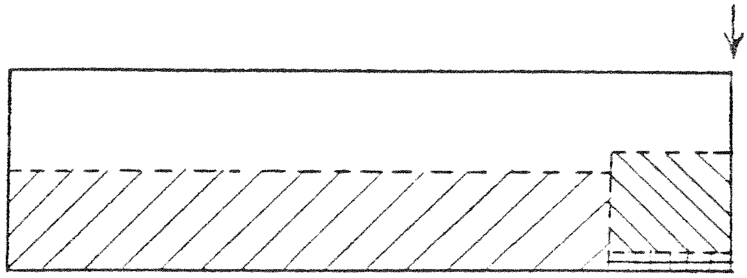

a. AT 40 DAYS, P = 2.0 KIPS

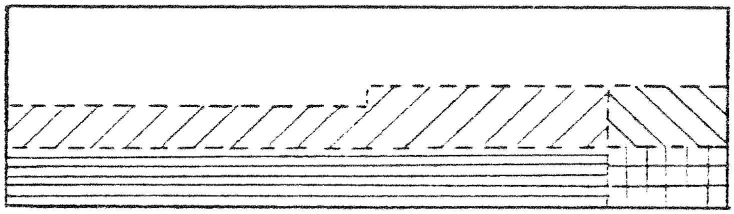

b. AT 60 DAYS, P = 2.0 KIPS

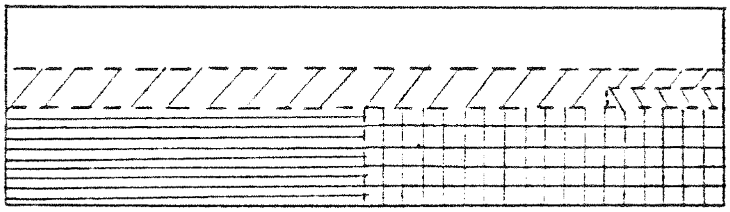

c. AT 60 DAYS, P = 3.0 KIPS

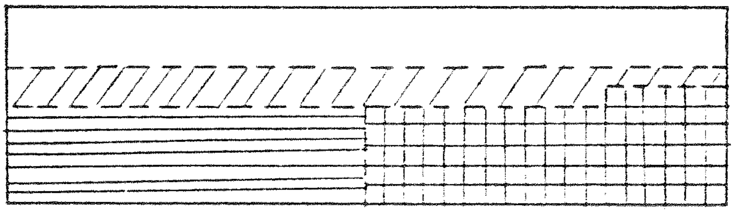

d. AT 80 DAYS, P = 3.0 KIPS

▨ CRACKED IN 1-DIRECTION

▧ CRACKED IN 2-DIRECTIONS

☰ COMPLETELY CRACKED IN 1-DIRECTION

⊞ COMPLETELY CRACKED IN 2-DIRECTIONS

FIG. 5.28 EXAMPLE 3 - CRACK PATTERN ACROSS DEPTH OF THE MIDSPAN SECTION AA FOR LOAD HISTORY

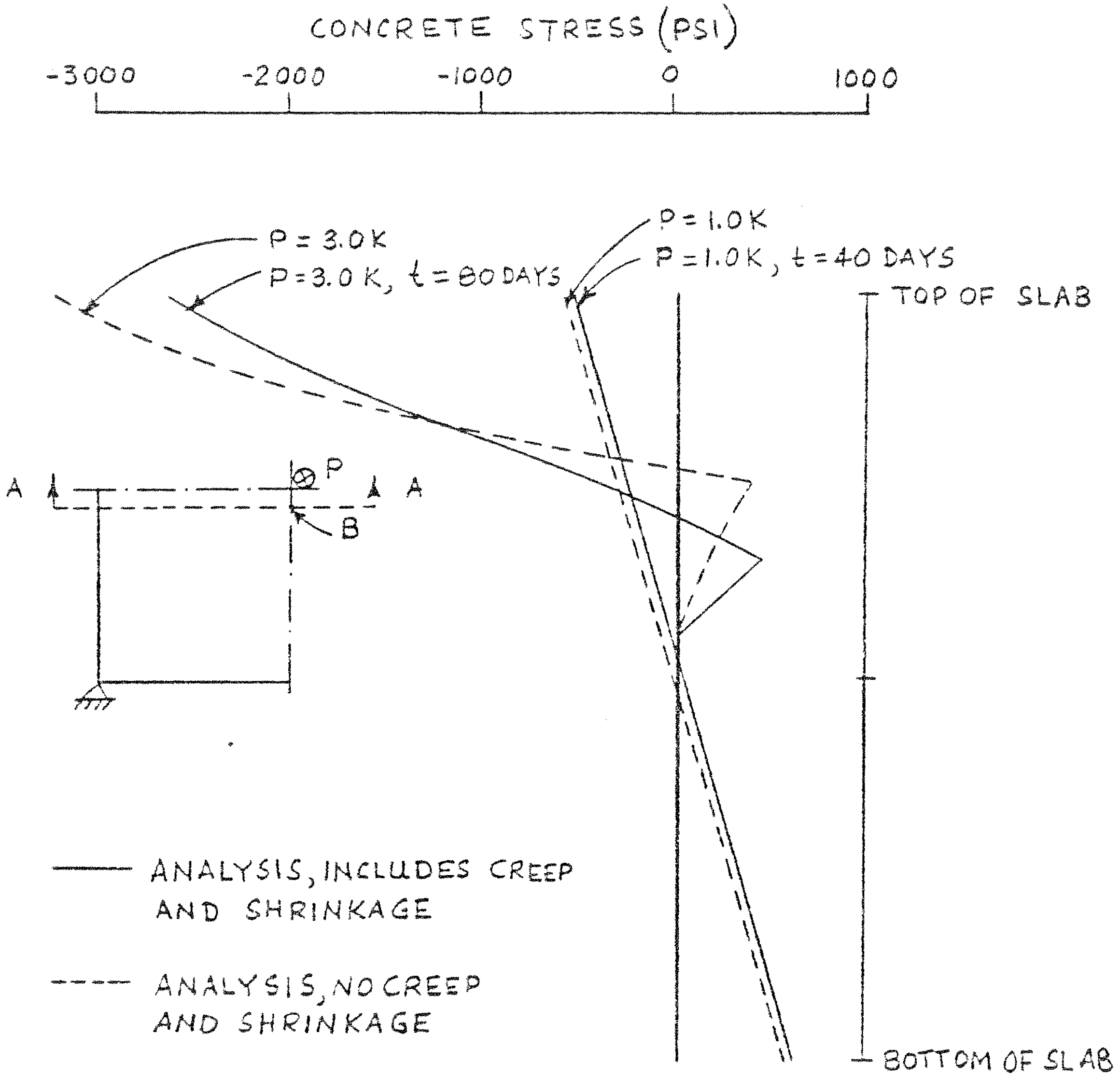

FIG. 5.29 EXAMPLE 3 - STRESS PROFILES AT POINT B OF MIDSPAN SECTION AA

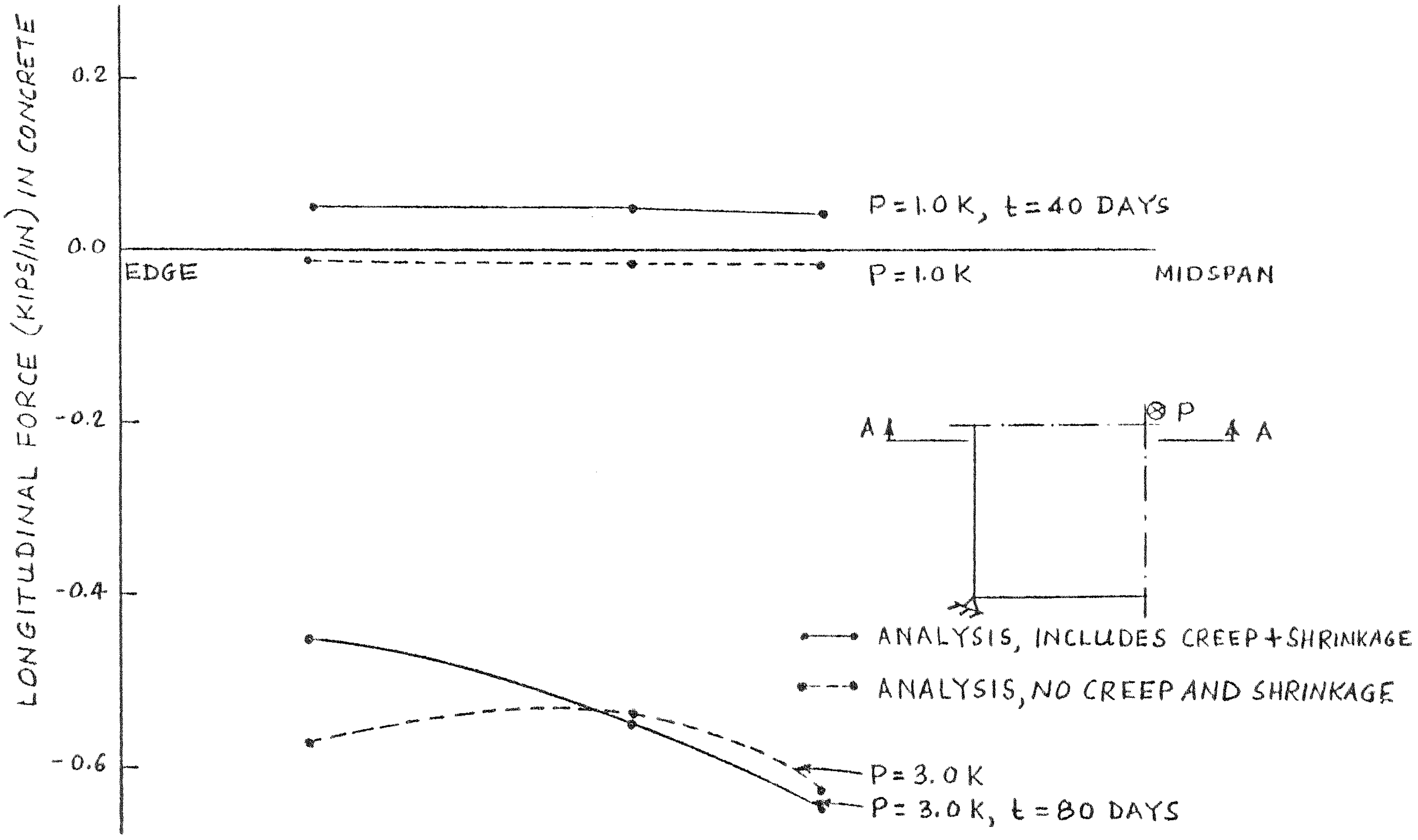

FIG. 5.30 EXAMPLE 3 - TRANSVERSE DISTRIBUTION OF LONGITUDINAL FORCE IN CONCRETE ACTING ON MIDSPAN SECTION AA

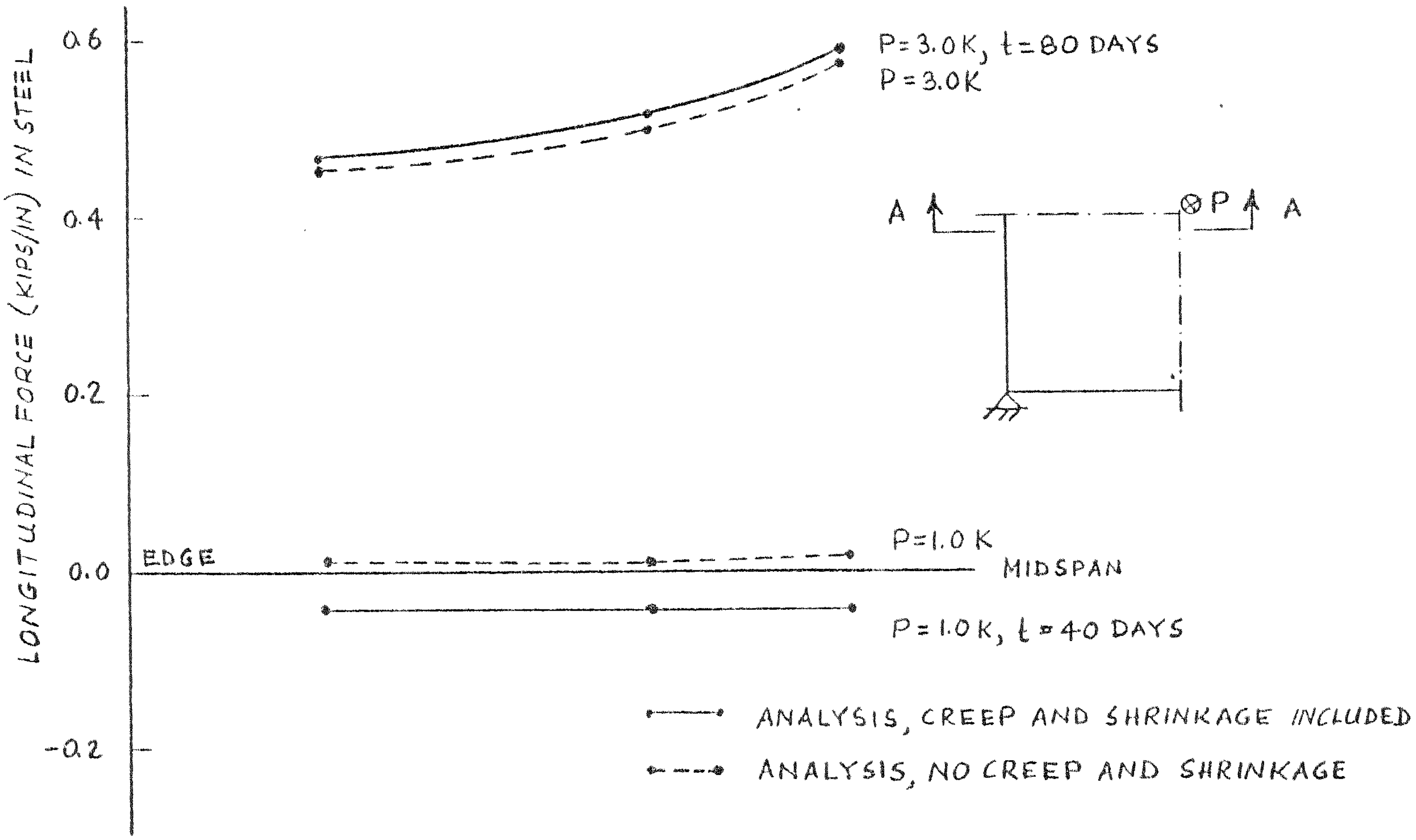

FIG. 5.31 EXAMPLE 3 - TRANSVERSE DISTRIBUTION OF LONGITUDINAL FORCE IN STEEL ACTING ON MIDSPAN SECTION AA

This is qualitatively similar to the behavior of the beam specimen under high stresses as observed in Example 1. The tensile forces in the steel reinforcement, Fig. 5.31, do not increase much as the moment-arm between the tensile and compressive forces do not change significantly.

5.5 Example 4 - Gable Hyperbolic Paraboloid Shell

The use of hyperbolic paraboloid (HP) shell roofs is common due to their elegant appearance, inherent high strength, and capability of spanning over large spans without intermediate supports. The last requirement is very important for such civic facilities as sports arenas, gymnasiums, convention halls, opera houses, theatre halls, etc. It is to be noted that these facilities are used by large gatherings of people and as such, particular emphasis has to be placed on their structural safety and serviceability.

One of the most common types of HP shell roofs in use is the gable HP shell roof as shown in Fig. 5.32.

According to the membrane theory, which is generally used for designing the gable HP roofs, under a uniformly distributed load, the shell proper is in a state of pure shear parallel to the straight line generators. This causes equal principal tensile and compressive stresses in the diagonal directions. Steel reinforcement is provided to carry the principal tension. Generally, the reinforcement is placed in two mutually perpendicular directions along the straight line generators for constructional simplicity. The shell thickness is determined from the minimum thickness required to safely withstand the compressive force. The elements of the supporting structure of the shell, namely, the crown and edge beams, are designed for the combined effects of the bending produced by self-weight and the accumulated

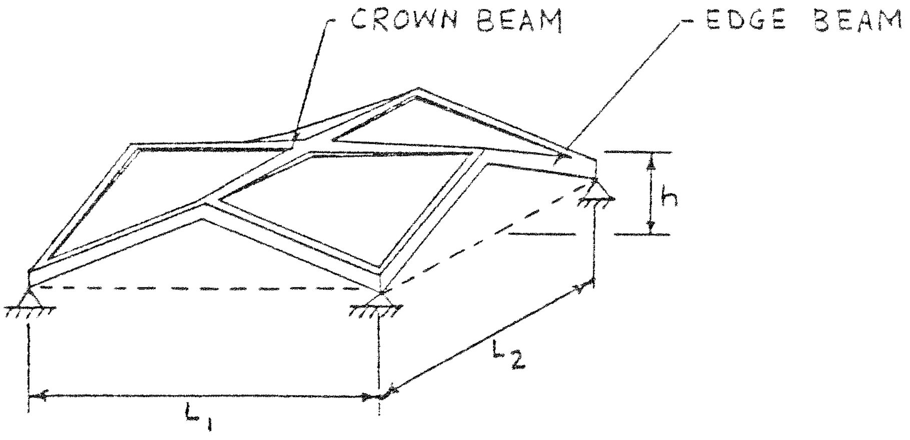

a. GENERAL VIEW

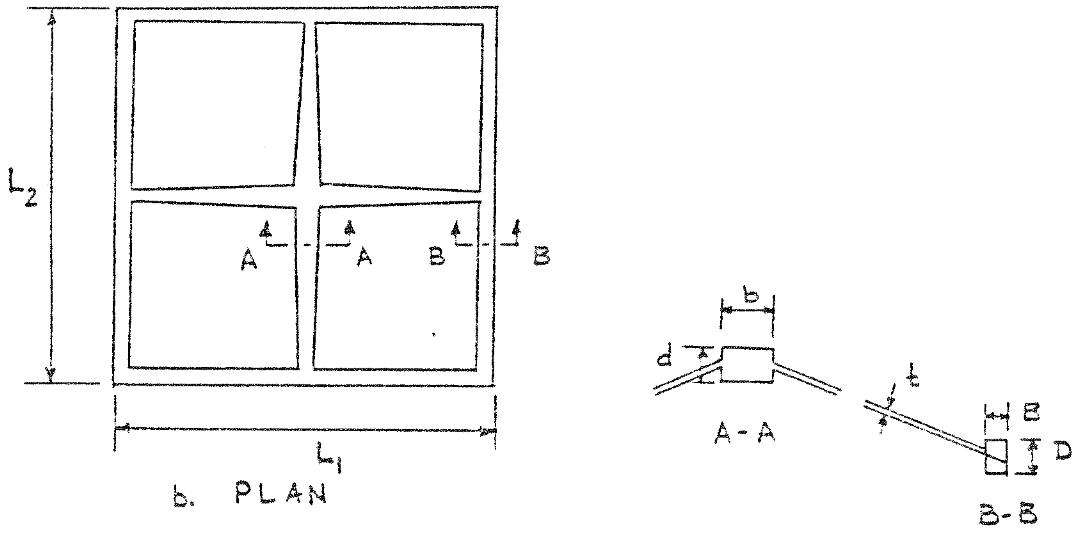

b. PLAN

d. SECTIONS

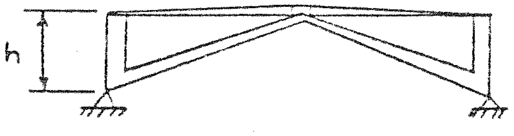

c. ELEVATION

FIG. 5.32 EXAMPLE 4 - GABLE HYPERBOLIC PARABOLOID SHELL compression transferred from the shell. Time-dependent environmental effects such as creep, shrinkage, temperature fluctuations, etc., are usually not considered, or if so, only in an approximate manner. However, the failure of an HP gable shell roof in Virginia, seven years after its construction [5.3], and the large vertical deflections at the crown (approximately 18 inches) observed in two similar roofs in the same area, underline the importance of the application of realistic and rational models, load conditions and methods for the analysis and design of such structures.

In the present study, a gable HP shell was analyzed to achieve primarily two objectives. First, the behavior of the gable HP shell under higher loads including the ultimate is investigated. Second, the response of the structure to creep and shrinkage effects is obtained in order to determine the long-term serviceability of such a structure. The study of the gable HP shell undertaken in this example can be divided into three main phases.

In the first phase, elastic analyses are performed, assuming uncracked concrete sections without reinforcement, to check the validity and reliablity of the model used to represent reality. To this end, two gable HP shells, from a series of such shells analyzed by Schnobrich [5.4,5.5], are picked for analyses.

The shells are 80' x 80', i.e., L1 = 80' and L2 = 80'. The shell thickness is 3 inches, i.e., t = 3". The edge beams are concentric with the shell mid-surface and are 12" x 16", i.e., B = 12" and D = 16". The crown beams are concentric with the shell mid-surface. The crown beam sizes of one specimen, henceforth referred to as gable A, are 8" x 24", i.e., b = 24" and d = 8". The crown beam sizes of the other specimen, henceforth referred to as gable B, are 12" x 48", i.e., b = 48" and d = 12".

Since only symmetric loads are considered, the analysis can be performed on 1/8th of the gable shell by taking advantage of symmetry. The mesh size chosen is 8 x 8. Figure 5.33 illustrates the mesh and nodes. Triangular shell elements are chosen to represent both the shell and the beams. This means that the beams, both edge and crown, are concentric with shell mid-surface. This is a departure from Schnobrich's analyses where the crown beams are assumed above the shell surface. Concrete properties are chosen to be the same as used by Schnobrich. Concrete modulus of elasticity is taken as 3×10^6 psi while Poisson's ratio is chosen as 0.15. Schnobrich used a 8 x 8 mesh but his finite elements were much more refined. For example, he uses a 27 DOF (degrees-of-freedom) triangular shell element and a 16 DOF rectangular beam element. In the present analyses a 15 DOF triangular shell element has been used for both the shell and the beams. The less refined shell element is chosen to limit the computer cost which may become prohibitive for a time-dependent step-by-step analysis where a large number of solutions are needed to trace the response history over a reasonable period of time. The elastic analyses are, therefore, performed to compare the results with those obtained by Schnobrich to see how accurately the current model is predicting the shell behavior.

Figures 5.34 to 5.39 compare some of the results obtained by the present analysis for gable A under dead load. The correspondence with Schnobrich's data is excellent considering the fact that higher order elements are used in Schnobrich's analyses. The discrepancy of the moments near the support, Fig. 5.38, is due to the inability of the present model to consider torsional rigidity. An interesting point to note is the large overestimation of the axial force in the

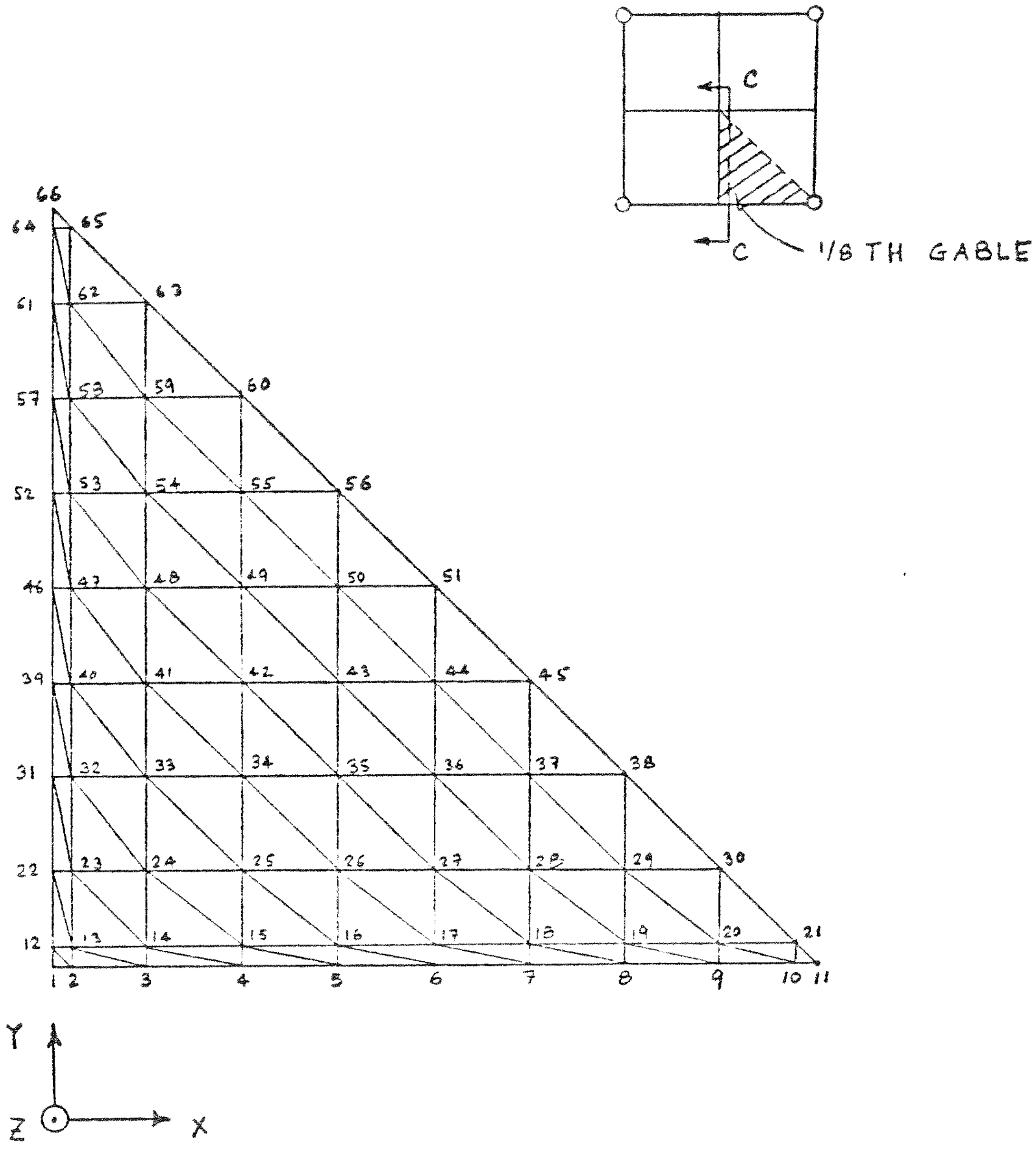

FIG. 5.33 EXAMPLE 4 - FINITE ELEMENT IDEALIZATION OF ONE-EIGHTH OF THE GABLE HP SHELL

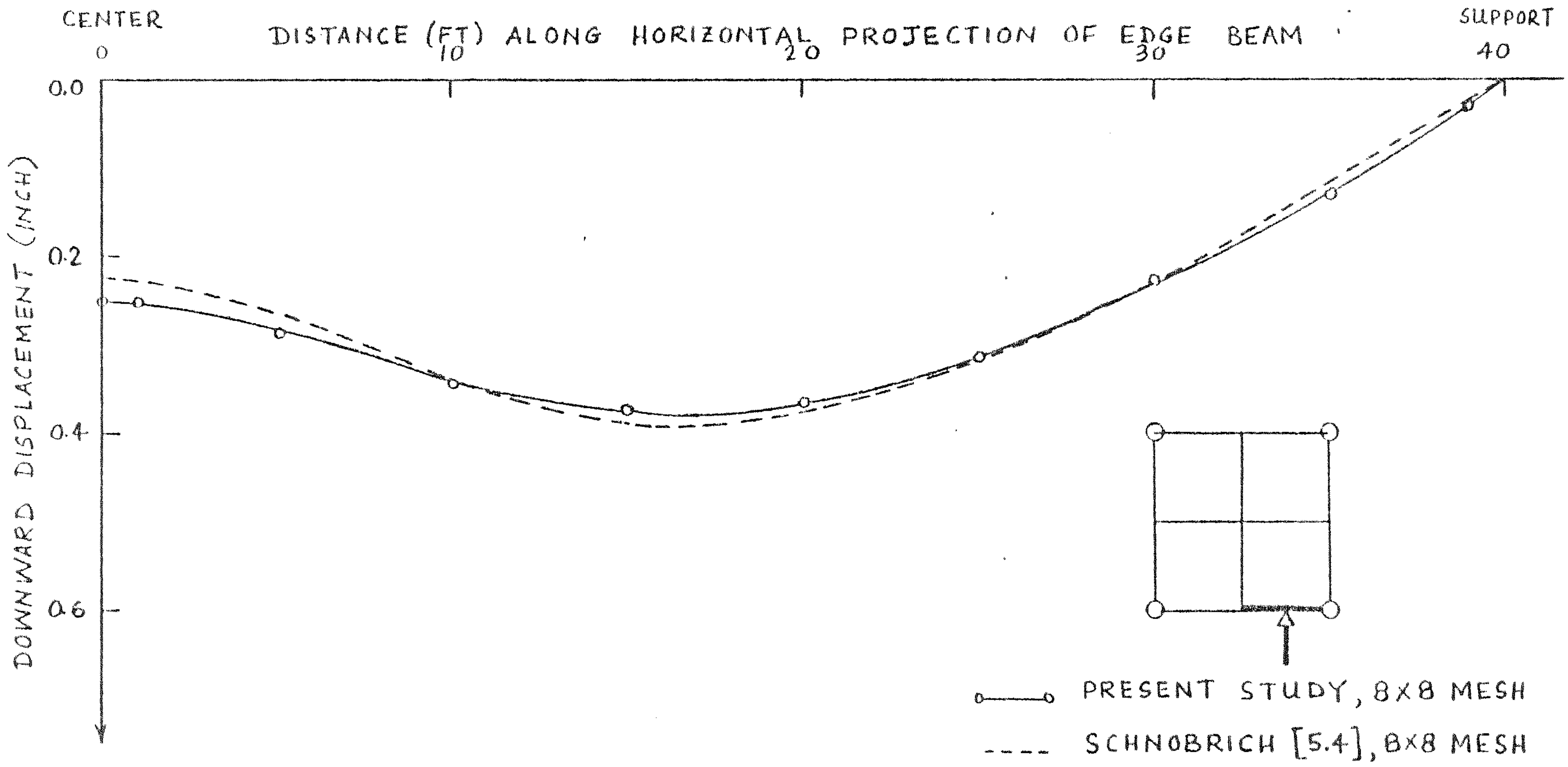

FIG. 5.34 EXAMPLE 4 - VERTICAL DISPLACEMENT PROFILE OF THE EDGE BEAM OF GABLE A FOR DEAD LOAD ELASTIC ANALYSIS

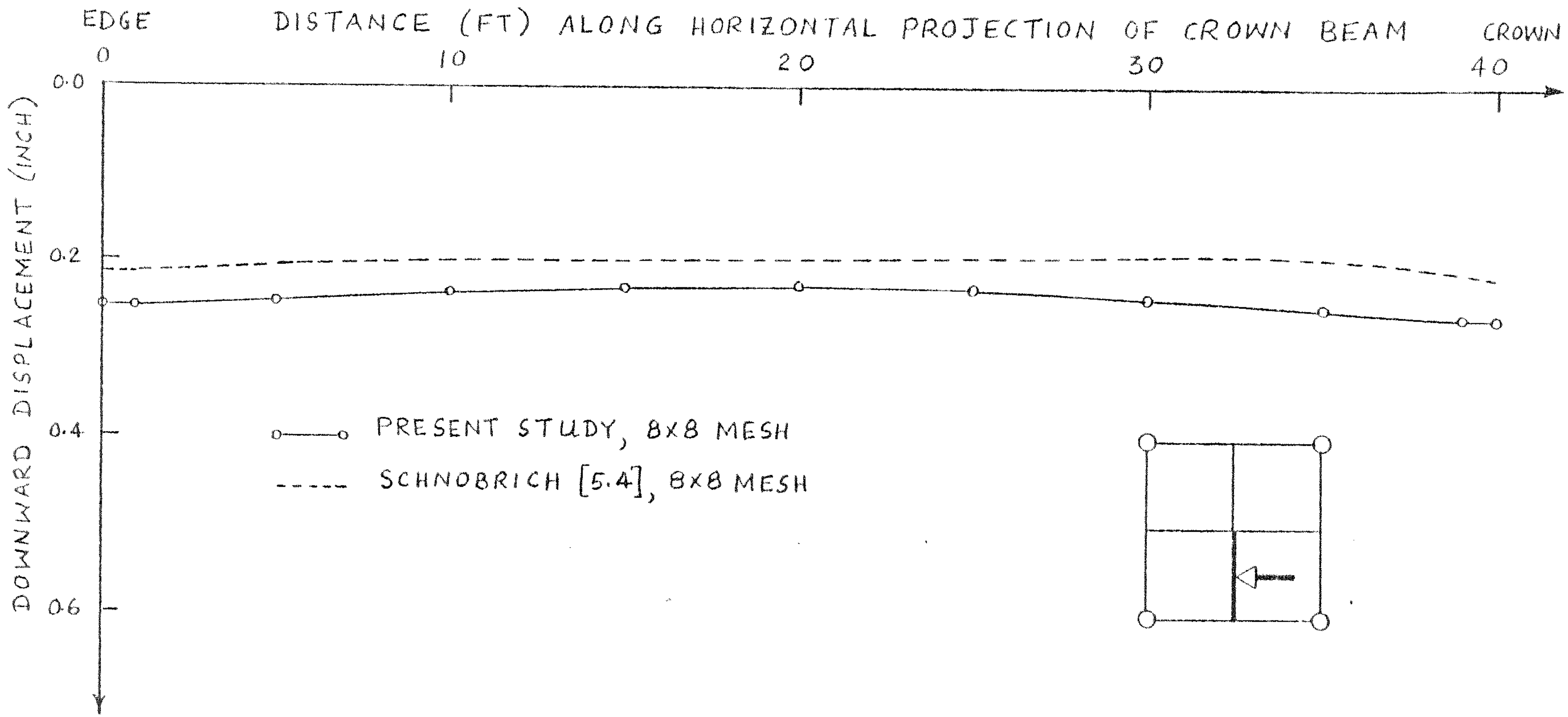

FIG. 5.35 EXAMPLE 4 - VERTICAL DISPLACEMENT PROFILE FOR THE CROWN BEAM OF GABLE A FOR DEAD LOAD ELASTIC ANALYSIS

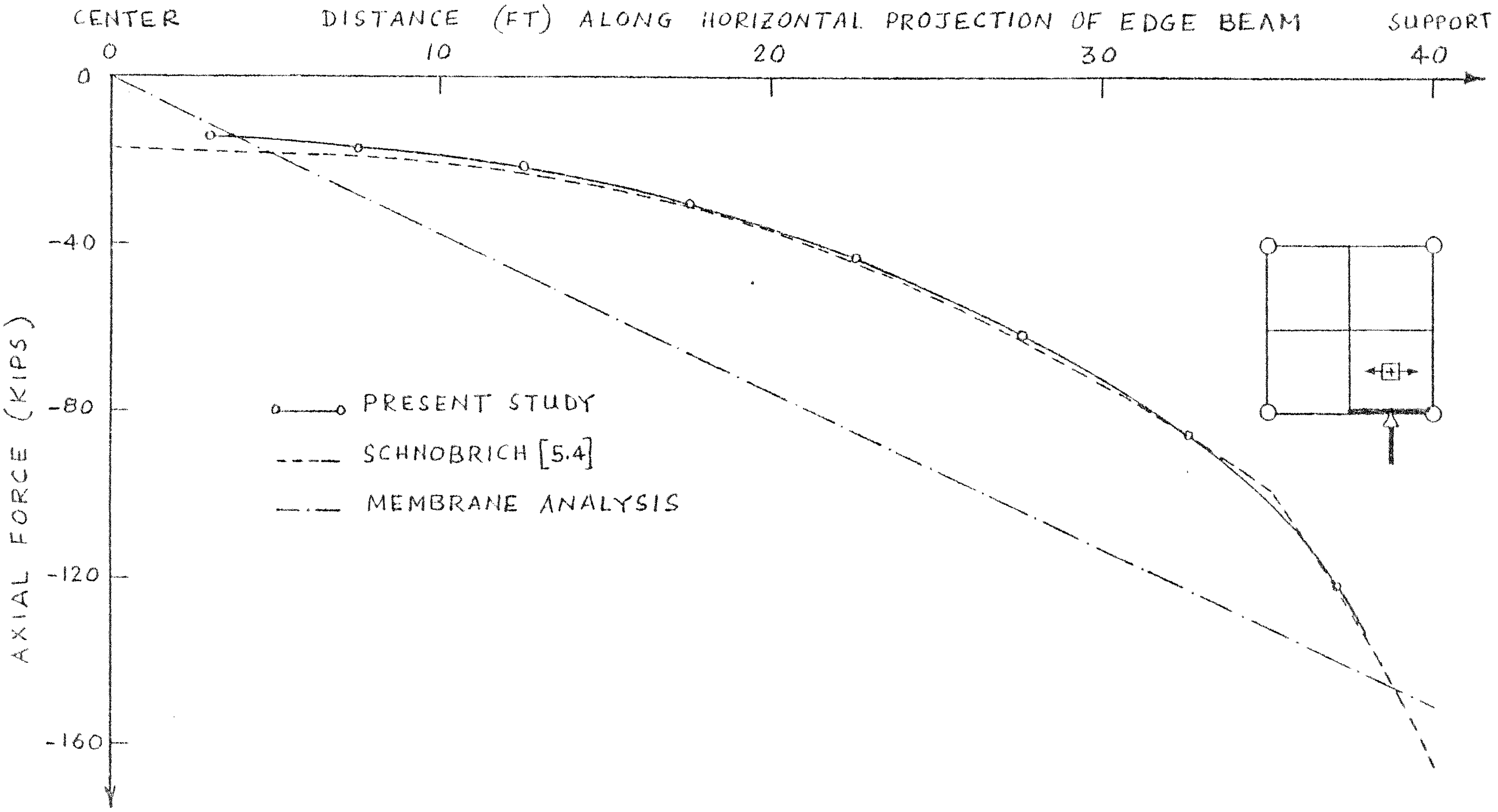

FIG. 5.36 EXAMPLE 4 - AXIAL FORCE DISTRIBUTION IN THE EDGE BEAM OF GABLE A FOR DEAD LOAD ELASTIC ANALYSIS

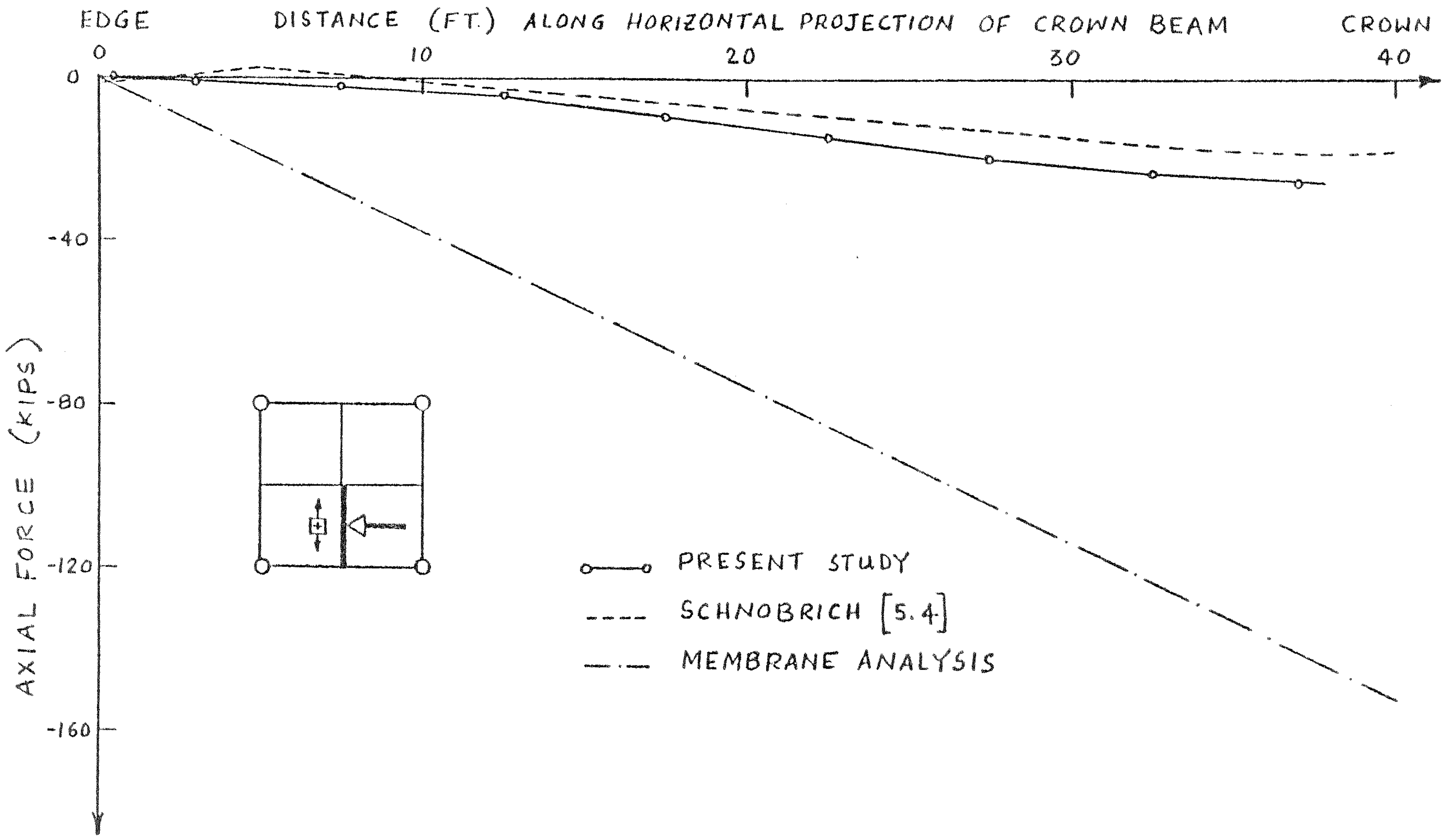

FIG. 5.37 EXAMPLE 4 - AXIAL FORCE DISTRIBUTION IN THE CROWN BEAM OF GABLE A FOR DEAD LOAD ELASTIC ANALYSIS

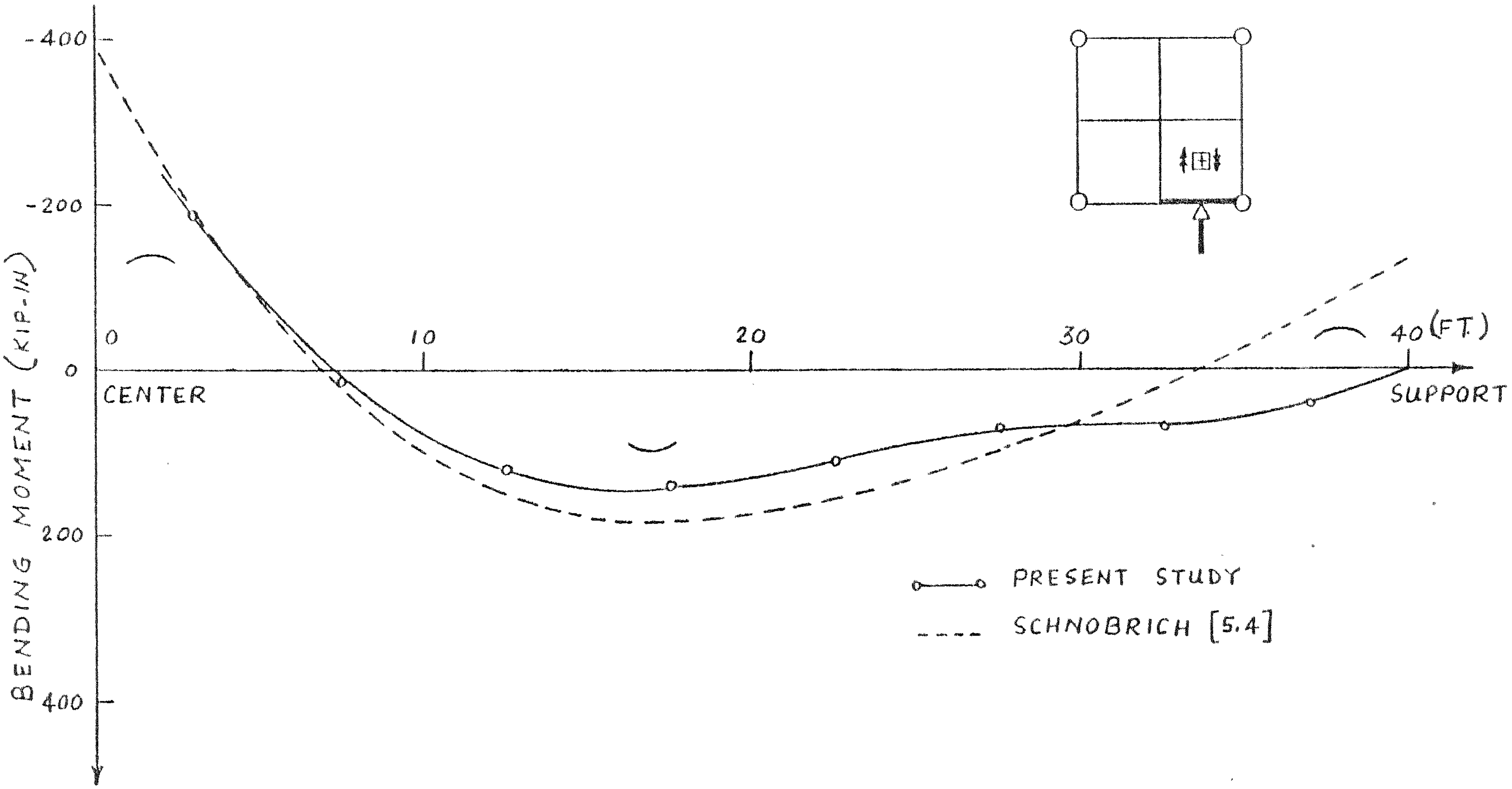

FIG. 5.38 EXAMPLE 4 - BENDING MOMENT DISTRIBUTION IN THE EDGE BEAM OF GABLE A FOR DEAD LOAD ELASTIC ANALYSIS

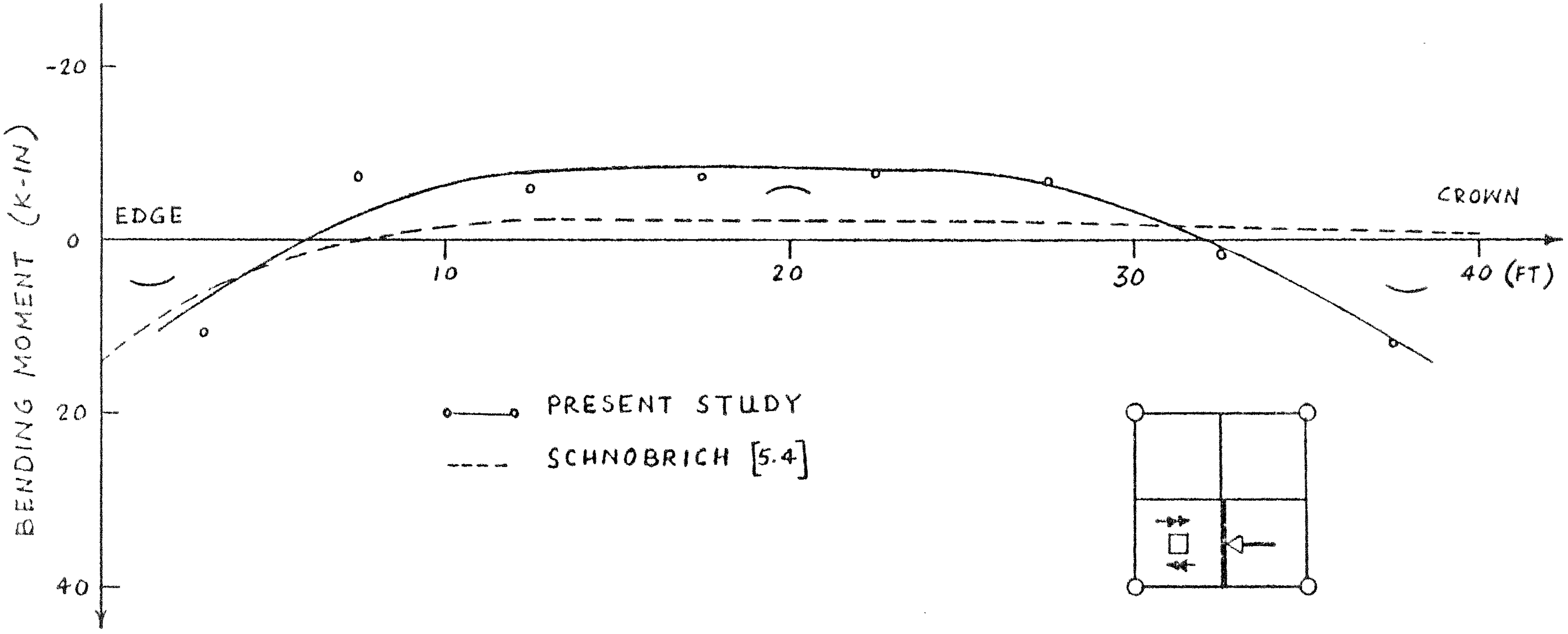

FIG. 5.39 EXAMPLE 4 - BENDING MOMENT DISTRIBUTION IN THE CROWN BEAM OF GABLE A FOR DEAD LOAD ELASTIC ANALYSIS

crown beam by the membrane analysis, Fig. 5.37. This would lead to larger crown beam sizes from design considerations than are actually needed. As will be shown later and as has been concluded by Schnobrich, larger crown beams may have deleterious effects on the overall performance of the gable shell roof.

Figure 5.40 illustrates the sensitivity of the crown beam vertical deflections to the dead load of the different components of the gable shell structure. The vertical deflections are very severe for the crown beam dead load alone. The dead loads in the shell and edge beams tend to reduce the vertical deflections. In fact, for gable A, the vertical deflections at the crown point for the dead load of the crown beam acting alone, is 2.4 times larger than the deflection due to dead load of the whole structure. It may be concluded from this that the vertical deflection of the crown beam is very much dependent on the size of the crown beam and the load placed on it. The vertical deflections of the edge beam are far less sensitive to the load placed on the edge beam alone (Fig. 5.41).

A static check is made for the dead load elastic analysis of gable A at section CC in Fig. 5.33. The results as summarized below show excellent correspondence. The force listed as tensile is actually the horizontal reaction at the support, while the compressive force is the integral of the stresses across section CC.

Force:	Tensile	203 kips	should be equal
	Compressive	203 kips	
	Error	0%	
Moment:	Internal	1622 k-ft.	should be equal
	External	1610 k-ft.	
	Error	1%	

To further illustrate the influence of the crown beam size on its deflection, the crown beam deflection profile for gable B (same as

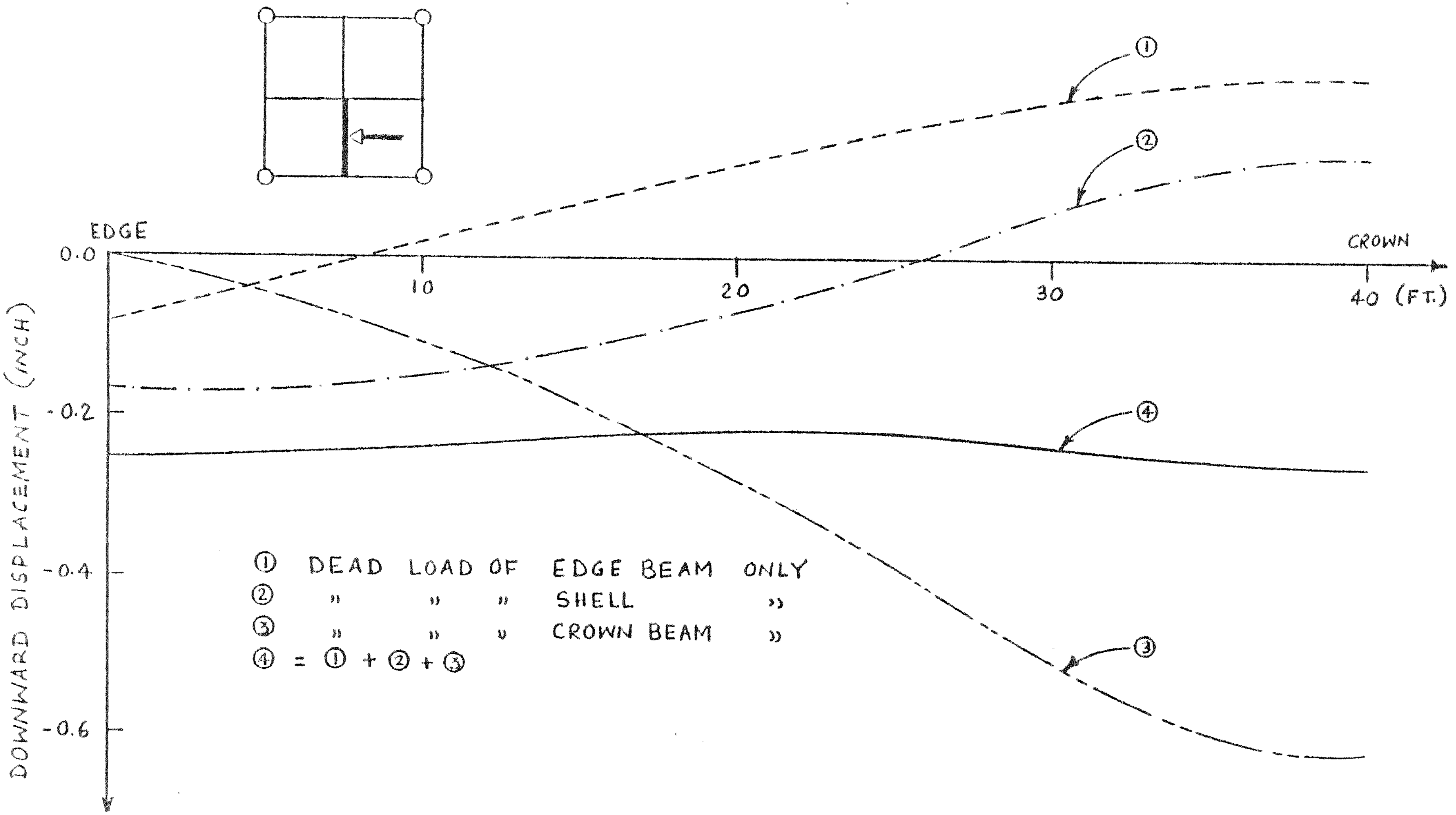

FIG. 5.40 EXAMPLE 4 - VERTICAL DISPLACEMENT PROFILES OF THE CROWN BEAM OF GABLE A FOR VARIOUS LOAD CONDITIONS

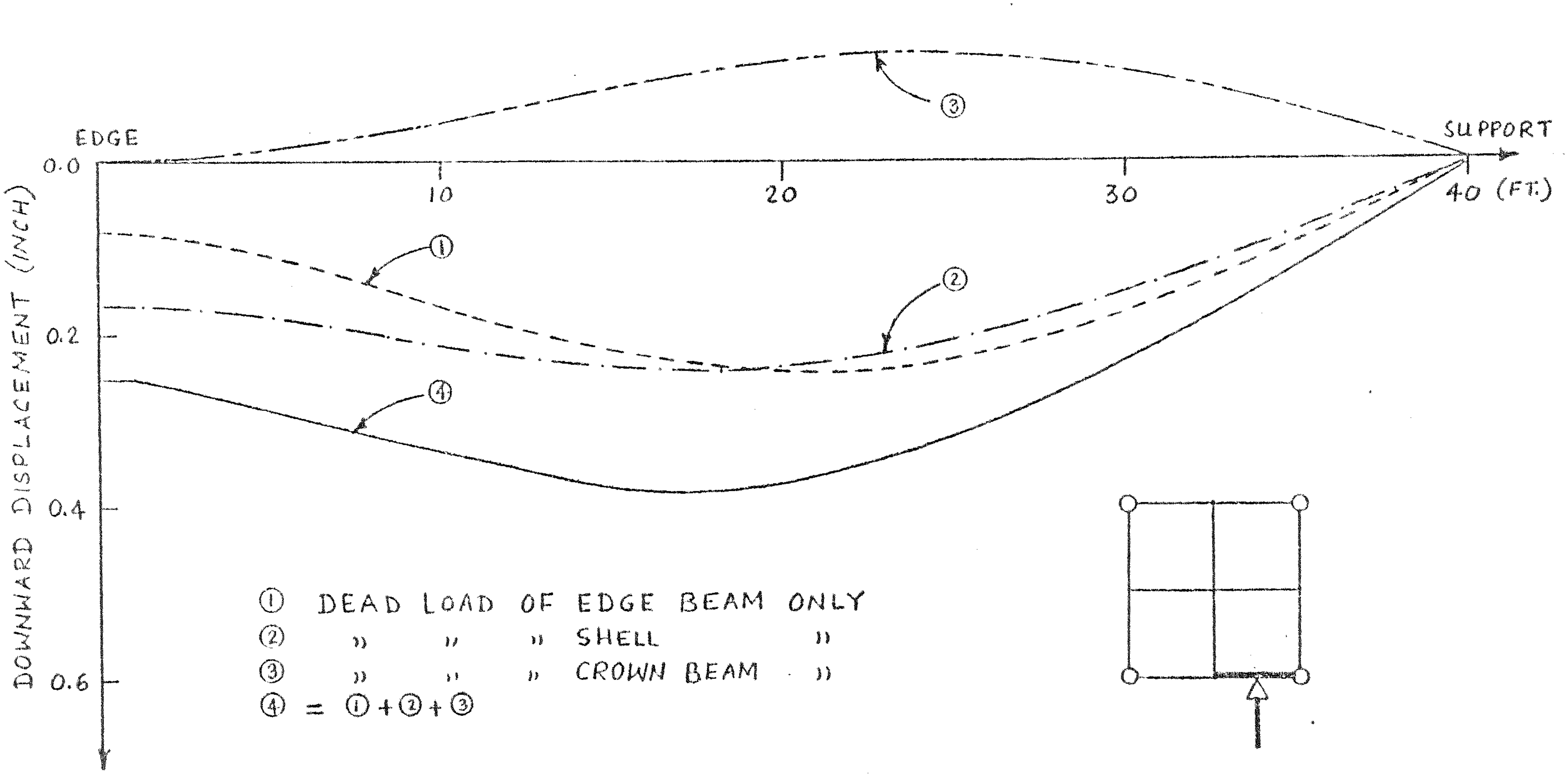

FIG. 5.41 EXAMPLE 4 - VERTICAL DISPLACEMENT PROFILES OF THE EDGE BEAM OF GABLE A FOR VARIOUS LOAD CONDITIONS

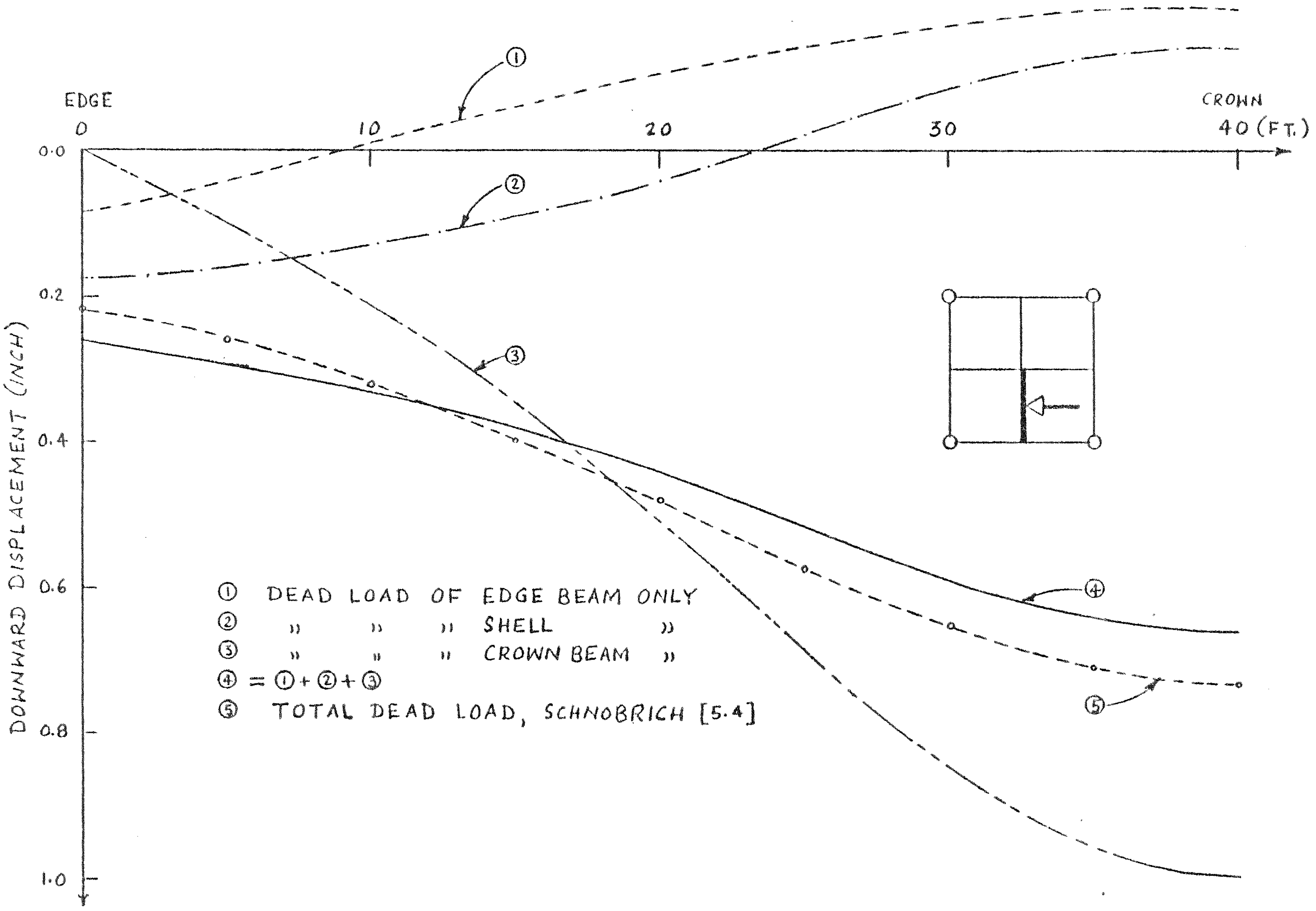

FIG. 5.42 EXAMPLE 4 - VERTICAL DISPLACEMENT PROFILES OF THE CROWN BEAM OF GABLE B FOR VARIOUS LOAD CONDITIONS

that for gable A, except a 12" x 48" crown beam instead of an 8" x 24" one is used) is plotted in Fig. 5.42. The vertical deflection at the crown is 2.5 times that for gable A.

In the second phase of the study, gable B has been analyzed to determine its ultimate load-carrying capacity. To this end, the gable has been designed by the membrane analysis and the steel reinforcement is put in as shown in Fig. 5.43. The layer systems, adopted for the edge and crown beams and for the shell proper, are also shown in Fig. 5.43. The entire gable is first analyzed for dead load and then multiples of 20 psf of uniformly distributed live load on the horizontal projection are added in the following way: 4, 1, 1, 0.5. At 6.5 times the live load, i.e., at a uniform live load of 130 psf over the entire gable shell, failure occurred.

Figure 5.44 presents the load-deflection curve at the crown point. The initial discontinuity of slope at the application of live load occurs because dead load is not uniformly distributed over the entire surface like the live load, but has different intensities at the crown beam, edge beam, and shell surfaces. The structure shows quite a bit of nonlinearity before failure.

Figure 5.45 presents the progressive crack pattern with load increments. The crack patterns correspond to those observed by Varghese and Mathai [5.6] in their experimental studies on micro-concrete gable shell models. The diagonal cracks progress through the depth with load increments. The diagonal crack which starts near the support and progresses upwards to the crown finally causes the steel reinforcement to yield. At this stage, the crack goes through the whole cross-section and the structure starts to deflect more and more, causing concrete to crush at several places, including the edge beam near the

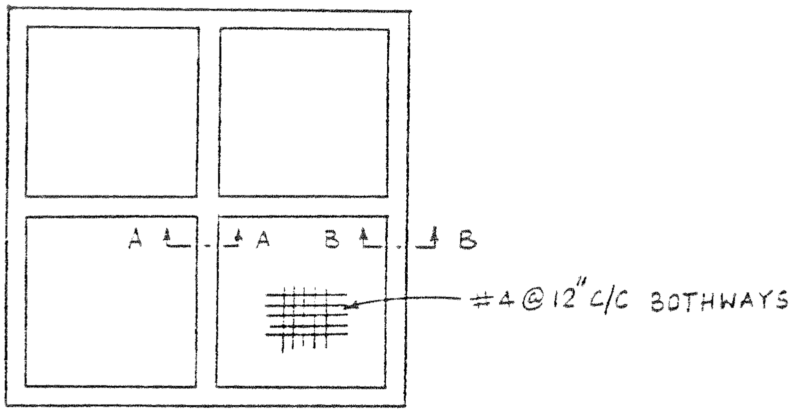

a. PLAN OF GABLE HP SHELL

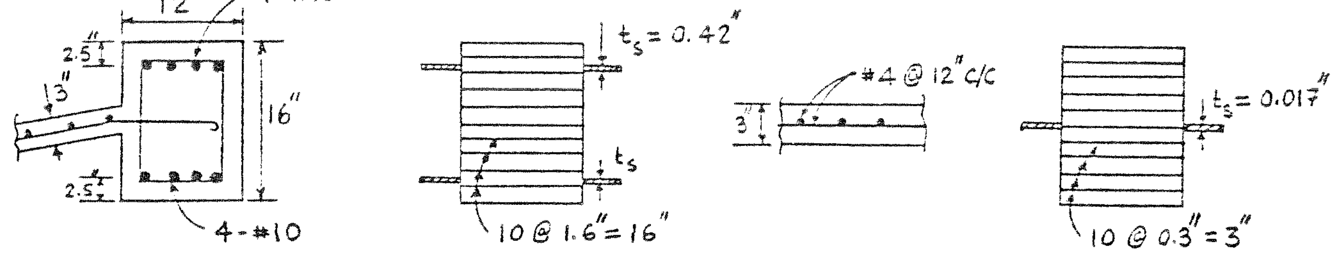

b. EDGE BEAM AND LAYER SYSTEM AT SECTION BB

C. SHELL PROPER AND LAYER SYSTEM (NOT TO SCALE)

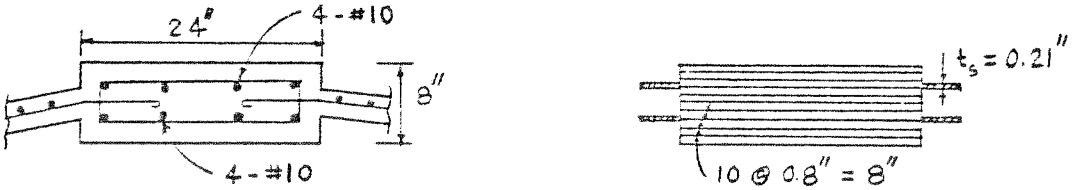

C. CROWN BEAM AND LAYER SYSTEM AT SECTION AA FOR GABLE A

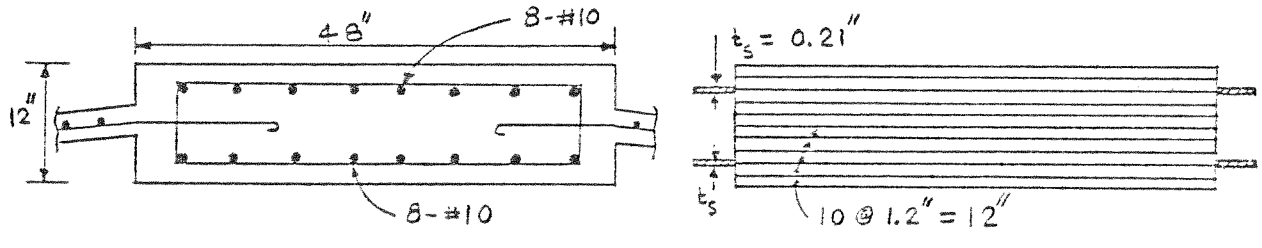

d. CROWN BEAM AND LAYER SYSTEM AT SECTION AA FOR GABLE B

FIG. 5.43 EXAMPLE 4 - REINFORCEMENTS AND LAYER SYSTEMS USED FOR THE NONLINEAR ANALYSES OF GABLE HP SHELL

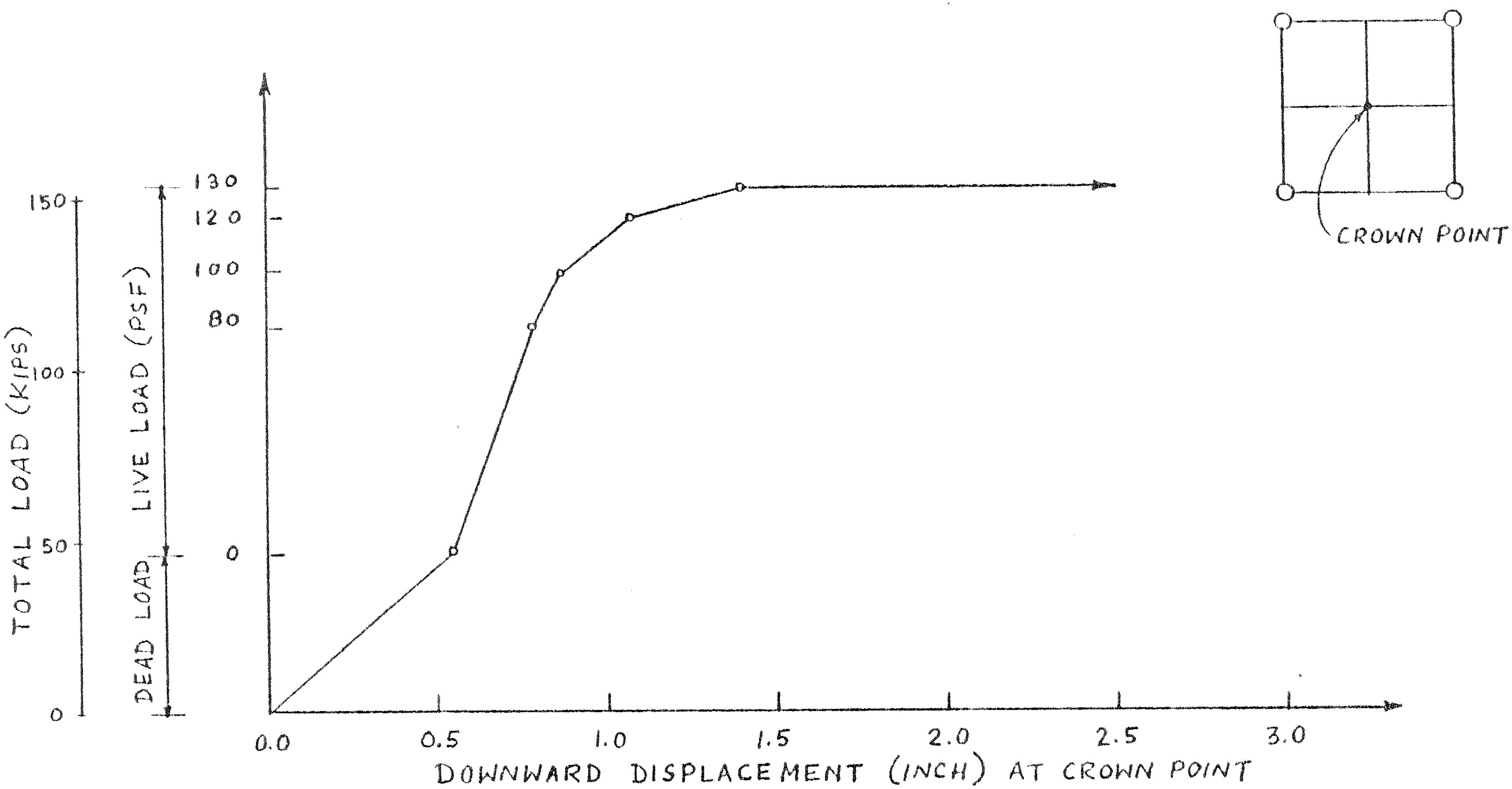

FIG. 5.44 EXAMPLE 4 - LOAD-DEFLECTION CURVE FOR THE CROWN POINT OF GABLE B

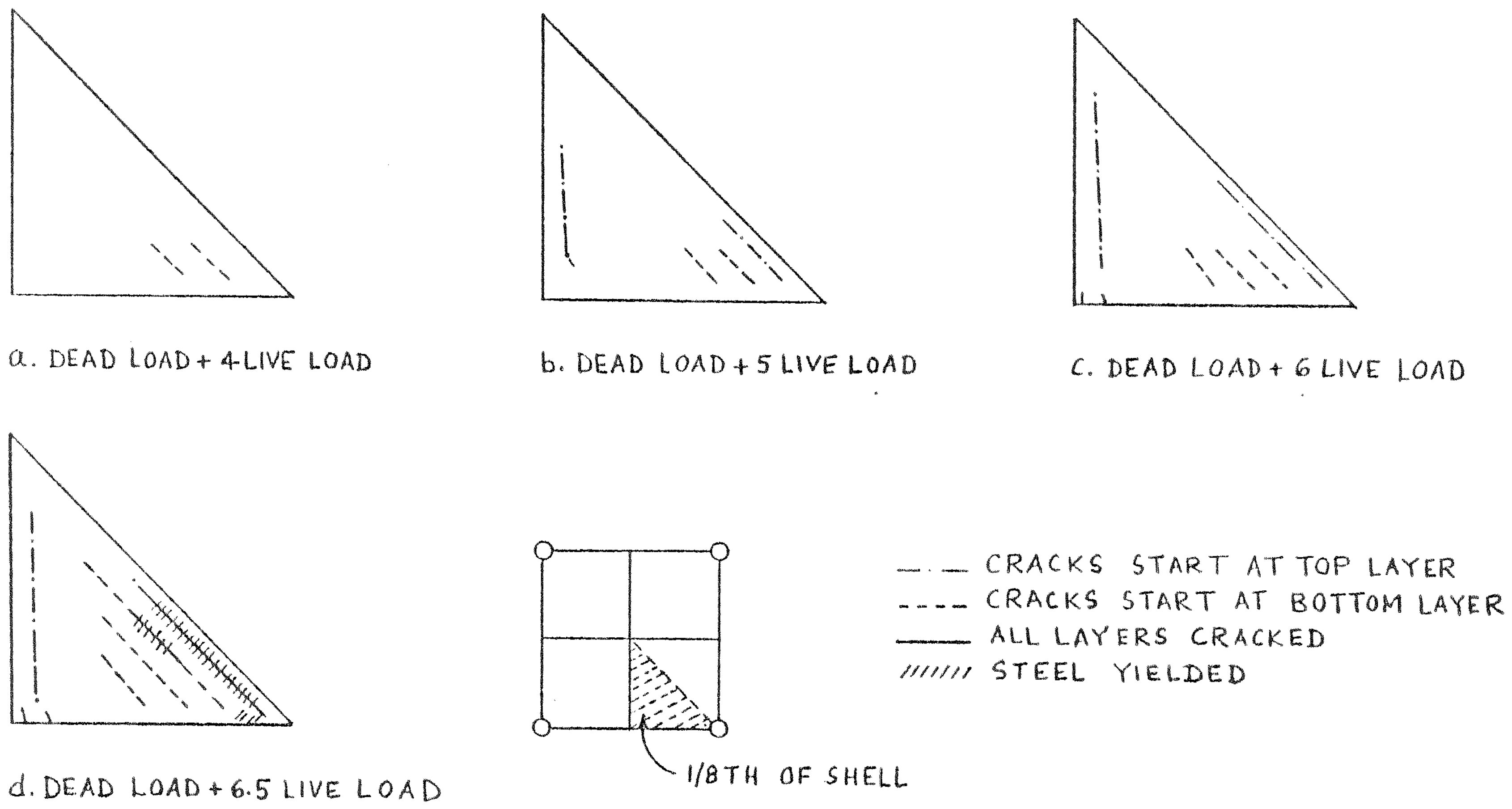

a. DEAD LOAD + 4 LIVE LOAD

b. DEAD LOAD + 5 LIVE LOAD

c. DEAD LOAD + 6 LIVE LOAD

d. DEAD LOAD + 6.5 LIVE LOAD

FIG. 5.45 EXAMPLE 4 - PROGRESSIVE CRACK PATTERNS FOR GABLE B FOR INSTANTANEOUS ULTIMATE LOAD ANALYSIS support. At this stage the structure is assumed to have failed as the displacement solution diverges. Figure 5.46 illustrates this. At a load level of DL + 6LL, the displacement solution converges in five iterations, while at a load level of DL + 6.5LL, the solution diverges, causing failure.

Figure 5.47 presents the load-deflection curve at the crown point for gable A which has also been analyzed for the ultimate load. The load-deflection pattern is similar to that of gable B, Fig. 5.44, but the ultimate load is found to be DL + 7.5LL, i.e., 150 psf of uniformly distributed live load is needed for failure. The larger crown beam of gable B, thus, lowers its ultimate capacity. Hence, care must be exercised in choosing the crown beam size for any gable HP shell. It is felt that some parametric studies are needed to bring to focus the sensitivity of the ultimate response of these types of shells to the crown beam sizes. The failure modes and crack patterns of gable A are very similar to those of gable B as shown in Fig. 5.48.

In the third phase of the analysis, gable B has been subjected to a time-dependent load history. The gable has been analyzed for dead load sustained from 28 to 180 days after casting, i.e., a period of over five months. Then, it is loaded with multiples of uniformly distributed load of 20 psf on the horizontal projection of the whole shell surface area until ultimate load is reached. ACI Committee 209 [3.5] recommended values have been chosen for creep and shrinkage effects.

Figure 5.49 presents the variation of the vertical deflection at the crown point due to the sustained dead load. It is interesting to know that the vertical deflection increased to a value 3.4 times

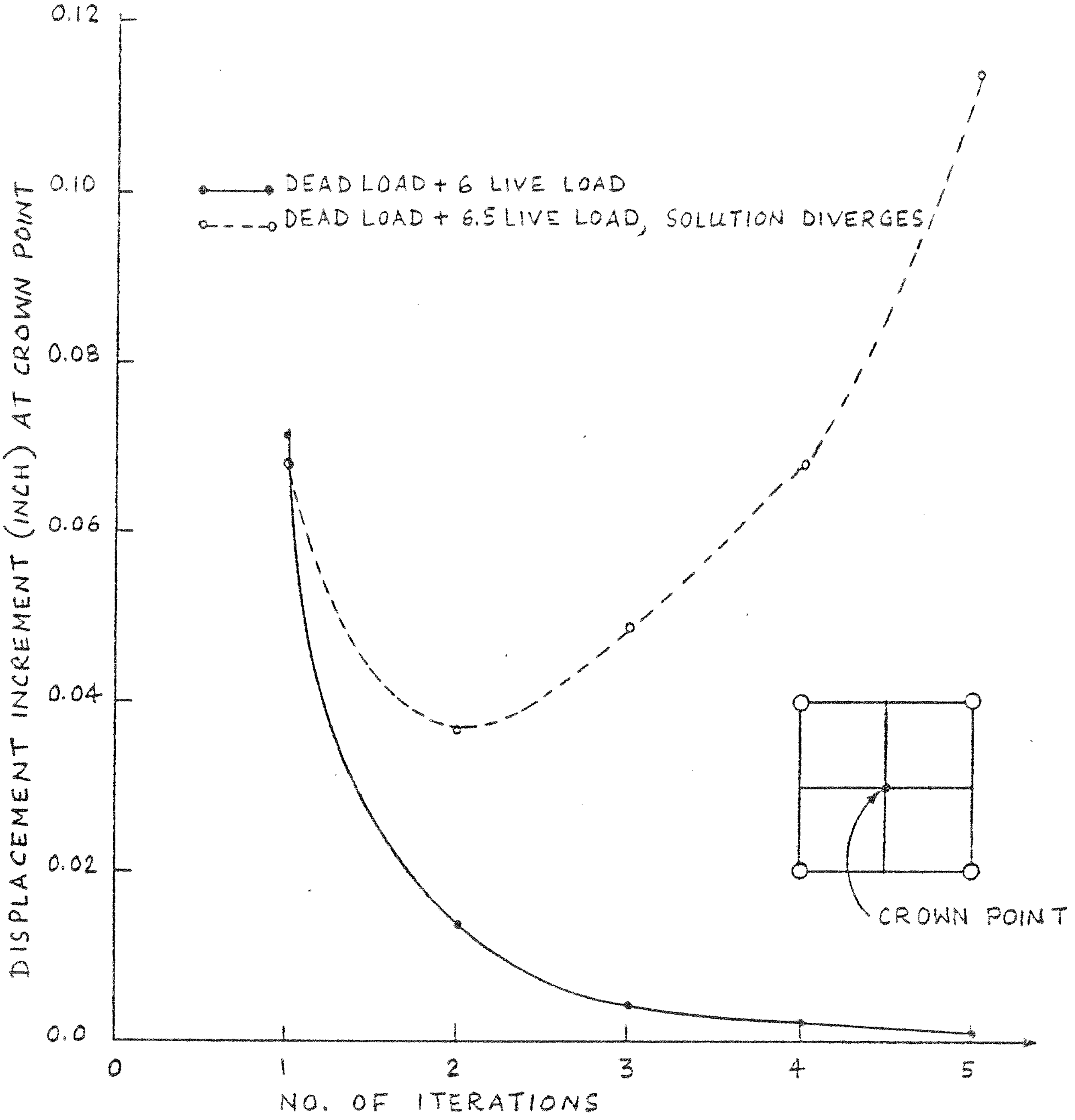

FIG. 5.46 EXAMPLE 4 - CONVERGENCE AND DIVERGENCE OF SOLUTIONS FOR GABLE B

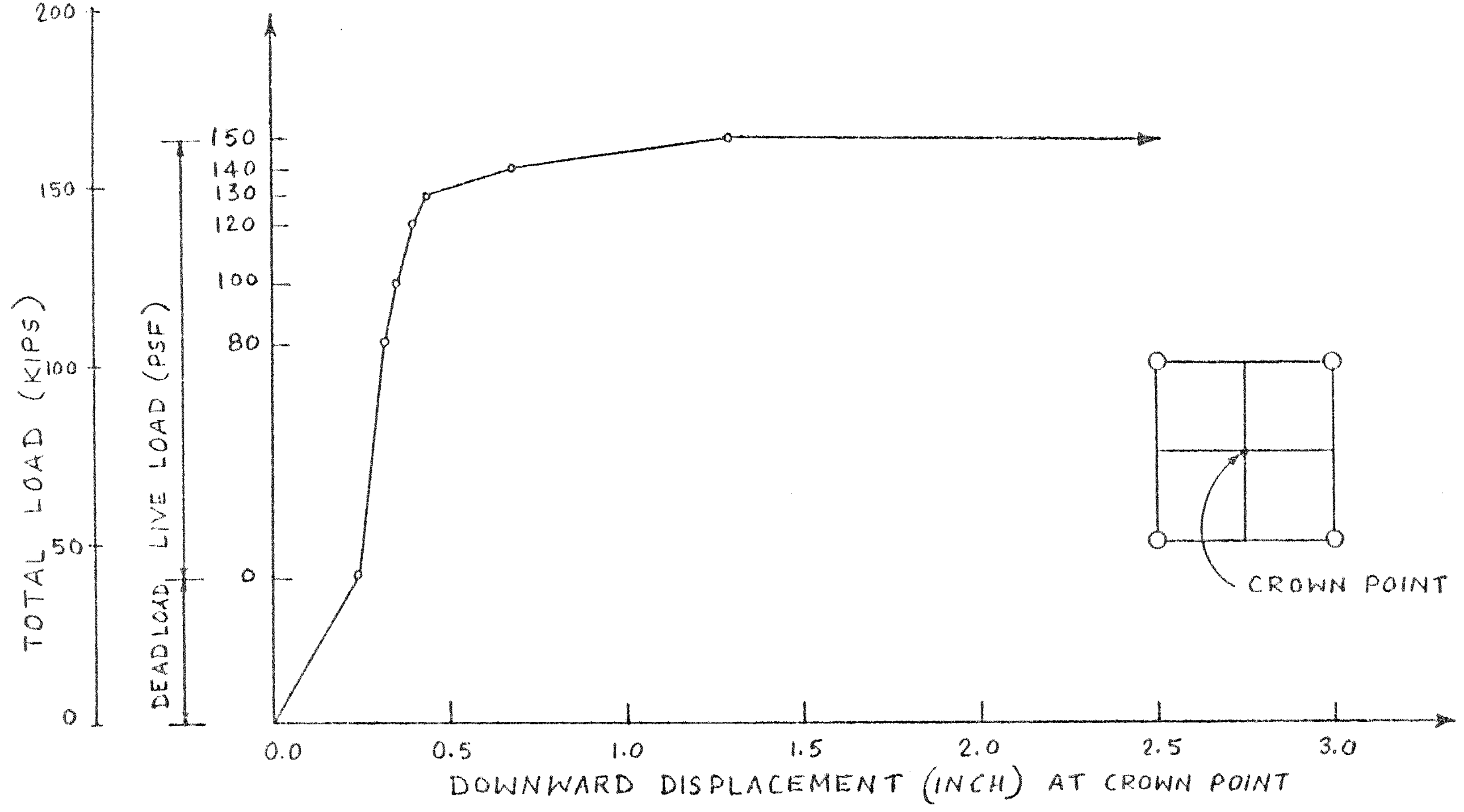

FIG. 5.47 EXAMPLE 4 - LOAD-DEFLECTION CURVE FOR THE CROWN POINT OF GABLE A

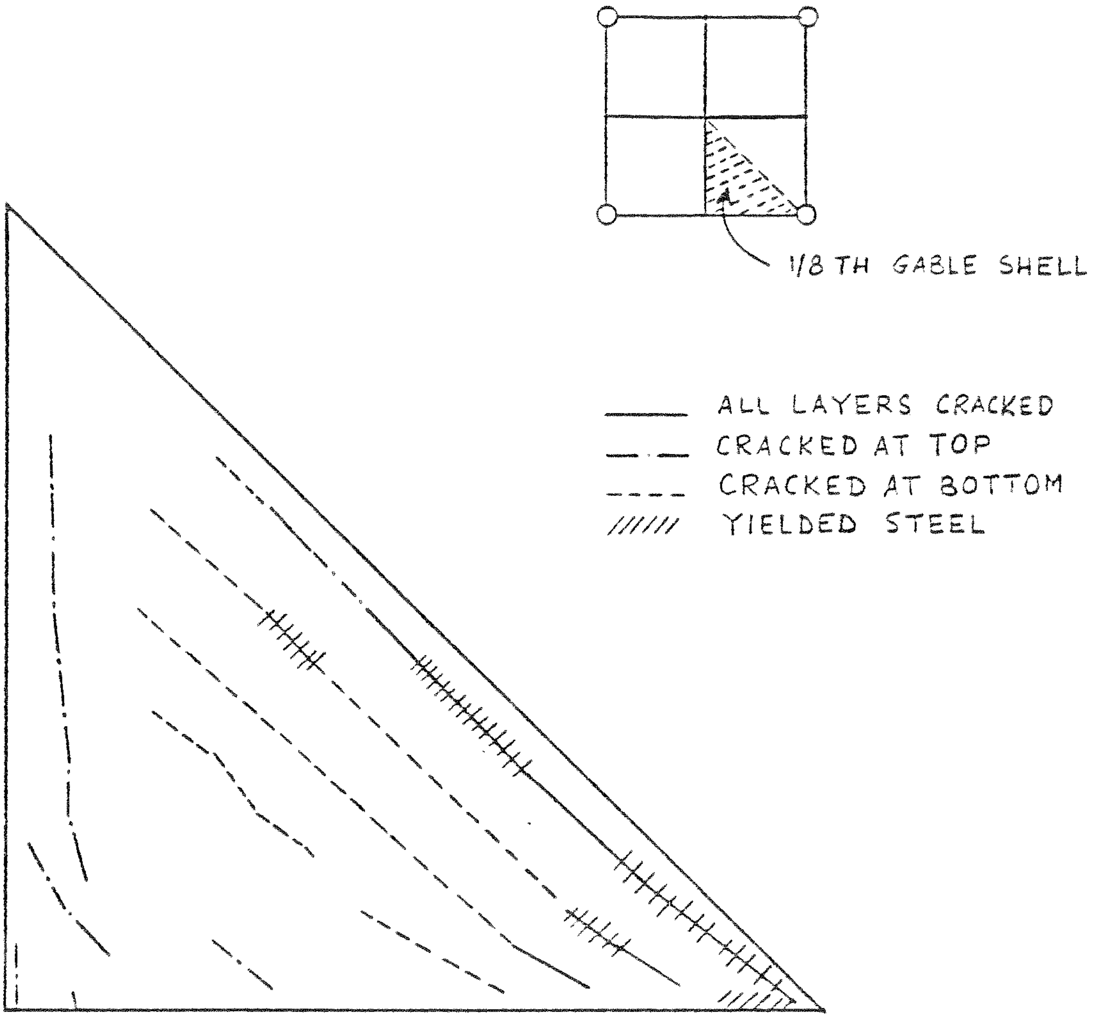

FIG. 5.48 EXAMPLE 4 - CRACK PATTERNS FOR GABLE A AT ULTIMATE LOAD

the value at the application of load. Figures 5.50 and 5.51 present the deflection profiles of the crown and edge beams with time. The increase in the vertical deflections is quite significant.

Figure 5.52 presents the variation in the bending moment and the axial force at midspan of the crown beam. The axial force increases from 50 kips to 140 kips while the bending moment goes from 140 k-ft. to 200 k-ft. Most of the axial force increment is taken by steel which goes from a stress of -2.5 ksi to -15.0 ksi. Concrete, at the same time, relaxes from -370 psi to -210 psi.

The increment in axial force of the crown beam with time suggests quite a significant amount of stress redistribution among the three structural components of the gable HP shell, namely, the crown beam, the edge beam and the shell proper. To investigate further, the axial forces in the edge beam, crown beam and the shell at the midspan section C-C, Fig. 5.53, have been calculated at different times after the application of the dead load. The results are summarized below.

Axial force at section C-C:

At application of dead load:

Crown beam = -57 kips 24%
Edge beam = -17 kips 7% } of total
Shell = -163 kips 69%

After 152 days of sustained dead load:

Crown beam = -138 kips 60%
Edge beam = -50 kips 22% } of total
Shell = -42 kips 18%

The above illustrates the significant redistribution of the stresses occurring in the structure due to creep and shrinkage effects. Due to shrinkage, the structure wants to shrink. The stiffer members

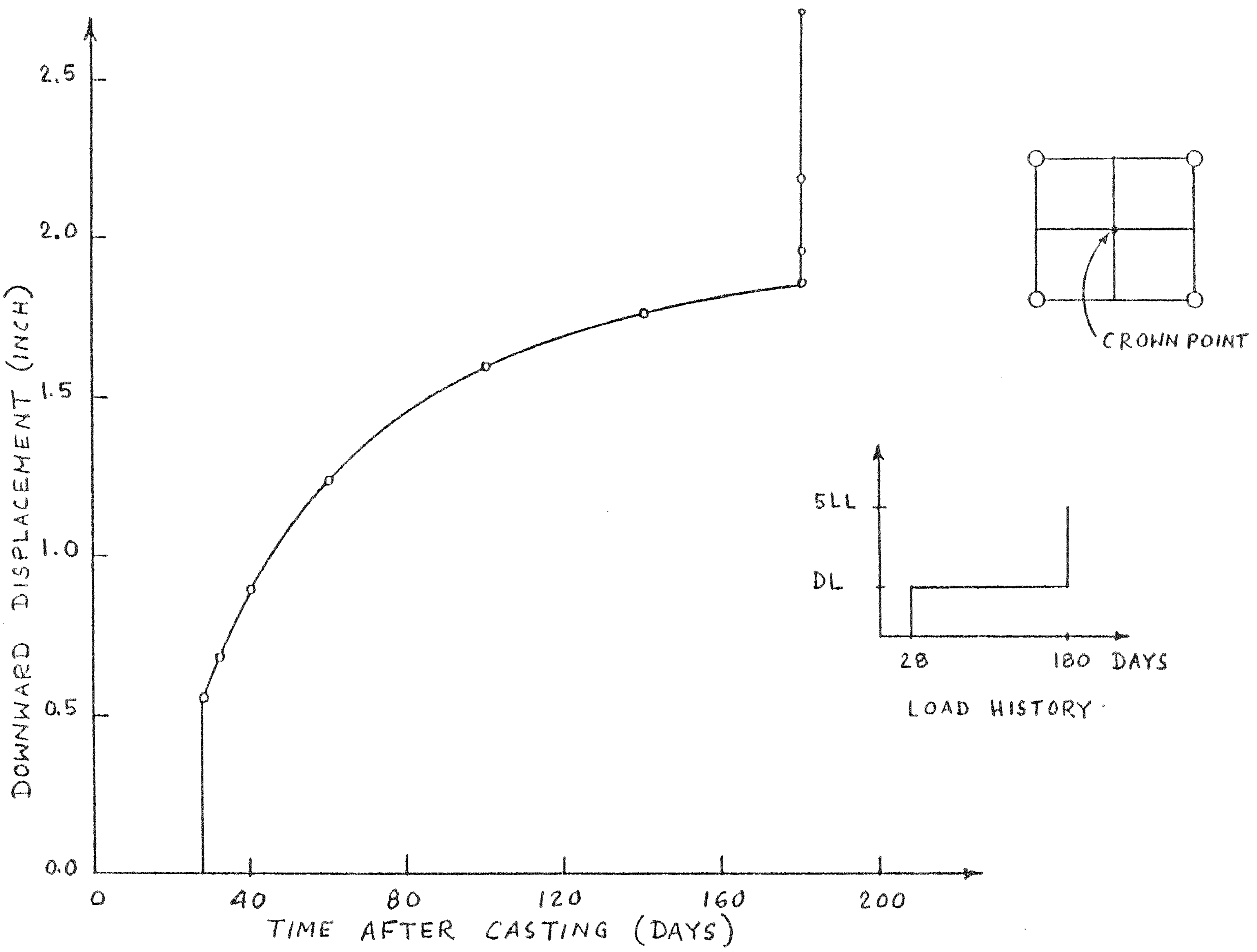

FIG. 5.49 EXAMPLE 4 - VERTICAL DISPLACEMENT AT THE CROWN POINT OF GABLE B DUE TO THE APPLIED LOAD HISTORY

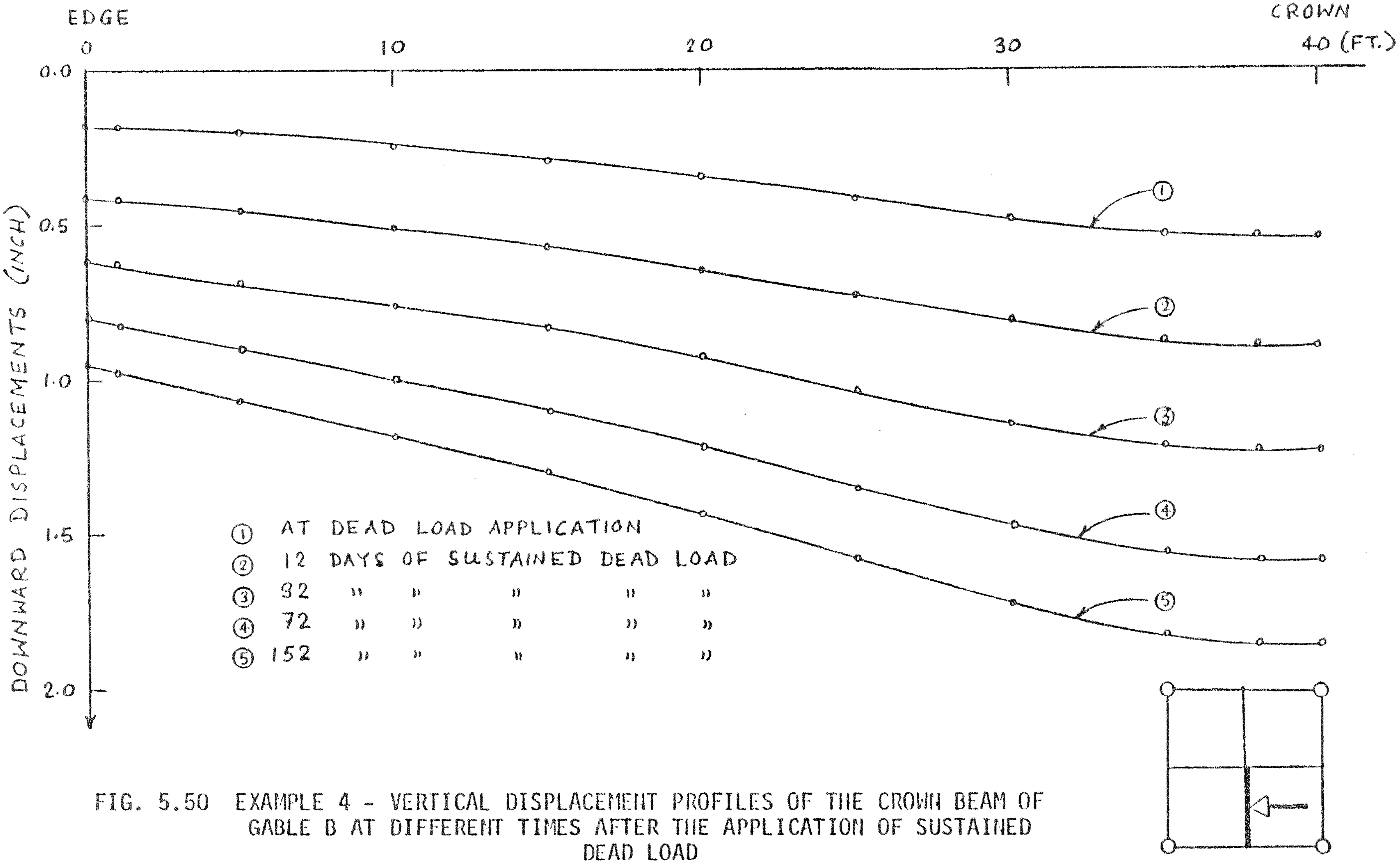

FIG. 5.50 EXAMPLE 4 - VERTICAL DISPLACEMENT PROFILES OF THE CROWN BEAM OF GABLE B AT DIFFERENT TIMES AFTER THE APPLICATION OF SUSTAINED DEAD LOAD

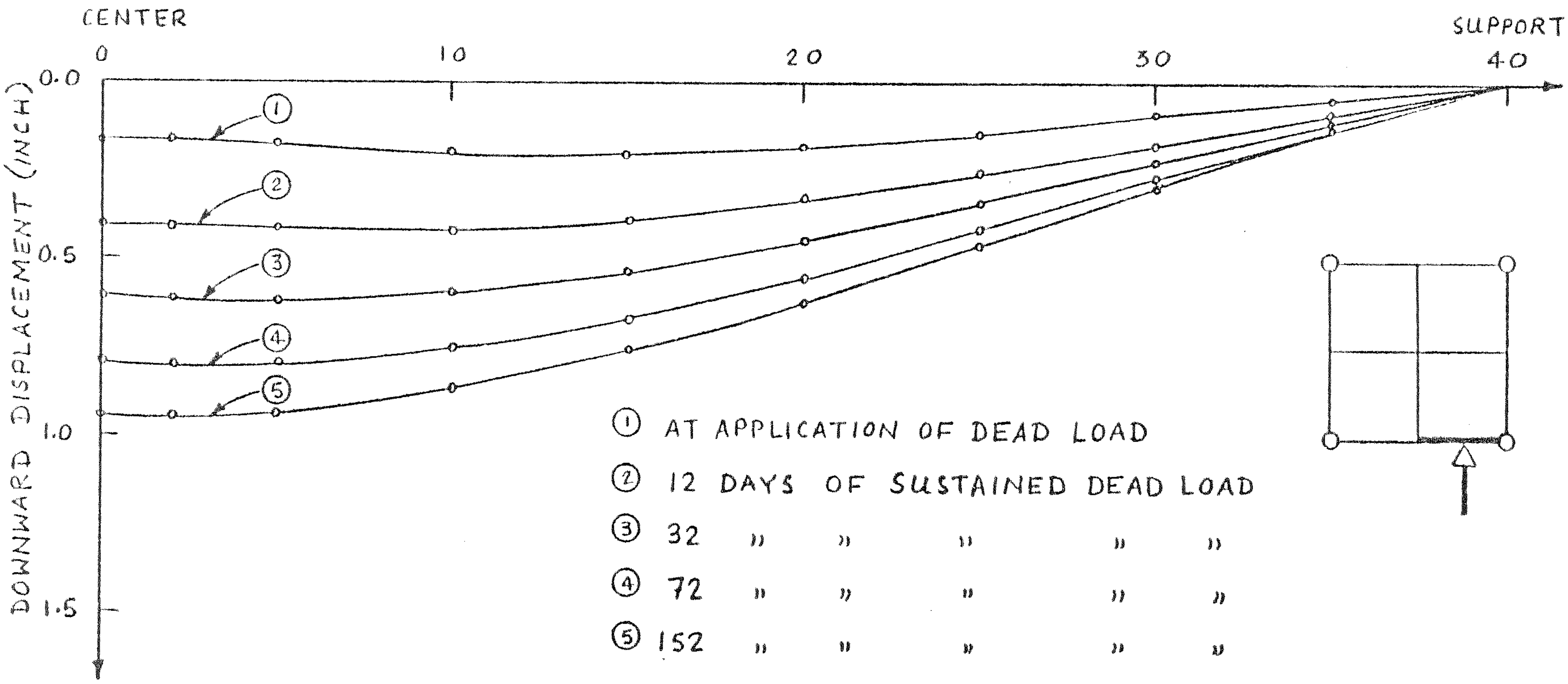

FIG. 5.51 EXAMPLE 4 - VERTICAL DISPLACEMENT PROFILES OF THE EDGE BEAM OF GABLE B AT DIFFERENT TIMES AFTER THE APPLICATION OF SUSTAINED DEAD LOAD

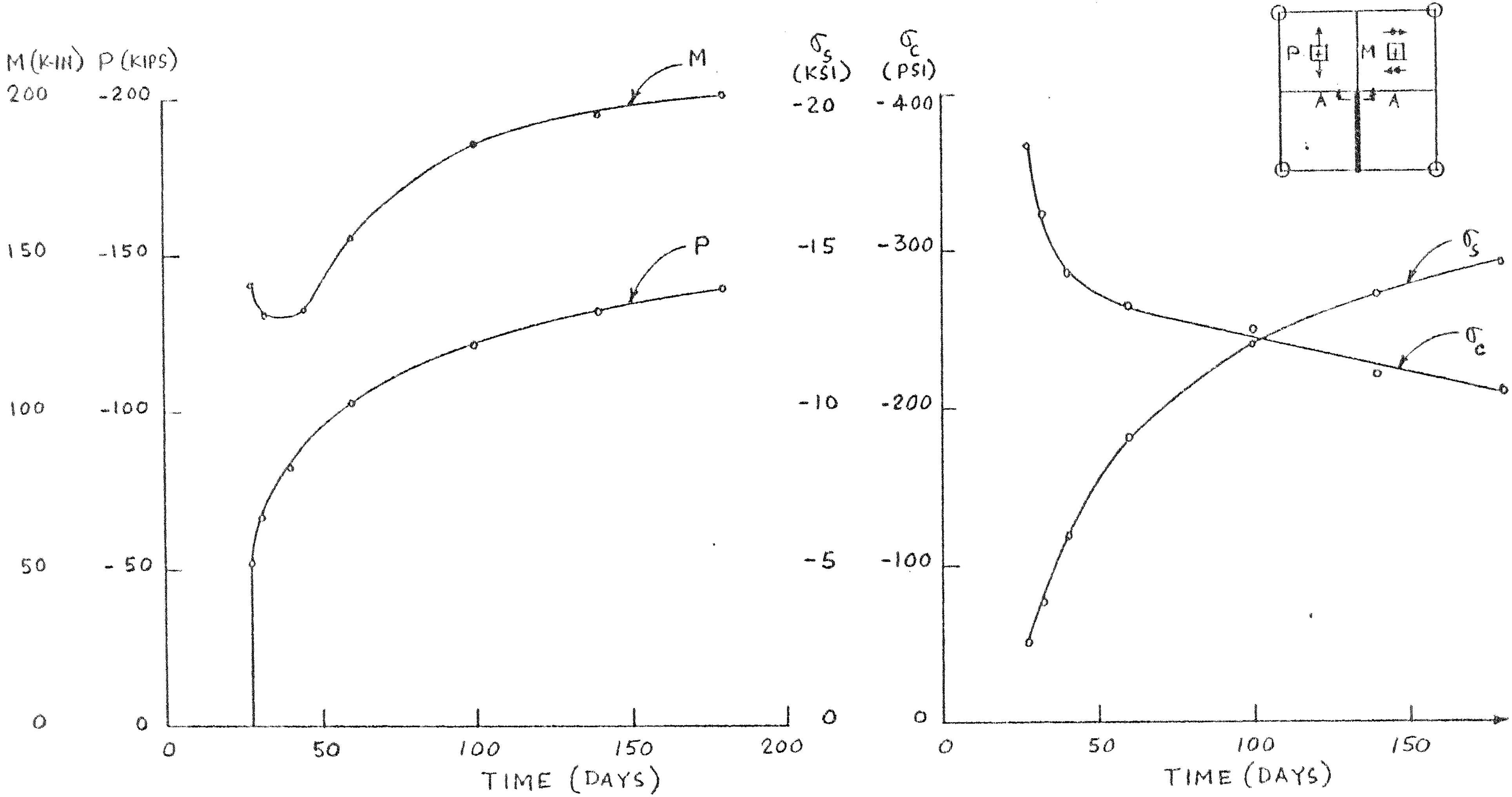

FIG. 5.52 EXAMPLE 4 - VARIATION OF AXIAL FORCE P, BENDING MOMENT M, CONCRETE STRESS AT THE TOP LAYER σ_c AND STEEL STRESS σ_s FOR THE MIDSPAN SECTION AA OF THE CROWN BEAM OF GABLE B AT DIFFERENT TIMES AFTER THE APPLICATION OF SUSTAINED DEAD LOAD

of the structure, namely, the edge and crown beams, restrain the less stiff shell from shrinking. This produces tensile forces in the shell and compressive forces in the edge and crown beams, causing some force redistribution. Due to creep, the shell concrete fibers, which are under compressive stress, relax. Part of this relaxed stress is picked up by the steel reinforcement in the shell; however, the main part is transferred to the stiffer edge and crown beams.

Figure 5.53 presents the transverse distribution of the net longitudinal membrane force in the shell at midspan section CC under sustained dead load. The portion of the longitudinal membrane force carried by the concrete alone is presented in Fig. 5.54. The longitudinal stresses carried by the reinforcing steel alone is shown in Fig. 5.55. The redistribution of the concrete stresses due to the creep and shrinkage effects is rather dramatic as illustrated in Fig. 5.54. In fact, most of the concrete in the shell passes from the compressive to the tensile state. This implies that a considerable amount of cracking may be expected in the shell concrete due to the creep and shrinkage effects depending on the magnitude of the sustained load and the concrete tensile strength. Steel compressive stresses, on the other hand, increases (Fig.5.55) as the steel reinforcement tries to restrain the concrete from shrinking. The transverse moment in the shell also indicates some redistribution (Fig.5.56).

Figure 5.57 presents the crack growth with elapsed time. The crack patterns occur generally in the same direction as seen in the case of instantaneous loading with an additional 100 psf of uniformly distributed loading.

Figure 5.58 compares the load-deflection curves at the crown

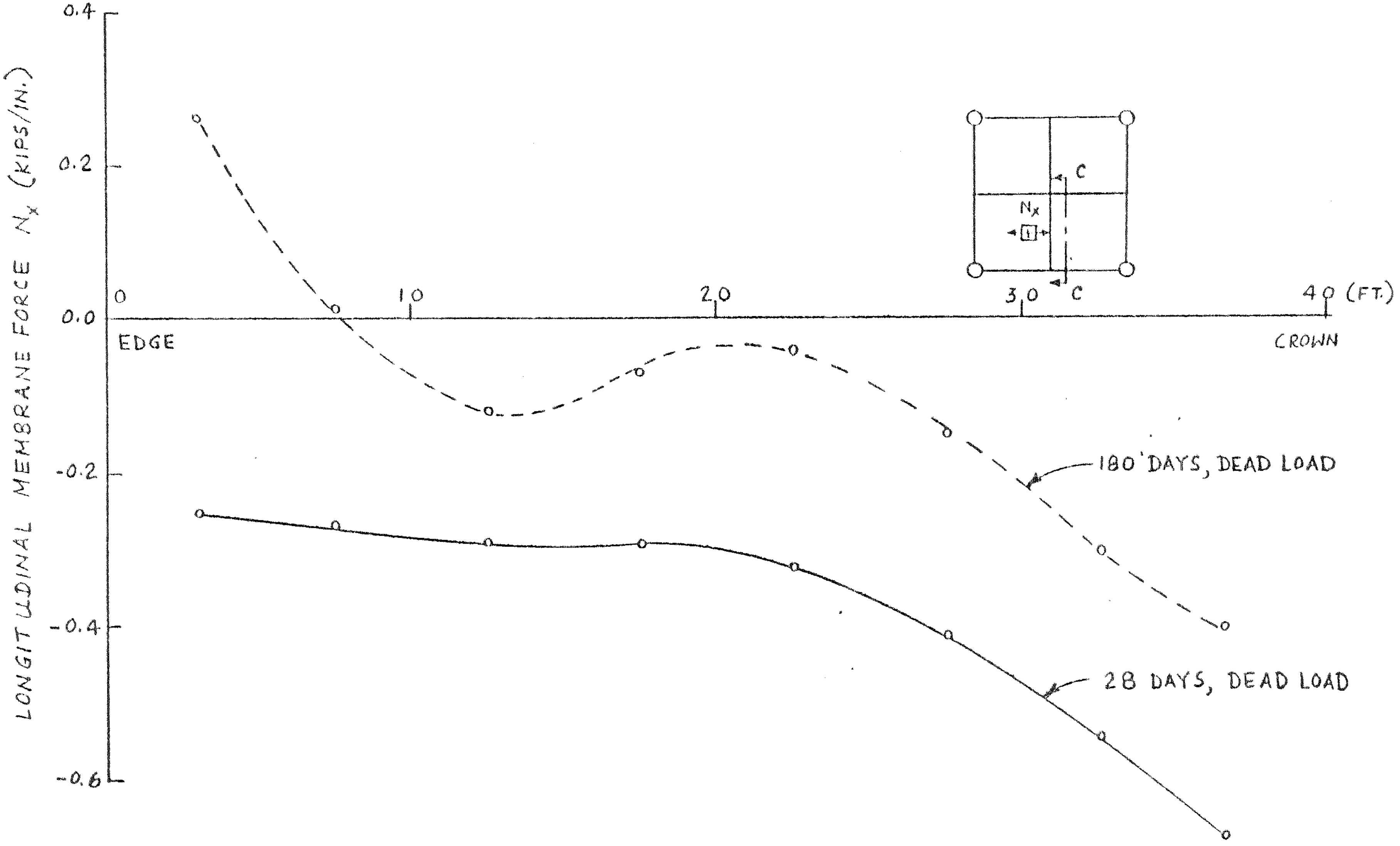

FIG. 5.53 EXAMPLE 4 - TRANSVERSE DISTRIBUTION OF THE NET LONGITUDINAL MEMBRANE FORCE FOR BOTH CONCRETE AND STEEL IN THE SHELL OF GABLE B AT THE MIDSPAN SECTION CC UNDER SUSTAINED DEAD LOAD

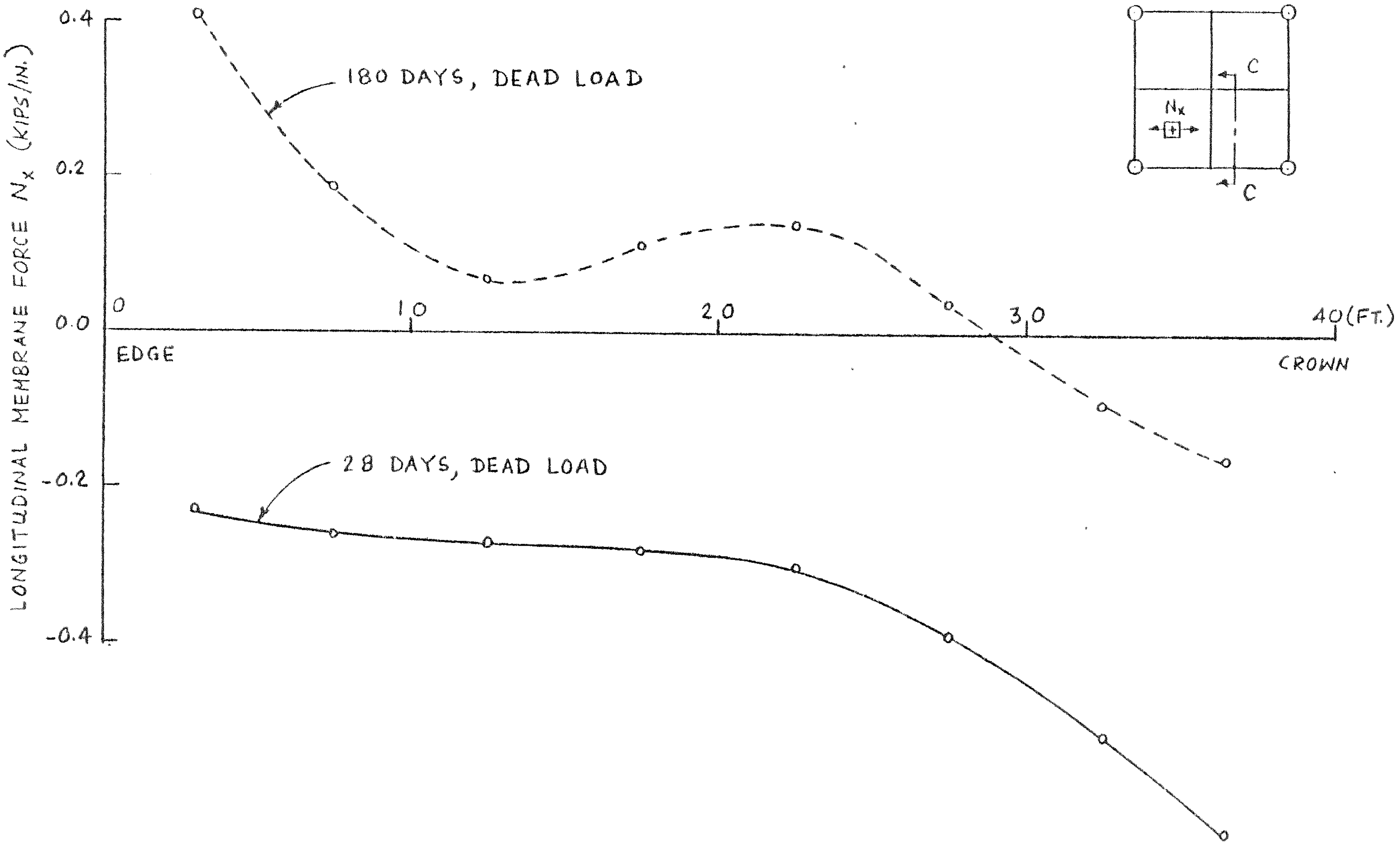

FIG. 5.54 EXAMPLE 4 - TRANSVERSE DISTRIBUTION OF THE LONGITUDINAL MEMBRANE FORCE FOR ONLY CONCRETE IN THE SHELL OF GABLE B AT THE MIDSPAN SECTION CC UNDER SUSTAINED DEAD LOAD

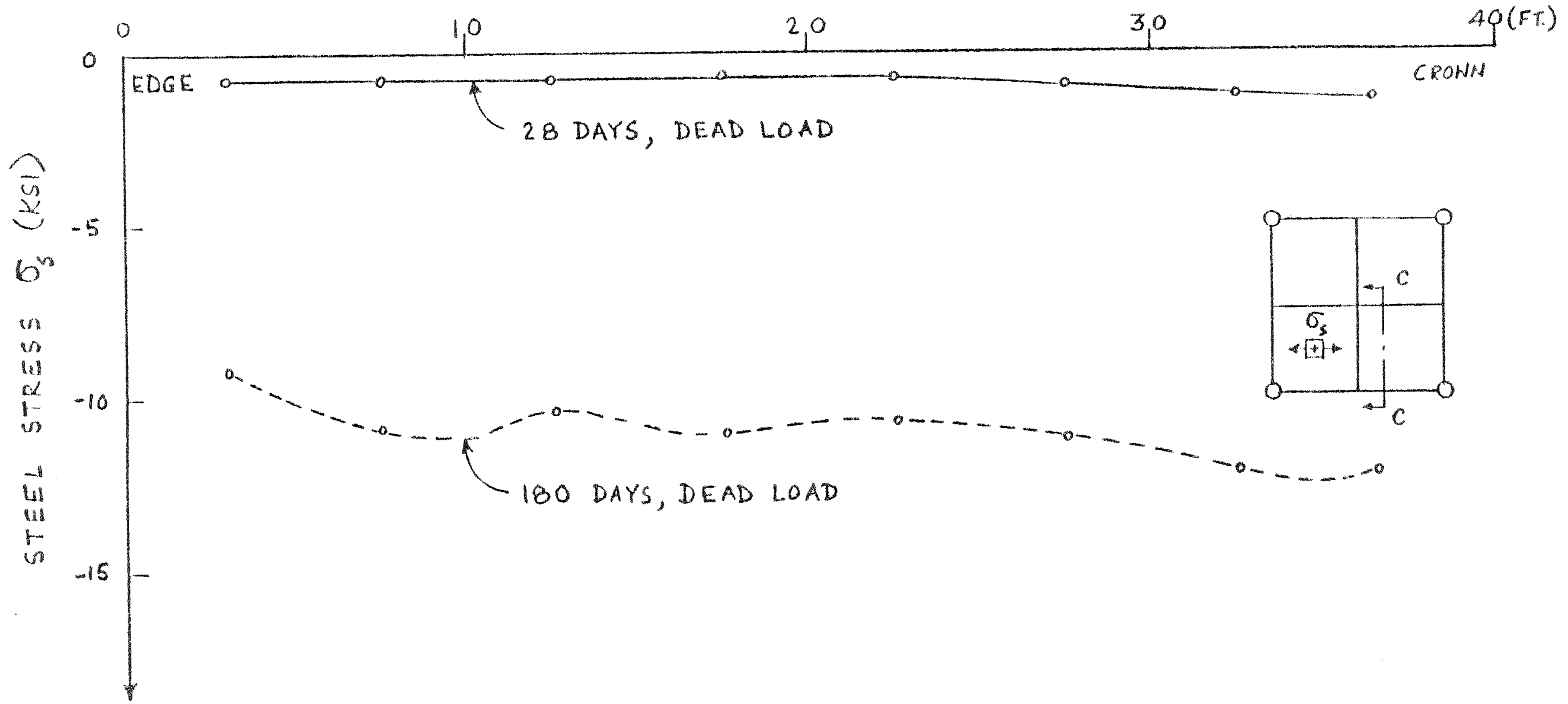

FIG. 5.55 EXAMPLE 4 - TRANSVERSE DISTRIBUTION OF STEEL STRESS IN THE SHELL OF GABLE B AT MIDSPAN SECTION CC UNDER SUSTAINED DEAD LOAD

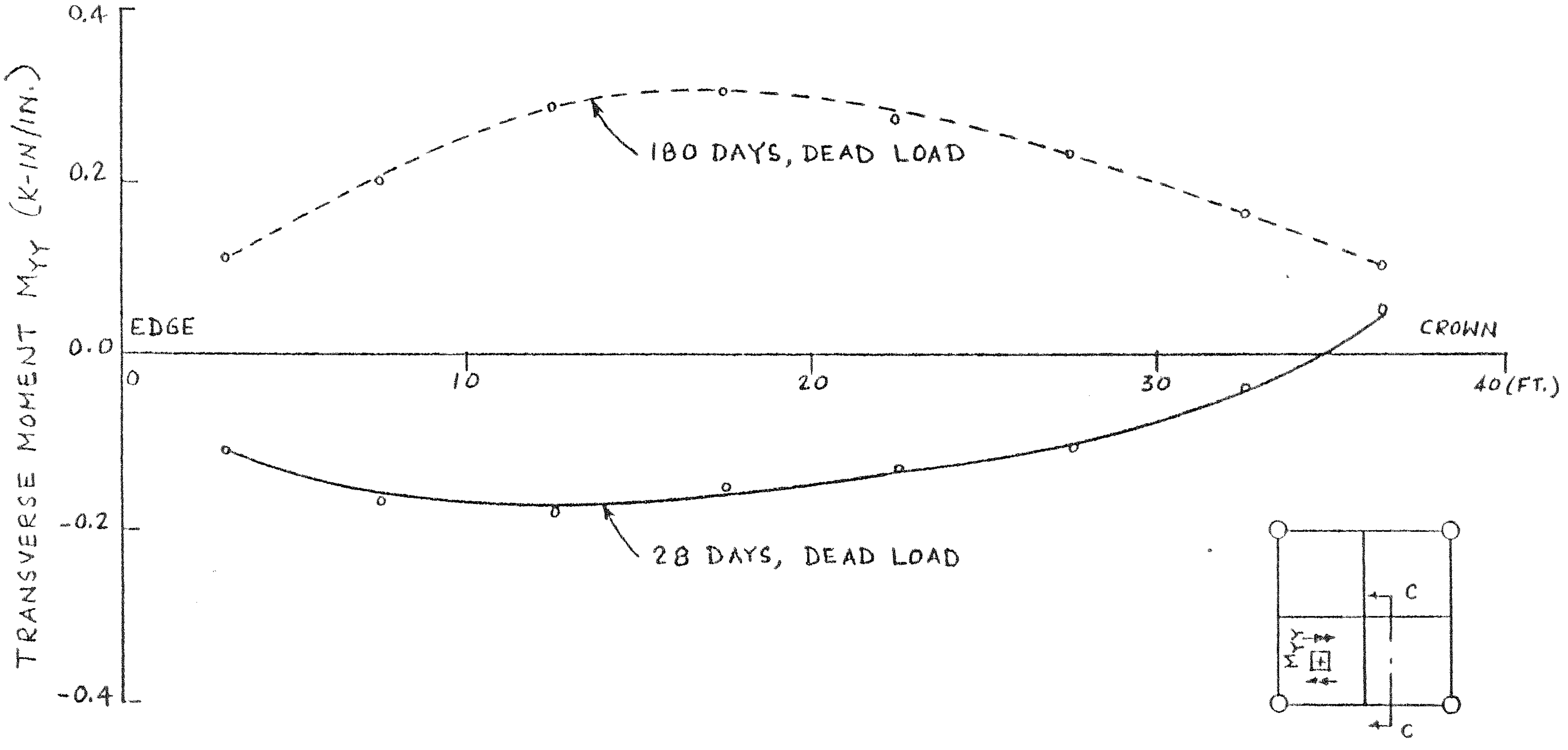

FIG. 5.56 EXAMPLE 4 - DISTRIBUTION OF TRANSVERSE MOMENT M_{YY} (K-in/in.) IN THE SHELL OF GABLE B AT MIDSPAN SECTION CC UNDER SUSTAINED DEAD LOAD

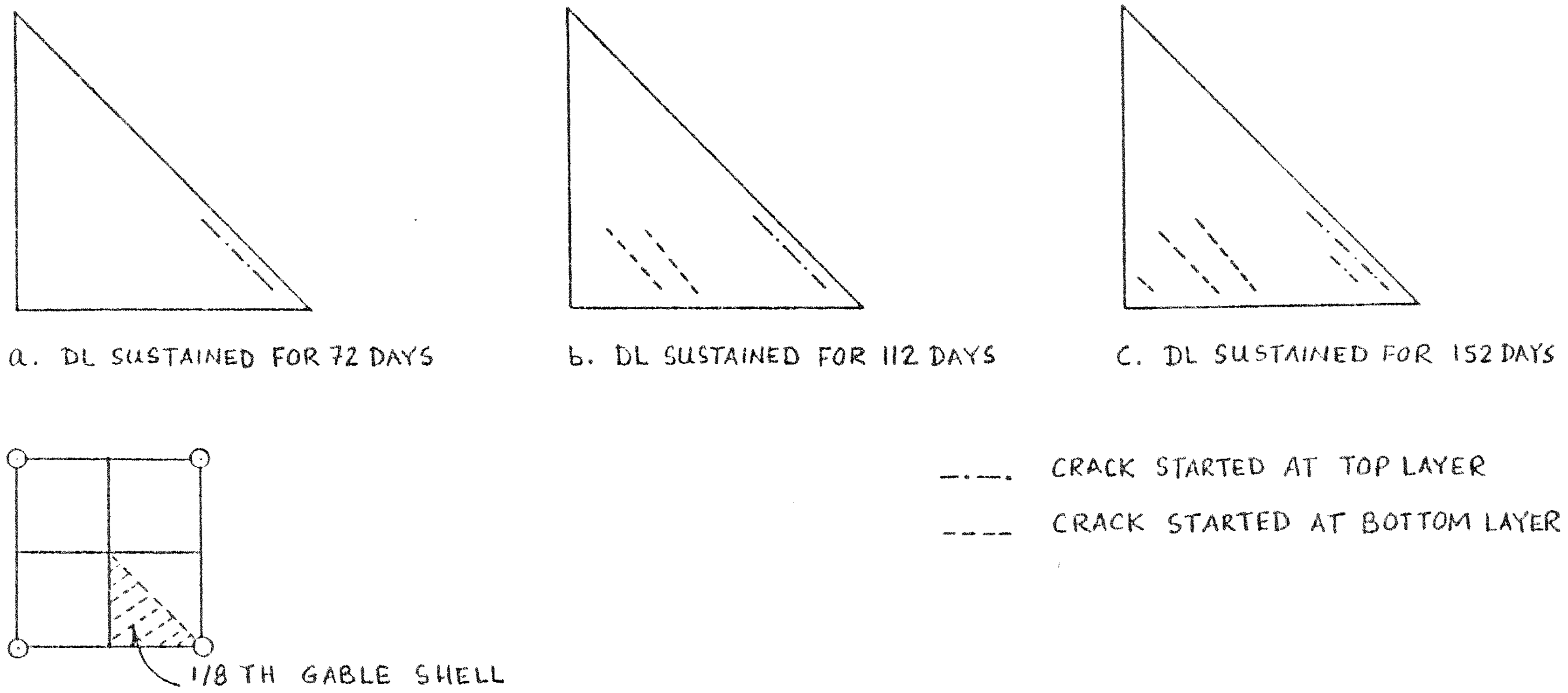
a. DL SUSTAINED FOR 72 DAYS

b. DL SUSTAINED FOR 112 DAYS

c. DL SUSTAINED FOR 152 DAYS

FIG. 5.57 EXAMPLE 4 - CRACK PATTERNS OF GABLE B FOR SUSTAINED DEAD LOAD

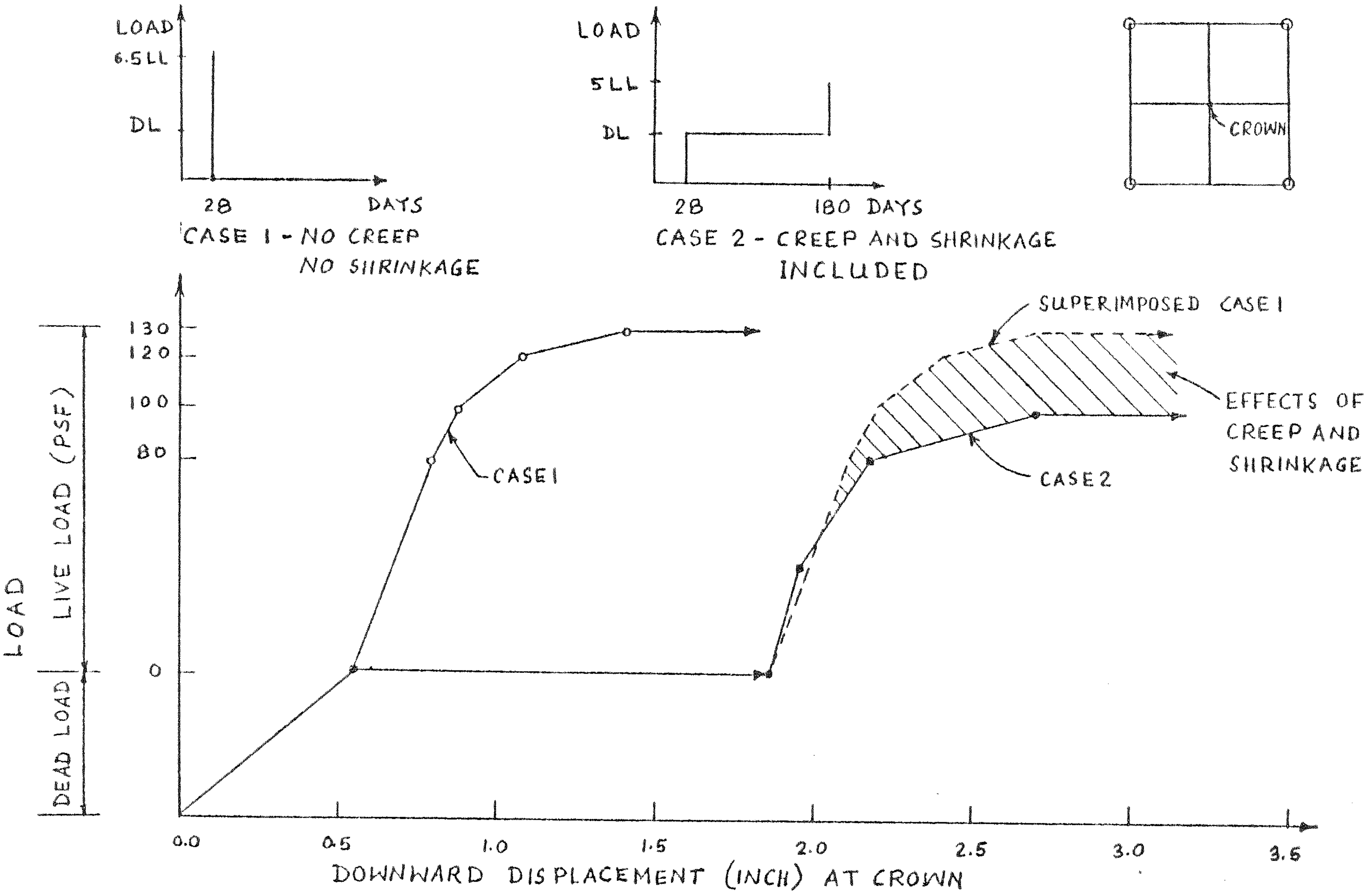

FIG. 5.58 EXAMPLE 4 - COMPARISON OF DEFLECTIONS AT CROWN OF GABLE B FOR INSTANTANEOUS LOAD AND TIME-DEPENDENT LOAD HISTORY

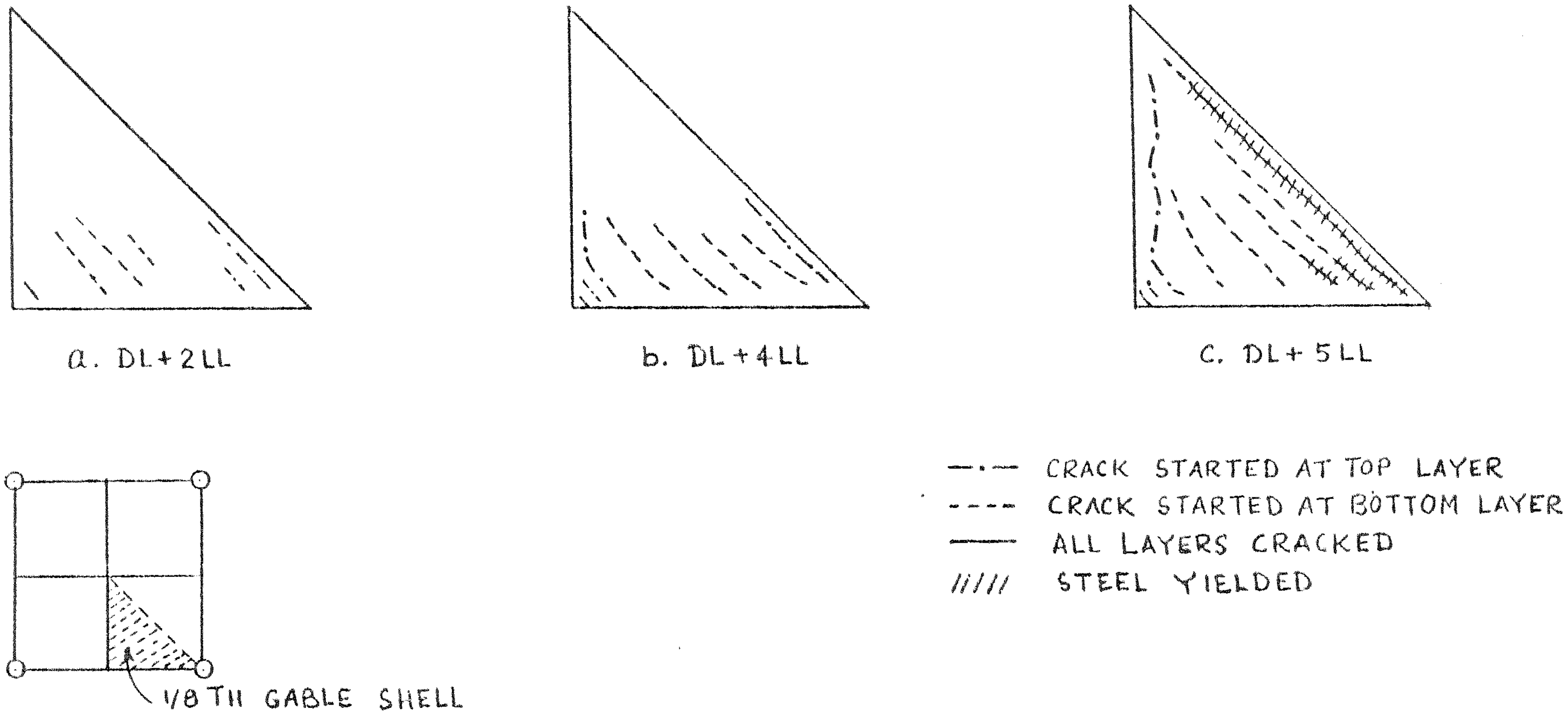

FIG. 5.59 EXAMPLE 4 - CRACK PATTERNS OF GABLE B WITH LIVE LOAD INCREMENTS AFTER SUSTAINED DEAD LOAD FOR 152 DAYS

point due to both instantaneous loading and time-dependent load history. The structure shows more degradation of stiffness because of the creep and shrinkage effects and fails at a uniformly distributed live load of 100 psf while it takes 130 psf, in the case of instantaneous loading, to cause failure.

Figure 5.59 presents the progressive crack patterns with increasing loads. The crack patterns and failure modes are very similar to those due to instantaneous loading, Fig. 5.45.

In conclusion, it may be stated that long time responses due to creep and shrinkage effects are important for gable HP shell roofs. Significant stress redistribution takes place between the different structural components, such as edge beams, crown beams, and the shell proper, of gable shells due to creep and shrinkage effects. The size of the crown beam and any concentrated live load over it exert a very notable influence on the behavior of such shells.

5.6 Computer Time

In the nonlinear method of analysis proposed in the present study, a series of piecewise linear solutions are performed to trace the nonlinear responses of structures. The total load is divided into a number of load increments and the total period of time under consideration is also divided into a number of time steps. An iterative approach is chosen for the solution of each load increment. This implies that the solution procedure is repeated for a large number of times. The computation time required is thus directly proportional to the total number of iterations performed in the solution procedure. The number of iterations is controlled by the total number of load increments and time steps for which solutions are desired. The number of iterations for each load increment will again depend on the magnitude of the increment, convergence criteria and allowable maximum number of iterations for each increment.

The computation effort required for each iteration may generally be divided into two major parts: (1) solution of the equilibrium equations, and (2) calculation of the internal stresses and reformulation of the current element stiffness. The computer time required for the first part is directly proportional to NM^2 where N is the number of equilibrium equations and M is the half band width of the structural stiffness matrix. The number of elements and the number of layers in each element determine the computational effort required for the second part.

Implementation of the output requests also contributes a sizeable portion to the total computer cost. The output cost is a function of the number of elements, the number of layers in each element, and whether output is requested for each iteration. A large amount of bookkeeping using tapes is required in the program, which adds to the computer cost.

The computer time required for the numerical examples on a CDC 7600 computer is shown in Table 5.1 for reference. The total cost is represented by the computing units (CU) as given in column (12). The central processor (CP) time and the peripheral processor (PP) units are given in columns (10) and (11), respectively. The conversion rate to computing units is given by CU = 3CP + 0.5PP.

The central processor time is generally used up in the numerical solution of the problem, whereas most of the peripheral processor time is used up in input/output and tape manipulations.

TABLE 5.1 COMPUTER TIME FOR THE EXAMPLES

EXAMPLE (1)	TYPE OF ANALYSIS (2)	NO. OF NODES (3)	NO. OF ELEMENTS (4)	NO. OF EQUATIONS (5)	LENGTH OF THE BLANK COMMON (6)	NO. OF TIME STEPS (7)	NO. OF LOAD INCREMENTS (8)	TOTAL NO. OF ITERATIONS (9)	CENTRAL PROCESSOR TIME (SEC.) (10)	PERIPHERAL PROCESSOR UNITS (11)	COMPUTING UNITS (12)
1	TIME-DEPENDENT	14	12	70	2760	29	31	84	23	709	585
2	INSTANTANEOUS	48	70	96	2346	1	8	36	20	340	297
2	TIME-DEPENDENT	48	70	96	2346	8	16	49	30	495	434
3	TIME-DEPENDENT	16	18	64	2836	20	29	134	47	1450	1197
4	INSTANTANEOUS	66	100	353	26243	1	5	23	62	1196	1085
4	TIME-DEPENDENT	66	100	353	26243	9	10	47	213	4183	3793

NOTE: The cost of executing a problem in the CDC 7600 computer at the Lawrence Berkeley Laboratory of the University of California is computed at a rate of $0.07 per Computing Unit (CU).

6. CONCLUSIONS

6.1 Summary

A numerical method of analysis has been developed to trace the quasi-static behavior of various types of reinforced concrete structures under instantaneous and sustained loads. Time-dependent environmental phenomena, such as creep and shrinkage effects, were considered to obtain the evolution of the field variables--deflections, strains and stresses--of these structures in elastic and inelastic regimes. Ultimate collapses of shear panels, slabs of arbitrary geometry and free-form shells were then predicted considering local failures in steel and concrete along with the deterioration of structural stiffness due to progressive cracking.

A finite element tangent stiffness formulation, coupled with a time step integration scheme, was developed to analyze reinforced concrete systems. Within a time step, an incremental load procedure, with an iterative approach to solve the equilibrium equations for each load increment, was adopted to trace the nonlinear behavior of such structures. Since all load changes are considered to occur at the beginning of a time step and the resultant state of stress is assumed to prevail throughout the time step, suitably small time steps should be taken in the analytical procedure.

The reinforced concrete composite section was represented as a layered systems consisting of concrete and 'equivalent smeared' steel layers. Perfect bond was assumed to exist between the concrete and steel layers. The layered system is capable of accounting for the effects of normal as well as flexural forces on a structural member.

Variations of properties through the depth of the member were then accommodated by allowing each layer to have different properties due to different materials or levels of deformation. Kirchhoff's assumption of plane sections remaining plane was then adopted to interrelate the displacements at various levels through the section depth and thus reduce each layer to a two-dimensional problem. Each layer is then in a state of plane stress. Stiffness properties of an element were obtained by integrating the contributions from all the layers across the section. The nonlinear behavior was taken into account by altering the material property matrix used to describe the behavior of each concrete or steel layer during the development of the element stiffness matrix.

Since each concrete layer was assumed to be under a state of plane stress, a nonlinear constitutive relationship, based on the available data from biaxial load tests, was chosen. Tensile cracking at a limiting stress level, tensile unloading after cracking and strain-softening phenomenon beyond the maximum compressive strength were all included in the material model. For long-time deformations in concrete zones, effects of stress history, partial creep recovery, aging, and temperature variations were considered.

The effects of stress history were accounted for by the application of the linear superposition method in the calculation of creep strains. The influence of temperature variations on creep strains were incorporated by the time-shift principle. These characterize concrete to be an aging viscoelastic thermorheologically simple material. Creep under biaxial state of stress was represented by the introduction of the creep Poisson's ratio observed in a uniaxial, sustained load test. Variations of creep compliance due to slump of concrete mix, size of members, relative environmental humidity and high stress levels were considered on the basis of the available experimental data. A creep compliance function was chosen on the basis of three considerations--it included all the important factors influencing creep, its parameters could very easily be determined from the experimental data, and it could be used in a very efficient computation procedure involving the stress state of the last time step only. A shrinkage model, based on experimental observations and sensitive to temperature and humidity changes, slump of concrete mix and sizes of members, was also adopted. The steel reinforcement was represented by a bilinear, strain-hardening model exhibiting the Bauschinger effect. The constitutive relations were based on the small displacement theory. Unloading paths were prescribed for stress reversal.

Finally, computations for the effects of instantaneous and sustained load were carried out for some typical examples, which include beams, panels, slabs and shells, employing triangular finite elements of membrane, plate bending and shell types. Numerical results were compared to available experimental data to check the applicability and validity of the method of analysis presented in this study.

6.2 Conclusions

1. The numerical method of analysis developed in the present study is capable of providing useful information about the responses of reinforced concrete shear panels, slabs of arbitrary geometry and free-form shells under instantaneous and sustained load conditions.

2. The creep model adopted in the present study includes the

important factors that influence creep of concrete. It is used in a very efficient computational procedure and its parameters can very easily be determined from the experimental data.

3. Long-time responses due to creep and shrinkage effects are important for shell-type structures as illustrated in the case of gable HP shell roofs. Design procedures for such structures should incorporate the effects of long-time behavior of concrete to determine both the serviceability and the ultimate safety criteria during the design life of such structures.

4. Significant stress redistribution takes place between the different structural components, such as edge beams, crown beams and shell proper, of a gable HP shell roof due to creep and shrinkage effects. These structural systems, composed of various types of members, should be analyzed to determine the redistribution of load-resisting forces in each component member. The participating members should be designed to resist both the short term as well as long term loads.

6.3 Recommendations for Future Studies

1. Further studies may be carried out for structural systems composed of various types of structural members, such as beams, panels, slabs, shells, etc., to assess the participation of each component in resisting the short term as well as long term loads. Insight into the interactive behavior of the component members will lead to safe and economic design of structural systems.

2. Constitutive models should account for the available experimental observations on the material behavior. However, it must be

remembered that considerable expense is incurred in the numerical nonlinear analysis of any moderately complex structural system. Parametric studies are needed to construct simple but realistic constitutive models to contain the computational efforts within reasonable limits.

3. Experimental work is needed to compile data on the long-time behavior of reinforced concrete wall panels, slabs and shells. At present, test data is sadly lacking in these areas.

4. To represent the shell-edge beams in the finite element analysis of reinforced concrete, a beam element is needed which can respond to torsion and shear forces also. A filament beam element may be developed for this purpose.

5. Geometric nonlinearity can be an important factor in determining the true nonlinear response of some shell-type structures and should be incorporated into the present method of analysis.

REFERENCES

1.1 Ngo, D. and Scordelis, A. C., "Finite Element Analysis of Reinforced Concrete Beams," ACI Journal, V. 64, No. 3, March 1967.

1.2 Ngo, D., Scordelis, A. C., and Franklin, H. A., "Finite Element Study of Reinforced Concrete Beams with Diagonal Tension Cracks," UC-SESM Report No. 70-19, University of California, Berkeley, December 1970.

1.3 Nilson, A. H., "Finite Element Analysis of Reinforced Concrete," Ph.D. Dissertation, Division of Structural Engineering and Structural Mechanics, University of California, Berkeley, March 1967.

1.4 Nilson, A. H., "Nonlinear Analysis of Reinforced Concrete by the Finite Element Method," ACI Journal, V. 65, No. 9, September 1968.

1.5 Franklin, H. A., "Nonlinear Analysis of Reinforced Concrete Frames and Panels," Ph.D. Dissertation, Division of Structural Engineering and Structural Mechanics, University of California, Berkeley, UC-SESM Report No. 70-5, March 1970.

1.6 Bresler, B. and Bertero, V., "Behavior of Reinforced Concrete under Repeated Loads," Journal of the Structural Division, ASCE, V. 94, No. ST6, June 1968.

1.7 Zienkiewicz, O. C., Valliappan, S., and King, I. P., "Elasto-Plastic Solutions of Engineering Problems - Initial Stress - Finite Element Approach," International Journal for Numerical Methods in Engineering, V. I, 1969.

1.8 Cervenka, V., "Inelastic Finite Element Analysis of Reinforced Concrete Panels under In-Plane Loads," Ph.D. Dissertation, Department of Civil Engineering, University of Colorado, Boulder, 1970.

1.9 Cervenka, V and Gerstle, K. H., "Inelastic Analysis of Reinforced Concrete Panels," Publication of International Association for Bridge and Structural Engineering, V. 31 - II, 1971.

1.10 Mufti, A. A., et al., "A Study of the Behavior of Reinforced Concrete Elements using Finite Elements," Structural Concrete Series No. 70-5, McGill University, Montreal, September 1970.

1.11 Mufti, A. A., et al., "A Finite Element Study of Reinforced Concrete Structures," Structural Concrete Series No. 71-8, McGill University, Montreal, October 1971.

1.12 Yuzugullu, O. and Schnobrich, W. C., "A Numerical Procedure for the Determination of the Behavior of a Shear Wall Frame System," ACI Journal, V. 70, No. 7, July 1973.

1.13 Darwin, D. and Pecknold, D. A., "Analysis of Reinforced Concrete Shear Panels under Cyclic Loading," *Journal of the Structural Division*, ASCE, V. 102, No. ST2, February 1976.

1.14 Valliappan, S. and Doolan, T. F., "Nonlinear Analysis of Reinforced Concrete," *Journal of the Structural Division*, ASCE, V. 98, No. ST4, April 1972.

1.15 Colville, J. and Abbasi, J., "Plane Stress Reinforced Concrete Finite Elements," *Journal of the Structural Division*, ASCE, V. 100, No. ST5, May 1974.

1.16 Nam, C. H. and Salmon, C. G., "Finite Element Analysis of Concrete Beams," *Journal of the Structural Division*, ASCE, V. 100, No. ST12, December 1974.

1.17 Melhorn, G., "Analysis of Plane Structures with Forces in Their Middle Plane Composed of Precast Concrete Panels," *IASS Bulletin No. 58*, August 1975.

1.18 Jofriet, J. C. and McNiece, G. M., "Finite Element Analysis of Reinforced Concrete Slabs," *Journal of the Structural Division*, ASCE, V. 97, No. ST3, March 1971.

1.19 Bell, J. C. and Elms, D., "Partially Cracked Finite Elements," *Journal of the Structural Division*, ASCE, V. 97, No. ST7, July 1971.

1.20 Bell, J. C., "A Complete Analysis of Reinforced Concrete Slabs and Shells," Ph.D. Dissertation, Department of Civil Engineering, University of Canterbury, Christchurch, New Zealand, 1970.

1.21 Dotroppe, J. C., Schnobrich, W. C., and Pecknold, D. A., "Layered Finite Element Procedure for Inelastic Analysis of Reinforced Concrete Slabs," *IABSE Publication 33-11*, 1973.

1.22 Berg, S., "Nonlinear Finite Element Analysis of Reinforced Concrete Plates," *Report No. 73-1*, Institutt for Statikk, Division of Structural Mechanics, Univeristy of Trondheim, Norway, February 1973.

1.23 Berg, S. Bergan, P. G., and Holand, I., "Nonlinear Finite Element Analysis of Reinforced Concrete Plates," *Paper M3/5*, 2nd International Conference on Structural Mechanics in Reactor Technology, Berlin, West Germany, September 1973.

1.24 Backlund, J., "Finite Element Analysis of Nonlinear Structures," Doctoral Thesis, Chalmers Technical University, Göteborg, Sweden, November 1973.

1.25 Schafer, H., Link, J., and Melhorn, G., "Zur Wirklichkeitsnahen Berechnung von Stahlbetonplatten Mit Der Finite Element Method," *Beton and Stahlbetonbau*, 11, 1975.

1.26 Wegner, R. and Duddeck, H., "Der Gerissenen Zustand Zweisetig Elagerter Platten unter Einzellasten - Nichtlineare Berechnung mit Finiten Elementen," Beton und Stahlbetonbau, 70, 1975.

1.27 Lin, C. S., "Nonlinear Analysis of Reinforced Concrete Slabs and Shells," Ph.D. Dissertation, Division of Structural Engineering and Structural Mechanics, University of California, Berkeley, UC-SESM Report No. 73-7, April 1973.

1.28 Lin, C. S. and Scordelis, A. C., "Nonlinear Analysis of Reinforced Concrete Shells of General Form," Journal of the Structural Division, ASCE, V. 101, No. ST3, March 1975.

1.29 Bell, J. C. and Elms, D. G., "A Finite Element Post Elastic Analysis of Reinforced Concrete Shells," Bulletin of the International Association for Shell and Spatial Structures, No. 54, April 1974.

1.30 Hand, F. R., Pecknold, D. A., and Schnobrich, W. C., "Nonlinear Layered Analysis of Reinforced Concrete Plates and Shells," Journal of the Structural Division, ASCE, V. 99, No. ST7, July 1973.

1.31 Suidan, M. T. and Schnobrich, W. C., "Finite Element Analysis of Reinforced Concrete," Journal of the Structural Division, ASCE, V. 99, No. ST10, October 1973.

1.32 Ngo, D., "A Network-Topological Approach to the Finite Element Analysis of Progressive Crack Growth in Concrete Members," UC-SESM Report No. 75-6, University of California, Berkeley, June 1975.

1.33 Rashid, Y. R., "Ultimate Strength Analysis of Prestressed Concrete Pressure Vessels," Nuclear Engineering Design, V. 7, 1968.

1.34 Rashid, Y. R. and Rockenhauser, W., "Pressure Vessel Analysis by Finite Element Techniques," Conference on Prestressed Concrete Pressure Vessels, Institute of Civil Engineers, London, 1968.

1.35 Wahl, H. W. and Kasiba, R. J., "Design and Construction Aspects of Large Prestressed Concrete (PWR) Containment Vessels, ACI Journal, V. 77, No. 5, May 1969.

1.36 Zienkiewicz, O. C., Owen, D. R. J., and Phillips, D. W., "Finite Element Method in Analysis of Reinforced and Concrete Structures," Paper M1/1, 1st International Conference on Structural Mechanics in Reactor Technology, Berlin, West Germany, September 1971.

1.37 Argyris, J. H., et al., "Recent Developments in the Finite Element Analysis of Prestressed Concrete Reactor Vessels," Paper H1/1, 2nd International Conference on Structural Mechanics in Reactor Technology, Berlin, West Germany, September 1973.

1.38 Bresler, B., "Some Factors in the Investigation of Long Term Behavior of Reinforced Concrete Structures," Laboratory Note No. LN/150/BB, Road Research Laboratory, DSIR, England, August 1962.

1.39 Selna, L. G., "Time-Dependent Behavior of Reinforced Concrete Structures," UC-SESM Report No. 67-19, University of California, Berkeley, 1967.

1.40 Selna, L. G., "Creep, Cracking and Shrinkage in Concrete Frame Structures," Journal of the Structural Division, ASCE, V. 95, No. ST12, December 1969.

1.41 Aas-Jackobsen, K., "Design of Slender Reinforced Concrete Frames," Bericht Nr. 48, Institut für Baustatik, ETH, Zürich, 1973.

1.42 Åldstedt, E., "Nonlinear Analysis of Reinforced Concrete Frames," Division of Structural Mechanics, Norwegian Institute of Technology, University of Trondheim, Norway, 1975.

1.43 Scanlon, A., "Time Dependent Deflections of Reinforced Concrete Slabs," Ph.D. Dissertation, Department of Civil Engineering, University of Alberta, Edmonton, Canada, December 1971.

1.44 Scanlon, A. and Murray, D. W., "Time Dependent Reinforced Concrete Slab Deflections," Journal of the Structural Division, ASCE, V. 100, No. ST9, September 1974.

1.45 Rashid, Y. R., "Nonlinear Analysis of Two-dimensional Problems in Concrete Creep," Journal of Applied Mechanics, Transactions of ASME, Paper No. 71-APMW-25, 1971.

1.46 Sarne, Y., "Material Nonlinear Time Dependent Three-dimensional Finite Element Analysis for Reinforced and Prestressed Concrete Structures, Ph.D. Dissertation, Department of Civil Engineering, Massachusetts Institute of Technology, Cambridge, 1975.

1.47 Scordelis, A. C., "Finite Element Analysis of Reinforced Concrete Structures," Proceedings of the Specialty Conference on Finite Element Methods in Civil Engineering, Montreal, June 1972.

1.48 Schnobrich, W. C., "Finite Element Determination of Nonlinear Behavior of Reinforced Concrete Plates and Shells," Proceedings of the Symposium on Nonlinear Techniques and Behavior in Struc-Analysis, Transport and Road Research Laboratory, Department of Environment, England, 1974.

1.49 Schnobrich, W. C., "Behavior of Reinforced Concrete Predicted by Finite Element Method," Proceedings of the Second National Symposium on Computerized Structural Analysis and Design, George Washington University, Washington, D. C., March 1976.

1.50 Wegner, R., "Finite Element Models for Reinforced Concrete," Preprint, Proceedings of the U.S. - Germany Symposium on Formulations and Computational Methods in Finite Element Analysis, Massachusetts Institute of Technology, Cambridge, August 1976.

2.1 Kupfer, H., Hilsdorf, H. K., and Rüsch, H., "Behavior of Concrete under Biaxial Stresses," ACI Journal, V. 66, No. 8, August 1969.

2.2 Bresler, B. and Pister, K. S., "Strength of Concrete under Combined Stress," ACI Journal, V. 55, No. 10, September 1958.

2.3 Liu, T. C., Nilson, A. H., and Slate, F. O., "Stress-Strain Response and Fracture of Concrete in Uniaxial and Biaxial Compression," ACI Journal, V. 69, No. 5, May 1972.

2.4 Robinson, G. S., "Behavior of Concrete in Biaxial Compression," Journal of the Structural Division, ASCE, V. 93, No. ST2, February 1967.

2.5 Atan, Y. and Slate, F. O., "Structural Lightweight Concrete under Biaxial Compression," ACI Journal, V. 70, No. 3, March 1973.

2.6 Buyukozturk, O., Nilson, A. H., and Slate, F. O., "Stress-Strain Response and Fracture of a Concrete Model in Biaxial Loading," ACI Journal, V. 68, No. 8, August 1971.

2.7 Liu, T. C., Nilson, A. H., and Slate, F. O., Biaxial Stress-Strain Relations for Concrete," Journal of the Structural Division, ASCE, V. 98, No. ST5, May 1972.

2.8 Saenz, L. P., Discussion of "Equation for the Stress-Strain Curve of Concrete," by Desayi and Krishnan, ACI Journal, V. 61, No. 9, September 1964.

2.9 Romstad, K. M., Taylor, M. A., and Herrman, L. R., "Numerical Biaxial Characterization for Concrete," Journal of the Engineering Mechanics Division, ASCE, V. 100, No. EM5, October 1974.

2.10 Kupfer, H. B. and Gerstle, K. H., "Behavor of Concrete under Biaxial Stresses," Journal of the Engineering Mechanics Division, ASCE, V. 99, No. EM4, August 1973.

2.11 Chen, A. C. and Chen, W., "Constitutive Relations for Concrete," Journal of the Engineering Mechanics Division, ASCE, V. 101, No. EM4, August 1975.

2.12 Darwin, D. and Pecknold, D., "Inelastic Model for Cyclic Biaxial Loading of Reinforced Concrete," SRS No. 409, University of Illinois at Urbana-Champaign, Illinois, July 1974.

2.13 Bresler, B. and Bertero, V., "Reinforced Concrete Prisms under Repeated Loads," Proceedings of the International Symposium on the Effects of Repeated Loading of Materials and Structural Elements, RILEM, Mexico City, 1966.

2.14 Rajagopal, K. R., "Nonlinear Analysis of Reinforced Concrete Beams, Beam-columns and Slabs by Finite Elements," Ph.D. Dissertation, Iowa State University, Ames, Iowa, 1976.

2.15 Hognestad, E., "A Study of Combined Bending and Axial Load in Reinforced Concrete Members," Bulletin Series No. 399, Bulletin No. 1, Engineering Experiment Station, University of Illinois, 1951.

2.16 Karsan, I. D. and Jirsa, J. O., "Behavior of Concrete under Compressive Loadings," Journal of the Structural Division, ASCE, V. 95, No. ST12, December 1969.

3.1 Freyssinet, E., "The Deformation of Concrete," Concrete Research, No. 8, 1951.

3.2 Vogt, F., "On the Flow and Extensibility of Concrete," Norges Tekniske Hoiskole, Norway, 1935.

3.3 Thomas, F. G., "Creep of Concrete under Load," International Association of Testing Materials, London Congress, April 1937.

3.4 Lynam, C. G., "Growth and Movement in Portland Cement Concrete," Oxford University Press, London, 1934.

3.5 ACI Committee 209, "Prediction of Creep, Shrinkage, and Temperature Effects in Concrete Structures," Paper SP 27-3, ACI Special Publications SP-27, April 1970.

3.6 Klieger, P., "Early High-strength Concrete for Prestressing," Proceedings of the World Conference on Prestressed Concrete, San Francisco, 1957.

3.7 Davis, R. E. and Davis, H. E., "Flow of Concrete under Sustained Compressive Stress," Proceedings, ASTM, Part II, V. 30, 1930.

3.8 Rüsch, H., Kordina, K., and Hilsdorf, H., "Der Einfluss des Mineralogischen Charakters der Zuschläge auf das Kriechen von Beton," Deuscher Ausschuss für Stahlbeton, Bulletin No. 146, 1963.

3.9 Bresler, B. (ed.), Reinforced Concrete Engineering, Volume I, John Wiley and Sons, New York, 1974.

3.10 England, G. L. and Ross, A. D., "Reinforced Concrete under Thermal Gradients," Concrete Research, V. 14, No. 40, March 1962.

3.11 Maréchal, J. C., "Le Fluage du Béton en Fonction de la Temperature," Materials and Structures, V. 2, No. 8, March/April 1969.

3.12 Neville, A. M. and Meyrs, B. L., "Creep of Concrete: Influencing Factors and Prediction," ACI Special Publication SP-9, March 1964.

3.13 Freudenthal, A. M. and Roll, F., "Creep and Creep Recovery of Concrete under High Compressive Stress," ACI Journal, V. 54, No. 12, June 1958.

3.14 Troxell, G. E., Raphael, J. M., and Davis, R. E., "Long-Time Creep and Shrinkage Tests of Plain and Reinforced Concrete," Proceedings, ASTM, V. 58, 1958.

3.15 Volterra, V., "Sur les Equations Integro-Differentielles et Leurs Applications," Acta Mathematica, Stockholm, 1912.

3.16 Lubliner, J. and Sackman, J., "On Aging Viscoelastic Materials," Journal of Mechanics and Physics of Solids, V. 14, 1966.

3.17 Gross, B., Mathematical Structure of the Theories of Viscoelasticity, Herrman, etc., Paris, 1953.

3.18 Mukaddam, M. A., "Behavior of Concrete under Variable Temperature and Loading," Interim Report to Oak Ridge National Laboratory, Reactor Division, Oak Ridge, Tennessee, 1969.

3.19 McHenry, D., "A New Aspect of Creep in Concrete and its Application to Design," Proceedings, ASTM, V. 43, 1943.

3.20 Arutyunyan, ., Some Problems in the Theory of Creep in Concrete Structures, Pergammon Press, New York, 1966.

3.21. Bresler, B. and Selna, L., "Analysis of Time-Dependent Behavior of Reinforced Concrete Structures," ACI Symposium on Creep of Concrete, ACI Special Publication SP-9, 1964.

3.22 Mukaddam, M. A. and Bresler, B., "Behavior of Concrete under Variable Temperature and Loading," ACI Seminar on Concrete for Nuclear Reactors, ACI Special Publication SP-34, 1972.

3.23 Mukaddam, M., "Creep Analysis of Concrete at Elevated Temperatures," ACI Journal, V. 71, No. 2, February 1974.

3.24 Zienkiewicz, O. C. and Cormeau, I. C., "Visco-plasticity--Plasticity and Creep in Elastic Solids--A Unified Numerical Solution Approach," International Journal for Numerical Methods in Engineering, V. 8, 1974.

3.25 Duke, C. M. and Davis, H. E., "Some Properties of Concrete under Sustained Combined Stresses," Proceedings, ASTM, V. 44, 1944.

3.26 Ross, A. D., "Experiments on the Creep of Concrete under Two-Dimensional Stressing,"

3.27 Glanville, W. H. and Thomas, F. G., "Studies in Reinforced Concrete-IV. Further Investigations on Creep or Flow of Concrete under Load," Building Research Technical Paper No. 21, London, 1939.

3.28 L'Hermite, R., "What Do We Know about the Plastic Deformation and Creep of Concrete?," RILEM Bulletin No. 1, March 1959.

3.29 Gopalakrishnan, K. S., Neville, A. M., and Ghali, A., "Creep Poisson's Ratio of Concrete under Multiaxial Compression," ACI Journal, V. 66, No. 12, December 1969.

3.30 Meyer, H. G., "On the Influence of Water Content and of Drying Conditions on Lateral Creep of Plain Concrete," Materials and Structures 2, 1969.

3.31 Neville, A. M., Creep of Concrete: Plain, Reinforced and Prestressed, North Holland Publishing Co., Amsterdam, 1970.

3.32 Roll, F., "Long-time Creep-recovery of Highly Stressed Concrete Cylinders," Symposium on Creep of Concrete, ACI Special Publication SP-9, March 1964

3.33 Becker, J. and Bresler, B., "FIRES-RC, A Computer Program for the Fire Response of Structures--Reinforced Concrete Frames," Report No. UCB FRG 74-3, Division of Structural Engineering and Structural Mechanics, University of California, Berkeley, July 1974.

3.34 King, I. P., "Finite Element Analysis of Two-dimensional Time Dependent Stress Problems," Report No. 65-1, Structures and Materials Research, University of California, Berkeley, 1965.

3.35 Zienkiewicz, O. C. and Watson, M., "Some Creep Effects in Stress Analysis with Particular Reference to Concrete Pressure Vessels," Nuclear Engineering and Design, No. 4, 1966.

3.36 Ross, A. D., "Creep of Concrete under Variable Stress," ACI Journal, V. 64, No. 9, March 1958.

3.37 Browne, R., "Properties of Concrete in Reactor Vessels," Proceedings of Conference on Prestressed Concrete Pressure Vessels, Group C, Paper 13, London, 1967.

4.1 Zienkiewicz, O. C., The Finite Element Method in Engineering Science, 2nd Edition, McGraw-Hill, London, 1971.

4.2 Strang, G. and Fix, G., An Analysis of the Finite Element Method, Prentice-Hall, Inc., Englewood Cliffs, N. J., 1973.

4.3 Turner, M. J., et al., "Stiffness and Deflection Analysis of Complex Structures," Journal of Aeronautical Science, V. 23, 1956.

4.4 Clough, R. W. and Felippa, C. A., "A Refined Quadrilateral Element for Analysis of Plate Bending," Proceedings of the 2nd Conference on Matrix Methods in Structural Mechanics, Wright-Patterson A.F.B., 1968.

4.5 Wilson, E. L., "Solid SAP - A Static Analysis Program for Three Dimensional Solid Structures," UC-SESM Report No. 71-19, University of California, Berkeley, March 1972.

5.1 Washa, G. W. and Fluck, P. G., "Effect of Compressive Reinforcement on the Plastic Flow of Reinforced Concrete Beams," ACI Journal, V. 49, October 1952.

5.2 Sackman, J. L. and Nickell, R. E., "Creep of a Cracked Reinforced Beams," Journal of the Structural Division, ASCE, V. 94, ST1, January 1968.

5.3 "Students Clear Gym Moments before Roof Fails," Engineering News Record, September 24, 1970.

5.4 Schnobrich, W. C., "Analysis of Hipped Roof Hyperbolic Paraboloid Structures," Journal of the Structural Division, ASCE, V. 98, ST7, July 1972.

5.5 Schnobrich, W. C., "Analysis of Hyperbolic Paraboloid Shells," Symposium on Concrete Thin Shells, ACI Special Publication SP-28, 1971.

5.6 Varghese, P. C. and Mathai, A. C., "An Experimental Study of the Behavior of Hyperbolic Paraboloid Shell Roofs under Uniformly Distributed Load," Indian Concrete Journal, January 1971.

APPENDIX A

INPUT INSTRUCTIONS FOR COMPUTER PROGRAM NOTACS

UNIVERSITY OF CALIFORNIA
November 1976

Department of Civil Engineering
Faculty Investigator: A. C. Scordelis

Computer Program for Nonlinear Analysis of Reinforced Concrete Panels, Slabs and Shells for Time-Dependent Effects

IDENTIFICATION

NOTACS - NOnlinear Time-dependent Analysis of Concrete Structures

Programmed by: A. F. Kabir, University of California, November 1976.

PURPOSE

The program is developed to trace the quasi-static responses of reinforced concrete shear panels, slabs of arbitrary geometry and free-form shell-type structures under sustained load conditions. Time-dependent environmental phenomena such as creep and shrinkage effects are considered to obtain the evolution of the field variables of such structures in elastic and inelastic regimes. Ultimate collapse loads are then predicted considering local failure in steel and concrete along with the deterioration of structural stiffness due to progressive cracking.

DESCRIPTION

A finite element tangent stiffness formulation, coupled with a time step integration scheme, is developed to analyze the reinforced concrete systems. Within a time step, an incremental load procedure, with an iterative approach to solve the equilibrium equations for each load increment, is adopted. The composite section of two different materials is modeled as a layer system consisting of concrete and "equivalent smeared" steel layers. Stiffness properties of an element are then obtained by integrating the contributions from all the layers across the section.

The material behavior of concrete is characterized by a nonlinear constitutive relationship for the biaxial state of stress. This includes tensile cracking at a limiting stress level, tensile unloading after cracking and the strain-softening phenomenon beyond the maximum compressive strength. For the deformations in the concrete zones, the effects of stress history, partial creep recovery, aging and temperature variations are considered. These characterize concrete to be an aging, viscoelastic thermorheologically simple material. Creep under the biaxial state of stress is represented by the introduction of Poisson's ratio which is observed in a uniaxial, sustained load test. The reinforcing steel, on the other hand, is represented by a bilinear, strain-hardening model exhibiting the Bauschinger effect. The unloading path due to stress reversal is also prescribed in the constitutive laws assumed for both steel and concrete.

The program is coded in the FORTRAN IV language. The blank common is dynamically dimensioned to either expand or shorten the blank common length to exactly match the requirements of the problem under consideration. This option makes it possible to use the central memory capacity of the computer in a very efficient manner greatly reducing the computer costs.

RESTRICTIONS

The numbers of nodal points, elements, load and time steps are restricted only by the available capacity of the computer. Other restrictions as to the maximum number of types of material properties and layer systems are given under input instructions.

FORM OF INPUT DATA

It is very important that the sequential order in the input of data is strictly adhered to and consistent units are used throughout a problem.

1. TITLE CARD (12A6)

Col. 1 to 72 - HED(I) = Title of problem to be printed with output for identification.

2. CONTROL CARD (8I5)

Col. 1 to 5 - NUMNP = number of nodal points

Col. 6 to 10 - NELTYP = number of element types

Col. 11 to 15 - NTIME = number of times at which analyses is requested

Col. 16 to 20 - ICREEP = creep analysis indicator
0 no analysis
1 analysis desired

Col. 21 to 25 - ISHRINK = shrinkage analysis indicator
0 no analysis
1 analysis desired

Col. 26 to 30 - NORM = convergence norm indicator
0 force norm
1 displacement norm

Col. 31 to 35 - KNORM = norm data indicator
0 norm values taken as percentages of previous force or displacement increment
1 input norm values

Col. 36 to 40 - KULT = ultimate analysis indicator
0 only ultimate analysis not required
1 only ultimate analysis required

3. OUTPUT CONTROL CARD (5I5)

Col. 1 to 5 - KOUT = output indicator
0 output at the end of all iterations
1 output at each iteration

Col. 6 to 10 - KDIS = output indicator for displacements in the element coordinates
0 no output
1 output desired

Col. 11 to 15 - KCUR = output indicator for curvature
0 no output
1 output desired

Col. 16 to 20 - KSTN = output indicator for strain
0 no output
1 output desired

Col. 21 to 25 - KITER = output indicator for unbalanced nodal loads
0 output for last iteration only
1 output for each iteration

4. CONVERGENCE NORM CARDS

a. FIRST CARD - FORCE OR DISPLACEMENT TOLERANCES (6F10.0)

Col. 1 to 10 - TOLER(1) = tolerance for force or displacement in global X-direction

Col. 11 to 20 - TOLER(2) = tolerance for force or displacement in global Y-direction

Col. 21 to 30 - TOLER(3) = tolerance for force or displacement in global Z-direction

Col. 31 to 40 - TOLER(4) = tolerance for moment or rotation about global X-direction

Col. 41 to 50 - TOLER(5) = tolerance for moment or rotation about global Y-direction

Col. 51 to 60 - TOLER(6) = tolerance for moment or rotation about global Z-direction

b. SECOND CARD - MAXIMUM ALLOWABLE VALUES (6F10.0)

Col. 1 to 10 - VMAX(1) = maximum force or displacement in global X-direction

Col. 11 to 20 - VMAX(2) = maximum force or displacement in global Y-direction

Col. 21 to 30 - VMAX(3) = maximum force or displacement in global Z-direction

Col. 31 to 40 - VMAX(4) = maximum moment or rotation about global X-direction

Col. 41 to 50 - VMAX(5) = maximum moment or rotation about global Y-direction

Col. 51 to 60 - VMAX(6) = maximum moment or rotation about global Z-direction

Note: (1) Global coordinate system XYZ follows a right hand rule and is shown in Fig. 1.

(2) The iteration for a given load step will stop when the magnitude of every component of the changes in nodal displacement or the resultant unbalanced nodal forces become smaller than its prescribed tolerances.

(3) The solution procedure is stopped when the magnitude of any component of the changes in nodal displacement or resultant unbalanced nodal forces for the above load step exceeds its prescribed maximum allowable value.

5. DAYS CARD (8F10.0)

Col. 1 to 80 - DAYS(I) = days after casting at which time each analysis is required. Total number of entries equals NTIME.

6. NODAL POINT COORDINATE CARD (7I5, 3F10.0, I5)

Col. 1 to 5 - N = node number

Col. 6 to 10 - ID(1,N) = translation in global X-direction

Col. 11 to 15 - ID(2,N) = translation in global Y-direction

Col. 16 to 20 - ID(3,N) = translation in global Z-direction

Col. 21 to 25 - ID(4,N) = rotation about global X-direction

Col. 26 to 30 - ID(5,N) = rotation about global Y-direction

Col. 31 to 35 - ID(6,N) = rotation about global Z-direction

boundary condition codes

0 free to move in the prescribed direction

1 fixed in the prescribed direction

Col. 36 to 45 - X(N) = global X-ordinate

Col. 46 to 55 - Y(N) = global Y-ordinate

Col. 56 to 65 - Z(N) = global Z-ordinate

Col. 66 to 70 - KN = node generation parameter

Note (1) The nodal point cards need not be in node-order sequence, but the node with the largest number has to be the last card. If cards are omitted, then nodal data for a series of nodes are generated. KN, the generation parameter on the last card of a mesh generation sequence, is the increment to be added to the previous nodal point number. The intermediate nodes are located at equal intervals along the straight line connecting the first and the last node specified. The boundary condition codes for the generated nodes are set equal to those for the first node in the series.

(2) Severe numerical difficulties may arise in the solution of the equilibrium equations if the stiffness associated with any global direction is zero or very close to zero. These difficulties may be avoided by restraining the degrees of freedom in the appropriate directions by the application of the boundary condition codes. The restraining of any degree of freedom causes the elimination of the equilibrium equation associated with that particular degree of freedom and thus prevent any instability in the solution of the equilibrium equations. The value of a global stiffness may become zero due to any one of the following reasons.

In the stiffness formulation for the plane stress element, the translational degree of freedom normal to the plane of the element and all the three rotational degrees of freedom are not considered. So, all the three global rotations must be constrained at a node where only plane stress elements meet. Furthermore, if these plane stress elements lie in the same global plane then the global translational degree of freedom associated with the direction normal to the plane of the elements must also be constrained.

For the plate bending element the three in-plane degrees of freedom, two translations and one rotation, are not considered in the element stiffness formulation. At any node, where only plate bending elements lying in the same global plane meet, the three global degrees of freedom associated with the two in-plane translations and one in-plane rotation must be constrained.

For the shell element, the in-plane rotation is not considered in the stiffness formulation. The in-plane rotation, at any node where coplanar shell element meet, is constrained if its direction coincides with the global direction. If the direction does not coincide with the global direction, then a fictitious rotational stiffness, about the normal to the shell surface at the node, is provided by a boundary spring element. The value of the fictitious rotational stiffness is taken to be about 10% of the bending stiffness of the shell to avoid any ill-conditioning due to large off-diagonal terms in the structural stiffness matrix which may occur if a very large value is used and the rotational stiffness contributes to more than one global degree of freedom.

7. ELEMENT GROUP CARDS

A sequence of cards is required for each type of element in the structure. The form of input data for each type will be described later.

8. LOAD CARDS

These cards are to be repeated for NTIME steps.

a. FIRST CARD - LOAD PARAMETERS (3I5, 3F10.0, 2I5)

Col. 1 to 5 - NLSTEP = number of load steps

Col. 6 to 10 - NITER = number of iterations allowed

Col. 11 to 15 - NLJ = number of loaded nodes

Col. 16 to 25 - PDL = fraction of dead load

Col. 26 to 35 - PDSL = fraction of distributed surface load

Col. 36 to 45 - PSPL = fraction of spring load

Col. 46 to 50 - NSTIM = number of load steps for creep and shrinkage analysis

Col. 51 to 55 - NITERT = number of iterations allowed for creep and shrinkage analysis

b. SECOND CARD - CONCENTRATED NODAL LOADS (I5, 6F10.0)

Omit this card if NLJ = 0, otherwise input NLJ cards

Col. 1 to 5 - N = node number

Col. 6 to 15 - RB(1) = concentrated load in global X-direction

RB(2) = concentrated load in global Y-direction

RB(3) = concentrated load in global Z-direction

RB(4) = concentrated moment about global X-direction

RB(5) = concentrated moment about global Y-direction

RB(6) = concentrated moment about global Z-direction

9. All the above data cards 1-8 are repeated for next problem to be solved.

10. Two blank cards are added at the end of the complete data deck.

7. ELEMENT GROUP CARDS

A. TYPE 1 - TRIANGULAR ELEMENTS

Three options are included in the triangular element formulation to take into account membrane action only, plate bending action only, and a combination of membrane and plate bending actions. Shear panels are usually assumed to be under membrane action only. Most of the slabs carry loads predominantly through plate bending action. Most of the shell-type structures respond to loads in a manner which may be described as a combination of membrane and plate bending actions. So, appropriate choices of any of the above options may be made to model shear panels, slabs, and shells for analysis.

A constant strain triangular (CST) element is used to model the membrane behavior while a linearly constrained curvature triangular (LCCT 9) element models the plate bending behavior. A combination of the above two elements is used to model the behavior of shell-type structures. The element cross-section is modeled as a layered system consisting of concrete and "equivalent smeared" steel layers. Variations of properties through the depth are then accommodated by allowing each layer to have different properties due to different materials or levels of deformation. A restriction is placed on the type of layer system that can be used for an element using the option of membrane action only. Since only in-plane forces are assumed to exist in such an element, the material properties about the mid-depth reference surface must be symmetric. Usually, one layer of concrete may be used to model elements using the option of membrane action only. The degrees of freedom associated with the above mentioned elements are illustrated in Fig. 2.

A1. CONTROL CARDS

a. FIRST CARD - ELEMENT TYPE (I5)

Col. 1 to 5 - NTYPE = type of element, input 1 for this case.

b. SECOND CARD - PROPERTY INDICATORS (5I5)

Col. 1 to 5 - NUMSH = number of triangular elements

Col. 6 to 10 - NUMCN = number of concrete material types, maxm. 4

Col. 11 to 15 - NUMST = number of steel material types, maxm. 6

Col. 16 to 20 - NTCL = number of types of concrete layer systems, maxm. 10

Col. 21 to 25 - NTSL = number of types of steel layer systems, maxm. 7

A2. CONCRETE MATERIAL PROPERTY CARDS

These cards are to be repeated for NUMCN times.

a. FIRST CARD - PROPERTY INDICATORS (4I5, 3F10.0)

Col. 1 to 5 - I = material type number

Col. 6 to 10 - JMT(I) = elastic material data indicator
1 input data
2 ACI formulae used

Col. 11 to 15 - JCR(I) = creep data indicator
1 input data
2 ACI formulae used

Col. 16 to 20 - JSH(I) = shrinkage data indicator
1 input data
2 ACI formulae used

Col. 21 to 30 - FC28(I) = compressive strength at 28 days after casting

Col. 31 to 40 - CNU(I) = Poisson's ratio

Col. 41 to 50 - RHO(I) = weight per unit volume

b. SECOND CARD - ELASTIC MATERIAL PROPERTIES (6F10.0)

Omit this card if JMT(I) = 2.

Col. 1 to 10 - EC(I) = modulus of elasticity, E_c

Col. 11 to 20 - FCC(I) = compressive strength, f'_c

Col. 21 to 30 - FTC(I) = tensile strength, f'_t

Col. 31 to 40 - CSC(I) = cracked shear constant, β

Col. 41 to 50 - USC(I) = ultimate compressive strain, ε_u

Col. 51 to 60 - UST(I) = ultimate tensile strain, ε_{ut}

c. CREEP DATA CARDS

Omit these cards if JCR(I) = 2. Otherwise, creep coefficients $a_i(\tau)$ and λ_i are to be provided from experimental creep curves. A computer program, employing the method outlined in the present study (pages 68-69, Sub-section 3.2.8) may be used.

c1. FIRST CARD - CONTROL PARAMETERS (2I5)

Col. 1 to 5 - NAGE(I) = number of ages at loading, τ, for which creep curves are generated, maxm. 15

Col. 6 to 10 - NSER(I) = number of terms in the creep compliance series, maxm. 4

c2. SECOND CARD - AGES OF CONCRETE, τ (8F10.0)

Col. 1 to 80 - SAGE(I,J) = ages for which creep curves are given, N=1,NAGE(I). Use second card if necessary.

c3. THIRD CARD - AGE SCALE FACTORS, $a_i(\tau)$(3E15.8)

Col. 1 to 45 - ACI(I,J) = age scale factors for creep compliance, J=1,NAGE(I)*NSER(I)

c4. FOURTH CARD - CREEP EXPONENTIAL FACTORS, λ_i (4F10.0)

Col. 1 to 40 - W1(I,J) = creep exponential factors, J=1,NSER(I)

c5. FIFTH CARD - TEMPERATURE SHIFT COEFFICIENTS, $\phi(T)$ (4F10.0)

Col. 1 to 40 - W2(I,J) = temperature shift coefficients, maxm. 4

d. SHRINKAGE DATA CARDS (3E15.8)

Omit these cards if JSH(I) = 2

Col. 1 to 45 - TEPSS(I,N) = total shrinkage strains at days when analysis needed, N=1,NTIME. Use second or more cards if necessary

e. CONCRETE MIX PARAMETERS (3F10.0)

If ACI formulae are not used for creep and shrinkage data, then standard mix parameters--SLUMP(I) = 2.7, SIZE(I) = 6.0 and RH(I) = 40.0--are to be input.

Col. 1 to 10 - SLUMP(I) = slump of concrete in inches

Col. 11 to 20 - SIZE(I) = maximum size of members in inches

Col. 21 to 30 - RH(I) = relative environmental humidity in percent

A3. STEEL MATERIAL PROPERTY CARD (I5, 3F10.0)

This card is to be repeated for NUMST times. No card is needed if NUMST = 0.

Col. 1 to 5 - N = steel material type number

Col. 6 to 15 - ES(N) = Young's modulus

Col. 16 to 25 - FYS(N) = yield stress

Col. 26 to 35 - ESTAR(N) = modulus for the strain-hardening portion

A4. CONCRETE LAYER SYSTEM CARDS

Repeat these cards for NTCL times.

a. FIRST CARD - CONTROL PARAMETERS (2I5)

Col. 1 to 5 - L = layer system type number

Col. 6 to 10 - NCLAY(L) = number of concrete layers, maxm. 20

b. SECOND CARD - LAYER DEPTH COORDINATES (8F10.0)

Col. 1 to 80 - ZC(J,L) = $\bar{z}$ coordinates to the layer boundaries, J=1, NCLAY(L)+1. Use second or more cards if necessary. See Fig. 3 for sign convention of $\bar{z}$ coordinates.

A5. STEEL LAYER SYSTEM CARDS

Repeat for NTSL times. Omit if NTSL = 0.

a. FIRST CARD - CONTROL PARAMETERS (3I5)

Col. 1 to 5 - L = layer system number

Col. 6 to 10 - NSLAY(L) = number of layers, maxm. 7

Col. 11 to 15 - IANG(L) = angle index

b. SECOND CARD - LAYER DATA (2I5, 3F10.0)

Repeat this card for NSLAY(L) times.

Col. 1 to 5 - J = layer number

Col. 6 to 10 - MTN(J,L) = material type number

Col. 11 to 20 - ZS(J,L) = $\bar{z}$ coordinate to center of the layer

Col. 21 to 30 - PS(J,L) = smeared thickness

Col. 31 to 40 - ALPH(J,L)= angle in degrees defining the direction of the reinforcement

Note (1) In Fig. 4 if S be the direction of the reinforcing bars, S' be the projection of S on the global X-Y plane, then

ALPH = α if IANG = 0

ALPH = β if IANG = 1

(2) Smeared thickness PS is given by PS = A_s/b, where A_s = area of one reinforcing bar and b = spacing between the bars as illustrated in Fig. 3.

A6. GRAVITY LOAD CARD (3F10.0)

Col. 1 to 10 - GM(1) = gravity load multiplier in X-direction

Col. 11 to 20 - GM(2) = gravity load multiplier in Y-direction

Col. 21 to 30 - GM(3) = gravity load multiplier in Z-direction

Note (1) Gravity load distributed in each of the global X,Y,Z directions is equal to the multiplier times the dead weight of concrete.

A7. ELEMENT LAYOUT CARDS (8I5, F5.0, I5, 4F7.0, I2)

Repeat for NUMSH times unless generated.

Col. 1 to 5 - MM = element number

Col. 6 to 10 - NODE(1) = node I

Col. 11 to 15 - NODE(2) = node J

Col. 16 to 20 - NODE(3) = node K

Col. 21 to 25 - MC = concrete material property indicator

Col. 26 to 30 - NCL = concrete layer system number

Col. 31 to 35 - NSL = steel layer system number

Col. 36 to 40 - LOCO = local coordinate system control code
0 element coordinate system ties with nodes I and J
1 element coordinate system is defined by specifying $\bar{x}$
2 element coordinate system is defined by specifying $\bar{y}$

Col. 41 to 45 - ANLO = angle in degrees from X-axis to projection of $\bar{x}$ or $\bar{y}$ on XY plane

Col. 46 to 50 - KN = element data generator parameter

Col. 51 to 57 - PN = uniformly distributed load normal to surface per unit surface area

Col. 58 to 64 - PT(1) = uniformly distributed load in X-direction per unit area on YZ plane

Col. 65 to 71 - PT(2) = uniformly distributed load in Y-direction per unit area on XZ plane

Col. 72 to 78 - PT(3) = uniformly distributed load in Z-direction per unit area on XY plane

Col. 79 to 80 - KOPT = element option
0 triangular shell element, CST + LCCT9
1 triangular membrane element, CST
2 triangular plate bending element, LCCT9

Note (1) Nodes I, J, and K are in counterclockwise order about $+\bar{z}$ axis (Fig. 5).

(2) Element cards must be in element number sequence. If cards are omitted, element data will be generated. The increment for the element number is one. The corresponding increment for nodal numbers is KN, i.e.

$$I_{i+1} = I_i + KN$$

$$J_{i+1} = J_i + KN$$

$$K_{i+1} = K_i + KN$$

(3) Concrete properties, layer systems, local coordinate systems, distributed loads and element option for the generated elements are the same as the first element in the series.

(4) Only the element number and KN need to be specified on the last card in a mesh generation sequence on which the variable NODE(1) is used as a control code for the computation of the element stiffness in the following way:

NODE(1) = -1: The element stiffness is the same as the first element in the series in both local and global coordinate systems. This occurs often in the slabs.

NODE(2) = -2: The element stiffness is the same as the first element in the series in their own local coordinates, but different in global coordinates, as sometimes happens in curved shells.

Otherwise, new element stiffness will be formed for each generated element.

(5) The local element coordinate system $\overline{xyz}$ is also a right-handed system similar to the global coordinate system XYZ (Fig. 6). Three options may be used to define the local element coordinate system (Fig. 6).

Case 1: LOCO = 0 $\bar{x}$ coincides with side IJ

Case 2: LOCO = 1 $\bar{x}$ is defined by specifying α

Case 3: LOCO = 2 $\bar{y}$ is defined by specifying β

$\overline{xy}$ is in the plane of triangle IJK. $\bar{z}$ is perpendicular to $\overline{xy}$ plane and its direction is given by the right hand rule. $\bar{x}'$, $\bar{y}'$ are the projections of $\bar{x}, \bar{y}$ on the global XY plane respectively.

B. TYPE 2 - BOUNDARY ELEMENT

a. FIRST CARD - TYPE PARAMETER (I5)

Col. 1 to 5 - NTYPE = element type number, input 2 for boundary elements

b. SECOND CARD - NUMBER OF ELEMENTS (I5)

Col. 1 to 5 - NUMBD = number of boundary elements

c. THIRD CARD - ELEMENT DATA (8I5, 2F10.0, E10.0)

One card per element (in ascending node N order) except where automatic element generation is used.

Col. 1 to 5 - N = node at which element is placed

Col. 6 to 10 - I = node I } nodes defining the direction

Col. 11 to 15 - J = node J } of boundary element, Fig. 7

Col. 16 to 20 - K = node K } Leave columns 11 to 25 blank

Col. 21 to 25 - L = node L } if only node I is needed.

Col. 26 to 30 - KD = code for translational displacement

Col. 31 to 35 - KR = code for rotational displacement

Col. 36 to 40 - KN = data generation parameter

Col. 41 to 50 - SD = specified translation along element axis

Col. 51 to 60 - SR = specified rotation about element axis

Col. 61 to 70 - TRACE = spring stiffness (set to 10^{10} if left blank) for translation and/or rotation

Note (1) The direction of the boundary element at node N is to be specified. This may be done in one of two ways (Fig. 7):

Case 1: A second nodal point I defines the positive direction of the element from node I to node N.

Case 2: Four nodal points I, J, K, and L specify the positive direction of the element as the normal to the plane defined by two intersecting straight lines (vectors $\underset{\wedge}{a}$ and $\underset{\wedge}{b}$ in Fig. 7).

Boundary elements are used in the analyses of thin shells to model the rotational constraint about the surface normal as shown in Fig. 7. $\underset{\wedge}{n}$ is given by the vector cross product $\underset{\wedge}{n} = \underset{\wedge}{a} \times \underset{\wedge}{b}$. The positive direction of the boundary element corresponds to the direction of $\underset{\wedge}{n}$.

Node I in Case 1 and nodes I, J, K, and L in Case 2 are used only to define the direction of the element, and if convenient may be any nodes used to define other elements. "Artificial nodes" may also be created to define directions of the boundary elements. These "artificial nodes" are input in the nodal point coordinate cards with all the boundary condition codes specified as 1.

The positive directions of the internal forces in the boundary element and their corresponding reactions acting on node N are shown in Fig. 7.

(2) The code for translational displacement, KD, may be either 0 or 1.

KD = 0: The node N is free to translate and the translational stiffness of the boundary is set to zero.

KD = 1: The translation SD and the spring stiffness TRACE are used by the program in the following way. The load P = TRACE*SD is applied at node N in the positive direction of the element if SD is positive. If TRACE is much greater than the stiffness of the structure at node N without the boundary element, then the net effect is to produce a displacement very nearly equal to SD. This code is used to find reactions at supports by setting SD = 0 and a high value for TRACE (TRACE = 10^{10} is automatically set if so desired).

(3) The code for rotation, KR, may be either 0 or 1. These two cases are completely analogous to the two cases for KD.

(4) Data generation parameter KN is used when a series of nodes are such that

(a) all have identical boundary element attached,

(b) all boundary elements have same directions,

(c) all specified displacements and rotations are identical, and

(d) the nodal sequence forms an arithmatic sequence, i.e., N, N+KN, N+2KN, and so on. In such cases, only the first and the last nodes in the sequence need to be input. KN is input in the last card of the sequence.

C. TYPE 3 - ONE-DIMENSIONAL TRUSS ELEMENT

This element was used to analyze concrete cylinders in Chapter 3 of the present study by employing a separate computer program. The element, however, will be incorporated into the program NOTACS at a later date.

OUTPUT DESCRIPTION

The output consists of two parts as follows.

A. INPUT CHECK PRINTOUT

The complete input and generated data are properly labelled and printed and may be used to check up on possible errors in punching, field specifications, and order of cards.

B. RESULTS

The results consist of the following quantities.

1. Time step, load step, and iteration numbers.
2. Total external nodal forces in the global coordinates.
3. Unbalanced nodal forces in the global coordinates.
4. Total nodal displacements in the global coordinates.
5. The following results for each triangular element.
    a. Centroidal curvatures in the local coordinates, if requested.
    b. Nodal displacements in local coordinates, if requested.
    c. Stresses in the local coordinates and material state and stress reversal indices for each concrete layer and steel layer.
    d. Elastic strains in the local coordinates for each concrete and steel layer, if requested.
    e. Creep strains in the local coordinates for each concrete layer, if creep analysis is performed.
    f. Shrinkage strains in the local coordinates for each concrete layer, if shrinkage analysis is performed.
6. The extensional and rotational stresses in each boundary element.

Note (1) Concrete layer stresses are output in the local coordinate system with positive directions defined in Fig. 8. The principal stresses, σ_1 and σ_2 (where $\sigma_1 > \sigma_2$) are also output and the angle α defining the principal direction and its projection α' in the global plane XY (Fig. 8). Crack directions are generally perpendicular to the principal direction 1. Tensile stress is positive and compressive stress is negative in sign.

(2) Explanation on the material state and stress reversal indices are printed at the end of all the triangular element output.

(3) Steel layer stress is in the direction of reinforcing bars. Tensile stresses are assumed positive while compressive stresses are taken to be negative.

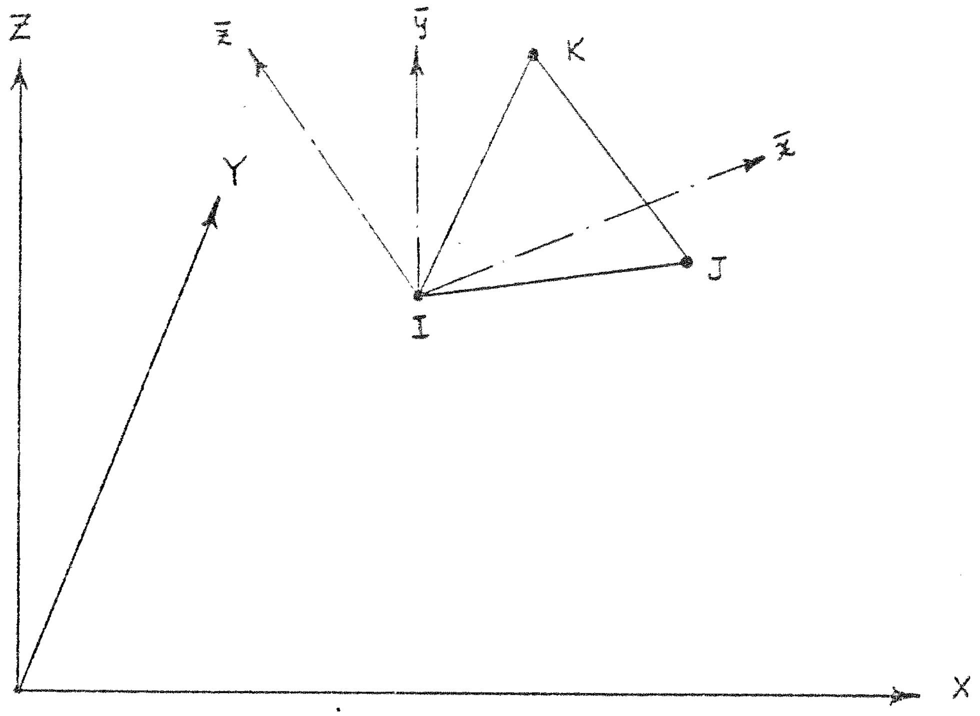

XYZ = GLOBAL COORDINATE SYSTEM, FOLLOWS RIGHT-HAND RULE

$\bar{x}\bar{y}\bar{z}$ = LOCAL ELEMENT COORDINATE SYSTEM, FOLLOWS RIGHT-HAND RULE SUCH THAT $\bar{z}$ IS PERPENDICULAR TO THE PLANE OF THE ELEMENT IJK. $\bar{x}$ AND $\bar{y}$ DEFINE THE PLANE OF THE ELEMENT IJK

FIG. 1 GLOBAL AND LOCAL ELEMENT COORDINATE SYSTEMS

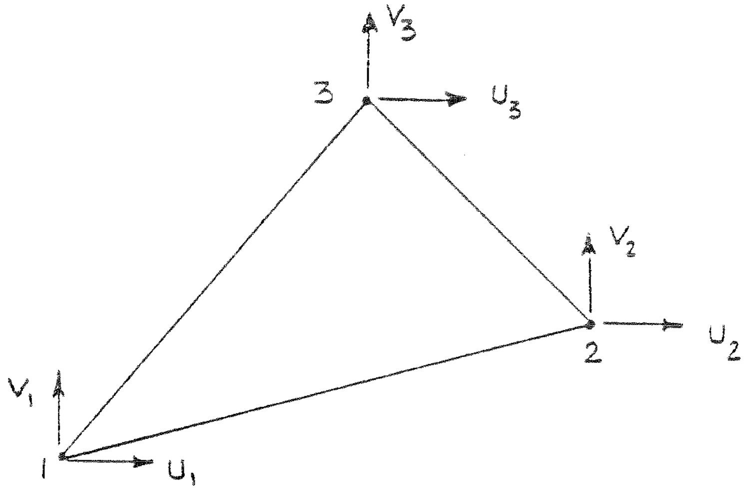

a. TRIANGULAR MEMBRANE ELEMENT (CST)

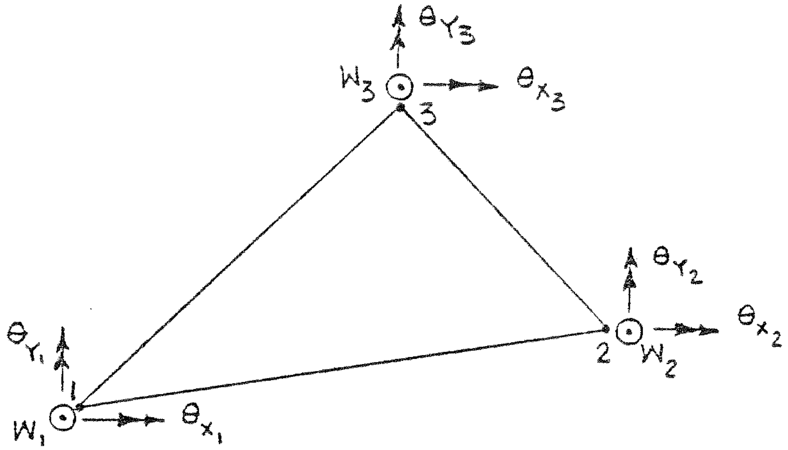

b. TRIANGULAR PLATE BENDING ELEMENT (LCCT9)

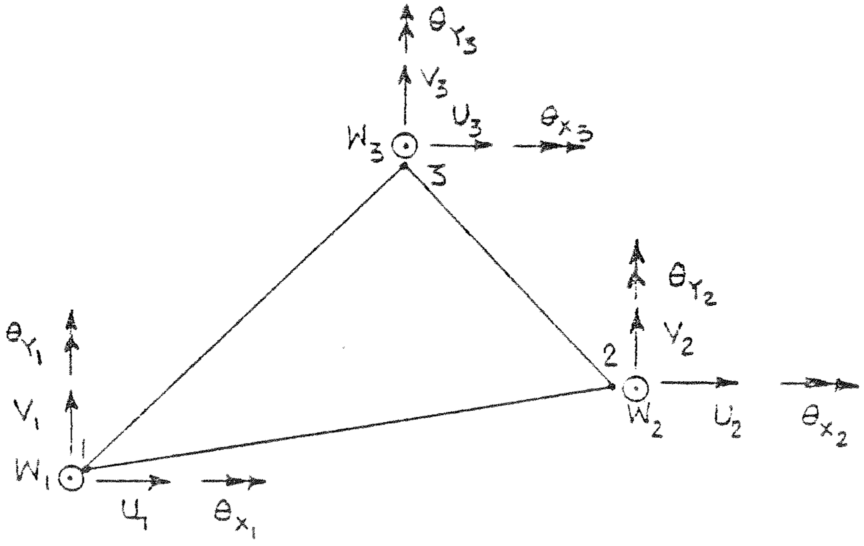

c. TRIANGULAR SHELL ELEMENT (CST+LCCT9)

FIG. 2 TRIANGULAR FINITE ELEMENTS

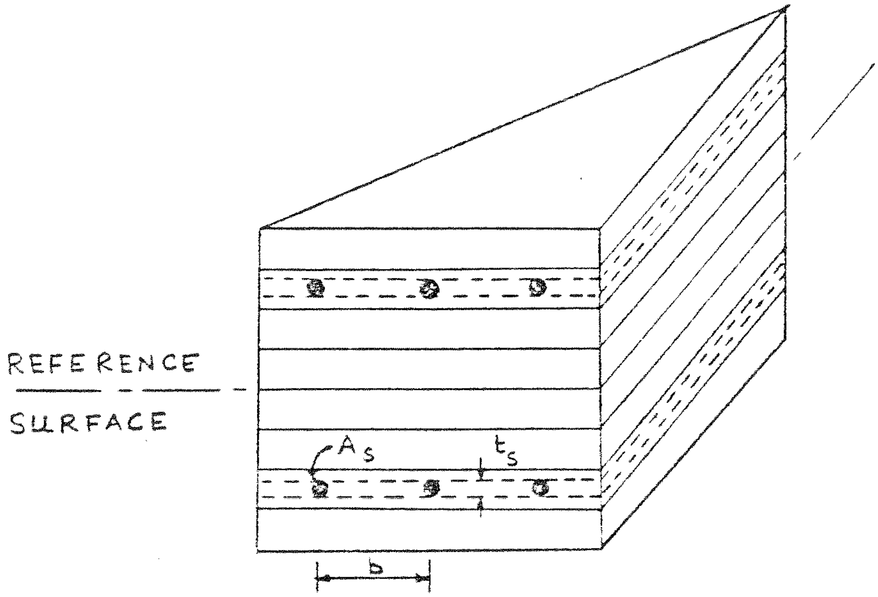

a. CONCRETE AND 'EQUIVALENT SMEARED' STEEL LAYERS

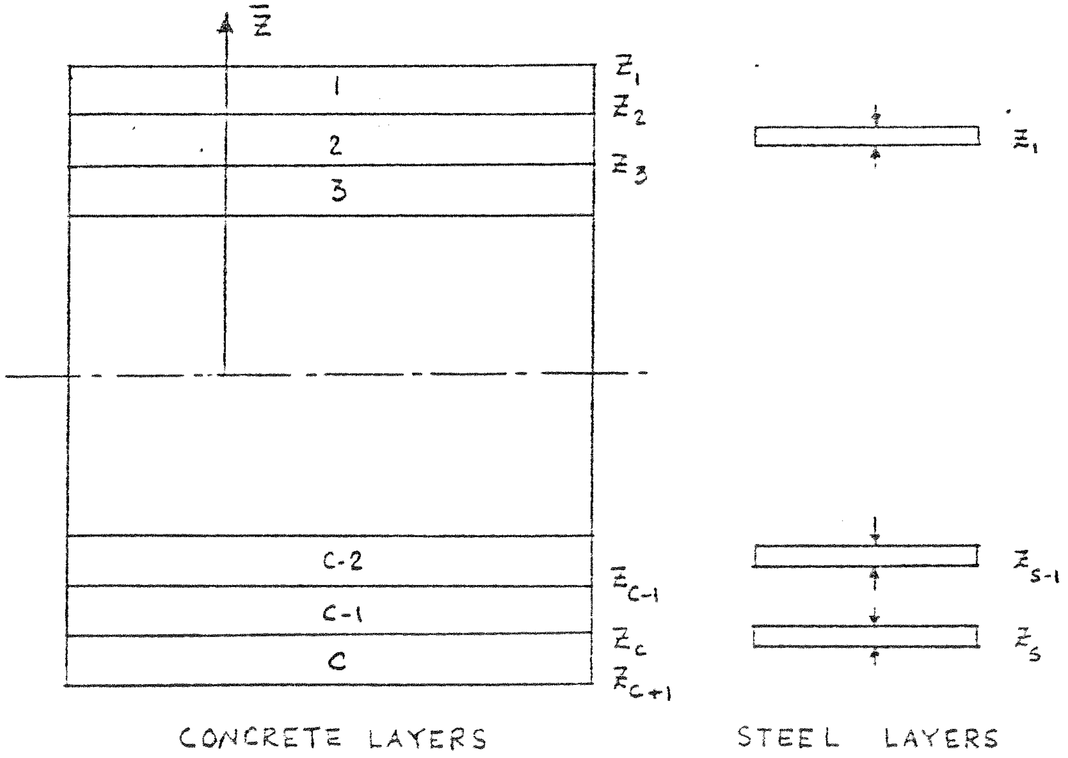

b. LAYER SYSTEM OF A TRIANGULAR ELEMENT

FIG. 3 LAYER SYSTEM OF A TRIANGULAR ELEMENT

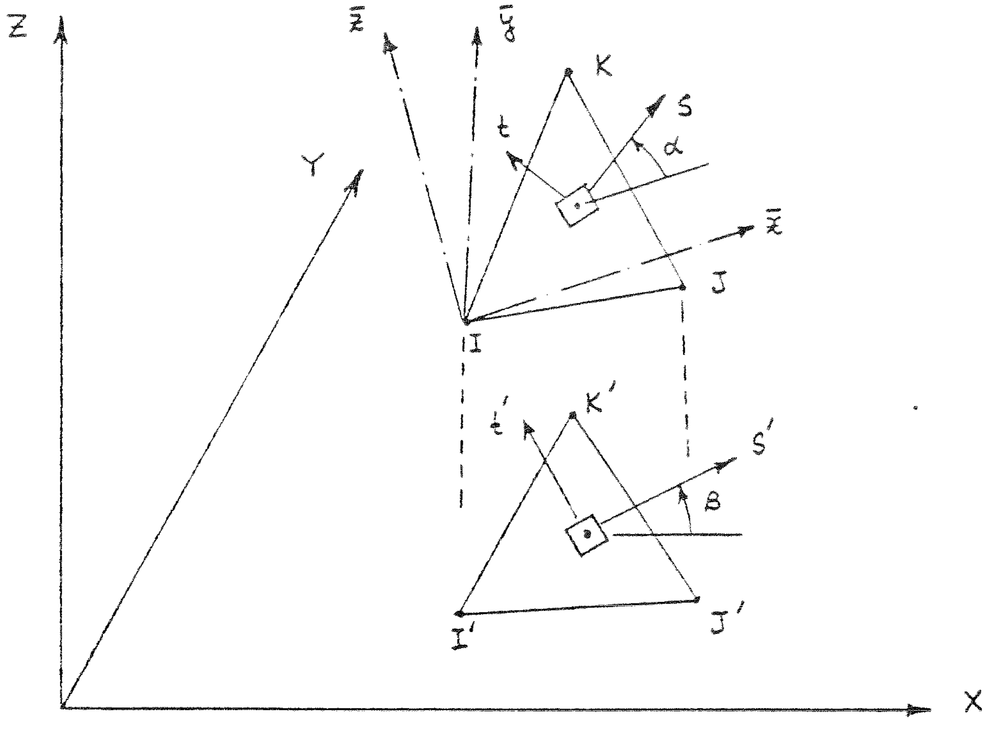

XYZ = GLOBAL COORDINATE SYSTEM

$\bar{x}\bar{y}\bar{z}$ = LOCAL ELEMENT COORDINATE SYSTEM ($\bar{z} \perp \Delta IJK$)

S = DIRECTION OF REINFORCING BAR IN THE PLANE OF ΔIJK

S' = PROJECTION OF S-AXIS TO GLOBAL XY PLANE

α = ANGLE FROM $\bar{x}$ TO S

β = ANGLE FROM X TO S'

FIG. 4 DIRECTION OF THE REINFORCING BARS IN A TRIANGULAR ELEMENT

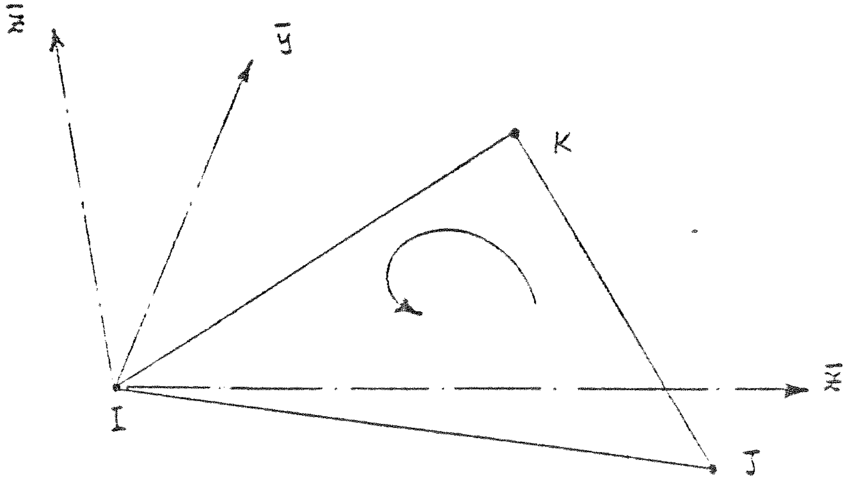

FIG. 5 NODE LAYOUT OF A TRIANGULAR ELEMENT

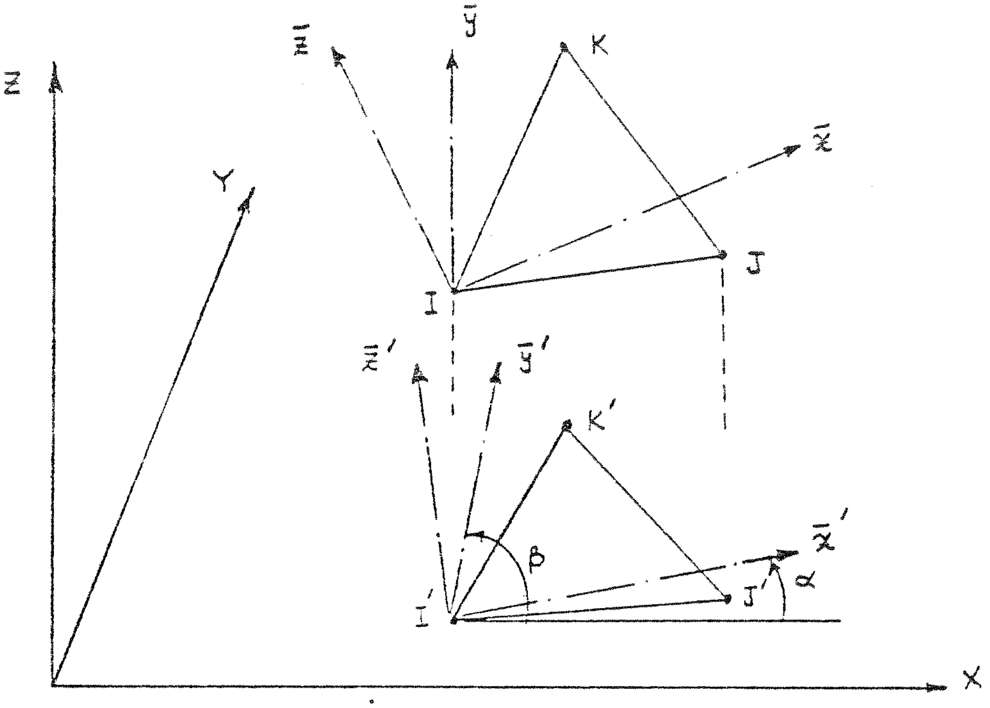

XYZ = GLOBAL COORDINATE SYSTEM

$\bar{x}\bar{y}\bar{z}$ = LOCAL ELEMENT COORDINATE SYSTEM

ΔIJK = ELEMENT WITH NODES IJK

ΔI'J'K' = ΔIJK PROJECTED ON GLOBAL XY PLANE

$\bar{x}'\bar{y}'\bar{z}'$ = PROJECTION OF $\bar{x}\bar{y}\bar{z}$ ON XY PLANE

CASE 1 : LOCO = 0 $\bar{x}$ COINCIDES WITH IJ
CASE 2 : LOCO = 1 $\bar{x}$ IS DEFINED BY SPECIFYING α
CASE 3 : LOCO = 2 $\bar{y}$ IS DEFINED BY SPECIFYING β

FIG. 6 DEFINITION OF LOCAL ELEMENT COORDINATE SYSTEM

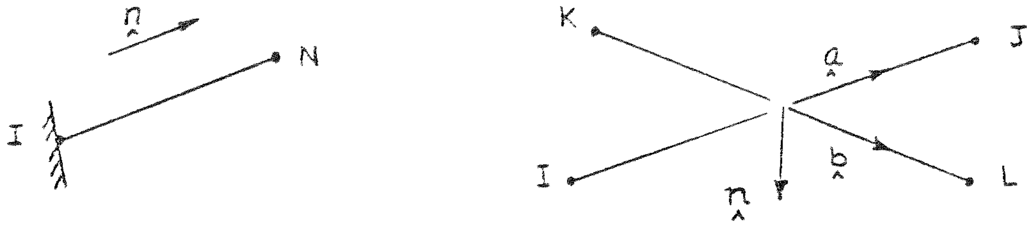

a. POSITIVE DIRECTIONS OF THE BOUNDARY ELEMENT

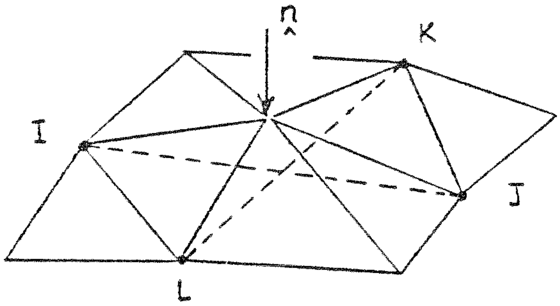

b. ROTATIONAL RESTRAINT ABOUT THE SURFACE NORMAL OF A THIN SHELL

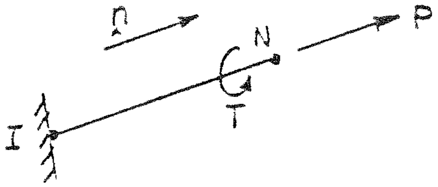

c. POSITIVE FORCES ON BOUNDARY ELEMENT

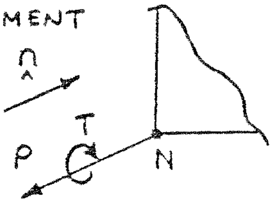

d. POSITIVE REACTIONS AT NODE N

FIG. 7 BOUNDARY ELEMENT

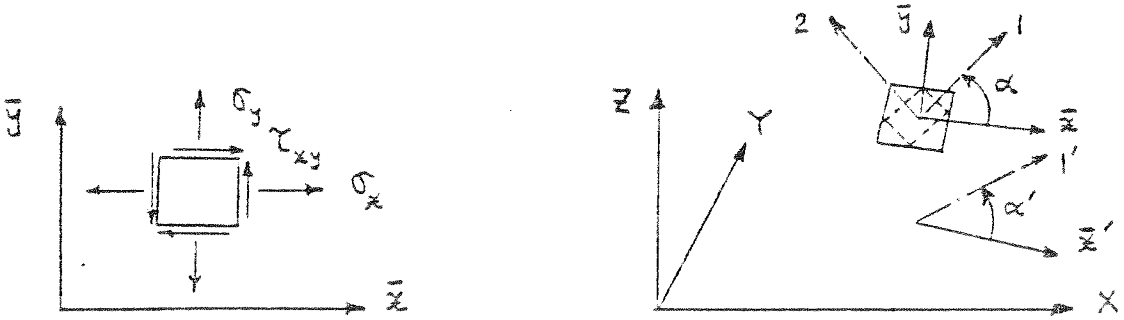

FIG. 8 SIGN CONVENTION FOR STRESS OUTPUT